UNIVERSITY OF SOUTHAMPTON

MULTI-WATT, DIODE-PUMPED PLANAR WAVEGUIDE LASERS

Catherine Louise Bonner

Submitted for the degree of Doctor of Philosophy

FACULTY OF SCIENCE

DEPARTMENT OF PHYSICS

MARCH 2000

UNIVERSITY OF SOUTHAMPTON

ABSTRACT

FACULTY OF SCIENCE
PHYSICS

Doctor of Philosophy

MULTI-WATT, DIODE PUMPED PLANAR WAVEGUIDE LASERS

By Catherine Louise Bonner

This thesis reports on progress towards diode-bar pumped crystal waveguide lasers with a hig power, high-quality output.

It is shown that in order to accommodate the highly divergent, non-diffraction limited output from diode-bar pump source, a waveguide with a relatively high numerical aperture (NA) is required. selection of suitable waveguide fabrication techniques, including liquid phase epitaxy (LPE), puls laser deposition (PLD) and direct bonding, were investigated. A Nd:GGG on YAG waveguid fabricated by PLD was found to have a loss <0.5dB/cm, the lowest so far reported for a PLD laye The waveguide lased on the four-level laser transition at around 1μm and, for the first time, on th quasi-three-level transition, around 940nm. However, the fluorescence spectrum of the guide wa significantly broadened with respect to bulk grown crystals. The fabrication technique of direc bonding was found to reliably produce good quality waveguides with losses <0.5dB/cm and in som cases as low as 0.2dB/cm. The waveguides had spectroscopic characteristics of the bulk material an the technique accommodates a wide range of material combinations. Both low and high NA structur can be fabricated and Nd:GGG/YAG (NA=0.75), Nd:YAG/YAG (NA=0.06), Nd:YAG/sapphir (NA=0.46) and Nd:YAG/glass (NA=0.82) direct bonded waveguide lasers were demonstrated.

Pumping the volume of a planar waveguide with the high average power of a diode-bar can lead to high inversion density and a high thermal load. This novel pumping regime was investigate experimentally and theoretically modelled. In parallel spectroscopic measurements by Dr. Stepha Guy at the University of Lyon, the Auger upconversion rate in Nd:YAG was measured to be $7x10^{3}s^{-1}$ significantly lower than had been reported previously. Modelling studies have shown how th upconversion, and the saturation of the absorption, can affect the gain available in an intensel pumped system. The model, and the value for the Auger rate, was consistent with experimenta amplifier measurements. The associated heat load for such a system was also modelled to compar the performance of a planar waveguide with bulk slab and bulk rod-shaped gain media. The mode showed that the planar waveguide maintains the thermal advantages of a slab geometry over that of rod, although slightly higher temperature rises and slightly lower thermal stress fracture limits wer predicted in a planar waveguide compared to an identical sized, but uniformly-pumped, bulk slab.

Advances in coupling diode-bar pump lasers to planar waveguides have been made. A 20W fibre lensed diode-bar, coupled with bulk cylindrical lenses, end-pumped an 80μm Nd:YAG plana waveguide and gave a maximum output power of 6.2W. The device had an optical-to-optica conversion efficiency of 31% and M^2 output beam quality of 3 x 140 in the guided and non-guided directions respectively. More compact, rod-lens focussing successfully coupled this pump source int sub-10μm waveguides, and an output power of 3.7W was obtained from an 8μm Nd:YAG waveguid laser. A first demonstration of proximity coupling a diode-bar to a waveguide, with no intervening optics, gave a coupling efficiency of ~90% into an 8μm Nd:YAG/sapphire direct bonded waveguide.

Techniques for improving the quality of the spatial mode output from the waveguide laser have beer considered. In the guided direction, a metal overlaid coating gave a slight improvement in the lase mode quality and also led to a polarised output. A better solution was found by designing the firs double-clad waveguides. Fabricated by direct bonding a five-layer, Yb:YAG/YAG/sapphir waveguide structure was proximity coupled to a 22W diode-bar pump laser. It gave a maximun output power of 2.2W in a side-pumped configuration. In the guided direction this laser had an outpu divergence with an M^2 very close to 1, consistent with fundamental laser mode operation. Spatia mode selection occurred due to the confined nature of the gain region, and not the cladding-pumping of a single mode core. In the non-guided direction initial experiments aiming to improve M^2 by using an unstable resonator design gave promising results but further work is required in this area.

At last gleams of light have come,

Charles Darwin in a letter to a friend, 1844

Acknowledgements

I can honestly say that I have thoroughly enjoyed my 3+ years at Southampton and the ORC – it's been great, and it's all been down to the people I've had the pleasure to work with and get to know. A few token words here hardly seems enough of an acknowledgement to the people I want to thank…….. but I'll have a go…

A huge THANKS to my supervisor, Dave Shepherd, for his enthusiasm, guidance and always having time to discuss the project – and for doing all that polishing of course! Thanks also to Anne Tropper and Dave Hanna who maintained an interest in the project and have been very supportive of the work.

This PhD would not have been possible at all without financial support from the EPSRC, Onyx and the ORC, so my thanks to them.

Over the last 3 years I have benefited and participated in a number of collaborations, with LETI, Onyx Optics Inc., Maxios Corp., FO.R.T.H and the PLD team at the ORC – thanks to all involved. Thanks also to all those I've worked with in the lab - Dave, Tom, Andy A, Stephan and Steve in the early days – (why were you all so tall?), and more recently Ping, Taj, Simon and Jacob. My thanks also to all the others in buildings 46 and 53 who've been a complete gold mine of information, advice and bits of lab equipment, particularly the lads in 4103 for putting up with my ever-positive attitude and the people in office 2071 who can make good tea in the mornings and know more about computers than I do.

Last, but not least in this list of thank-yous come the network of family and friends who despite having no idea what a waveguide is and no burning desire to find out, have been there for me over the past 3 years. The words thank-you are just not enough.

Table of Contents

Chapter 1 Introduction

1.1 Overview

This thesis will describe the results of three years of research into diode-bar pumped waveguide lasers. The overall aim of the study is to develop compact, high-power lasers that exploit the benefits of a planar waveguide geometry, creating simple, efficient devices with as few components as possible. The thesis discusses the component requirements of a diode-bar pumped waveguide laser, both in terms of the planar waveguide and the diode-bar pumping scheme. A selection of waveguide fabrication techniques are evaluated and a preferred method established. Then, after considering the implications high-power, high-intensity pumping may have on the material, a number of different methods of diode-bar pumping are investigated. The spatial quality of the laser output is a significant property of the laser and the work described in the final experimental chapter considers measuring and improving the output beam quality.

The work undertaken in the course of researching this thesis was carried out with the help and collaboration of a number of researchers and institutions working in the field. Details of these collaborations are given here and later in the relevant chapters. The pulsed laser deposited waveguides used in chapter 4 were grown by A.A.Anderson at the FO.R.T.H laser research facility in Crete[a] and as such form part of the work that was submitted towards the award of his PhD[b]. All of the direct bonded waveguides described in this thesis were fabricated by H. Meissner et al at Onyx Optics INC[c]., California, USA, some as part of a US SBIR Phase I project. The spectroscopy measurements mentioned in chapter 5 were carried out by Dr. Stephan Guy at the University of Lyon, France. The subsequent work described in chapter 5 on a Nd:YAG amplifier was undertaken with Dr. Guy at the University of Southampton. The liquid phase epitaxy waveguides used in experiments described in chapters 6 and 7 were grown by B.Ferrand et al at LETI in Grenoble, France[d] as part

[a] FO.R.T.H.-Hellas, P.O. Box 1527, Heraklion, 711 10, Greece
[b] A.A.Anderson, *'Crystalline Planar Waveguide Lasers Fabricated by Pulsed Laser Deposition'*, PhD Thesis, University of Southampton, (1998)
[c] Onyx Optics INC., 6552 Sierra Lane, Dublin, CA 94568, USA
[d] LETI (CEA- Technologies Avancées), C.E.N.G., 85X-38041, Grenoble, Cedex, France

of a British Council Alliance Program. The Nd:YAG waveguide laser results briefly mentioned in part of chapter 7 were obtained by Ray Beach at Maxios Laser Corporation[e], California, USA. They are included in this thesis with his kind permission.

1.2 Introduction to the area of research

The improvement in diode-pumped solid-state lasers over the last 15-20 years is well recognised [1-6]. Bulk lasers, particularly rare-earth doped $Y_3Al_5O_{12}$ (YAG), are providing compact, high quality, high-power devices for laser radar [7], laser marking [8] and medical applications [9]. This has come about partly due to the increasing availability of laser diode-bars. These provide a high-power, efficient, relatively cheap source of pump photons and are now the pump source of choice for many solid-state laser applications. Unfortunately the need to produce a small circular beam from the diode-bar in order to pump a bulk solid-state laser increases the complexity, and reduces the efficiency of the system. The waveguide may offer a way of obtaining laser output without the need for such intermediary optics, and the aim here is to develop compact, high average power, waveguide devices.

The field of waveguide research and technology is broad and still expanding, with most of the research effort directed in the area of integrated optics for telecommunications [10] and sensors [11], as well as a growing interest in high-power lasers [12] and amplifiers [13]. Waveguide devices are discussed in the next section.

1.3 Guided wave devices

Electromagnetic radiation at optical wavelengths can be confined by means of total internal reflection at a boundary. From Snell's law [14] optical confinement is found to be obtained if the refractive index of the core region is higher than that of the surrounding region. Waveguides offer a number of advantages over bulk laser materials due to this higher refractive index, light guiding core. A number of waveguide geometries exist and a few examples are given in figure 1.1

[e] Maxios Laser Corp., 6552 Sierra Lane, Dublin, CA 94568, USA

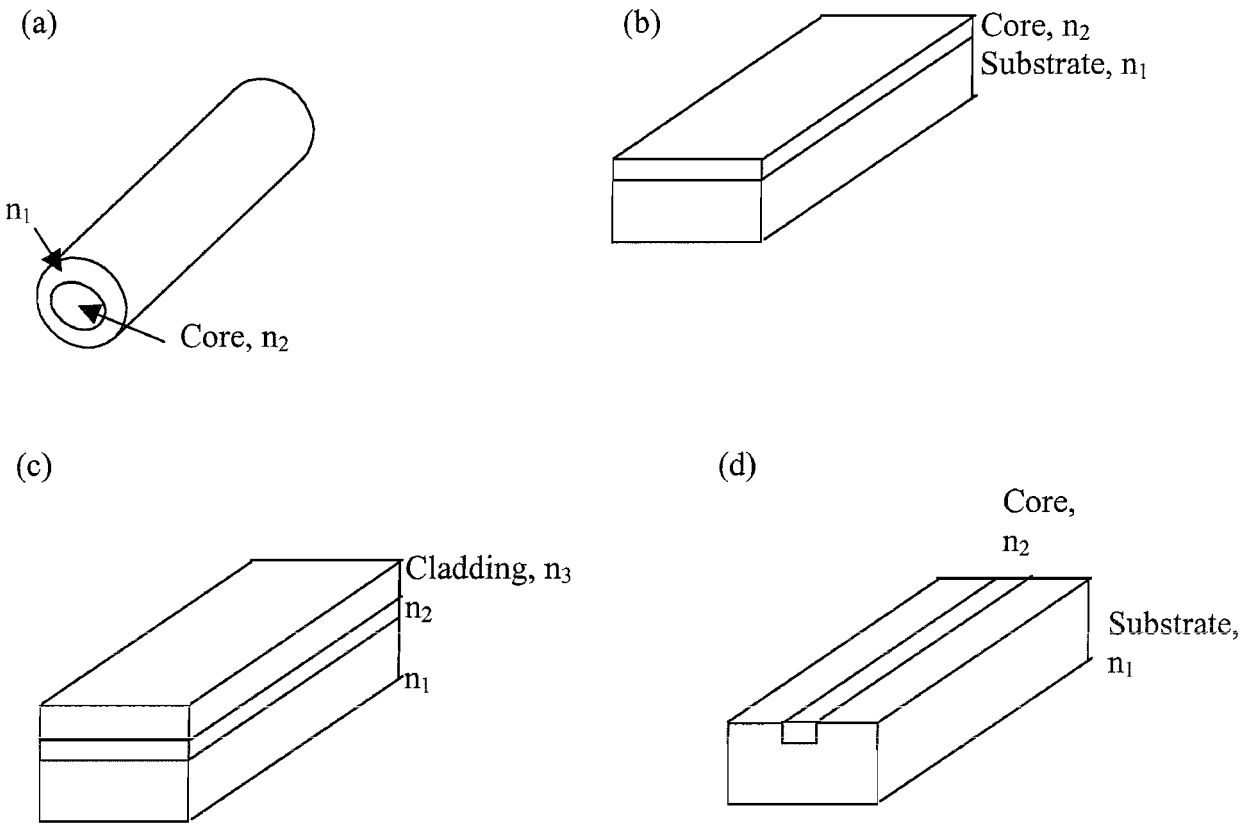

Figure 1.1 Some basic waveguide structures with $n_2 > n_1, n_3$ (a) Optical fibre waveguide, (b) Planar waveguide, (c) Planar waveguide with cladding layer, (d) Channel waveguide

In a waveguide structure the radiation is confined within the core and does not suffer from the diffraction effects normally associated with propagation. The confinement allows a small beam area to be maintained over a long distance. This translates into higher intensity length products being available than in a comparable bulk medium, consequently a waveguide amplifier provides higher gain per unit pump power than a comparable bulk medium would do and, if the waveguide has low propagation loss, low threshold lasers are possible. In some cases laser transitions that are not easily obtainable in the bulk, can be accessed in a waveguide due to this increased gain.

Perhaps the most well-known waveguide design is the optical fibre. This has a high refractive index light guiding core surrounded by a cladding material of a lower refractive index. Optical fibres have usually been made from glass and can have very low propagation losses (~0.2dB/km). For laser devices this has allowed long fibres to

be used to compensate for the low pump absorption generally present in a glassy host material, and the optical fibre has successfully demonstrated its versatility as a laser medium. Many different lasers and amplifiers have been constructed in glass fibres [15-18], and recent work has demonstrated output powers in excess of 100W in a single spatial mode [19], based on a double-clad geometry.

1.4 Planar crystal waveguides

The work described in this thesis focuses on planar crystal waveguides of the structure shown in figure 1.1 (b). These waveguides are composed of a core, a substrate and a protective cladding layer added above the core if necessary (figure 1.1 (c)). Both the substrate and the cladding materials are of a lower refractive index than the core. A channel-type waveguide structure can also be fabricated, as shown in figure 1.1(d), but this type of waveguide has not formed part of the work discussed here.

Using a crystal gain media instead of a glass is of interest for a number of reasons. The sharp absorption peaks in crystals offer short pump absorption lengths which result in compact devices. The high emission cross-section also allows high gain to be generated in these small structures. Crystals can also offer much larger non-linear and electro-optic coefficients than glasses, enhancing their potential functionality. Optical fibres have been fabricated using crystals [20] but they have not, so far, lent themselves to the compact, integrated concepts obtainable with planar devices.

The planar waveguide offers light confinement in a single direction only, but this can be enough to obtain performances which exceed that possible from bulk systems, as long as the waveguide propagation losses are low enough. One of the major advantages of using a planar waveguide comes from the slab geometry of the gain material. It is well known that laser media with high aspect ratio, slab shapes have improved thermal limitations compared to cylindrical rods [21, 22]. This makes the slab shape attractive for high power laser systems where the accompanying large thermal load can often cause optical distortions and even fracture. Planar thin film waveguides can be seen as an extreme case of the slab geometry, with typical aspect ratios of ~1000 to 1 for the core region. The planar geometry also makes these waveguides compatible with high-power diode arrays, such that the beam reshaping

that is often employed to circularise the pump beam in bulk laser systems can be simplified or even eliminated. For example high-power diode pumping of bulk materials has been achieved by many means including reflective pumping chambers [23], fibre coupling [24], lens ducts [25] and various beam-shaping systems [26]. However, the basic geometrical compatibility with a planar waveguide can lead to significant simplification of the diode coupling scheme and hence to very compact systems. A planar waveguide can in principle be in-plane pumped with diode-bars [27,28,29], or face pumped with diode stacks [30] with no coupling optics at all. In addition a planar waveguide offers easy access to the guided wave in the planar thin film, allowing the possibility of integrating various functions into a monolithic device. Examples of such integration could be switching components [31], grating reflectors or filters [32] and polarisation control methods [33].

However, the list of advantages that waveguides have over bulk materials must be balanced by consideration of the coupling efficiency associated with launching light into the waveguide. This efficiency obviously effects the overall device efficiency and every attempt must be made to ensure the best possible launch of pump light is achieved.

With the foregoing as background it has been the aim of the work described in this thesis to use the advantages afforded by the slab geometry of a planar waveguide, in combination with high-power diode-bar pumping, to produce compact, multi-Watt output power devices. Such devices would have good potential for power scaling and enhanced functionality and will be especially suitable for applications where a small device footprint is important.

1.5 Laser ions

The work reported in this thesis has mainly used Nd^{3+} as the active laser ion. Chapter 7 also describes work involving the Yb^{3+} ion. The following sections give brief descriptions of these trivalent rare-earth metal ions, with energy level diagrams showing the relevant laser transitions.

The electronic structure of the rare-earth transition metal ions means that each ion is effectively screened from interactions with neighbouring ions. The energy level manifolds, and hence the spectroscopy of these ions depends upon the crystal field strength surrounding them, and thus the electronic screening effect means that the spectroscopic changes moving from one host crystal to another are relatively small. Here, two host materials, YAG and GGG, are used.

1.5.1 The Nd^{3+} ion

Figure 1.2 shows a general energy level diagram for the Nd^{3+} ion and the major laser transitions in this system.

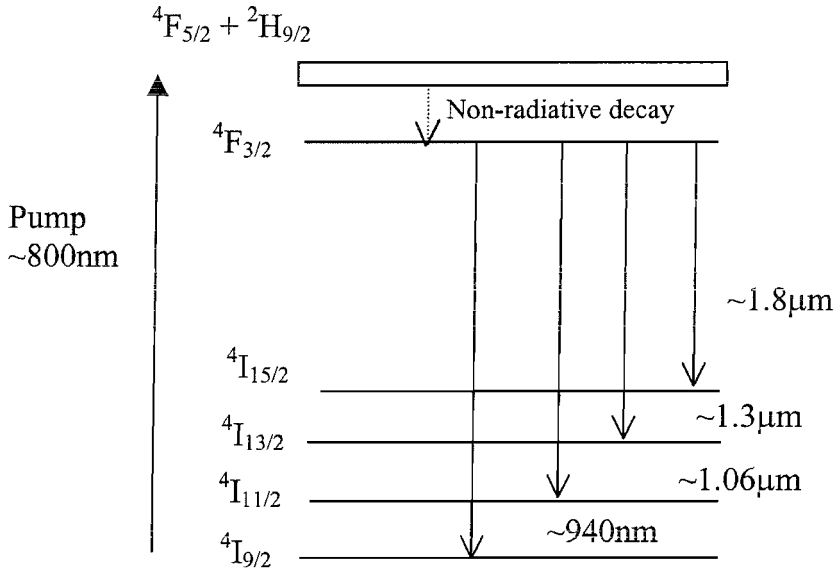

Figure 1.2 Energy level diagram for the Nd^{3+} ion.

The upper laser level is the long lived $^4F_{3/2}$ level which has a lifetime in 1at.% doped YAG of 230μs [34]. The most common laser transition is from the $^4F_{3/2} \rightarrow {}^4I_{11/2}$ levels and corresponds to a four-level laser transition with emission around 1.06μm. This transition has been used extensively throughout this thesis.

Another transition reported in this work is $^4F_{3/2} \rightarrow {}^4I_{9/2}$, corresponding to emission around 940nm. This transition has recently been of interest to researchers as a method

of generating blue emission by frequency doubling in a non-linear material [35]. This transition is known as 'quasi-three-level', as the lower laser level is part of the ground state manifold, and has a small but significant thermal population at room temperature. Several other transitions occur in the Nd^{3+} ion, including the 1.3μm and 1.8μm emissions shown in figure 1.2.

A suitable pump wavelength for this ion is around 800nm, pumping ground state electrons into the higher levels of the ion. Non-radiative decay processes then occur depopulating these higher lying levels and populating the $^4F_{3/2}$ level instead. High-power, high-intensity pumping of the Nd^{3+} ion and the problems associated with a large population inversion are considered in chapter 5.

1.5.2 The Yb^{3+} ion

Ytterbium has also been used as a dopant ion in work described in this thesis. Figure 1.3 shows a generalised energy level diagram for the ion and the major laser transitions in this system.

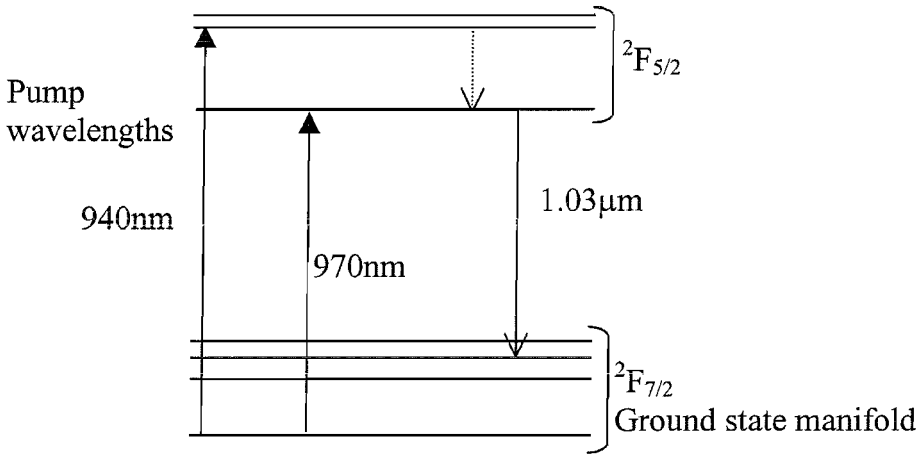

Figure 1.3 Energy level diagram for the Yb^{3+} ion

The Yb^{3+} ion has some interesting features that can provide advantages over the widely used Nd^{3+} system. The energy level diagram shown in figure 1.3 clearly shows that the pump wavelengths are closer to the laser wavelength in this system than for the 1.06μm transition in Nd:YAG. This smaller difference in energy means there is a

more efficient transfer of energy from pump to laser photons and less thermal load is put on the gain medium. Other benefits include the longer upper laser level ($^4F_{5/2}$) fluorescence lifetime. (This lifetime is 1.16msecs compared to around 230μs for Nd^{3+} in YAG). Ytterbium also only has one excited 4f manifold, so in contrast to Nd^{3+}, the processes of concentration quenching and upconversion (as discussed in chapter 5) are not significant, even at high doping levels.

Ytterbium also has broad absorption bands well suited to diode-pumping. Diodes are readily available at wavelengths around 940nm and 970nm, both of which provide suitable pumping photons.

Drawbacks to Yb^{3+} as an active laser ion come from its quasi-three-level nature. This means that some of the laser photons generated are reabsorbed by the population in the lower laser level, leading to a higher threshold than in a four-level laser.

1.6 Laser host crystals

YAG ($Y_3Al_5O_{12}$) and GGG ($Gd_3Ga_5O_{12}$) have been used as the laser host crystal materials in this work. These are both optically isotropic garnet materials with a cubic structure. In YAG the trivalent rare earth dopant ion substitutes for the Y^{3+} ion in the crystal lattice, and in GGG the dopant substitutes for the Ga^{3+} instead. The cubic structure of the crystal lattice leads to unpolarised fluorescence and absorption spectra. Both materials are well suited to waveguide fabrication. They are highly stable and do not undergo phase transitions in the solid phase. In addition they have hardness and physical fracture limits compatible with known fabrication techniques and optical finishing processes. These mechanical properties also make for a laser host material capable of operation under high power pumping.

The high refractive indicies, 1.816 in YAG and 1.96 in GGG at 633nm [36], are particularly attractive for combining with a lower refractive index substrate material in order to produce high numerical aperture (NA) waveguides suitable for diode-bar pumping. In the work described here these materials have been used in particular with

sapphire, glass and in combination (Nd:GGG on YAG) to produce this type of high NA waveguide.

Some details of waveguide fabrication techniques are given in the next section and also later on in the relevant chapters on high NA waveguides.

1.7 Optical waveguide fabrication methods

Numerous methods of waveguide fabrication have been demonstrated. Therefore it is not possible, in this thesis, to give full details of all the known techniques. However, it is useful to examine the development of waveguide fabrication and to discuss some of the methods of manufacture including those used to produce the waveguides described in this thesis.

Ion beam implantation, involving firing a beam of accelerated ions at a bulk piece of material was the technique used to produce many early lasing waveguide devices [37]. The waveguide region is formed by the incoming ions colliding and disordering the atomic nuclei of the bulk material. The 'stopping region', just below the surface of the material displays a positive or negative change in refractive index depending on the material. Examples of bulk materials in which waveguides have been formed by this technique include garnets [37, 38], glasses [39] and $LiNbO_3$ [40]. Losses from these waveguides were found to be ~1-2 dB/cm, which is usually too high for efficient devices.

Indiffusion is a technique whereby metal ions that have been evaporated onto the surface of a substrate material are then diffused into the substrate at high temperature. Examples of waveguides successfully grown by this technique include titanium diffused into sapphire [41] and, more commonly, rare-earth ions and titanium diffused into $LiNbO_3$ [42, 43]. Waveguides fabricated in this way are generally low loss but $LiNbO_3$ does not appear to be a suitable material for high power operation as high intensity pump light leads to photorefractive damage within the crystal. The process of indiffusion has yet to be proven in high power laser materials such as YAG,

however, with further work indiffusion could perhaps become a useful fabrication technique for future devices made from high power laser materials.

Ion exchange [44] is a technique that has been successfully used for a number of years to produce low loss glass waveguides. Similarly the technique of proton exchange into $LiNbO_3$ and $LiTaO_3$, first reported in 1982 [45], has been extensively used to produce waveguides. The losses of these waveguides can be as low as 0.1dB/cm [46]. However these fabrication techniques do not appear to be widely applicable to many different laser hosts.

In fabrication techniques where the higher refractive index layer is grown on top of a lower index substrate it is desirable to do so epitaxially, i.e. to grow the layer as a single crystal. Semiconductor layer devices are grown using the technique of MBE (Molecular Beam Epitaxy). This involves evaporating sources of atoms or molecules under strict control. Monolayers of each material can be grown and the technique is commonly used to grow, for example, quantum well devices where it is crucial to control defect density. The technique of MBE has also been used to grow dielectric crystal waveguides [47], although with losses of the order of ~1dB/cm.

Liquid phase epitaxy (LPE) has produced some of the lowest loss (~0.05dB/cm) rare-earth doped waveguides so far reported [48]. This loss figure approaches the optical scattering loss of the bulk material. The excellent crystalline quality of material grown by LPE is due to the carefully controlled fabrication process [49]. A wafer of the crystalline substrate material is dipped into a melt. The melt contains a mix of oxides including rare-earth dopants, and is mechanically stirred to ensure homogeneity of the mix. The temperature of the melt is reduced below the saturation temperature and the compounds in the melt condense to form the desired garnet crystal layer on the substrate. The substrate acts as a seed crystal so an epitaxial layer is able to grow with the same structure as the substrate. High quality crystals can be grown at speeds of up to 2μm/minute and YAG doped with Nd, Yb, Tm and Er [48, 50-52] have all been grown successfully on YAG substrates, making low loss, high optical quality planar waveguides.

The LPE process is used on an industrial scale to manufacture high quality microchip laser crystals, with a layer of Q switch material grown on top of Nd:YAG [53]. The advantages of LPE, particularly for industry, include the ability to use large numbers of substrates with large areas and the option to grow multilayers. However suitable melt conditions must be found for the material that is to be grown and LPE requires that any lattice mismatch between the substrate and the core layer to be grown must be small. This severely limits the material combinations that can be used, and often means that material combinations providing a suitable difference in refractive index cannot be grown by LPE. This means the technique is not well suited to growing high NA waveguides. Putting additional non-laser-active dopants into the core layer can increase the refractive index [13] but this may then have the effect of broadening the optical transitions of the dopant ion. This broadening results in an undesirable reduction in the peak cross-section values.

Other techniques that are considered to be more favourable for producing high NA waveguides are discussed below. However, these techniques have not matched the very low propagation losses achieved with waveguides manufactured by LPE.

PLD has recently been applied to the growth of optical waveguide devices [54] as it has the ability to grow layers of a variety of different materials. Chapter 4 gives further details of the fabrication technique which involves using a vacuum chamber and a high power laser to evaporate the surface of a target material, the resulting plasma then impinges onto the surface of a substrate forming a film. This relatively low cost, easy to use, versatile fabrication system has produced a number of waveguide devices [55, 56]. However, in order to grow good quality crystalline films from the plasma of target material landing on the substrate, the substrate must act as a template for the layer. This means that materials with similar lattice structure and similarly sized lattice constants form the best waveguide combinations. This requirement, similarly to LPE, limits the fabricator's choice of material combinations and thus the waveguide NA. It should be noted that some material combinations do exist, such as Nd:GGG on YAG [57] that provide a large NA with a small lattice mis-match, but these are limited in number. In addition, the ablation of the target material can result in high optical scattering losses in the waveguide due to the presence of particulates in the as-grown layer [55]. The waveguide layer itself can also be of a

slightly different stoichiometry than the original target material, due to the composition of the plasma plume resulting from the ablation process. This, and possibly other mechanisms, mean that the absorption and emission spectra are slightly broadened compared to the bulk material, with the result that lasing performance is slightly impaired [58].

It seems as though one of the most promising techniques for fabricating high quality waveguides with no limits on material combinations, and thus NA, may be direct bonding. Further fabrication details and results from direct bonded waveguide lasers will be given in chapter 4, just a brief introduction is given here.

The versatile, fabrication process of direct bonding simply involves contacting the surfaces of the two materials to be bonded. The surfaces must have been chemically cleaned and polished flat, to a surface roughness of just a few nm. The two materials are held together by Van der Waals forces. In some instances the composite is heated to around 300° C to further strengthen the bond, but this is below the temperature at which diffusion would take place, so the substrate and superstrate are not chemically modified at all. There appears to be little restriction to the materials that can be bonded in this way [59], and as well as the planar slab waveguides described in chapter 4 other structures that have been bonded with this technique include composite laser rods [60], thick waveguide/bulk slabs [30] and core doped rods [61].

The major advantage that direct bonding has over other manufacturing methods that have been mentioned so far is that very different materials can be bonded together without adversely affecting the properties of either material. However, the materials should preferably have similar thermal expansion co-efficients if heat treatment forms part of the bonding process, or if it will have a significant thermal load in operation. After bonding each material maintains the characteristics of the original bulk material, and there is no observable broadening of the fluorescence spectra.

While direct bonding can be somewhat labour intensive, it provides a means of obtaining high quality, high NA, low loss waveguides and seems to be the best fabrication process developed to date for the type of structures that are at the heart of the work described in this thesis.

1.8 Synopsis

Following on from this introduction the body of the thesis is organised into 7 other chapters.

Chapter 2 provides some details of the theoretical concepts that form the basis of this thesis. The nature of the propagation of light in a waveguide is discussed along with the relevant laser and amplifier theory that is used in later chapters. The experimental techniques that were employed in the work described in the thesis are outlined in chapter 3. The experimental studies undertaken are then described in chapters 4-7.

Chapter 4 covers the fabrication and waveguide laser testing of waveguides grown by PLD and direct bonding. As outlined in the previous section, both these technique are capable of producing high numerical aperture waveguides. Chapter 5 concentrates on the effects of the high–power, high-intensity pumping of a common laser material – Nd:YAG. The possible implications that such pumping could have on the performance of a planar waveguide device are considered. Then in chapter 6 the results of high-power, diode-bar pumping such a waveguide are reported. Chapter 7 discusses methods of improving the spatial beam quality of the waveguide laser output.

Finally chapter 8 concludes the thesis with some remarks summarising the work and progress to date. Consideration is also given to promising future areas of study and other possible directions of the work.

1.9 References

[1] T.Y.Fan, R.L.Byer, IEEE J. Quantum Electron., **24**, pp.895-911 (1988)

[2] S.C.Tidwell, J.F.Seamans, M.S.Bowers, A.K.Cousins, IEEE J. Quantum Electron., **28**, pp.997-1009 (1992)

[3] D.C.Hanna, W.A.Clarkson, pp.1-18, *'Advances in Laser and Applications'* Proceedings of the Fifty Second Scottish Universities Summer School in Physics, D.M.Finlayson, B.D.Sinclair, eds. IOP Publishing (1998)

[4] J.J.Zayhowski, Optical Materials, **11**, pp.255-267 (1999)

[5] B.D.Sinclair, Optical Materials, **11**, pp.217-233 (1999)

[6] A.Giesen, H.Hugel, A,Voss, K.Wittig, U.Brauch, H.Opower, Appl. Phys. B, **58**, pp.365-372 (1994)

[7] I.Melngailis, W.E.Keicher, C.Freed, S.Marcus, B.E.Edwards, A.Sanchez, T.Y.Fan, D.L.Spears, Proc. of IEEE, **84**, pp.227-267 (1996)

[8] P.Loosen, pp.287-317, *'Advances in Laser and Applications'* Proceedings of the Fifty Second Scottish Universities Summer School in Physics, D.M.Finlayson, B.D.Sinclair, eds. IOP Publishing (1998)

[9] M.M.Abreu, R.A.Sierra, P.A.Netland, Opthalmic Surgery and Lasers, **28**, pp.305-310 (1997)

[10] H.Nishihara, M.Haruna, T.Suhara, *'Optical Integrated Circuits'*, McGraw-Hill, New York (1989)

[11] P.V.Lambeck, Sensors and Actuators B, **8**, pp.103-116 (1992)

[12] C.L.Bonner, C.T.A.Brown D.P.Shepherd, W.A.Clarkson, A.C.Tropper, D.C.Hanna, B.Ferrand, Opt. Lett., **23**, pp.942-944 (1998)

[13] D.P.Shepherd, C.T.A.Brown, T.J.Warburton, D.C.Hanna, A.C.Tropper, B.Ferrand, Appl. Phys. Lett., **71**, pp.876-878 (1997)

[14] R.Guenther, pp.78-83, *'Modern Optics'*, John Wiley and Sons Ltd, New York, USA (1990)

[15] J.Stone, C.A.Barrus, Appl. Opt., **13**, pp.1256-1258 (1974)

[16] I.Y.Allain, M.Monerie, H.Poignant, Electron. Lett., **26**, pp.261-263 (1990)

[17] J.Hecht, pp.73-77, *'Laser Focus World'* Penwell Publishing, California, USA, **34 (7)** (1998)

[18] D.Richardson, H.Offerhaus, J.Nilsson, A.Grudinin, pp.92-94, *'Laser Focus World'* Penwell Publishing, California, USA, **35 (6)** (1999)

[19] V.Dominic, S.MacCormack, R.Waarts, S.Saunders, S.Bicknese, R.Dohle, E.Wolak, P.S.Yeh, E.Zucker, *'Technical Digest of Conference on Lasers and Electro-Optics'*, 1999 Post deadline paper CPD11

[20] J.Stone, C.A.Burns, A.G.Dentei, B.I.Miller, Appl. Phys. Lett., **29**, pp.37-39 (1976)

[21] W.Koechner, *'Solid State Laser Engineering'*, Springer - Verlag, Berlin, Chaps 6.3 and 7.3 (1996)

[22] J.M.Eggleston, T.J.Kane, K.Kuhn, J.Unternahrer, R.L.Byer, IEEE J. Quantum Electron. **QE-20**, pp.289-301 (1984)

[23] J.J.Chang, E.P.Dragon, C.A.Ebbers, I.L.Bass, C.W.Cochran, OSA TOPS on Advanced Solid State Lasers, pp.300-304 (1998)

[24] M.Karszewski, U.Brauch, K.Contag, S.Ergard, A.Giesen, I.Johannsen, C.Stewart, A.Voss, OSA TOPS on Advanced Solid State Lasers, pp.296-299 (1998)

[25] R.J.Beach, Appl. Opt., **35**, pp.2005-2015 (1996)

[26] W.A.Clarkson, D.C.Hanna, Opt. Lett., **21**, pp.375-377 (1996)

[27] U.Griebner, H.Schonnagel, R.Grunwald, S.Woggon, in *'Technical Digest of Conference on Lasers and Electro-Optics'* 1997, pp.307-308

[28] D.P.Shepherd, C.L.Bonner, C.T.A.Brown, W.A.Clarkson, A.C.Tropper, D.C.Hanna, H.E.Meissner, Opt. Commun., **160**, pp.47-50 (1999)

[29] C.L.Bonner, T.Bhutta, D.P.Shepherd, A.C.Tropper, IEEE J. Quantum Electron., **36**, pp.236-242 (2000)

[30] A.Faulstich, H.J.Baker, D.R.Hall, Opt. Lett., **21**, pp.594-596 (1996)

[31] H.Suche, R.Wessel, S.Westenhöfer, W.Sohler, S.Bosso, C.Carmannini, R.Corsini, Opt. Lett., **20**, pp.596-598 (1995)

[32] I.Baumann, S.Bosso, R.Brinkmann, R.Corsini, M.Dinard, A.Greiner, K.Schäfer, J. Söchtig, W.Sohler, H.Suche, R.Wessel, IEEE J. Selected Topics in Quantum Electron. **2**, pp.355-365 (1996)

[33] C.T.A.Brown, R.D.Harris, D.P.Shepherd, A.C.Tropper, J.S.Wilkinson, B.Ferrand, IEEE Photon. Technol. Lett., **10**, pp.1392-1394 (1998)

[34] S.Singh, R.G.Smith, L.G.Van Uitert, Phys. Rev. B., **10**, pp.2566-2572 (1974)

[35] M.Pollnau, G.W.Ross, W.A.Clarkson, P.G.R.Smith, P.E.Britton, D.C.Hanna in *'Technical Digest of Conference on Lasers and Electro-Optics'*, 1997, Post deadline paper CPD32

[36] D.L.Wood, K.Nassau, Appl. Opt., **29**, pp.3704-3707 (1990)

[37] P.J.Chandler, S.J.Field, D.C.Hanna, D.P.Shepherd, P.D.Townsend, A.C.Tropper, L.Zhang, Elec. Lett., **25**, pp.985-986 (1989)

[38] S.J.Field, D.C.Hanna, A.C.Large, D.P.Shepherd, A.C.Tropper, P.J.Chandler, P.D.Townsend, L.Zhang, Opt. Commun., **86**, pp.161-166 (1991)

[39] D.P.Shepherd, D.J.B.Brink, J.Wang, A.C.Tropper, D.C.Hanna, G.Kakarantzas, P.D.Townsend, Opt. Lett., **19**, pp.954-956 (1994)

[40] S.J.Field, D.C.Hanna, A.C.Large, D.P.Shepherd, A.C.Tropper, P.J.Chandler, P.D.Townsend, L.Zhang, Opt. Lett., **16**, pp.481-483 (1991)

[41] L.M.B.Hickey, E.Martins, J.E.Roman, W.S.Brocklesby, J.S.Wilkinson, Opt. Lett., **21**, pp.597-599 (1996)

[42] M.Hempstead, J.S.Wilkinson, L.Reekie, IEEE Photon. Tech. Lett., **4**, pp.852-855 (1992)

[43] R.Brinkman, W.Sohler, H.Suche, Elec. Lett., **27**, pp.415-417 (1991)

[44] T.Izawa, H.Nakagome, Appl. Phys. Lett., **21**, pp.584-586 (1971)

[45] J.L.Jackel, C.E.Rice, J.J.Veselka, Appl. Phy. Lett., **41**, pp.607-608 (1982)

[46] E.Lallier, J.P.Pochelle, M.Papuchon, Q.He, M.de Micheli, D.B.Ostrovsky, Elec. Lett., **28**, pp.1428-1429 (1992)

[47] E.Daran, D.P.Shepherd, T.Bhutta, P.Lahoz, *'Technical Digest of Conference on Lasers and Electro-Optics'*, 1999 Paper CThD4

[48] I.Chartier, B.Ferrand, D.Pelenc, S.J.Field, D.C.Hanna, A.C.Large, D.P.Shepherd, A.C.Tropper, Opt. Lett., **17**, pp.810-812 (1992)

[49] B.Ferrand, D.Pelenc, I.Chartier, Ch.Wyon, J. Crys. Growth. **128**, pp.966-969 (1993)

[50] D.Pelenc, B.Chambaz, I.Chartier, C.Wyon, D.P.Shepherd, D.C.Hanna, A.C.Large, A.C.Tropper, Opt. Commun., **115**, pp.491-497 (1995)

[51] A.Rameix, C.Borel, B.Chambaz, B.Ferrand, D.P.Shepherd, T.J.Warburton, D.C.Hanna, A.C.Tropper, Opt. Commun., **142**, pp.239-243 (1997)

[52] D.P.Shepherd, D.C.Hanna, A.C.Large, A.C.Tropper, T.J.Warburton, C.Borel, B.Ferrand, D.Pelenc, A.Rameix, P.Thony, F.Auzel, D.Meichenin, J. Appl. Phys., **76**, pp.7651-3 (1994)

[53] F.Leplingard, P.Pierrard, J.P.Herriau, G.Bocqueho, *'Miniature Coherent Light Sources in Dielectric Media,- Les Houches Summer School,'* Short Seminar 1997

[54] D.S.Gill, R.W.Eason, J.Mendiola, P.J.Chandler, Mater. Lett., **25**, pp.1-10 (1995)

[55] D.S.Gill, A.A.Anderson, R.W.Eason, T.J.Warburton, D.P.Shepherd, Appl. Phys. Lett., **69**, pp.10-12 (1996)

[56] A.Anderson, R.W.Eason, L.M.B.Hickey, M.Jelinek, C.Grivas D.S.Gill, N.Vainos, Opt. Lett., **22**, pp.1556-1558 (1997)

[57] C.L.Bonner, A.A.Anderson, R.W.Eason, D.P.Shepherd, D.S.Gill, C.Grivas, N.Vainos, Opt. Lett., **22**, pp.988-990 (1997)

[58] A.A.Anderson, '*Crystalline Planar Waveguide Lasers Fabricated by Pulsed Laser Deposition*', PhD Thesis, University of Southampton, pp. 65-70 (1998)

[59] C.T.A.Brown, C.L.Bonner, T.J.Warburton, D.P.Shepherd, A.C.Tropper, D.C.Hanna, H.E.Meissner, Appl. Phys. Lett., **71**, pp.1139-41 (1997)

[60] H. Brusselbach, D.S.Sumida, Opt. Lett., **21**, pp.480-482 (1996)

M.G.Tani, F.L.Naranjo, N.P.Barnes, K.E.Murray, G.E.Lockard, Opt. Lett., **20**, pp.872-874 (1995)

[61] A.Lucianetti, R.Weber, W.Hodel, H.P.Weber, A.Papashvili, V.A.Konyushkin, T.T.Basiev, Appl. Opt., **38**, pp.1777-1783 (1999)

Chapter 2 Waveguide laser theory

2.1 Introduction

This chapter introduces the theoretical concepts underpinning the work described in this thesis. The chapter is subdivided into three sections. The first section describes the propagation of light in a planar waveguide using the simple model of a slab waveguide. The model deals with a general five-layer asymmetric slab structure and is then applied to the simpler cases of a three-layer asymmetric slab structure and a symmetric five-layer structure. Both types of planar waveguide have been used experimentally in the work discussed in this thesis. The second section contains details of bulk laser theory and the modelling of threshold and slope efficiency for three- and four-level laser systems. This is then modified to account for a waveguide geometry, and the theoretical performance of bulk and waveguide lasers are compared. The final section discusses how to define waveguide laser beam quality.

2.2 Optical waveguide theory

The propagation modes of a waveguide structure are very important in determining the properties of a waveguide laser. For example the lasing modes propagating in the waveguide define the output beam quality, and the laser threshold and efficiency characteristics are dependant on both the pump and signal mode sizes and overlap.

There are many ways in which to describe the propagation of light in a waveguide. Numerous textbooks [1,2,3,4,5] deal with the task and merely an introduction to the subject will be given here. The analysis used in this chapter is similar to that described by Yariv [1] and Lee [2]. It is restricted here to finding the propagation modes of structures with one dimensional guidance. Details of other approaches are given in the references and include; classical propagating ray analysis based on geometrical optics [3], the WKB method [4] for graded refractive index waveguides, and other numerical beam propagation methods [5].

2.2.1 Five-layer asymmetric slab waveguide

The three-layer asymmetric slab waveguide considered in many textbooks is one of the most straightforward geometries to examine. However some of the waveguides examined during the course of this thesis consisted of five layers. In order to investigate these structures a general five-layer asymmetric slab (planar) model has been developed and then generalised to a five-layer symmetric, and a three-layer asymmetric case.

A schematic diagram of the asymmetric structure is shown in figure 2.1. The elements of the waveguide are; a substrate (region 5), considered infinitely thick in this analysis, a thin inner cladding layer of a higher refractive index than the substrate (region 4), a thin, high-index core layer (region 3), an outer cladding layer (region 2) and a superstrate (region 1), which is also considered to be infinitely thick.

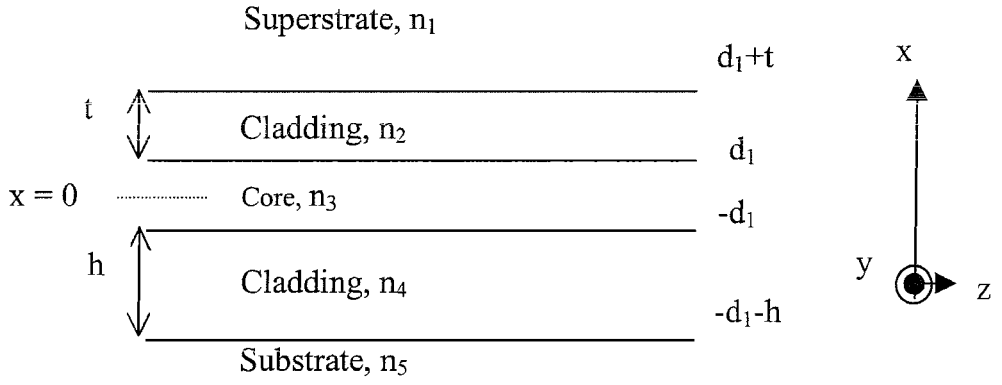

Figure 2.1 Schematic diagram of an asymmetric slab waveguide

The light propagates in the z-direction and is confined in the waveguide by total internal reflection (TIR) at the core-cladding interface or at the cladding-superstrate and cladding-substrate interfaces. TIR at an interface between two media means that the angle of propagation, θ_p, in the bouncing-beam model (as shown in figure 2.2) must be greater than the critical angle, θ_c, for the interface. If this is true then the light is described as travelling in a guided mode, where p is the mode number.

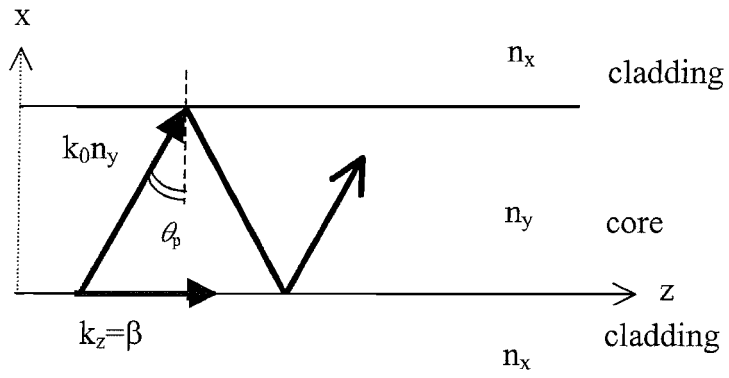

Figure 2.2 Diagram illustrating TIR and the propagation constant β

The overall condition for guidance in the structure shown in figure 2.1 is, $n_3>n_2,n_4>n_1,n_5$, where the refractive index of a region m is given by n_m, i.e. the refractive index of the core must be greater than the refractive indices of the cladding layers, which are in turn greater than those of the superstrate and substrate layers. For instance TIR would occur at the core-cladding boundary of figure 2.2 when θ_p was greater than θ_c given by equation 2.1 (from Snell's law).

$$\theta_c = \sin^{-1}\left(\frac{n_x}{n_y}\right) \qquad 2.1$$

Waveguide theory is often not formulated in terms of the propagation angle θ_p, but in terms of β, the propagation constant. Figure 2.2 illustrates β, which is related to the optical path length seen by the guided mode. The propagation constant in the direction in which the wavefront moves is given by k_0n_y, where the wavenumber, $k_0 = 2\pi/\lambda$ and λ is the wavelength of the light in free space. The propagation constant along the guided (z) direction is therefore:

$$k_z = k_0n_y\sin\theta_p = \beta \qquad 2.2$$

The quantity $n_y\sin\theta_p$ in equation 2.2 is often labelled n_{eff} and is known as the effective index of a mode. Thus the propagation constant can be rewritten as:

$$\beta = k_0n_{eff} \qquad 2.3$$

For the guidance condition to be satisfied θ_p must be greater than θ_c and so n_{eff} must satisfy the condition $n_3 > n_{eff} > n_1, n_5$.

In order for the mode to maintain its shape as it propagates along z, β must be the same in all five layers. Propagation constants can be defined for the +x and –x directions in the core, cladding, superstrate and substrate regions. The propagation constants in the ±x direction in the core describe an oscillatory TIR wave. The propagation constants in the ±x direction in the cladding describe, both the oscillatory nature of the guided wave when $n_2, n_4 > n_{eff} > n_1, n_5$ and the rate of decay of the evanescent field with distance from the core boundary when $n_{eff} > n_2, n_4$. While in the substrate and superstrate the ±x direction propagation constants represent only the rate of decay of the evanescent field, as n_{eff} is always greater than n_1, n_5.

Electromagnetic waves propagating in the five-layer structure obey Maxwell's equations and these equations form the basis of the following analysis. Equations 2.4 – 2.7 show Maxwell's equations in their general form:

$$\underline{\nabla} \times \underline{E}(\underline{r}, t) = -\frac{\partial \underline{B}(\underline{r}, t)}{\partial t} \qquad 2.4$$

$$\underline{\nabla} \times \underline{H}(\underline{r}, t) = \frac{\partial \underline{D}(\underline{r}, t)}{\partial t} + \underline{J}(\underline{r}, t) \qquad 2.5$$

$$\underline{\nabla} \bullet \underline{D}(\underline{r}, t) = \rho(\underline{r}, t) \qquad 2.6$$

$$\underline{\nabla} \bullet \underline{B}(\underline{r}, t) = 0 \qquad 2.7$$

where, $\underline{E}$, $\underline{H}$ are electric and magnetic fields respectively.

$\underline{D}$ is the electric displacement vector.

$\underline{B}$ is the magnetic flux density.

ρ, $\underline{J}$ are the charge and current densities respectively.

t is time, $\underline{r}$ is a position vector in space.

$\underline{D}$ and $\underline{E}$ are related by $\underline{D} = \varepsilon_0\varepsilon_r\underline{E} = \varepsilon\underline{E}$, and ε_0, ε_r are respectively the permittivity of free space and the relative permittivity of the material. Also, $\underline{B} = \mu_0\mu_r\underline{H} = \mu\underline{H}$, where μ_0,μ_r are the permeability of free space and the relative permeability of the medium respectively.

Assuming there is no current flow (no current sources present) in the material, $\underline{J}=0$, equations 2.4 and 2.5 can be rewritten in terms of $\underline{E}$ and $\underline{H}$ only:

$$\underline{\nabla} \times \underline{E}(\underline{r},t) = -\frac{\partial}{\partial t}\mu\underline{H}(\underline{r},t) \qquad 2.8$$

$$\underline{\nabla} \times \underline{H}(\underline{r},t) = \frac{\partial}{\partial t}\varepsilon\underline{E}(\underline{r},t) \qquad 2.9$$

For a transverse electric (TE) polarised wave (with $\underline{E}$ orientated along the $\underline{y}$ direction) the $\underline{E}$-field can be separated into its spatial and temporal components:

$$\underline{E}(\underline{r},t) = E_y(x,z)e^{i\omega t} \qquad 2.10$$

where ω is angular frequency, and the field variations are independant of y.

The TE modes only are considered for analysis here. These show the general behaviour of modes in the waveguide and in practice, the polarised laser outputs obtained during the course of this work were found to be TE polarised (see results in chapter 7). The solution to Maxwell's equations in each of the five layers, should lead to oscillatory solutions only in region 3, evanescent solutions only in regions 1 and 5, and both types of solution in regions 2 and 4.

The spatial component of the $\underline{E}$-field can therefore be characterised in the five regions as follows:

$$E_y(x,z) = \begin{Bmatrix} E_1 e^{-\alpha_1 x} \\ E_2 e^{-\alpha_2 x} + E_2' e^{\alpha_2 x} \\ \cos(kx + \Psi) \\ E_4 e^{\alpha_4 x} + E_4' e^{-\alpha_4 x} \\ E_5 e^{\alpha_5 x} \end{Bmatrix} e^{-ik_z x} \quad \text{in the regions} \quad \begin{cases} x \geq d_1 + t \\ d_1 \leq x < d_1 + t \\ -d_1 \leq x < d_1 \\ -(d_1 + h) \leq x < -d_1 \\ x < -(d_1 + h) \end{cases}$$

2.11

where E_1, E_2, E_2', E_4, E_4' E_5, are electric field amplitude coefficients

Ψ is a phase offset

k_z is the wave number in the z direction

α_1, α_2, k, α_4, α_5 are transverse wave numbers obtained from the solution of the wave equation, derived from Maxwell's equations in each region.

$$\nabla^2 \underline{E}(\underline{r},t) = -\mu\varepsilon \frac{\partial^2}{\partial^2} \underline{E}(\underline{r},t) \qquad 2.12$$

with: $$\alpha_1 = \sqrt{k_z^2 - \omega^2 \mu_1 \varepsilon_1} \qquad 2.13$$

$$\alpha_2 = \sqrt{k_z^2 - \omega^2 \mu_2 \varepsilon_2} \qquad 2.14$$

$$k = \sqrt{\omega^2 \mu_3 \varepsilon_3 - k_z^2} \qquad 2.15$$

$$\alpha_4 = \sqrt{k_z^2 - \omega^2 \mu_4 \varepsilon_4} \qquad 2.16$$

$$\alpha_5 = \sqrt{k_z^2 - \omega^2 \mu_5 \varepsilon_5} \qquad 2.17$$

where ε_m, μ_m, are, respectively, the permittivity and permeability of region m.

Equations 2.13 –2.17 can also be expressed as

$$\alpha_m = k_0 \sqrt{n_{eff}^2 - n_m^2} \qquad 2.18$$

and

$$k = k_0 \sqrt{n_3^2 - n_{eff}^2} \qquad 2.19$$

where $k_0 = \omega\sqrt{\mu_0\varepsilon_0}$ and $n_m = \sqrt{\frac{\varepsilon_m}{\varepsilon_0}}$

In order to find the relative field amplitude coefficients the boundary conditions that E_y and H_z are continuous across the layer interfaces must be used [1], i.e E_y and H_z are continuous across the planes $-d_1$, $-(d_1+h)$, d_1 and d_1+t. H_z is found from equation 2.8:

$$H_z(x,z) = \frac{i}{\omega\mu}\frac{\partial}{\partial x}E_y(x,z) \qquad 2.20$$

Application of the boundary conditions produces a set of simultaneous equations which can then be solved to obtain solutions 2.21-2.26

$$E_1 = \frac{\left[1+\left(\frac{\alpha_2-\alpha_1}{\alpha_2+\alpha_1}\right)\right]\cos(kd_1+\Psi)e^{-\alpha_2 t}}{\left[1+\left(\frac{\alpha_2-\alpha_1}{\alpha_2+\alpha_1}\right)e^{-2\alpha_2 t}\right]e^{-\alpha_1(d_1+t)}} \qquad 2.21$$

$$E_2 = \frac{\cos(kd_1+\Psi)e^{\alpha_2 d_1}}{\left[1+\left(\frac{\alpha_2-\alpha_1}{\alpha_2+\alpha_1}\right)e^{-2\alpha_2 t}\right]} \qquad 2.22$$

$$E_2' = \frac{\left(\frac{\alpha_2-\alpha_1}{\alpha_2+\alpha_1}\right)\cos(kd_1+\Psi)e^{-\alpha_2(d_1+2t)}}{\left[1+\left(\frac{\alpha_2-\alpha_1}{\alpha_2+\alpha_1}\right)e^{-2\alpha_2 t}\right]} \qquad 2.23$$

$$E_4 = \frac{\cos(-kd_1+\Psi)e^{\alpha_4 d_1}}{\left[1+\left(\frac{\alpha_4-\alpha_5}{\alpha_4+\alpha_5}\right)e^{-2\alpha_4 h}\right]} \qquad 2.24$$

$$E_4' = \frac{\left(\frac{\alpha_4 - \alpha_5}{\alpha_4 + \alpha_5}\right)\cos(-kd_1 + \Psi)e^{-\alpha_4(d_1+2h)}}{\left[1+\left(\frac{\alpha_4 - \alpha_5}{\alpha_4 + \alpha_5}\right)e^{-2\alpha_4 h}\right]} \qquad 2.25$$

$$E_5 = \frac{\left[1+\left(\frac{\alpha_4 - \alpha_5}{\alpha_4 + \alpha_5}\right)\right]\cos(-kd_1 + \Psi)e^{-\alpha_4 h}}{\left[1+\left(\frac{\alpha_4 - \alpha_5}{\alpha_4 + \alpha_5}\right)e^{-2\alpha_4 h}\right]e^{-\alpha_5(d_1+h)}} \qquad 2.26$$

Evaluating boundary conditions at $x=d_1$ and using $\tanh x = \frac{e^x - e^{-x}}{e^x + e^{-x}}$ gives:

$$\tan(kd_1 + \Psi) = \left(\frac{\alpha_1\alpha_2 + \alpha_2^2 \tanh\alpha_2 t}{k\alpha_2 + k\alpha_1 \tanh\alpha_2 t}\right) \qquad 2.27$$

and similarly evaluating boundary conditions at $x=-d_1$ gives:

$$\tan(kd_1 - \Psi) = \left(\frac{\alpha_4\alpha_5 + \alpha_4^2 \tanh\alpha_4 h}{\alpha_4 k + \alpha_5 k \tanh\alpha_4 h}\right) \qquad 2.28$$

Using the relationship $\tan(x)=\tan(x\pm p\pi)$ where p is any integer, equations 2.27 and 2.28 can be combined to eliminate Ψ:

$$2kd_1 - \tan^{-1}\left(\frac{\alpha_4\alpha_5 + \alpha_4^2 \tanh\alpha_4 h}{\alpha_4 k + \alpha_5 k \tanh\alpha_4 h}\right) - \tan^{-1}\left(\frac{\alpha_1\alpha_2 + \alpha_2^2 \tanh\alpha_2 t}{\alpha_2 k + \alpha_1 k \tanh\alpha_2 t}\right) = p\pi \qquad 2.29$$

Equation 2.29 can be numerically solved in order to find a value for k, equations 2.13-2.17 can then be used to find the values of k_z, α_1, α_2, α_4, α_5 and ψ is given by equations 2.27 and 2.28. Equation 2.29 is known as the mode guidance condition equation [1] for a mode number p.

This analysis has only considered the TE modes of the waveguide. Transverse magnetic (TM) solutions (where H is polarised along the y direction) can be found from the duality in Maxwell's equations [2].

2.2.2 Five-layer symmetric slab waveguide

In practice an asymmetric five-layer planar waveguide has not been fabricated or used during the course of the work described here, however the model developed in section 2.2.1 can now be generalised to describe a symmetric five-layer structure that was used in experiments described in chapter 7. A schematic diagram of the general symmetric five-layer waveguide structure is shown in figure 2.3.

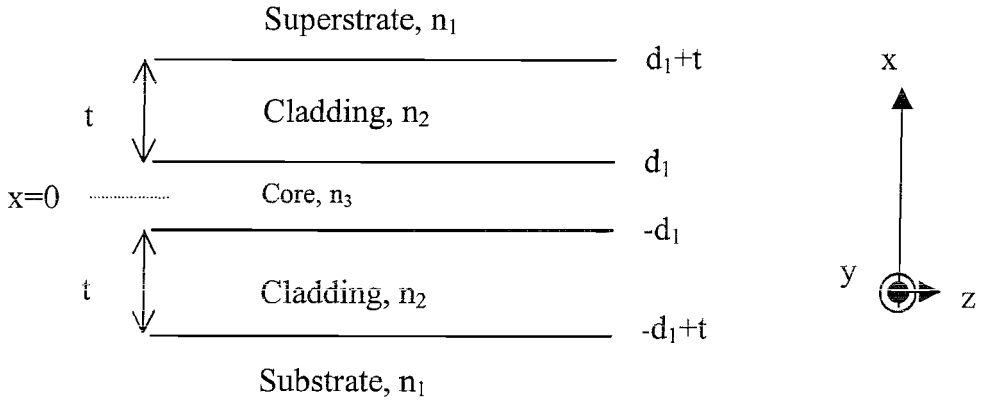

Figure 2.3 Diagram of a five-layer symmetric waveguide

The five-layer, or double-clad, structure investigated in chapter 7 was composed of a thin (~10μm), high index core of rare-earth-doped YAG, a thin inner cladding (~10μm) of undoped YAG, and a thick (~500μm) outer cladding of Sapphire.

A symmetric structure is expected to have even ($\psi=0$) and odd ($\psi=\pi$) modes within its core. The mode guidance conditions for this geometry are as follows [6].
For the even modes:

$$\tan(kd_1) = \left(\frac{\alpha_1 \alpha_2 + \alpha_2^2 \tanh \alpha_2 t}{k\alpha_2 + k\alpha_1 \tanh \alpha_2 t} \right) \qquad 2.30$$

and for the odd modes:

$$\cot(kd_1) = -\left(\frac{\alpha_1\alpha_2 + \alpha_2^2 \tanh\alpha_2 t}{k\alpha_2 + k\alpha_1 \tanh\alpha_2 t}\right) \qquad 2.31$$

These conditions can be seen as a special case of the mode guidance condition (2.29), where $\alpha_1=\alpha_5$, $\alpha_2=\alpha_4$, h=t and p=0,2,4.... for the even modes or p=1,3,5..... for the odd modes. Once again these conditions can be solved numerically.

2.2.3 **Three-layer asymmetric slab waveguide**

The most common type of waveguide structure examined in this thesis was the three-layer asymmetric planar waveguide. The light is confined to propagate within the core region by reflection at the boundaries with the substrate material and the cladding layer, which is often air. The condition for guidance is that the core index is greater than the cladding or substrate index.

Equation 2.29 can easily be generalised to a three-layer structure by setting h=0, t=0 and $\alpha_1=\alpha_2$, $\alpha_4=\alpha_5$ such that,

$$2kd_1 - \tan^{-1}\left(\frac{\alpha_1}{k}\right) - \tan^{-1}\left(\frac{\alpha_5}{k}\right) = p\pi \qquad 2.32$$

This is in agreement with other reported analysis [2].

2.3. Laser theory

2.3.1 Introduction

This section will discuss basic laser theory and apply the theory to a planar waveguide geometry. Comparisons between bulk lasers and waveguide lasers will be made. The laser system considered is shown in figure 2.4. This shows the energy level diagram for a typical four-level laser system, such as the $^4F_{3/2} \rightarrow {}^4I_{11/2}$ 1.1μm transition in

neodymium which has been extensively investigated in this thesis. In a four-level laser system an incoming pump photon excites an electron from its low energy ground state to some higher energy excited state. This higher energy electron loses energy via a non-radiative decay process. It then occupies a metastable upper laser level and can undergo stimulated emission from here to a lower laser level. Finally the electron decays back to the ground state, via a non-radiative transition, and the cycle can start again.

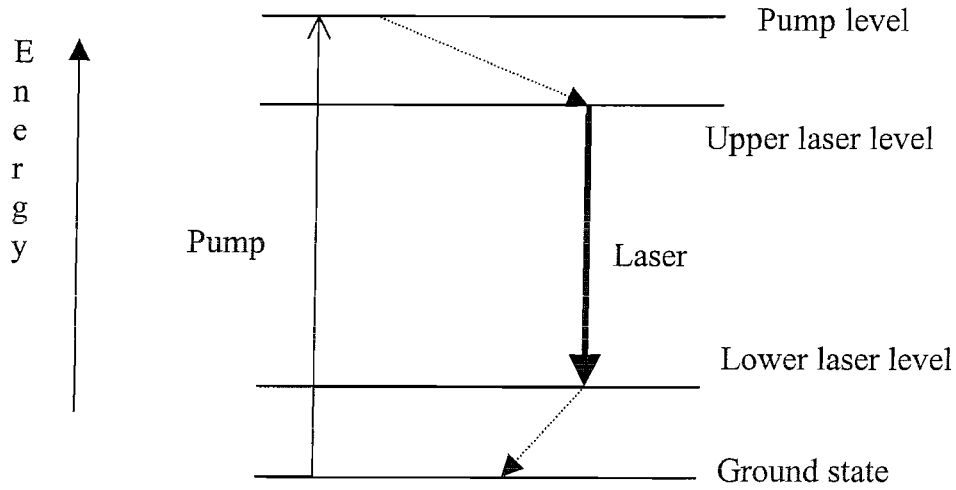

Figure 2.4 Basic four-level laser system

Another type of laser system, known as quasi-three-level, operates when the lower laser level is part of the ground state manifold. Figure 2.5 shows the energy level diagram for this type of laser. Examples of quasi-three-level transitions include the $^4F_{3/2} \rightarrow {}^4I_{9/2}$ transition around 0.9μm in neodymium and the $^2F_{5/2} \rightarrow {}^2F_{7/2}$ transition around 1030nm in ytterbium, which have also been studied in this thesis. Three-level laser systems suffer from additional loss not present in four-level systems due to the thermally-populated lower laser level. Electrons in this level reabsorb laser photons that have undergone stimulated emission adding to the overall loss of the transition.

An analysis of a longitudinally-pumped quasi-three-level system will be used to derive expressions for the threshold and output power of a laser (following Risk [7] and Kubodera and Otuska [8]), allowing for the asymmetric mode-shape often found

in planar waveguides. This result will then be extended to apply to a four-level laser and to a side-pumped geometry.

2.3.2 Quasi-three-level lasers

The energy level diagram for a typical quasi-three-level laser is shown in figure 2.5.

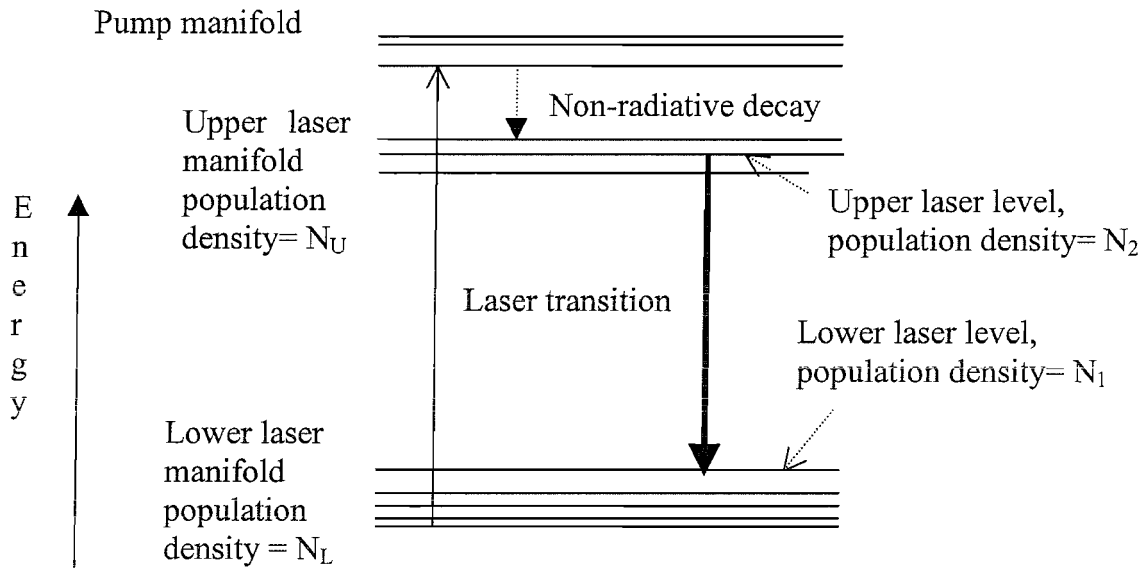

Figure 2.5 Energy level diagram of a typical quasi-three-level transition

The lower laser level population density, N_1, can be expressed as $N_1 = f_1 N_L$, where f_1 is the fraction of the lower laser manifold population density residing in the appropriate Stark-level. Similarly N_2, the upper laser level population density, is given by $N_2 = f_2 N_U$, where f_2 is the fraction of N_U in the Stark-level forming the upper laser level. The steady-state rate equations for N_1, N_2 and the population inversion density, $\Delta N = N_2 - N_1$, can now be written assuming negligible depletion of the ground state. In this analysis the effects of spatial hole burning are neglected [9] and the pump light is considered to make just one pass through the laser medium.

$$\frac{dN_1(x,y,z)}{dt} =$$

$$-f_1 Rr(x,y,z) - \frac{N_1(x,y,z) - N_1^{\,0}}{\tau} + \frac{f_1 c \sigma_e [N_2(x,y,z) - N_1(x,y,z)]}{n} \Phi \phi(x,y,z) = 0 \qquad 2.33$$

$$\frac{dN_2(x,y,z)}{dt} =$$

$$f_2 Rr(x,y,z) - \frac{N_2(x,y,z) - N_2{}^0}{\tau} - \frac{f_1 c\sigma_e[N_2(x,y,z) - N_1(x,y,z)]}{n}\Phi\phi(x,y,z) = 0 \qquad 2.34$$

By subtracting 2.33 from 2.34:

$$\frac{d\Delta N(x,y,z)}{dt} =$$

$$(f_1 + f_2)Rr(x,y,z) - \frac{\Delta N(x,y,z) - \Delta N^{\,0}}{\tau} - \frac{(f_1 + f_2)c\sigma_e \Delta N(x,y,z)}{n}\Phi\phi(x,y,z) = 0 \qquad 2.35$$

where τ is the lifetime of the upper level, $\Delta N^0 = N_2{}^0 - N_1{}^0$ is the unpumped population inversion density, c is the speed of light in a vacuum, σ_e is the laser emission cross section and n is the refractive index of the laser material.

R is the rate of pumping: $$R = \frac{P_p(1 - e^{-\alpha_p l})}{h\upsilon_p} \qquad 2.36$$

where it is assumed that the pump propagation losses in the waveguide are negligible compared to the absorption loss,

and Φ is the number of photons in the cavity: $$\Phi = \frac{2nlP_L}{ch\upsilon_L} \qquad 2.37$$

where l is the length of the laser gain medium, P_P is the incident pump power, P_L is the intracavity laser power travelling in one direction, h is Planck's constant, υ_p and υ_L are the pump and laser frequencies respectively and α_p is the absorption coefficient of the pump in the gain medium.

r(x,y,z) and ϕ(x,y,z) are respectively, the normalised pump and signal distributions such that:

$$\int_{\text{cavity}} r(x,y,z)dV = \int_{\text{cavity}} \phi(x,y,z)dV = 1 \qquad 2.38$$

writing $f=f_1+f_2$ and noting that $N_1^0 >> N_2^0$ in thermal equilibrium, enables equation 2.35 to be rearranged to give [7]:

$$\Delta N(x,y,z) = \frac{f\tau R r(x,y,z) - N_1^0}{1 + \frac{c\sigma_e \tau}{n} f\Phi\phi(x,y,z)} \qquad 2.39$$

The growth in the propagating signal intensity, I(x,y,z), related to the gain, g(x,y,z) is given by [7]:

$$\frac{dI(x,y,z)}{dz} = g(x,y,z)I(x,y,z) \qquad 2.40$$

The laser condition stating that round-trip loss must equal round-trip gain in the cavity can be expressed as equation 2.41 for small values of loss.

$$\int_{\text{roundtrip}} dP_L(z) = 2\int_0^l \frac{dP_L(z)}{dz}dz = P_L(L+T) \qquad 2.41$$

where L is the round-trip cavity loss exponent excluding any mirror losses, and T is the natural logarithm of the output mirror reflectivity. T is approximately equal to the mirror transmission for high values of mirror reflectivity.

$P_L(z)$ is the single-pass intracavity power at a point z and is found by integration:

$$P_L(z) = \int_{-\infty}^{\infty}\int_{-\infty}^{\infty} I(x,y,z)\,dxdy \qquad 2.42$$

Differentiating 2.42 with respect to z gives:

$$\frac{dP_L(z)}{dz} = \int_{-\infty-\infty}^{\infty}\int^{\infty}\frac{dI(x,y,z)}{dz}dxdy \qquad 2.43$$

Using equations 2.40, 2.41 and 2.43:

$$2\int_0^l\int_{-\infty-\infty}^{\infty}\int^{\infty} g(x,y,z)\, I(x,y,z)\, dxdydz = P_L(L+T) \qquad 2.44$$

Equation 2.44 can then be rewritten using $\Delta N(x,y,z)$ from 2.39 and the expressions $g(x,y,z)=\sigma_e\Delta N(x,y,z)$ and $I(x,y,z) = \left(\frac{ch\upsilon_L}{2n}\right)\Phi\phi(x,y,z)$. Equation 2.45 then describes a bulk laser above threshold.

$$2\int_0^l\int_{-\infty-\infty}^{\infty}\int^{\infty}\frac{ch\upsilon_L}{2n}\left[\frac{f\sigma_e\tau Rr(x,y,z) - N_1^{\,0}\sigma_e}{1+\frac{c\sigma_e\tau}{n}f\Phi\phi(x,y,z)}\right]\Phi\phi(x,y,z)dxdydz = P_L(L+T) \qquad 2.45$$

2.3.3 Application to waveguide lasers

To apply equation 2.45 to a planar waveguide laser the values of $\phi(x,y,z)$ and $r(x,y,z)$, the normalised pump and signal distributions, must be evaluated. In a channel waveguide, or an optical fibre, it is assumed that the pump and signal spot size remain the same throughout the gain medium. However this is not the case for the non-guided plane of a thin-film waveguide. Instead the normalisation uses the approximation of an average spot size propagating in the non-guided plane of the gain medium. The normalised pump and signal distributions, calculated to satisfy the condition 2.38, are given in 2.46 and 2.47, where $w_{p(x,y)}$ are the pump beam spot sizes in the x (guided) and y (non-guided) directions respectively, and $w_{L(x,y)}$ are the corresponding signal beam spot sizes.

$$r(x,y,z) = \frac{2\alpha_p}{\pi w_{px} w_{py}(1-e^{-\alpha_p l})}\exp\left(\frac{-2x^2}{w_{px}^2}\right)\exp\left(\frac{-2y^2}{w_{py}^2}\right)\exp(-\alpha_p z) \qquad 2.46$$

$$\phi(x,y,z) = \frac{2}{\pi w_{Lx} w_{Ly} l} \exp\left(\frac{-2x^2}{w^2_{Lx}}\right) \exp\left(\frac{-2y^2}{w^2_{Ly}}\right) \qquad 2.47$$

These equations (2.46 and 2.47) are combined with 2.45, 2.36 and 2.37 to give:

$$2\int_0^l \int_{-\infty}^{\infty}\int_{-\infty}^{\infty} \frac{ch\upsilon_L \Phi}{2n} \frac{\left[\frac{2\sigma_e \tau f P_p \alpha_p}{h\upsilon_p \pi w_{px} w_{py}} \exp\left(\frac{-2x^2}{w^2_{px}}\right)\exp\left(\frac{-2y^2}{w^2_{py}}\right)\exp(-\alpha_p z) - N_1{}^0 \sigma_e\right]}{\left[1 + \frac{2c\sigma_e \tau f \Phi}{n\pi w_{Lx} w_{Ly} l} \exp\left(\frac{-2x^2}{w^2_{Lx}}\right)\exp\left(\frac{-2y^2}{w^2_{Ly}}\right)\right]} \times$$

$$\frac{2}{\pi w_{Lx} w_{Ly} l} exp\left(\frac{-2x^2}{w^2_{Lx}}\right)\exp\left(\frac{-2y^2}{w^2_{Ly}}\right) dxdydz = \Phi \frac{ch\upsilon_L}{2nl}(L+T)$$

2.48

2.48 can be simplified with the substitutions 2.49 to the following (2.50):

$$a_{px} = \exp\left(\frac{-2x^2}{w^2_{px}}\right) \qquad a_{py} = \exp\left(\frac{-2y^2}{w^2_{py}}\right)$$

$$a_{Lx} = \exp\left(\frac{-2x^2}{w^2_{Lx}}\right) \qquad a_{Ly} = \exp\left(\frac{-2y^2}{w^2_{Ly}}\right) \qquad 2.49$$

$$\int_0^l \int_{-\infty}^{\infty}\int_{-\infty}^{\infty} \frac{\left[\frac{2\sigma_e \tau f P_p \alpha_p}{\pi h\upsilon_p w_{px} w_{py}}(a_{px})(a_{py})\exp(-\alpha_p z) - N_1^0 \sigma_e\right]\left[\frac{4}{\pi w_{Lx} w_{Ly}}(a_{Lx})(a_{Ly})\right]}{\left[1 + \frac{2\sigma_e \tau f P_L}{h\upsilon_L w_{Lx} w_{Ly}}(a_{Lx})(a_{Ly})\right]} dxdydz = (L+T)$$

2.50

It is now possible to solve this equation numerically to give the input/output characteristics of the laser as a function of the signal and pump powers P_L and P_p.

At threshold the output laser power is zero, i.e. P_L=0. Substitution of P_L=0 into 2.50 results in an expression for the threshold pump power, P_{th} :

$$P_{th,guide} = \frac{\pi h\upsilon_p}{4\sigma_e \tau f(1-e^{-\alpha_p l})}\left[\left(w_{px}^{\ 2} + w_{Lx}^{\ 2}\right)^{1/2}\left(\overline{w_{py}}^{\ 2} + \overline{w_{Ly}}^{\ 2}\right)^{1/2}\right] \times \left[L_{guide} + T + 2N_1^{\ 0}\sigma_e l\right] \qquad 2.51$$

where the use of average spot sizes in the non-guided direction is indicated as $\overline{w_y}^{\ 2}$ [10] where

$$\overline{w}_y^{\ 2} = \frac{1}{l}\int_0^l w(z)^{\ 2}\, dz \qquad 2.52$$

L_{guide} in equation 2.51 represents the round trip propagation loss exponent, $e^{-L} = \exp(-2\alpha_g l)$, where α_g is the guide propagation loss coefficient at the laser wavelength.

The slope efficiency of a laser, $s\varepsilon$, is the gradient of a plot of output laser power versus input pump power. It is a useful characteristic of the laser and describes how efficiently input pump power is converted into output power. $s\varepsilon$ can be evaluated numerically by finding the required P_p for a range of values of P_L substituted into equation 2.50. Slope efficiency is also discussed in section 2.3.5.

2.3.4 Four-level laser systems

To use the laser modelling described in sections 2.3.2 and 2.3.3 to describe a pure four-level waveguide laser the population density of the lower level, and thus the reabsorption loss term must be set to zero. This leads to the following expression:

$$P_{th,guide} = \frac{\pi h\upsilon_p}{4\sigma\tau f(1-e^{-\alpha_p l})}\left[\left(w_{px}^{\ 2} + w_{Lx}^{\ 2}\right)^{1/2}\left(\overline{w_{py}}^{\ 2} + \overline{w_{Ly}}^{\ 2}\right)^{1/2}\right] \times \left[L_{guide} + T\right] \qquad 2.53$$

Equation 2.53 agrees with the results from the modelling of four-level lasers found in the literature, [11].

The numerical evaluation of equation 2.50 with N_1^0 set to 0 can give the required P_p for a range of values of P_L. This allows the calculation of the slope efficiency of four-level laser systems

2.3.5 Comparison of bulk and waveguide lasers

To demonstrate some of the advantages of a waveguide laser over a comparable bulk system, the theoretical laser threshold and slope efficiency for each system will now be compared.

Rearranging equation 2.51 to allow for the non-guided circularly symmetric geometry of a longitudinally-pumped bulk laser gives:

$$P_{th,bulk} = \frac{\pi h\upsilon_p}{4\sigma_e f\tau(1-e^{-\alpha_p l})}\left[\overline{w^2}_{pbulk} + \overline{w^2}_{Lbulk}\right] \times \left[L_{bulk} + T + 2N_1^0\sigma_e l\right] \qquad 2.54$$

If the condition that $w_L \approx w_p$ is set, in order to obtain a good slope efficiency, the pump power threshold is proportional to $\overline{w_p^2}$, the pump spot size radius averaged over the gain medium. Therefore the lowest threshold is obtained using a focusing scheme that minimises $\overline{w_p^2}$. This is achieved by focusing to a beam waist size of:

$$w_{p(L)} = \sqrt{\frac{\lambda_{p(L)} l}{2\sqrt{3}\pi n}} \qquad 2.55$$

where $\lambda_{p(L)}$ is the pump (or laser) wavelength. This is somewhat tighter than confocal focusing. The optimum average spot size is then given by:

$$\overline{w^2_p} = \frac{\lambda_p l}{\sqrt{3}\pi n} \qquad 2.56$$

The threshold obtainable in a bulk laser with these optimum spot sizes is found by substituting 2.56 into 2.54.

$$P_{th,bulk} = \frac{h\upsilon_p l}{4\sqrt{3}\sigma f \eta (1-e^{-\alpha_p l})}\left(\lambda_p + \lambda_L\right) \times \left(L_{bulk} + T + 2N_1^0 \sigma l\right) \qquad 2.57$$

The ratio of waveguide to bulk laser threshold in the same material is found by division of 2.51 by 2.57:

$$\frac{P_{th,guide}}{P_{th,bulk}} = \frac{\frac{\pi h\upsilon_p}{4\sigma\tau f\left(1-e^{-\alpha_p l}\right)}\left[\left(w_{px}^2 + w_{Lx}^2\right)^{1/2}\left(\overline{w_{py}}^2 + \overline{w_{Ly}}^2\right)^{1/2}\right]\left[L_{guide} + T + 2N_1^0\sigma_e l\right]}{\frac{h\upsilon_p l}{4\sqrt{3}\sigma\tau f\eta\left(1-e^{-\alpha_p l}\right)}\left(\lambda_p + \lambda_L\right)\left[L_{bulk} + T + 2N_1^0\sigma_e l\right]} \qquad 2.58$$

If the output coupler transmission is set to be equal to twice the round trip cavity loss exponent, L, to ensure a good output efficiency in both cases, then,

$$\frac{P_{th,guide}}{P_{th,bulk}} = \left(w_{px}^2 + w_{Lx}^2\right)^{1/2}\left[\frac{\sqrt{3}\pi n}{l(\lambda_p + \lambda_L)}\right]^{1/2}\left[\frac{3\alpha_g + N_1^0\sigma_e}{3\alpha_b + N_1^0\sigma_e}\right] \qquad 2.59$$

Where α_g and α_b are, respectively, the guide and bulk propagation loss coefficients at the laser wavelength. Using equation 2.59, figures 2.6 and 2.7 illustrate situations in which a waveguide geometry will have the greatest advantage over a bulk system. Equation 2.59 shows that this is usually with long lengths of gain material and small guided spot sizes, however the overall increase in loss in a waveguide may offset the advantages over a bulk system. Waveguide fabrication can result in larger propagation losses than in bulk, meaning $L_{guide} > L_{bulk}$. Therefore every effort must be made to keep waveguide losses to a minimum, preferably below 1dB/cm. A simple calculation (ignoring upconversion, saturation and other effects) of the gain available from a

diode-bar pumped Nd:YAG waveguide with typical spot sizes of 2μm X 1mm and 10W of absorbed pump power leads to 226dB. Experimentally diode-pumped gains of 52dB per Watt of absorbed pump power were obtained in a 5mm length of a 3.8μm thick Nd:YAG waveguide [12]. These values show that at least for Nd:YAG, the gain available from a short length of waveguide sample is so high that propagation losses of ~1dB/cm will not stop laser action, however the loss will affect the performance and efficiency of the device, as shown on the following graphs. Figures 2.6 and 2.7 show curves plotted with different reabsorption loss values ($N_1^0\sigma_e$), corresponding to various laser transitions investigated in this thesis.

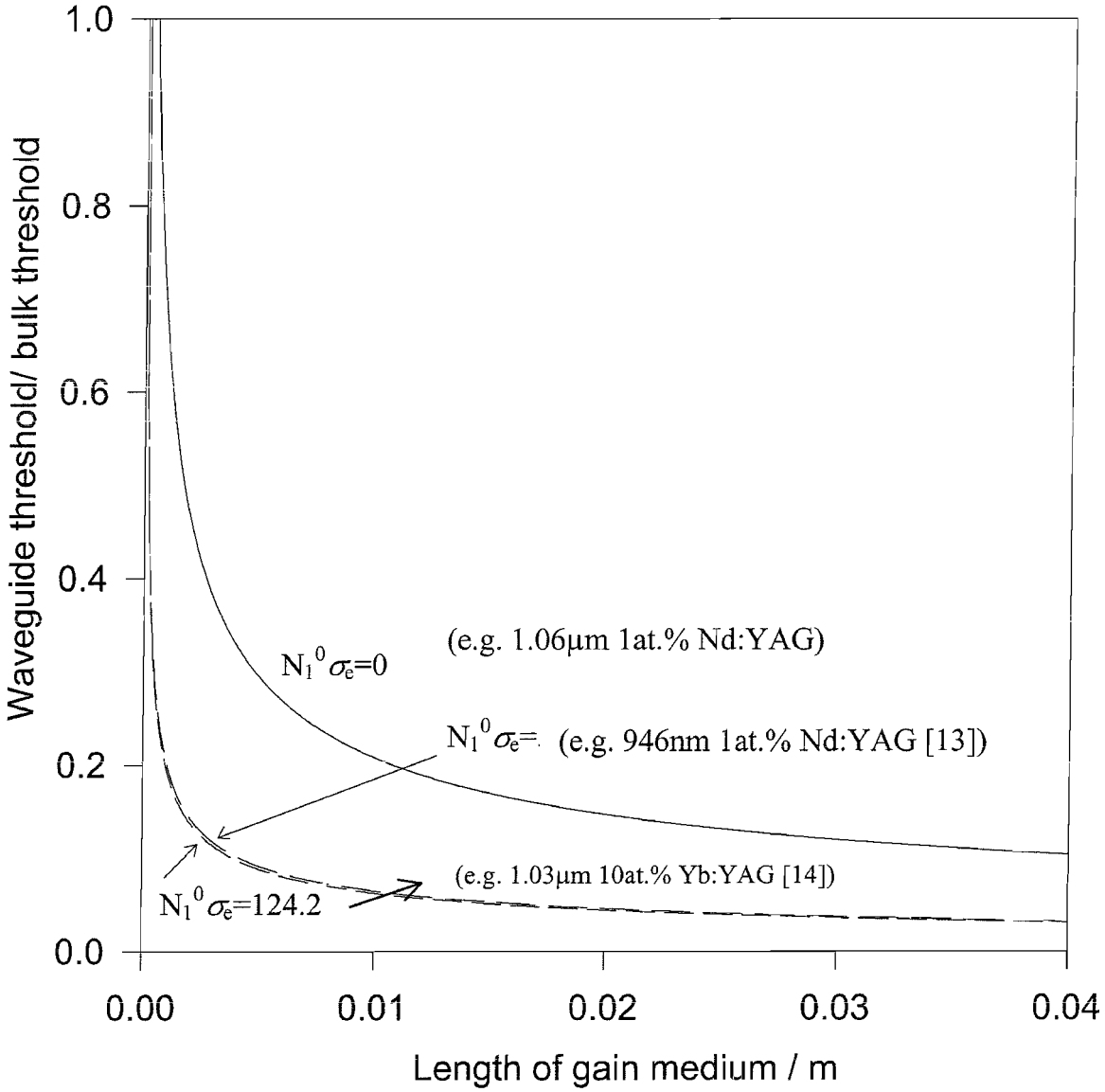

Figure 2.6 Graph showing the advantage of waveguide geometry over bulk with longer lengths of gain medium

The bulk loss is assumed to be 0.03dB/cm [15], the waveguide loss used is typical for an LPE waveguide, 0.1dB/cm [16], and n=1.82 (for YAG) at 633nm [17]. The guided direction pump and laser spot sizes are set to 2μm and the pump wavelength is 808nm. Figure 2.6 shows that the waveguide geometry has the greatest advantage over bulk for long lengths of gain material.

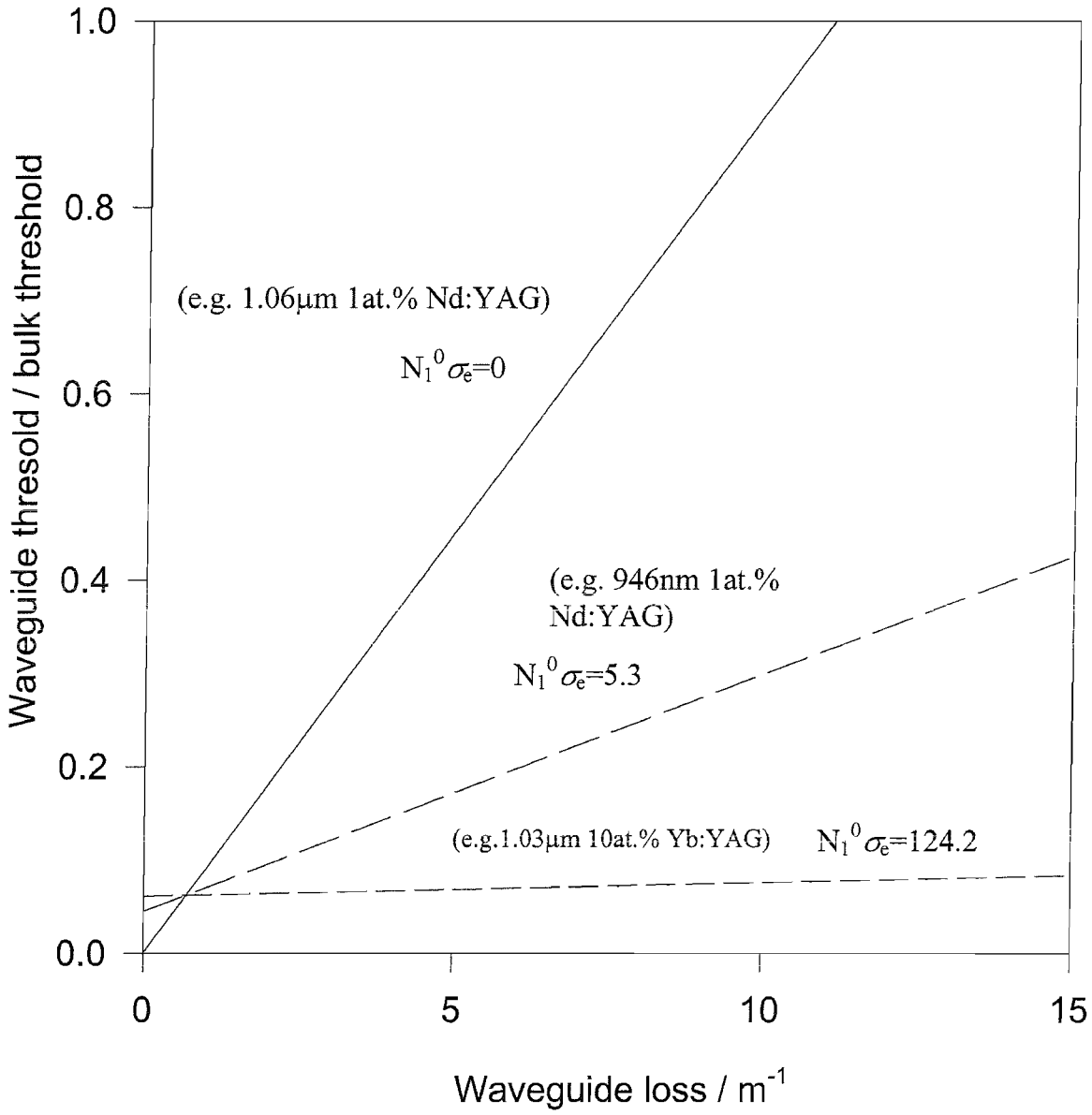

Figure 2.7 Plots showing advantage of a low loss waveguide laser over a bulk laser

Figure 2.7 illustrates that the benefit of a waveguide geometry is most apparent when using low loss waveguides, the graph is produced for a fixed, 1cm, length of gain medium. One area where propagation losses are less important is in a quasi-three-level laser where the reabsorption losses dominate. The losses in the waveguide are

then comparable to those in the bulk, giving the waveguide a significant advantage. Both figures 2.6 and 2.7 show that a waveguide laser performs comparatively better than a bulk laser for laser systems with higher $N_1{}^0\sigma_e$ values.

The slope efficiency, $s\varepsilon$, is given by [7]:

$$\frac{dP_L}{dP_p} = s\varepsilon = \left(\frac{T}{T+L}\right)\frac{\upsilon_L}{\upsilon_p}(1-e^{-\alpha_p l})\frac{dS}{dF} \qquad 2.60$$

This ratio depends on: $(1-\exp(-\alpha_p l))$, the absorption efficiency of the incident pump photons, the efficiency of conversion of absorbed pump photons into laser photons (dS/dF), the associated quantum defect, (υ_L/υ_p) and T/(L+T), the fraction of laser photons lost from the cavity through the output coupler compared to the total loss. dS/dF is a quantity that contains the overlap and geometrical factors associated with the conversion of pump photons into laser emission.

The difference in the slope efficiency between a waveguide and a bulk laser is mainly due to the extra propagation loss in the waveguide reducing the laser efficiency. In order to obtain the same slope efficiency from both types of laser system a higher transmission output coupler is required in the waveguide case, but this in turn increases the overall loss in the cavity resulting in a higher laser threshold. However, small spot sizes, a well confined mode and low propagation losses can still combine to result in a waveguide laser with a lower threshold, and the same slope efficiency as a comparable bulk laser.

2.3.6 Waveguide laser with uniform population inversion

Modifications are made to the threshold expression given in equation 2.51 for side-pumping, due to the different pump and signal spatial distributions. A side-pumped waveguide laser is shown in figure 2.8, with the doped layer defined by the limits $-d<x<d$, $-l/2<y<l/2$, and $0<z<W$.

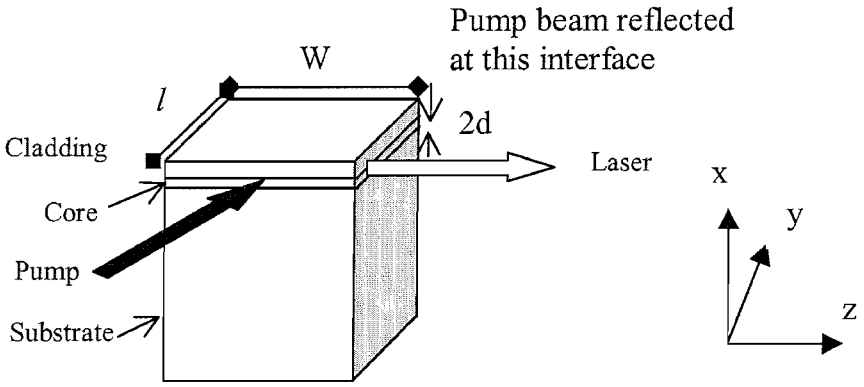

Figure 2.8 Layout of a side-pumped waveguide laser

The analysis is based on the same principle described earlier in section 2.3.2, however the normalised expressions for the pump distribution, r, and signal distribution, ϕ, are changed to account for the new pumping geometry. A uniform inversion is assumed, both along the waveguide pumping length, l and the waveguide width, W. This situation approximates the case of a side-pumped waveguide where the pump beam makes a double pass through the gain material, as used later with proximity coupling. Details of this pumping scheme will be given in later chapters. The laser photon distribution is assumed to be invariant along z, but to have fundamental Gaussian modes in the x and y directions. The normalised expressions for r_0 and s_0 are given in equations 2.61 and 2.62. This analysis assumes that the pump and signal are both well contained within the waveguide core, and so is applicable to the case of a high numerical aperture waveguide.

$$\text{For} \begin{cases} -\infty < x < \infty \\ -l/2 < y < l/2 \\ 0 < z < W \end{cases} \qquad r = \sqrt{\frac{2}{\pi}} \frac{\exp\left(-\frac{2x^2}{w_{px}^2}\right)}{W l w_{px}}$$

elsewhere $r = 0$ 2.61

$$\text{For}\begin{cases} -\infty < x < \infty \\ -\infty < y < \infty \\ 0 < z < W \end{cases} \qquad \phi = \frac{2}{\pi} \frac{\exp -\left(\frac{2x^2}{w_{Lx}^{\ 2}} + \frac{2y^2}{w_{Ly}^{\ 2}} \right)}{W w_{Lx} w_{Ly}}$$

elsewhere $s_0 = 0$ 2.62

The threshold of such a three-level laser is obtained by substituting r and ϕ into 2.45 and solving for P_L=0 as previously. This gives:

$$P_{th} = \frac{\sqrt{\pi} h \upsilon_p l \left[L_{guide} + T + 2N_1^0 \sigma_e W \right]}{2\sqrt{2} f \sigma_e \tau \left[1 - \exp^{-\alpha_p W} \right]} \left(w_{Lx}^2 + w_{px}^2 \right)^{1/2} \qquad 2.63$$

Once again the slope efficiency can be found from numerically solving 2.45 to give the input/output characteristic of the laser

2.5 Beam Quality – the M^2 measurement

In recent years the topic of laser beam quality has seen much debate within the laser community. A measurement of 'beam quality' is clearly required to fully quantify a laser beam, however it is not yet a solidly defined technical term and its measurement can be carried out in a number of ways. Standards [18] are being developed and tested which will hopefully lead to a uniform, less ambiguous approach to describing a laser beam in the future. A theoretical discussion of M^2 beam quality will be given here, as the second moment based M^2 values have been used to describe beam quality in the majority of this thesis. The experimental technique used for these measurements can be found in the next chapter (section 3.10).

It is important to know how a beam will behave as it propagates through the elements in a laser cavity. In particular how the beam focuses after a lens is crucial to laser design. A fundamental Gaussian mode will focus to the minimum possible waist diameter and diverge least on passing through a lens. It has diffraction-limited

performance. A measurement of M^2 beam quality can be made by analysing how an arbitrary beam diverges and focuses compared to this diffraction-limited behaviour.

2.5.1 Measuring beam width

In order to compare the divergence of an arbitrary beam to that of a diffraction limited beam, and thus find an M^2 value, a method of defining and measuring the beam width must be found.

A popular technique measures the radius, r, at which the intensity falls to $1/e^2$ of some peak intensity, however this is only valid for Gaussian beams with $M^2=1$ and not for beams containing higher order modes [19].

A more mathematically rigorous definition uses the second moment of the beam intensity distribution I(r).

This is defined as [19]:

$$\overline{r^2} = \frac{\int_{-\infty}^{\infty} (r - r_0)^2 I(r) dA}{\int_{-\infty}^{\infty} I(r) dA} \qquad 2.64$$

where A is the area over which the integration is performed, and r_0 is the centre of gravity of the beam.

For a beam with circular symmetry equation 2.64 becomes [19]:

$$\overline{r^2} = \frac{2\pi \int_{-\infty}^{\infty} r^3 I(r) dr}{\int_{-\infty}^{\infty} I(r) dA} \qquad 2.65$$

and the spot size radius, W_r, (defined as the $1/e^2$ radius of a Gaussian profile) is related to the second moment as in equation 2.66:

$$W_r = \sqrt{2\overline{r^2}} \qquad 2.66$$

However if a beam, for example a diode-bar, is non-circularly symmetric it is useful to express equation 2.64 in rectangular co-ordinates. The second moment of the beam intensity distribution I(x,y) across the co-ordinate x (or y) is:

$$\overline{r_x^2} = \frac{\int_{-\infty}^{\infty}\int_{-\infty}^{\infty}(x - x_0)^2 I(x,y)dxdy}{\int_{-\infty}^{\infty}\int_{-\infty}^{\infty} I(x,y)dxdy} \qquad 2.67$$

where x_0 is the centre of gravity of the beam.

This second moment obeys a rigorous, universal free-space propagation rule [19, 20]:

$$\overline{r_x^2(z)} = \overline{r_{0x}^2} + \overline{r_\theta^2} \times (z - z_0)^2 \qquad 2.68$$

where r_{0x} is the variance at the beam waist, r_θ is the variance of the angular spread of the beam from the waist and z_0 is the position of the beam waist along the z axis. This quadratic propagation dependence has been found to be true for all types of laser beams; Gaussian or non-Gaussian, single or multi-transverse mode. However equation 2.68 is only rigorously true when beam widths are defined by the second moment of intensity method. Any attempt to universally define or measure beam quality must therefore use second moments beam widths.

Substituting a Gaussian beam profile, described by, $I(x)=\exp[-2x^2/w_x^2]$, into equation 2.67 gives $w_x = 2\sqrt{r_x^2}$. This is detailed in equations 2.69-2.71.

$$\overline{r_x^2} = \frac{\int_{-\infty}^{\infty} x^2 e^{-2x^2/w_x^2} dx}{\int_{-\infty}^{\infty} e^{-2x^2/w_x^2} dx} \qquad 2.69$$

using the standard integrals

$$\int_{-\infty}^{\infty} e^{-ax^2} dx = \sqrt{\frac{\pi}{a}} \qquad \int_{-\infty}^{\infty} x^2 e^{-ax^2} dx = -\frac{d}{da}\sqrt{\frac{\pi}{a}}$$

and setting $\frac{2}{w_x^2} = a$

$$\text{gives } \overline{r_x^2} = \frac{-\frac{d}{da}\sqrt{\frac{\pi}{a}}}{\sqrt{\frac{\pi}{a}}} = \frac{1}{2a} \qquad 2.70$$

$$\text{thus } w_x = \sqrt{4\overline{r_x^2}} \qquad 2.71$$

For a beam that is separable in the x and y directions:

$$< \overline{r^2} >=< \overline{r_x^2} > + < \overline{r_y^2} > \qquad 2.72$$

$$\text{which gives: } < \overline{r^2} >= \frac{w_r^2}{4} + \frac{w_r^2}{4} \qquad \text{and thus} \qquad w_r = \sqrt{2\overline{r^2}}$$

in agreement with the circularly symmetric beam width given in equation 2.66.

It is then logical to define the spot size or beam width, W, of an arbitrary beam as:

$$W_x \equiv \sqrt{4\overline{r_x^2}} \qquad W_y \equiv \sqrt{4\overline{r_y^2}} \qquad 2.73$$

The beam widths, W_x and W_y, based on second moments will propagate in free space as a Gaussian spot (of size w(z)) would do, except the far-field spreading of the beam would be multiplied by a factor M^2. The beam width of any arbitrary beam defined in this way can then be written [20]:

$$W_x^2(z) = W_{0x}^2 + M_x^4 \times \left(\frac{\lambda}{\pi W_{0x}}\right)^2 (z - z_{0x})^2 \qquad 2.74$$

and

$$W_y^2(z) = W_{0y}^2 + M_y^4 \times \left(\frac{\lambda}{\pi W_{0y}}\right)^2 (z - z_{0y})^2 \qquad 2.75$$

where M_x and M_y are characteristic parameters of the particular beam. The near-field far-field product can be written using M_x and M_y as in equations 2.76.

$$W_{0x} \times W_x(z) \approx M_x^2 \times \frac{z\lambda}{\pi} \qquad W_{0y} \times W_y(z) \approx M_y^2 \times \frac{z\lambda}{\pi} \qquad 2.76$$

Thus the M^2 value gives a measure of the 'quality' of an arbitrary beam and poor quality, less ideal beam profiles will have larger near-field far-field products, i.e. $M^2>1$. Using this convention an arbitrary laser beam can be fully characterised in both directions with the six parameters; W_{0x}, W_{0y}, z_{0x}, z_{0y}, M_x^2, M_y^2.

The overall beam quality of a laser depends on the laser design itself, for instance the shape of the cavity, the emitting area and thermal effects in the gain medium. For example diode lasers have a highly astigmatic emitting region. The output from this region is non-diffraction limited in the non-guided direction, leading to a large difference in M^2 values in the x and y directions. M^2 is also affected by aberrations introduced by optics used to focus and direct the output beam. Methods of spatial mode control for improving the output laser beam quality of a waveguide laser will be discussed in chapter 7.

2.6 References

[1] A.Yariv, *'Quantum Electronics'*, Chap.13, Wiley (1989)

[2] D.H.Lee, *'Electromagnetic Principles of Integrated Optics'*, Chap.4, Wiley (1986)

[3] A.W.Snyder. J.D.Love, *'Optical Waveguide Theory'*, Chaps.1-5, Chapman and Hall (1983)

[4] D.H.Lee, *'Electromagnetic Principles of Integrated Optics'*, Chap.5, Wiley (1986)

[5] H.J.W.M.Hoekstra, G.J.M.Krijen, P.V.Lambeck, Opt. Comm., **94**, pp.506-508 (1992)

[6] C.L.Bonner, T.Bhutta, D.P.Shepherd, A.C.Tropper, IEEE J. Quantum Electron., **36**, pp.236-242 (2000)

[7] W.P.Risk, J. Opt. Soc. Am. B, **5**, pp.1412-1423 (1988)

[8] K.Kubodera, K.Otsuka, J. Appl. Phys., **50**, pp.653-659 (1979)

[9] T.Y.Fan, R.L.Byer, IEEE J. Quantum Electron., **23**, pp.605 612 (1987)

[10] M.F.J.Digonnet, C.J.Gaeta, Appl. Opt., **24**, pp.333-342 (1985)

[11] W.A.Clarkson, D.C.Hanna, J. Modern Optics, **36**, pp.483-498 (1989)

[12] D.P.Shepherd, C.T.A.Brown, T.J.Warburton, D.C.Hanna, A.C.Tropper, B.Ferrand, Appl. Phys. Lett., **71**, pp.876-878 (1997)

[13] D.C.Hanna, A.C.Large, D.P.Shepherd, A.C.Tropper, I.Chartier, B.Ferrand, D.Pelenc, Appl. Phys. Lett., **63**, pp.7-9 (1993)

[14] P.Lacovara, H.K.Choi, C.A.Wang, R.L.Aggarwal, T.Y.Fan, Opt. Lett., **16**, pp.1089-1091 (1991)

[15] T.Nishimura, T.Omi, Jpn. Appl. Phys., **14**, pp.1011 (1975)

[16] I.Chartier, B.Ferrand, D.Pelenc, S.J.Field, D.C.Hanna, A.C.Large, D.P.Shepherd, A.C.Tropper, Opt. Lett., **17**, pp.810-812 (1992)

[17] D.Pelenc, *'Guide d'onde laser en Nd:YAG et Yb:YAG per E.P.L.'*, PhD Dissertation, Département Optronique du LETI, C.E.N.G. 85X 38041, France (1992)

[18] ISO/DIS standard 11 146, *'Optics and Optical Instruments, Lasers and Laser related equipment, Test methods for laser beam parameters'*, International Organisation for Standardisation, P.O. Box 65, CG1211, Geneve, Switzerland (1997)

[19] M.W.Sasnett Chap. 9. pp.132-142, *'The Physics and Technology of Laser Resonators'* D.R.Hall, P.E.Jackson, eds., IOP Publishing, (1989)

[20] A.Seigman, *'How to (maybe) measure laser beam quality'*, TUL1, Tutorial at OSA Annual meeting, Long Beach, California, USA, 12-17 October (1997)

Chapter 3 Experimental techniques

3.1 Introduction

This chapter will describe various experimental techniques and equipment used throughout this project and discussed in the following chapters. Most of the techniques are well known in the field while others have arisen specifically from this work. Further details will be given in the relevant experimental chapter if clarification is required.

3.2 Laser sources

The pump lasers used in this study are given in table 3.1. In some cases a number of lasers of the same type have been used but are not listed separately, for example the three JenOptik 10W laser diode-bars all used for proximity coupling experiments.

Model	Laser Type	Wavelength Range	Output power	$M^2_{x,y}$
Coherent Innova 70-4	Argon-Ion (Ti:sapphire pump)	458nm-528nm	6W	1,1
Spectra Physics 3900	Ti:sapphire	750nm-1000nm	1W	1,1
OptoPower OPC-AO20	Diode-bar	~808nm	20W	1,2000-~3000
JenOptik JOLD-20-CPNN	Diode-bar	~808nm	10W	1,2000-~3000
Siemens Dilas 62	Diode-bar	~940nm	20W	1, 2000-~3000

Table 3.1 Pump laser sources used in this project

Laser diode-bars have become the high power pump source of choice for an increasing number of solid state laser applications. Their cost is rapidly reducing and

prices of less than $100 per Watt are predicted to be available in the near future [1]. They have been used extensively in this project and so some details of their structure and function will be given in this chapter. More discussion on their use experimentally will follow in chapters 4 and 6.

A typical laser diode-bar is shown in figure 3.1. Each diode emitter has an aperture ~1 μm x ~200 μm and a diode-bar is composed of a linear array of a number (typically around 20) of identical emitters.

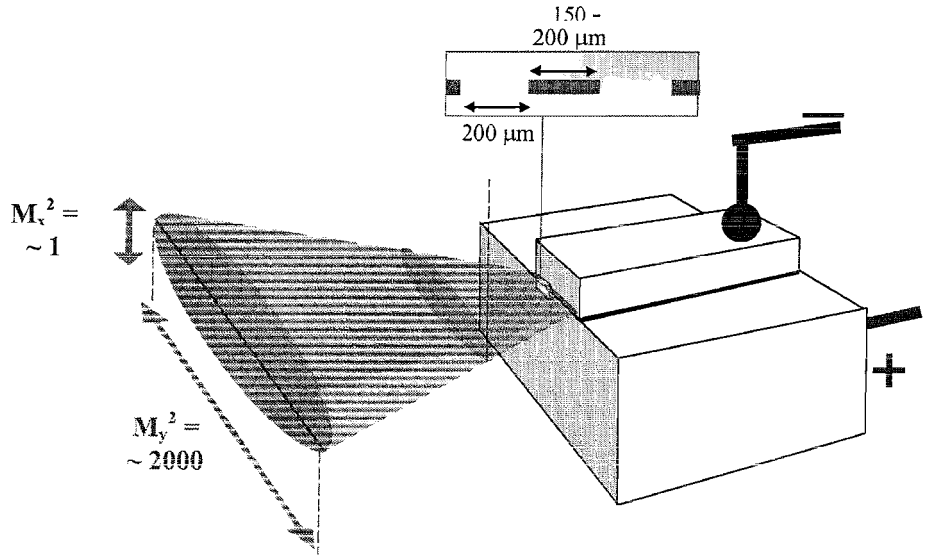

Figure 3.1 A typical laser diode-bar

The width of the diode-bar is ~10mm and output powers of up to 60W with a drive current of ~50Amps are now readily available. The diode-bar is a very compact, efficient source of pump photons and its multi-Watt output powers are far higher than normal argon-ion pumped Ti:sapphire laser systems. The main disadvantage of the diode-bar is its highly astigmatic and non-diffraction-limited output beam. The small emission aperture in the vertical plane produces a highly divergent beam, and it has become common practice to attach a fibre lens directly in front of the emitters to collimate the output beam for refocusing into the laser medium. Some of the diode-bars used in the course of this work were fibre-lensed in house by Dr. W. A. Clarkson, although it is possible to buy such devices commercially [2]. The lenses used here were spherical-aberration-free acylindrical fibres. The output from the fibre-lensed

diode-bar had a $1/e^2$ spot-size diameter of 325μm in the collimated axis and an M^2 of typically ~2. Fibre lensing the diode-bar gives a more manageable laser pump source. However the penalty is a slightly reduced x-direction beam quality caused by trying to collimate such a divergent beam. Further details of fast axis diode-bar collimation are given in reference 3.

Methods of diode-bar manufacture often result in a degree of 'smile', this is illustrated in figure 3.2.

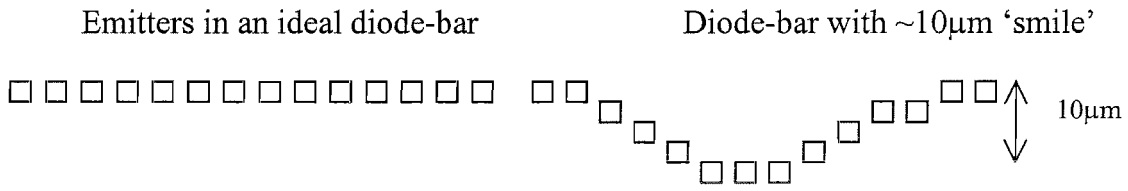

Figure 3.2 Diode-bar 'smile'

The 'smile' occurs when the diode-bar array is not perfectly straight and can be between 1-30μm [4], the degree of bending an end user is willing to tolerate will depend on the application.

Various methods [5] have been devised to further modify the highly elliptical, if collimated, output from a fibre-lensed diode-bar to produce a more circular beam. The aim being to equalise the M^2 values in both planes for circularly symmetric end-pumping of bulk or fibre lasers.

Some degree of wavelength tuning is possible with diode lasers by externally controlling the temperature of the laser-cavity. In this study the diode-bars were mounted on water-cooled heatsinks and tuning of around 0.25nm per degree Celsius was available by adjusting the temperature of the circulating water.

The other lasers used in this work had beam quality close to diffraction-limited. An argon-ion laser was used as the pump source for the Ti:sapphire laser. The argon-ion laser output is composed of nine discreet lines, and was operated in the multi–line mode in order to get the maximum power from the Ti:sapphire laser. The Ti:sapphire

laser system has a broad tuning range and its operating wavelength was selected using a birefringent filter in the laser cavity and one of two mirror sets optimised for the wavelength region required. The diffraction-limited beam quality and broad tunability makes the Ti:sapphire laser ideal for investigating the spectroscopy, basic laser performance and propagation loss of planar waveguides.

3.3. Laser pumping configurations

There are 3 basic configurations for pumping a planar laser gain medium; end-, side- or face-pumping. These schemes are illustrated in figure 3.3.

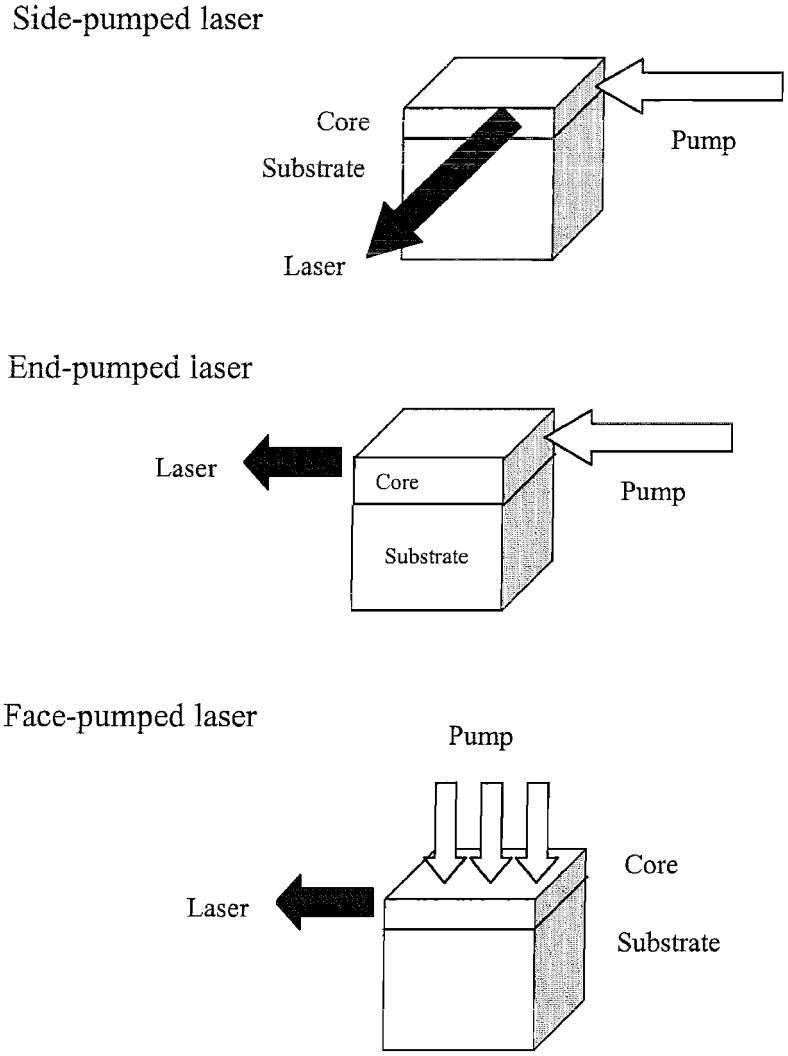

Figure 3.3. Laser pumping schemes

The work described in this thesis has been carried out using the end-pumping and side-pumping techniques only. Face-pumping has been investigated by other workers

[6] and the advantage of face-pumping planar waveguides is that it allows pumping with a stack composed of many diode bars. However the drawback is that it requires special pumping techniques to achieve efficient pump absorption in the thin core.

End-pumping, operates with the pump and the laser signal propagating collinearly in the waveguide core. As a result a very good overlap of the pump and the signal can be achieved leading to an efficient device with a low laser threshold (see equations 2.51 and 2.60). In a side-pumped laser, the pump and laser signal beams propagate at 90^0 to one another in the plane of the waveguide core. Although the overlap between the two beams may be relatively poor, resulting in a higher threshold laser than in an end–pumped geometry, there are a number of advantages to the side-pumping scheme. A side-pumped laser is straightforward to scale to higher powers, as the pump power absorbed can be increased with the length of the pumping face. A diode-bar pump source in particular is well suited to side-pumping a waveguide, as the geometry of the diode emission area is matched to the planar waveguide shape. This can reduce the focusing requirements in the non-guided plane. Another advantage of side-pumping over end-pumping is that the laser signal and the pump beam are not in the same direction. This reduces the wavelength constraints placed on the cavity mirrors and can lead to a simpler cavity design.

The techniques associated with diode-bar pumping are discussed further in chapter 6. They range from launching pump light into the waveguide with bulk cylindrical optics and spherical-aberration-free rod lenses, to just proximity coupling using no intervening optics at all.

3.4 Signal detection

The laser experiments carried out were across the range 0.9μm – 1.1μm, within the wavelength response range of a silicon photodiode (~0.4 μm – 1.1 μm). Large area silicon photodiodes were used throughout the project for signal detection, (most often model number RS-651-996). Wavelength pass (colour) filters were used to block the shorter wavelength pump light. The large area detector made for easy signal alignment, but at the expense of a slow response time, however this was not a

limitation for the CW signals used throughout this thesis. The detector output was amplified and then displayed on an oscilloscope screen or a digital multi-meter for analysis. The response of the silicon detector is not uniform across its entire wavelength range, but no wavelength correction has been made for the majority of detectors used in the course of this thesis as, in general, it was not the aim of the work to obtain extremely accurate spectroscopic measurements. These measurements were not required as well-known, well-documented laser materials such as Nd-doped YAG have been used throughout the experiments.

Wavelength-selective measurements, as often required in laser and fluorescence experiments, were taken using an EG&G Princeton Applied Research Model 1235 Digital Triple Grating Spectrograph. The signal is focused on the entrance slit and is then incident on one of three selectable gratings. The gratings act to spatially separate the wavelengths in the beam and these spatially separated components are then detected by a silicon CCD array. A computer interfaced to the spectrograph with appropriate software displays the spectra obtained. The three different gratings (ruled with 150, 600 or 1200 lines/mm) have different resolutions. The highest resolution grating, with 1200 lines/mm, provides wavelength information over a 60nm range. The spectrograph was calibrated using helium and argon discharge lamps with known spectral characteristics and the calibration was verified with a neon lamp.

A CCD array Cohu 4800 camera (model ER-5001) was used for low power signal detection and beam profiling. A computer interfaced to the camera and running beam analyser software (Beam View Analyser from Big Sky Software and Coherent) was used for this purpose.

3.5 Launching light into a waveguide

Methods for launching pump light into the waveguide core differ depending on the pump source. The experimental arrangement shown in figure 3.4 was used with the diffraction limited Ti:sapphire pump laser for the diagnostic analyses discussed in this chapter. Further details of diode-bar pumping schemes will be given in chapter 6.

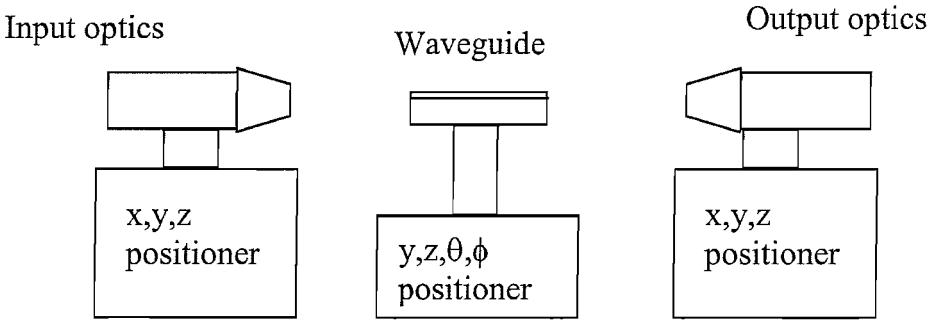

Figure 3.4 Launching light into a waveguide

The waveguide end-faces are polished parallel to each other, and to an optically smooth finish. The waveguide is mounted on a precision manipulator with two translational and two angular adjustments (y,z,ϕ,θ,). It is positioned with its end-faces perpendicular to the incoming light beam. The input and output optics are mounted on three-axis (x,y,z) positioners and can be either microscope objectives or cylindrical lenses. To end-launch pump light the input optics are gradually moved closer (to <1cm) to the end-face of the waveguide and fringes of unlaunched pump light are observed in a Lloyd's mirror effect [7] after the waveguide. The optimum launch position, and the optimum vertical position of the waveguide, is when the fringes are most widely separated. The output optics are then positioned after the waveguide to focus the output at the required position, for instance onto a screen, detector or power meter.

3.6 Measurement of launch and absorption efficiency (ηA)

In a waveguide experiment it can be difficult to measure the efficiency, η, with which light is launched into the waveguide, and the pump absorption, A, separately. However a transmission measurement can be used to obtain a combined value of launch x absorption (ηA), and this parameter is then useful for calculating the total power absorbed by the waveguide.

A detector can be positioned after the output optics in figure 3.4 to collect all the pump power (both through and around the guide) $P_{det(waveguide)}$, from a pump source launched into the waveguide, P_p. This power can be written as:

$$P_{det(waveguide)} = (P_p \times T_{input} \times (1-R_{input}) \times \eta \times (1-L_{guide}) \times (1-A) \times (1-R_{output}) \times T_{output}) + (P_p \times T_{input} \times (1-R_{input}) \times (1-\eta) \times (1-R_{output}) \times T_{output}) \quad 3.1$$

and similarly the pump power transmitted when the pump source is focused through the substrate only, $P_{det(substrate)}$, can be written as:

$$P_{det(substrate)} = (P_p \times T_{input} \times (1-R_{input}) \times (1-R_{output}) \times T_{output}) \quad 3.2$$

where T_{input} and T_{output} represent the transmissions of the input and output optics, R_{input} and R_{output} are the reflectivities of the input and output waveguide faces, η is the efficiency of launching the pump light into the waveguide, L_{guide} is the term for the single-pass propagation losses of the waveguide and A is the fraction of launched power that is absorbed. The first term in equation 3.1 is the power fraction that has been transmitted through the waveguide, the second term is the power fraction that has passed through the cladding layer or substrate instead of being coupled into the waveguide.

P_p, T_{input} and T_{output} are all easily measured and the Fresnel reflectivities of the waveguide faces are calculated using equation 3.3.

$$R_{input} = R_{output} = \left(\frac{n_{guide} - n_{air}}{n_{guide} + n_{air}} \right)^2 \quad 3.3$$

where n_{guide} is the refractive index of the waveguide material and n_{air} is the index of the air surrounding the waveguide. For 1at% Nd:YAG with n_{guide} = 1.81633 at 633nm [8] and n_{air} = 1, R_{input} = 0.926. The term L_{guide} in equation 3.1 is discarded, as A>> L_{guide} when the pump wavelength is tuned to the absorption peak of the waveguides

examined in this thesis. This means a suitable length of guide can be chosen such that single-pass propagation losses are negligible.

Equations 3.1, 3.2 and 3.3 can now be used to obtain a launch x absorption (ηA) measurement. Two power measurements are taken; one with the pump light launched through the waveguide ($P_{det(waveguide)}$), and the other measuring the pump light transmitted when focused through the substrate only ($P_{det(substrate)}$). By approximating that $n_{guide} = n_{substrate}$, a value of ηA is obtained from equation 3.4.

$$\eta A = 1 - \frac{P_{det(waveguide)}}{P_{det(substrate)}} \qquad 3.4$$

This measure of combined launch and absorption efficiency is a useful quantity to know when assessing waveguide performance, as it allows absorbed pump power to be calculated from incident pump power. It can also be calculated with a measurement (P_{det}) of the pump light transmitted over an air space without the waveguide sample present, instead of measuring ($P_{det(substrate)}$). Care must then be taken to include the terms R_{input} and R_{output} in equation 3.4 to account for the Fresnel reflections from the waveguide faces.

3.7 Waveguide characterisation

Information about the modal, spectroscopic and loss properties of a waveguide layer are important in quantifying device performance. In this section some waveguide characterisation techniques used in this thesis will be discussed.

3.7.1 Dark m-line prism coupling [9]

Dark m-line prism coupling is an experimental technique useful for determining the effective index of a propagating mode (equation 2.3) and it can also be used to verify the film thickness and refractive index. The technique was used to characterise waveguide layers grown by pulsed laser deposition (PLD), where the composition and

thickness of the growth were not certain. A waveguide sample is shown in figure 3.5, it has a three-layer asymmetric slab structure.

A diverging beam of light is coupled into the waveguide layer using a high index prism [10]. Each waveguide mode excited and guided has a characteristic propagation angle, θ_p, shown in figure 2.2, chapter 2. This guided mode angle, θ_p, which is directly related to the mode effective index, is a function of the mode number p, the cladding, guide and substrate indices; n_1, n_2 and n_3 respectively (in figure 3.5), the polarisation of the mode and the waveguide depth. If the thickness and the substrate index are known then one value of θ_p will define the index of the waveguide layer, however if the thickness is not known two values of θ_p are required and n_2 is obtained by solving for the two independent variables [11]. To obtain θ_p the arrangement shown in figure 3.5 was used.

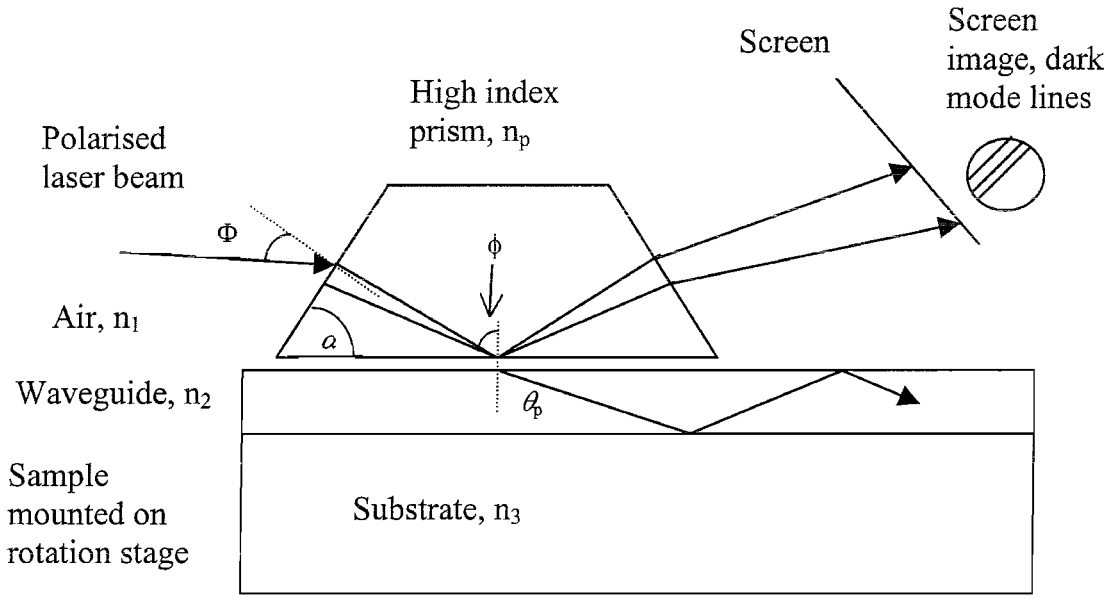

Figure 3.5 Dark m-line prism coupling arrangement

Prism coupling is achieved with a high index, single isosceles prism clamped onto the waveguide with a small air gap separating the prism and the surface. A sufficient air gap of ~1μm is created by dust between the two surfaces. Light incident at the air gap at an angle greater than the critical angle will be totally internally reflected out of the prism. However some light can instead be transmitted by the evanescent field coupling into the waveguide at this point, but only if the propagation constant of the light corresponds to a guided mode.

where, $n_p \sin \phi = n_{eff} = n_2 \sin \theta_p$ 3.5

The refractive index of the prism must be higher than that of the waveguide layer for this coupling to occur so a high index rutile (TiO_2) prism was used. This material is birefringent, and has n_e = 2.872 exciting TE modes, and n_o = 2.584 exciting TM modes, with the optical axis perpendicular to the plane of the page in figure 3.5. These refractive indices are quoted at λ = 633nm [12], as the light source used was a helium-neon laser. At angles where light is coupled into the waveguide modes there will be a reduction in the reflected intensity, this is observed on the screen in figure 3.5 as a series of dark lines. A typical set of lines was photographed and is reproduced in figure 3.6.

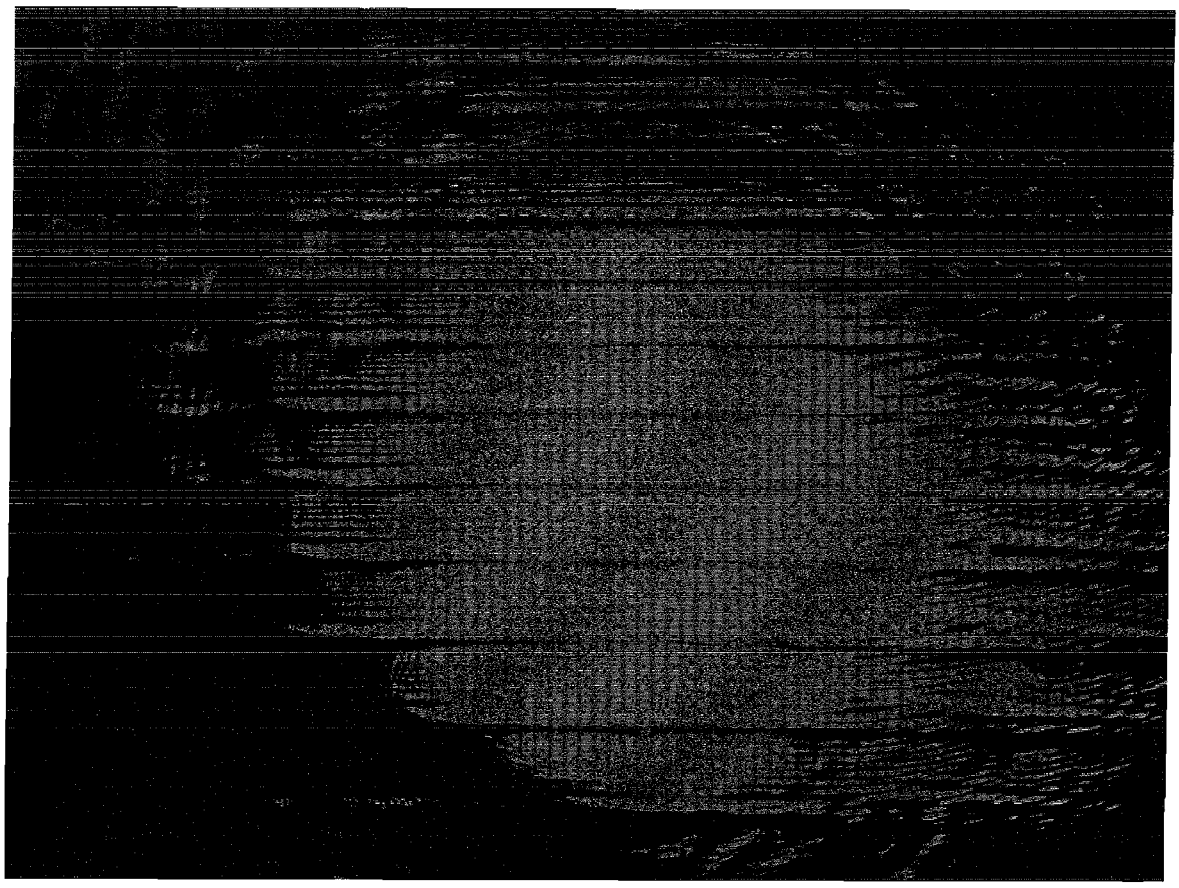

Figure 3.6 Set of dark m-lines from a pulsed laser deposited waveguide film

The incident angle, Φ, at which a 'dark m-line' occurs is measured and related to the angle of incidence inside the prism (equation 3.6), using Snell's law.

$$\sin \Phi = n_p \sin(\phi - \alpha) \qquad 3.6$$

where α is the prism base angle.

Using equations 3.5 and 3.6 a value for n_{eff}, the effective mode refractive index, can be found.

$$n_{eff} = n_p \sin\left[\sin^{-1}\left(\frac{\sin\Phi}{n_p}\right) + \alpha\right] \qquad 3.7$$

This gives the propagation constant, $\beta = k_0 n_{eff}$, for the mode. When β is known for two modes along with the actual mode numbers, these are substituted into the guidance condition for a three-layer asymmetric slab waveguide, equation 2.32. This gives two equations that can be solved for d_1, the waveguide depth, and the refractive index of the waveguide [11]. These solutions were found iteratively using a computer program. Pulsed laser deposited waveguides are discussed further in chapter 4.

3.7.2 Fluorescence spectroscopy

To obtain the fluorescence spectrum of the dopant ion in the waveguide laser host material it is necessary to excite the ion by pumping with a laser wavelength tuned to an appropriate absorption band. Figure 3.7 shows the experimental arrangement.

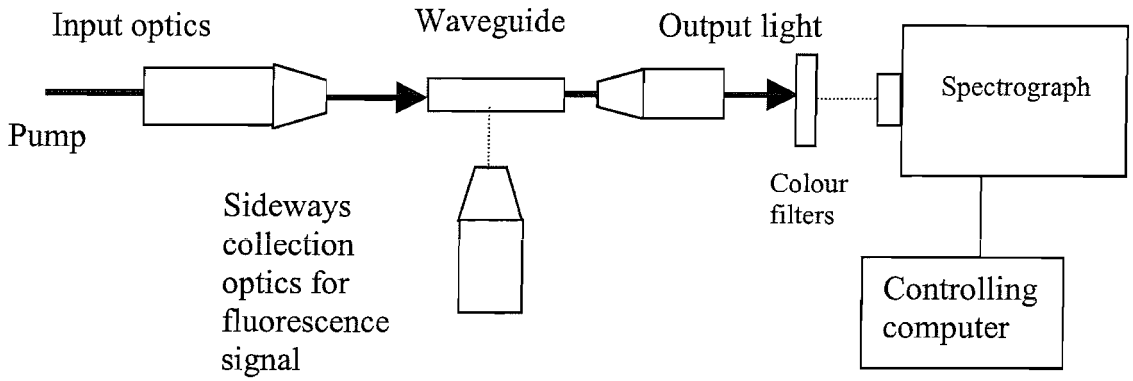

Figure 3.7 Experimental set-up for fluorescence measurements

The pump light is launched into the waveguide and the output is composed of unabsorbed pump light and excited fluorescence. The excess pump light is removed with colour filters and neutral density filters as required. The fluorescence is then imaged onto the input slits of the EG&G triple grating spectrograph. Alternatively fluorescence emitted from the side of the waveguide is collected with a spherical lens and focused into the spectrograph, avoiding the problems of unabsorbed pump light and the reabsorption effects present in quasi-three-level systems. After selecting a centre wavelength and one of the gratings available, the spectrum can be viewed on the controlling computer. The resolution of the spectrograph is determined by the input slit aperture and the grating used. It is important to know whether the spectra obtained are limited by the resolution of the equipment. Emission from the Ti:sapphire pump laser has a relatively narrow linewidth of <1nm so this is used to test the resolution of the spectrograph. All of the fluorescence spectra examined in the project have features broader than this pump spectrum. It can therefore be inferred that the spectra obtained were not limited by the resolution of the instrument.

3.7.3 Fluorescence lifetime measurement

The radiative lifetime of the upper laser level is a significant characteristic of a laser transition and, as shown in both section 2.3.2 and in equation 2.51, it has an effect on the laser threshold. Measurement of the fluorescence lifetime is one way of highlighting any spectroscopic differences to a bulk sample that may have resulted from waveguide fabrication.

The experimental arrangement for this measurement is shown in figure 3.8. Pump light, tuned to a wavelength in an appropriate absorption band of the dopant ion, is launched into the waveguide, as it was for measurement of the fluorescence spectrum in figure 3.7. The pump light is chopped by an optical chopper taking care that the opening and closing time is much faster than the fluorescence lifetime. The output is first filtered to remove any residual pump light and then detected on a photodiode linked to an oscilloscope. Providing the detector and oscilloscope have fast enough response times, a rough measurement of the lifetime can be obtained directly from the fluorescence signal on the oscilloscope.

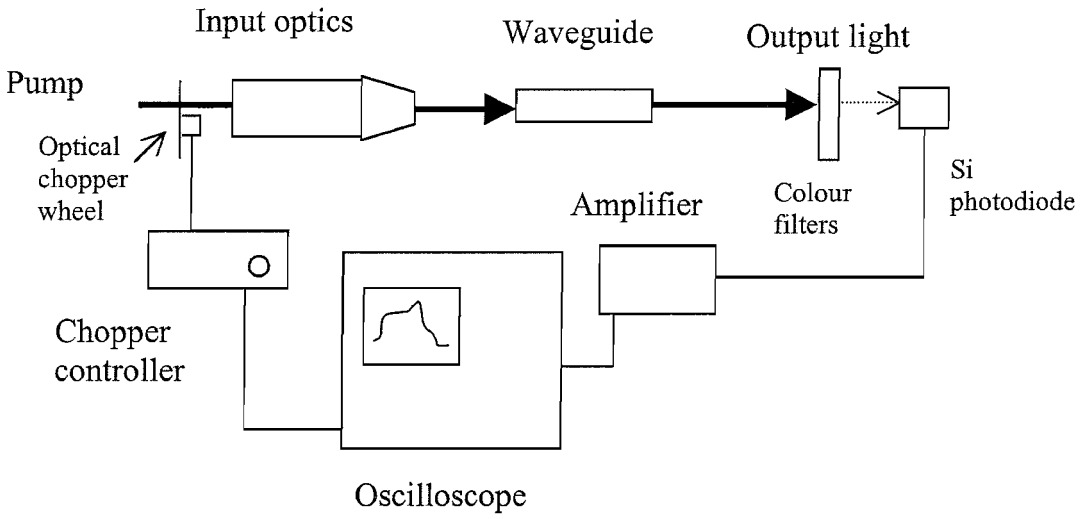

Figure 3.8 Experimental set-up for fluorescence lifetime measurements

A better analysis would be to use a storage oscilloscope to record the exponential decay and then fit a straight line to a log plot of the decay. This method was used by Dr. Stephan Guy for the spectroscopic analysis of Nd:YAG in chapter 5.

3.7.4 Absorption spectroscopy

The white light transmission spectrum from a waveguide can be used to obtain the value of the absorption coefficient [13]. The spectrum can also be compared to the absorption of the bulk material to examine any broadening effects.

The experimental set-up for taking these measurements is similar to that shown in figure 3.7, but the pump laser is replaced with a broad spectral, white light, source. A tungsten lamp was used and coupled into the waveguide either with a microscope objective or with a single mode optical fibre. Optimum white light coupling was achieved with the fibre by first optimising the launch of a helium-neon laser into the waveguide using the fibre. Then the input end of the fibre was transferred to the tungsten lamp, and the white light was coupled into the waveguide. The output was detected and displayed on the controlling computer of a spectrograph or monochromator. To eliminate the wavelength dependent response of the system from the absorption measurements a spectrum of the white light source alone was taken over the same wavelength range as examined for the waveguide. The waveguide

transmission spectrum divided by just the white light spectrum then gives a normalised plot of transmitted intensity with wavelength.

3.8 Propagation loss measurement

Laser action in a gain medium requires that the round trip gain at the lasing wavelength is greater than or equal to the round trip loss. A number of factors contribute to the loss in the laser cavity; transmission of the mirrors, scattering losses in the waveguide due to the fabrication technique (for instance particulates present in pulsed laser deposited waveguides [14]), and the quality of the polished end-faces. The waveguide end-faces must be polished to an optically smooth finish, and be parallel to each other to avoid walk-off of the laser beam. An autocollimator, or examination of the back reflections from the end-faces, was used to achieve parallelism. The quality and smoothness of the polishing was monitored with an optical microscope.

Many methods for measuring waveguide propagation loss have been reported, for example imaging the scattered light component [15]. An alternative method is to measure the power difference between light coupled into the waveguide using a prism and that coupled out again through another prism after propagating a known distance through the waveguide [16]. One very accurate technique is to measure the finesse of the Fabry-Perot cavity made by the end-faces of the waveguide [17]. However this requires a single frequency probe laser and single-mode channel waveguides, and so it was not used with the multi-mode waveguides investigated in this thesis. Loss and absorption in optical fibres are commonly measured using a method known as 'cut-back'. This technique compares the transmitted power launched through different lengths of the same fibre. However 'cut-back' is a destructive technique not well suited for use with the samples used in this work, which are typically limited to small lengths.

The following techniques were used successfully to measure waveguide loss during the course of this project.

3.8.1 Waveguide transmission measurement

The transmission of light through a waveguide can provide an idea of the propagation loss. The experimental set-up is similar to figure 3.7. The light launched into the waveguide is tuned away from any of the absorption bands of the active laser ion and the power transmitted through the waveguide is measured. The waveguide output is imaged onto a power meter detector instead of the EG&G spectrograph shown in figure 3.7, and the power meter reading, $P_{detector}$ noted. Care is taken to ensure that only light transmitted through the waveguide is collected by the detector. The transmission of the waveguide is then given by:

$$T_{waveguide} = \frac{P_{detector}}{P_p} \bullet \frac{1}{T_{output} T_{input}} \bullet \frac{1}{\left(1 - R_{input}\right)\left(1 - R_{output}\right)} = \eta \exp(-\alpha_g l) \qquad 3.8$$

$P_{detector}$ and P_p, the incident pump power at the waveguide input face, can be measured with the detector and the other quantities; T_{input}, T_{output}, R_{input}, R_{output}, can be measured or calculated as appropriate. The value obtained for the transmission will then contain a component due to actual waveguide loss, $\exp(-\alpha_g l)$ and a component from the efficiency of the launch into the waveguide, η. It is a difficult task to separate these two factors, but by assuming a launch efficiency of 100%, this transmission measurement can at least give an upper limit for the waveguide loss.

3.8.2 Findlay-Clay method

One technique that is not dependant on the launch conditions into the waveguide, and which has been used extensively throughout this project, is the Findlay-Clay technique [18]. Providing the launch conditions remain constant between measurements, knowledge of the actual launch efficiency is not required for the evaluation of propagation loss. The method follows from the laser threshold equations derived in chapter 2, and is suitable for applying to waveguide lasers that operate with a broad range of output couplers.

The Findlay-Clay technique was originally used to measure the scattering loss in bulk laser systems. From equation 2.54 the absorbed power threshold for a three-level laser is related to the output coupling by,

$$P_{th} = C \times [2\alpha_g l - \ln(R_1 R_2) + 2N_1^0 \sigma_e l] \qquad 3.9$$

Where C is a constant containing information about the launch and absorption efficiency, the laser material parameters and the pump and signal spatial properties. Any loss due to butting mirrors to the end faces of the waveguide is assumed to be negligible and the other terms in the equation are as defined in chapter 2. The propagation loss term of the waveguide, α_g, can be determined by plotting a graph of the threshold, P_{th}, versus the natural logarithm of the mirror reflectivities, $\ln(R_1R_2)$. Here. With thresholds obtained using a number of different output couplers a straight line graph is produced with an intercept on the $-\ln(R_1R_2)$ axis of $-(2\alpha_g l + 2\sigma_e N_1^0 l)$, or just $-2\alpha_g l$ for a four-level laser system. The propagation loss term can then be easily calculated from this intercept.

3.9 Waveguide laser experiments

Construction of a laser resonator requires a laser gain medium, here the waveguide core, and optical feedback at the laser wavelength. This feedback can be provided in a number of ways and three different methods, all creating plane-plane resonators, were used in this work. The first, and most straightforward, was provided by Fresnel reflections from the polished end-faces of the waveguide. The reflection of around 8% (for YAG) at the air – waveguide boundary was enough in a high gain medium to sustain laser action. The second technique involved directly coating a mirror onto each end-face of the waveguide crystal. This process produces an excellent quality laser cavity, however once the mirror coating has been applied it is not possible to modify the cavity by attaching a mirror with a different reflectivity. The third technique for forming a waveguide laser cavity is the most versatile. Thin substrate mirrors with dielectric coatings are butted to the end-faces of the waveguide. The mirrors are held in place by the surface tension of a small drop of Fluorinert FC-70 fluorinated liquid. The fixture can be made semi-permanent by gluing the mirror to

the crystal with a small drop of glue. It is then a simple task to change to a mirror of a different reflectivity to create a different laser cavity.

One problem that arises with laser cavities made from thin substrate mirrors is due to the small gap created between the end-face of the waveguide and the mirror. This leads to a Fabry-Perot etalon structure, composed of one reflection from the waveguide boundary and one from the mirror boundary. The transmission function of the Fabry-Perot structure depends on the etalon spacing which can vary along the length of the waveguide [19]. This variation in transmission was not helpful in quantifying waveguide laser experiments and so, where mirror transmission is important (such as in a Findlay-Clay analysis), laser cavities were formed, where possible, by the other two techniques outlined in this section.

Laser experiments carried out in the course of this thesis with a Ti:sapphire pump source, used the arrangement shown in figure 3.10. Further details of the arrangement for diode-bar pumped waveguides will be given in chapter 6.

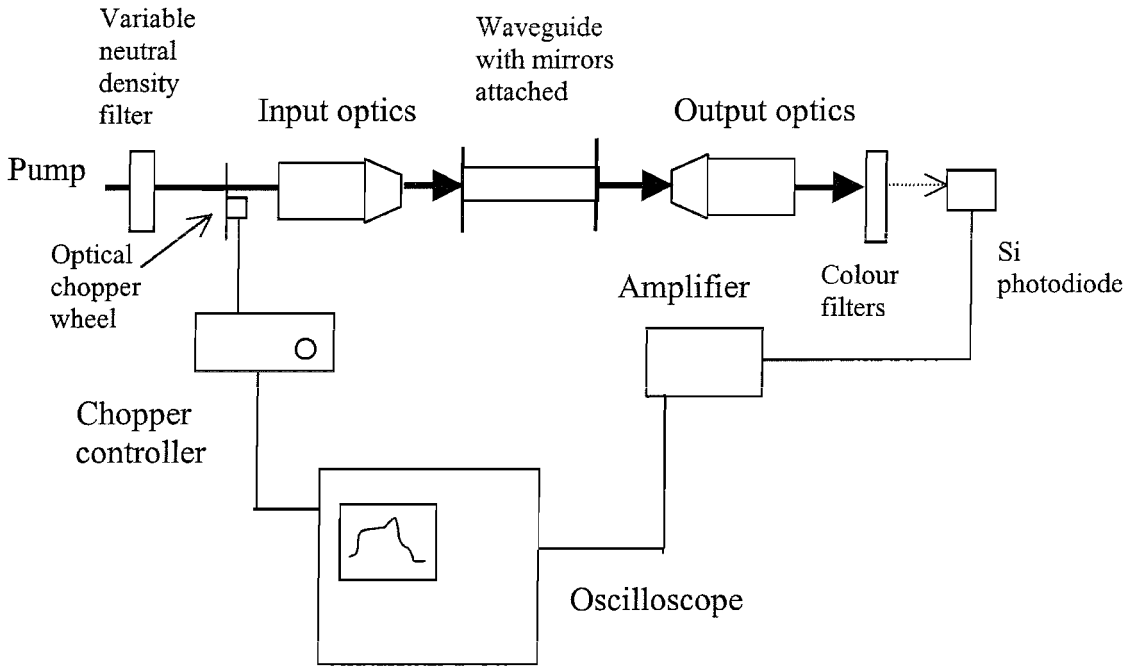

Figure 3.10 Configuration for waveguide laser experiments

The output from the waveguide can be directly imaged onto the silicon photodiode with colour filters blocking any residual pump light. The pump radiation is chopped

and the amplified signal from the photodiode is observed on the oscilloscope. The smooth fluorescence shape changes to sharp spikes as laser action begins and this experimental arrangement allows lasing to be observed in real time. The input pump power incident on the waveguide can be reduced with the variable neutral density filter wheel to find the laser threshold. The pump launch into the waveguide can be optimised using the input optic (x,y,z) positioner, and the position of the waveguide can also be adjusted to find the lowest laser threshold. This set-up does not however allow examination of the laser wavelength. For this the EG&G triple grating spectrograph must be used in place of the silicon photodiode. The arrangement is then similar to that used in figure 3.7 to measure a fluorescence spectrum.

The slope efficiency of the laser can be found by increasing the input pump power and taking measurements of the corresponding waveguide laser output power on a suitable detector. It is important to take into account the wavelength transmission of any colour or neutral density filters used.

3.10 M^2 measurement

An important characteristic of a laser beam is its beam quality, or M^2 value. As shown in table 3.1 a diode-bar has M^2 values far from 1 and this has an effect on the beam quality of a diode-bar pumped waveguide laser. Beam quality has been discussed theoretically in chapter 2. Here details of the M^2 measurement technique used in the course of this thesis are given. M^2 values were estimated from the divergence angle of the laser beam using equation 2.76:

$$\tan^{-1}\left(\frac{W(z)}{z}\right) = \theta_{div} = M^2 \frac{\lambda}{\pi W_0} \qquad 3.10$$

θ_{div} is the far-field divergence half angle and W_o is the waist size of the beam. A plot of the spot size radius, W, versus distance from the waist can therefore be used to find θ_{div}, and hence the M^2 value if the waist spot size, W_o, is known. Care must be taken however in defining the spot size of a laser beam. A common convention [20] used for beams made up of several modes is to define an aperture radius letting through

86.5% of the total power in the beam. Alternatively a scanning knife edge technique is used, this involves gradually obscuring the beam with the knife edge moved along the measurement axis (e.g in the x- or y-direction), and measuring the power in the remaining unblocked beam. The distance between the two knife edge positions obscuring 6.7% and 93.3% of the total power in the beam corresponds to the $1/2e^2$ spot size diameter of the beam [20]. A more accurate spot size measurement technique for beams made up of several modes is obtained from measurement of the second moment of the intensity distribution, I(r). The second moment is described in chapter 2 (equation 2.67) and defined as:

$$\overline{r^2} = \frac{\int_{-\infty}^{\infty}\int_{-\infty}^{\infty}(x - x_0)^2 I(x,y)dxdy}{\int_{-\infty}^{\infty}\int_{-\infty}^{\infty} I(x,y)dxdy} \qquad 3.11$$

The beam width, W, of an arbitrary beam is then given by:

$$W_{x,y} \equiv \sqrt{4\overline{r^2}_{x,y}} \qquad 3.12$$

The technique used to measure the intensity profile of a laser beam from which the second moment can then be found, is shown in figure 3.11.

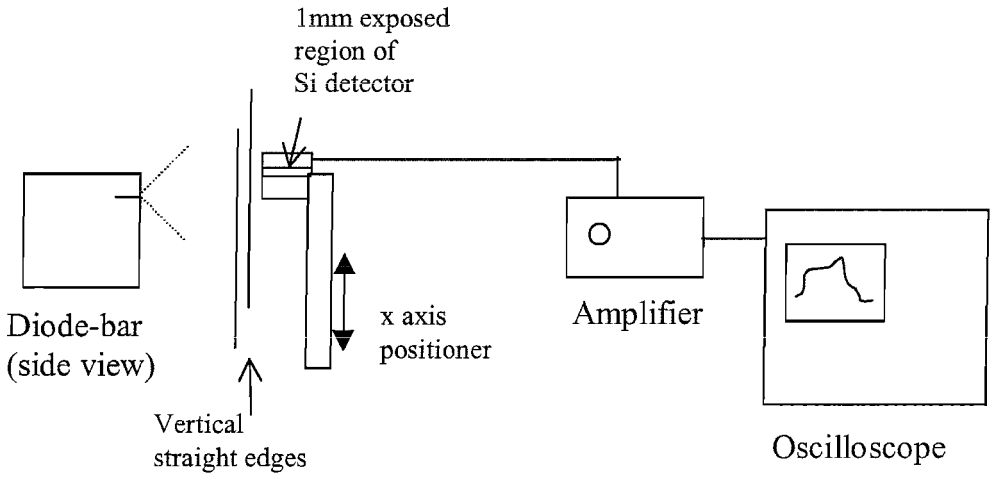

Figure 3.11 Laser beam profiling measurement (vertical(x) profile)

This technique has been developed specifically for measuring high power, divergent beams, such as the output from a diode-bar. Spatial profiles of more manageable beams could easily be obtained from a CCD camera linked to a computer with appropriate beam analyser software.

A pair of vertical straight edges are used to make a thin (~1mm) vertical slit, this selects the portion of the beam to be sampled. The face of a large area silicon detector is masked off to leave a thin (~1mm) horizontal detector region. This prevents saturation of the detector by the high power beam, and ensures a sufficient profile resolution. The detector is mounted on a x-axis positioner and linked to an oscilloscope or digital voltmeter to display the output. The full intensity profile is built up from detector readings sampled at a series of equally spaced vertical displacements. Profiles obtained from the scanned spot of the detector can be obtained at different positions within the beam to check uniformity. The technique can be easily modified to take measurements in the horizontal (y) plane. Once the profile of the intensity distribution is obtained the following procedure gives the second moment value and thus the beam width:

(i) Any background noise present during the experiment is subtracted.
(ii) The centre of gravity of the profile, i.e. the x-position at which there is an equal area under the curve at either side, is located.
(iii) The position of the profile on the ordinate axis is adjusted so that x=0 is at the centre of gravity of the profile.

(iv) The profile is normalised [20] such that: $\int_{-\infty}^{\infty} I(x)dA = 1$

(v) The second moment (3.11) is found from the summation: $\sum_{-\infty}^{\infty} x^2 I(x) = \overline{r_x^2}$

(vi) The value of $\overline{r_x^2}$ is then used in equation 3.12 to obtain the beam waist radius.

As well as this time consuming technique there are a number of commercial ISO standard [21], M^2 measurement devices available that can be used if W_0 is not known. One example is the Coherent Modemaster which works by focusing a collimated input beam of up to ~20mm diameter, and profiling the beam through the focus using

two scanning 45^0 knife edges [22]. This device was used where possible in the work described here. In situations where it was not possible to use the Coherent Modemaster, for instance with too powerful or too large a diameter beam, a measurement of beam width was made with one of the techniques described in this section. The most accurate method of measuring beam width was with a scanning slit producing an intensity profile of the beam, however this was also the most time consuming. For this technique to be accurate it is important that the beam size is large enough that the slit width (~1mm) does not limit the resolution of the measurement. Therefore it is not suitable for use with beam sizes <~2-3cm. For smaller spot sizes and a swifter measurement the knife edge method or an aperture radius passing 86.5% of the total power of the beam were used. The techniques outlined in this section were used, as appropriate, to measure spot sizes in the work described in this thesis.

3.11 Proximity coupling diode-bars to waveguides

A significant portion of the work described in this thesis concerns the diode-bar pumping of waveguides. Some consideration will now be given to the experimental technique used in the simplest coupling scheme - proximity coupling. Details of other techniques and coupling arrangements will be given later in chapters 4 and 6 as appropriate.

The concept of proximity coupling for a side-pumped waveguide laser is illustrated in figure 3.12. The waveguide is aligned next to the diode-bar with no intervening optics and all of the diode light is coupled directly into the waveguide.

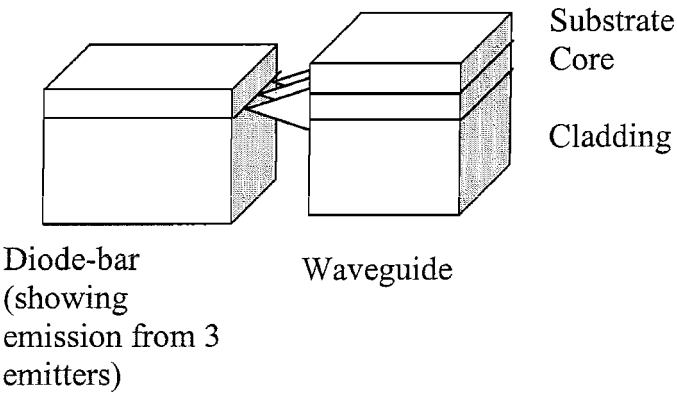

Figure 3.12 Proximity coupling a diode-bar to a waveguide

Before proximity coupling, the properties of the diode-bar must be considered carefully. As discussed in section 3.2 and illustrated in figure 3.1 a diode-bar consists of a linear array of around 20 emitters. These have dimensions ~1μm x ~150μm and this leads to a highly divergent, approximately diffraction limited output of typically 30-40^0 perpendicular to the plane of the emitters. This divergence was measured by profiling the beam as outlined in section 3.10. An optical microscope from Elliot Scientific, with a CCD camera linked to a monitor was used to examine the emitters while operating at low power. With magnification of ~300, 1mm on the monitor screen represented 3μm features on the sample. The microscope showed that in some cases the laser diode array was set back from the submount of the diode-bar (see figure 3.13). This distance varied between diodes, even those from the same manufacturer, and was observed to be from 0-~100μm. One manufacturer's specifications were [4], 'The front facet of the diode-bar may lie a minimum of 10μm in front of or behind the front surface of the submount, and the submount may extend a maximum of 50μm beyond the front surface of the heat spreader, and must not be recessed behind it at all.'

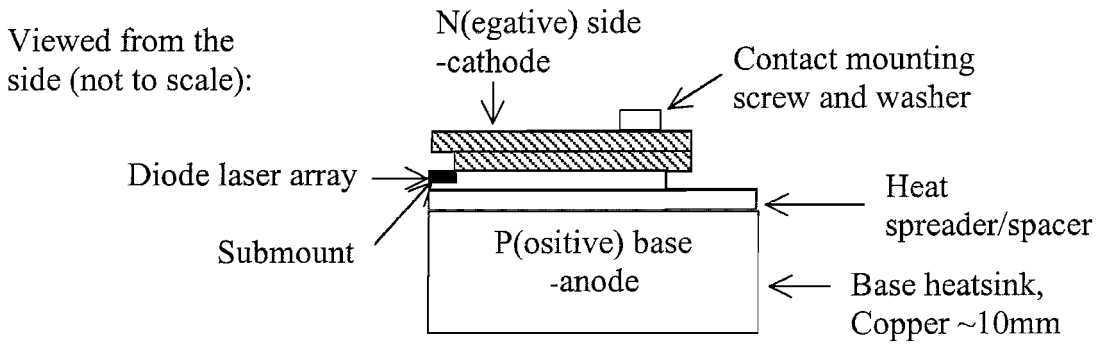

Figure3.13 Detail of a typical diode-bar

In order to achieve efficient proximity coupling an appropriate choice of waveguide must be made. Chapter 4 will discuss the matching of a waveguide to a diode-bar pump source in more detail. However in this case it can be seen that the waveguide should have a numerical aperture sufficient to contain the quickly diverging diode-bar output and be positioned very close to the emitting region. A diode-bar with emitting region protruding from the diode-bar packaging is therefore desirable. For maximum

collection efficiency the waveguide input face should match the emission length of the pump source, (i.e.> 10mm.)

Care must be taken with the alignment of the system as the facet of the diode-bar is extremely fragile and contacting the waveguide with any of the emitters can cause serious, irreversible damage. Total destruction of one or all of the emitters can also occur through short circuiting the diode-bar. This electrical malfunction can happen during operation if the positive (p) side of the diode-bar is suddenly brought to ground, for instance by electrical contact with a piece of hardware, like the optical table, that is held at ground for safety reasons. It is important to shield the p side of the diode-bar from any components that could cause the diode-bar to short circuit, including dust and dirt that could fall across the facet.

To satisfy these positioning requirements the experimental arrangement shown in figure 3.14 was used, giving accurate manual positioning down to the micron level.

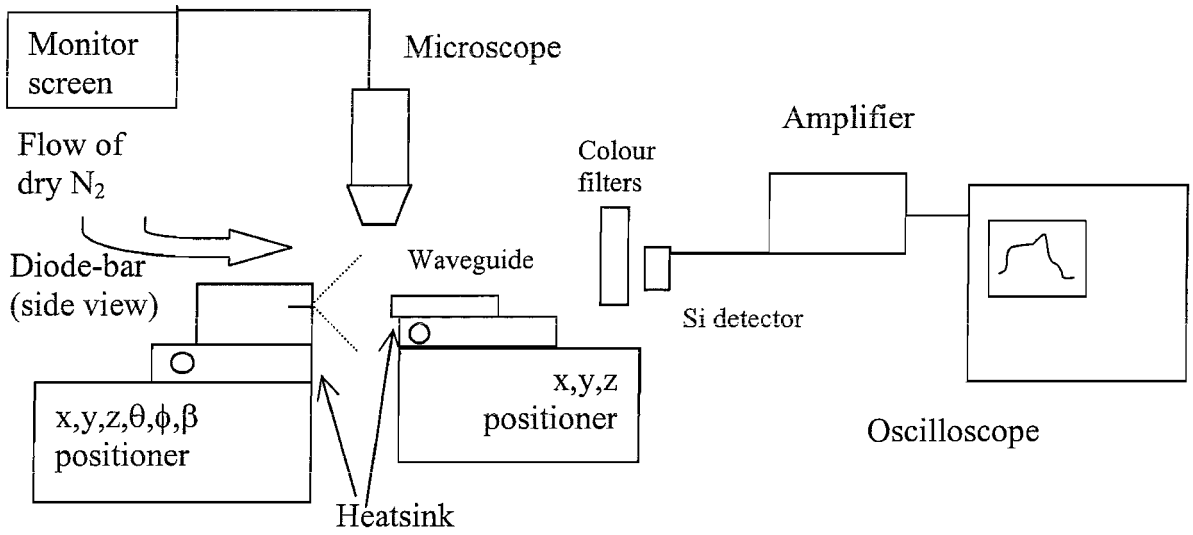

Figure 3.14 Experimental apparatus for proximity coupling

The waveguide was held on a three-axis positioner allowing three (x,y,z) translation adjustments, and the diode was on a six-axis positioner that had three translation (x,y,z) and three rotation (θ,ϕ,β) adjustments. This control of the angular position of the diode relative to the waveguide was important in maintaining uniform separation, (down to ~10μm) of the two, over the entire emitting region (~10mm). A constant

flow of dry nitrogen was pumped across the diode-bar facet, to keep it free of dust and dirt particles that may damage the emitters. Both the waveguide and the diode-bar were mounted on copper heatsinks. Temperature control was provided by recirculating water coolant flowing through the heatsinks. This helped remove heat deposited in the waveguide from high-power diode-bar pumping and provided some wavelength tuning of the diode-bar.

The microscope was mounted above the set-up and monitored the separation of the waveguide laser components which were gradually moved closer together. The alignment and launch position were optimised by monitoring the characteristic diffraction pattern of the unabsorbed pump radiation after the waveguide and using the fluorescence signal emitted from the waveguide core. This was detected on a silicon detector with colour filters removing any unabsorbed pump light. Using this technique a launch efficiency of ~90% was measured for an 8μm Nd:YAG on sapphire waveguide. Further proximity-coupled waveguide laser results are given in chapters 6 and 7.

3.12 References

[1] *'Review and forecast of laser markets:1999-part II'* pp.52-72 Laser Focus World, Penwell Publishing (Feb. 1999)

[2] OptoPower Corp. 1998 product catalogue, e.g product number H01 A001 mmm-FC/100

[3] P.Loosen, pp.287-317, *'Advances in Laser and Applications'* Procedings of the Fifty Second Scottish Universities Summer School in Physics, D.M.Finlayson, B.D.Sinclair, eds. IOP Publishing (1998)

[4] OptoPower Corp., Tuscon, Arizona, USA, Private Communication and product information (1998)

[5] for example, W.A.Clarkson and D.C.Hanna, Opt. Lett., **21**, pp.869-871 (1996), S.Yamaguchi, T.Kobayashi, Y.Saito, K.Ciba, Opt. Lett., **20**, pp.898-900 (1995) and G.Feugnet, C.Bussac, C.Larat, M.Schwarz, J.P.Pochelle, Opt. Lett., **20**, pp.157-159 (1995)

[6] A.Faulstich, H.J.Baker, D.R.Hall, Opt. Lett., **21**, pp.594-594 (1996)

[7] E.Hecht *'Optics'*, 2nd Ed., p.345, Addison-Wesley Publishing Corp. Inc. (1974)

[8] D.Pelenc, *'Guide d'onde laser en Nd:YAG et Yb:YAG per E.P.L.'*, PhD Dissertation, Département Optronique du LETI, C.E.N.G. 85X 38041 Grenoble, France (1992)

[9] R.Ulrich and R.Torge, Appl. Opt., **12**, pp.2901-2908 (1973)

[10] D.H.Lee, Chap. 6, *'Electromagnetic Principles of Integrated Optics'*, Wiley (1986)

[11] A.A.Anderson, *'Crystalline Planar Waveguide Lasers Fabricated by Pulsed Laser Deposition'*, PhD Thesis, University of Southampton, pp.53-56 (1998)

[12] D.N.Nikogosyan, *'Properties of Optical and Laser Related Materials: A Handbook'*, John Wiley and Sons Ltd (1997)

[13] C.F.McConaghy, K.F.Hugenberg, D.Sweider, M.Lowery, R.A.Becker, IEEE J. Lightwave Technol., **13**, pp.83-87 (1995)

[14] A.A.Anderson, C.L.Bonner, D.P.Shepherd, R.W.Eason, C.Grivas, D.S.Gill, N.Vainos, Opt. Comm., **144**, pp.183-186 (1997)

[15] Y.Okamura, A.Miki, S.Yamamoto, Appl. Opt., **25**, pp.3405-3408 (1986)

[16] Y.Okamura, S.Yoshinaka, S.Yamamoto, Appl. Opt., **23**, pp.3892-3894 (1983)

[17] R.Regener, W.Sohler, Appl. Phys. B, **36**, pp.143-147 (1985)

[18 D.Findlay and R.A.Clay, Phys. Lett., **20**, pp.277-278 (1966)

[19] C.T.A.Brown, *'Nd –doped Crystal Waveguide Lasers and Amplifiers'*, PhD Thesis, University of Southampton, pp.49-50 (1997)

[20] M.W.Sasnett Chap. 9, pp.132-142, *'The Physics and Technology of Laser Resonators'* D.R.Hall, P.E.Jackson, eds. IOP Publishing (1989)

[21] ISO/DIS standard 11 146, *'Optics and Optical Instruments, Lasers and Laser related equipment, Test methods for laser beam parameters'*, International Organisation for Standardisation, P.O. Box 65, CG1211, Geneve, Switzerland (1997)

[22] A.Seigman, *'How to (maybe) measure laser beam quality'*, TUL1, Tutorial presentation at OSA Annual meeting, Long Beach, California, USA, 12-17 October 1997

Chapter 4 High numerical aperture waveguides for diode-bar pumping

4.1 Introduction

The slab geometry of a planar waveguide is well matched to the asymmetric output from a diode-bar and, as discussed in the next chapter, the geometry also copes well with the heat deposited by high-power pump lasers. These qualities have led to new initiatives in developing high-power, rare-earth-doped, planar waveguide lasers. The diode-bar pumped schemes that have been reported so far range from face pumping [1] of relatively thick waveguide slabs, to methods of in-plane pumping [2], the most simple technique being a proximity-coupled diode-bar and waveguide [3]. Details of diode-bar pumped waveguide lasers are covered in chapter 6.

The first section of this chapter will theoretically consider the waveguide structure and the high numerical aperture (NA) required to accommodate a diode-bar, or a similarly divergent, pump source. Two techniques that have recently been found to be particularly well suited to fabricating high NA waveguides are; pulsed laser deposition (PLD) and direct bonding. Details of the fabrication and characterisation of waveguides produced by these two techniques will be described in sections 4.3 and 4.4

4.2 Numerical aperture considerations

The properties of diode-bars were discussed in chapter 3. The emission aperture of a bar is typically 1cm x 1μm, as shown in figure 3.1. This leads to an asymmetric output with M^2 values of ~1 X~2000-3000. In order to obtain a collimated output beam, suitable for refocusing into the waveguide, a high NA cylindrical lens can be used. Section 3.2 describes how this was achieved with an acylindrical fibre lens in front of the diode.

A waveguide structure suitable for pumping with a fibre-lensed diode-bar must match the output from the diode package. For a waveguide assumed to have a three-layer

step index structure of core thickness 2d, a multi-mode pump beam ($M^2>1$) can be efficiently launched into a multi-mode waveguide providing the waveguide NA is greater than or equal to the sine of the pump beam divergence angle in radians. This is expressed as:

$$NA \geq \sin\left(\frac{\lambda M^2}{\pi w_0}\right) \qquad 4.1$$

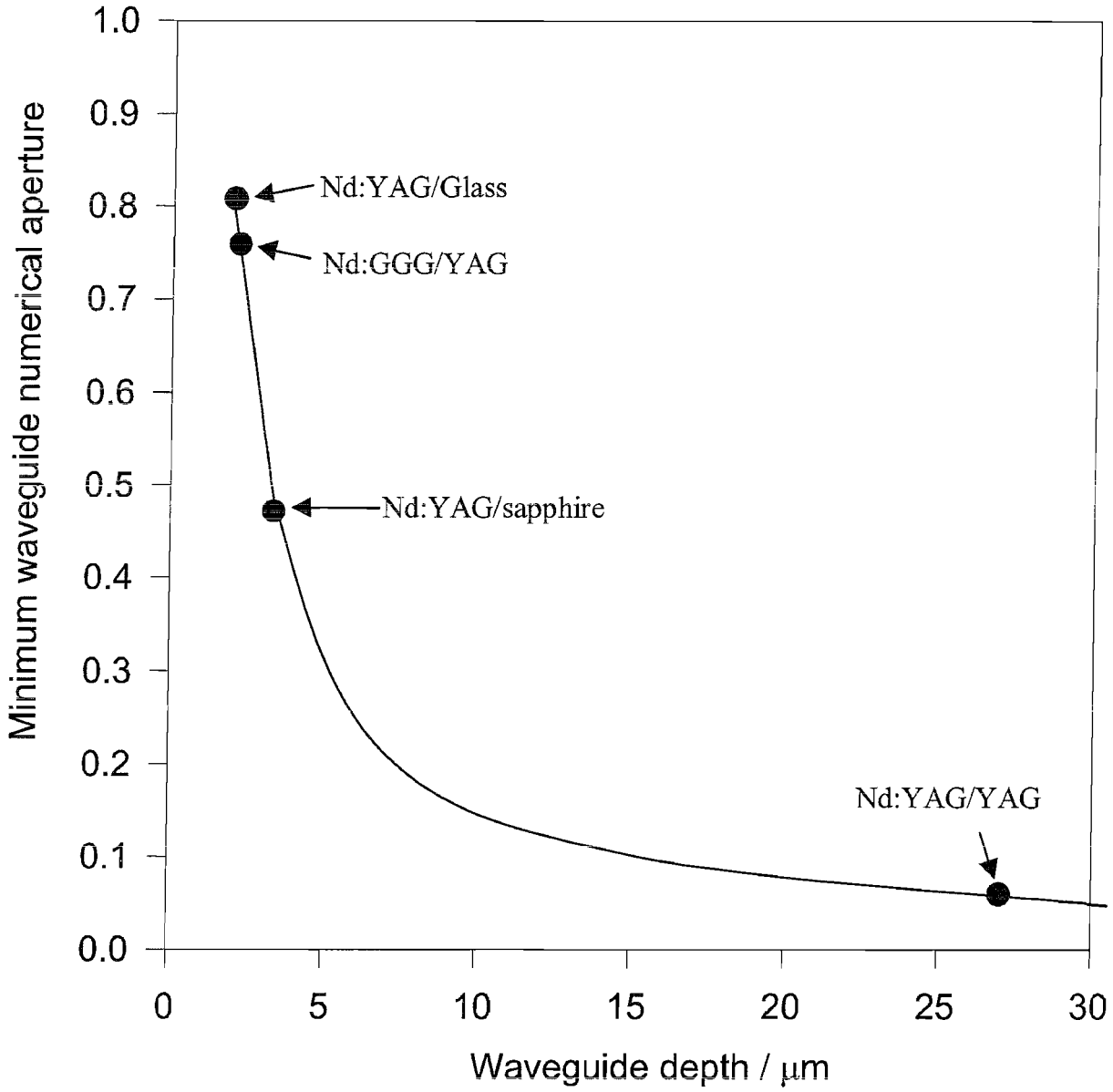

Figure 4.1 A graph showing the minimum waveguide numerical aperture required to confine a pump beam of a given spot size with $M^2 = 2$.

Equation 4.1 can be approximated to:

$$NA \geq \frac{\lambda M^2}{2d} \qquad 4.2$$

Figure 4.1 illustrates equation 4.2 graphically, for a diode-bar pump wavelength around 800nm.

The graph is plotted for a pump beam with an $M^2=2$ (typical for the fibre-lensed diodes used here) and shows the relationship between waveguide depth and the minimum NA required. The circles show particular values of NA corresponding to material combinations used in this thesis. A point to note from the graph is that the guided wave gain per unit pump power will vary inversely with 2d, so the points on the graph to the left (i.e the higher NA combinations) will see a greater advantage from the waveguide geometry. It can be seen from the graph that $2d<5\mu m$ requires a NA greater than 0.3. This condition can normally only be satisfied with the core and surrounding cladding made from different materials as the refractive index change that is obtained from just doping a material does not usually provide a very high NA. The numerical aperture of a waveguide is calculated from equation 4.3.

$$NA = \sqrt{n_{guide}^2 - n_{substrate}^2} \qquad 4.3$$

Waveguides with NA of 0.3 and above have been successfully fabricated by pulsed laser deposition [4] and direct bonding [5], details of these techniques are given in sections 4.3 and 4.4 of this chapter. Another waveguide fabrication technique that has been used with solid-state-laser material for high-power operation is liquid phase epitaxy (LPE) [6]. However this process, like PLD, requires that any lattice mis-match between the core and the substrate or cladding layers is very small. This severely limits the choice of material combinations possible. However recently some material combinations have been found to give a suitable NA and have a small enough lattice mis-match to enable a waveguide layer to be grown by PLD (for example Nd:GGG on YAG [4]).

A more stringent requirement is placed on waveguides used for proximity coupling to diode-bars. Without a collimating fibre lens in front of the diode emitters the half angle of divergence can be as much as 40^0 in the vertical (x) direction. This requires a waveguide with a NA around 0.7 or greater to contain the beam. However, as subsequent chapters will show, a YAG/Sapphire waveguide combination with a NA of ~0.5 can be sufficient to contain the diode-bar output in certain circumstances. The diode's high divergence also means that the further the waveguide is from the diode facet the thicker the guiding core region must be to contain the output. However a thick and high NA core will support a large number of laser modes, reducing the output laser beam quality, which is often undesirable in a high power application. One way of overcoming this is with a double-clad, five-layer waveguide structure, as described in chapter 7.

4.3 High numerical aperture waveguides grown by pulsed laser deposition (PLD)

4.3.1 Fabrication

PLD is a relatively simple and versatile method of fabricating thin films of various materials [7]. It is well suited to growing complex oxides and was first used to fabricate high temperature superconducting thin films. It has gone on to prove itself capable of growing ferroelectrics, photorefractives, ceramics, glasses and other materials. Recently the PLD technique has been applied to the growth of GGG layers on YAG substrates [8-10], with a view to producing lasing structures.

GGG waveguide lasers have been previously fabricated by ion-implantation [11, 12] and liquid-phase-epitaxy [13], but the guides described here have much higher numerical apertures. The overall PLD process and its development has been summarised in references 14 and 15, and details of the exact deposition technique used for the waveguides discussed in this chapter has been given by A. A. Anderson in reference 16.

The apparatus used for pulsed laser deposition is shown in figure 4.2.

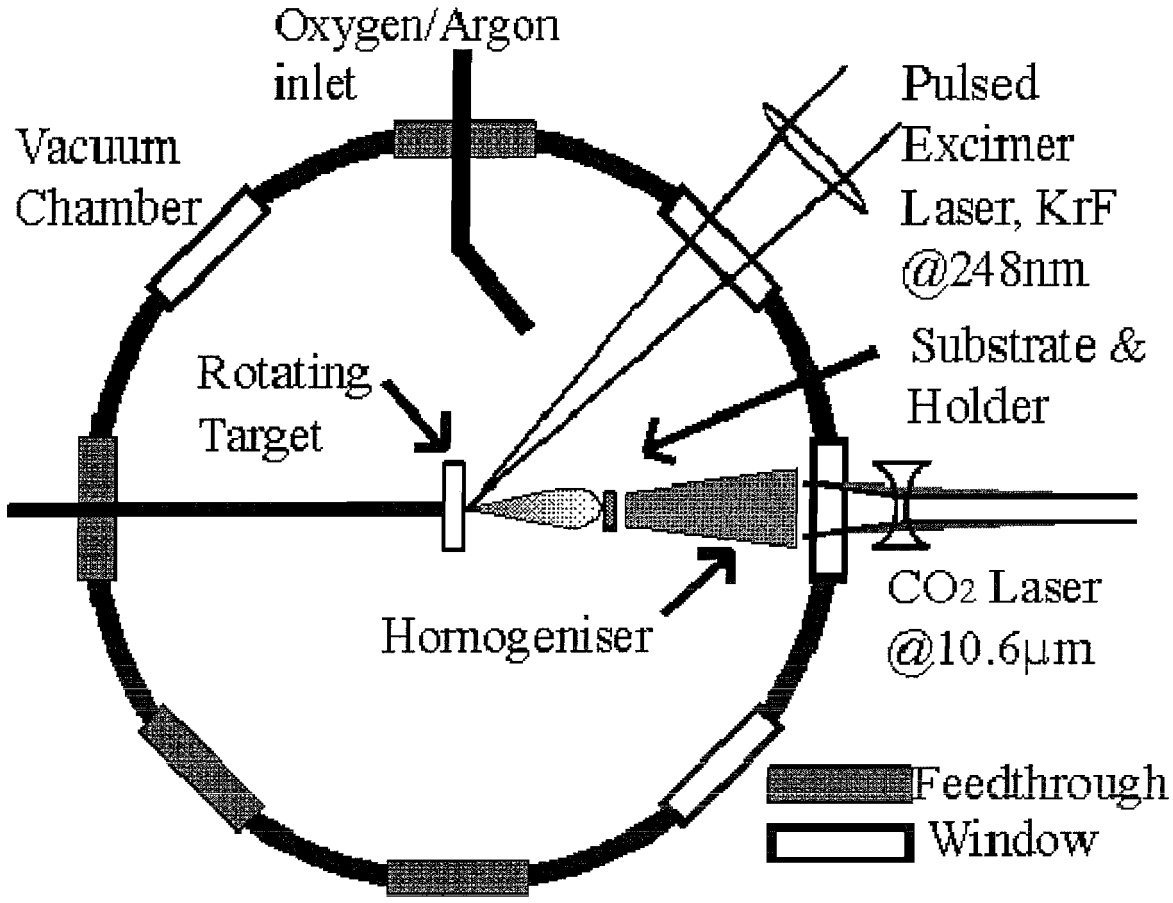

Figure 4.2 Schematic diagram of the basic apparatus used for pulsed laser deposition

A pulsed krypton fluoride excimer laser (here the laser had a pulse duration of 20ns at a repetition rate of 20Hz) is focused through the transparent window of a vacuum chamber onto a target of the material that will be deposited. With a high enough energy density on the target a small amount of the material will expand explosively into a highly directed plasma plume, as shown in figure 4.2. The plume is made up of neutral atoms, ions, larger molecules, solid pieces of the target and molten material. These components pass across the vacuum with velocities that are slightly mass dependant and then impinge on the surface of a substrate. It is usual practice to heat the substrate to provide further energy to the arriving species, in this set-up a 100W CO_2 laser was used as the heating source. Under the correct conditions the arriving plasma plume will coalesce to form a crystalline film of the target material on the substrate. If the target material is chosen to have a higher refractive index than the substrate, then the deposited layer can form a waveguide.

In the past optical thin films produced by PLD have exhibited high optical scattering losses. This was due to the large areal number density of micron and sub-micron sized particulates within the laser plume, which go on to form part of the thin film on the substrate and contribute to scattering loss. The particulate size is comparable to the optical wavelength and losses can be from 10-30dB/cm. When compared to losses as low as 0.05dB/cm for films grown by liquid phase epitaxy [17] it can be seen that improvements in the PLD technique are required. The growth of garnet films (e.g YAG and GGG studied here) is quite tolerant to particulates, but this will still lead to losses higher than the 1dB/cm usually required for a waveguide device.

Previous attempts at growth had produced visually inhomogeneous guides with many surface particulates [8]. The first laser action in one of these waveguides was achieved in a 2.6μm thick Nd:GGG layer (refractive index 1.965 at 633nm [18]) grown on an undoped YAG substrate (refractive index 1.82 at 633nm [18]). However the losses were as high as 6dB/cm and no significant output power was obtained. This section gives details of an improvement in this result based on a fabrication technique using a 1at.% Nd-doped crystal target rather than a ceramic composite target, and an improved spatial homogeneity of heating [19]. A deposition rate of ~0.4μm/min was obtained. The waveguide fabricated showed losses reduced by an order of magnitude and efficient laser operation at both 1.060μm on the four-level transition ($^4F_{3/2} \rightarrow {}^4I_{11/2}$) and 937nm on the quasi-three-level transition ($^4F_{3/2} \rightarrow {}^4I_{9/2}$) [4].

4.3.2 Waveguide layer characterisation

Several different doped and undoped GGG thin films were successfully grown on undoped YAG substrates by the PLD process described. The thickness of the waveguides produced was measured using a Tencor alpha-step 2000 surface profiler. The films varied from 3μm to 30μm, depending on the duration of the deposition. Due to the non-uniformity of the ablation plume, the guide thickness varied from the edges to the centre of the waveguide. The thin film that formed the waveguide laser device detailed in section 4.3.5 was measured to be 7μm at the edges and 9μm at its centre. This measurement was taken over the waveguide width of 8mm.

The thickness of the waveguides was also characterised with dark m-line prism coupling [20], as described in chapter 3, section 3.7.1. This gave an initial indication of the quality of the thin films as it was easier to prism couple light into a low loss waveguide than one with significant scattering loss. The thickness of the film was calculated from measurement of the mode angles and knowledge of the mode number of at least two modes. Some of the layers were visually inhomogeneous with dark, hazy surfaces and many surface particulates, no dark modes were discernible from these samples. Overall the calculations of the layer thickness using dark m-lines agreed fairly well with the readings from the alpha step surface profiler, and the waveguide laser film clearly showed over 20 guided TE modes.

4.3.3 Waveguide spectroscopy

The crystalline quality of the as grown films was compared to bulk GGG and assessed by spectroscopic analysis. The experimental techniques used here have been described in chapter 3 section 3.7. The Nd:GGG fluorescence spectrum was obtained by end-launching Ti:sapphire pump light at 808nm into the waveguide and observing the output on an OMA 2000 spectrometer. The waveguide fluorescence spectra in the regions of interest are shown in figure 4.3.

For the four level transition around 1.06μm (4.3(a)) and the quasi-three-level transition around 940nm (4.3(b)), the spectra are already as good as those previously obtained for an annealed PLD Nd:GGG waveguide [8], however they are broadened and slightly shifted in comparison to the bulk spectra [11]. This is not surprising due to the stress that would be induced by the lattice mismatch between the epitaxially grown waveguide layer and the substrate.

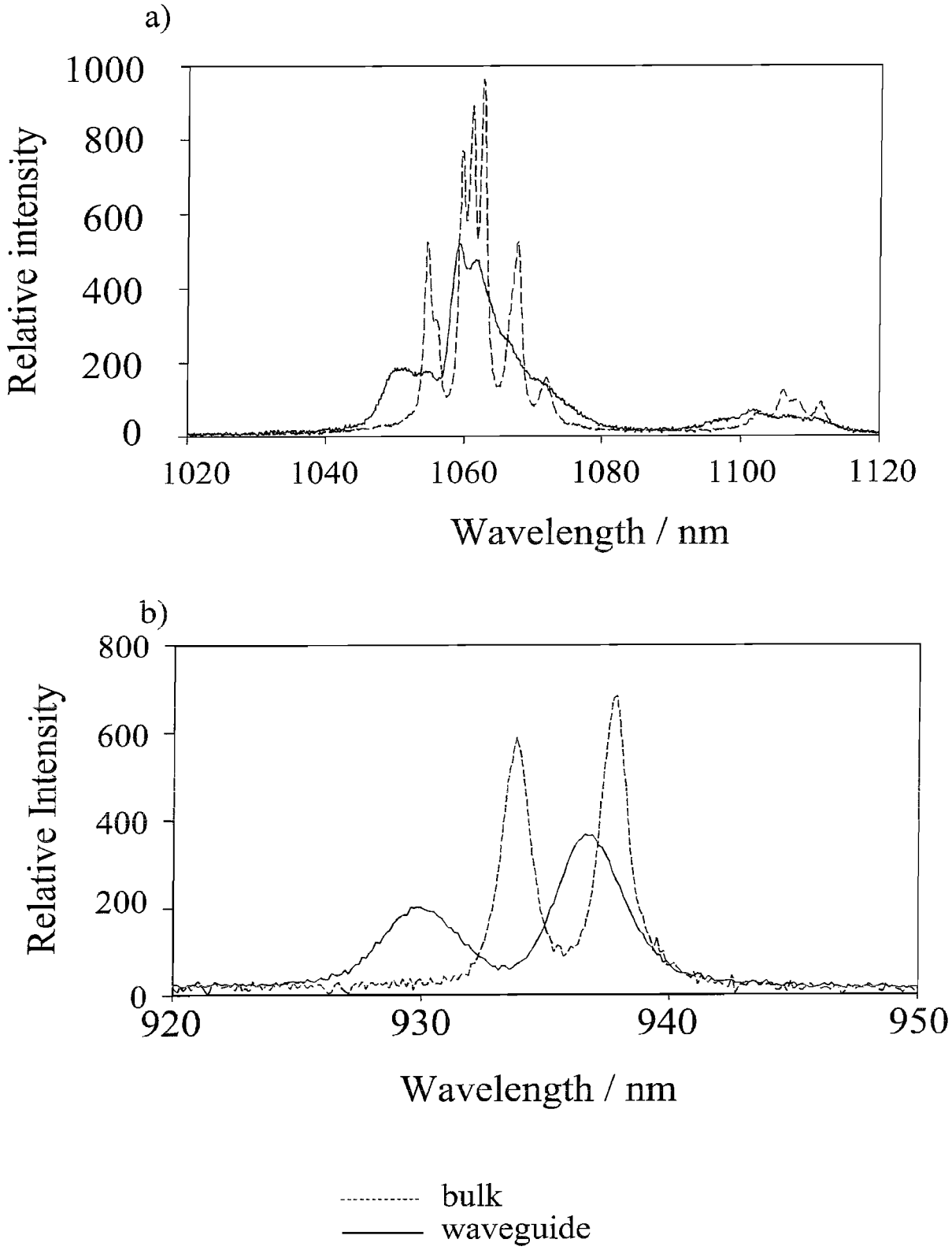

Figure 4.3 Fluorescence spectra of the Nd:GGG waveguide laser film described in sections 4.3.5 and 4.3.6. Fluorescence spectra around the $^4F_{3/2} \rightarrow {}^4I_{11/2}$ (a) and the $^4F_{3/2} \rightarrow {}^4I_{9/2}$ (b) transitions are shown compared to bulk.

It should be noted that the 940nm fluorescence will also be slightly affected by weak ground state absorption at these wavelengths (~0.1dB/cm).

The fluorescence lifetime was measured by chopping the pump beam and observing the fluorescence decay with a photodiode and oscilloscope, giving a value of 260±20μs. This appears to be in good agreement with reported lifetimes for neodymium doping levels of 1at.% or less [21-23].

The waveguide was then annealed for six hours at a temperature of 1015°C in a constant, 1 litre/min, flow of oxygen.

Previously this had been found to improve the fluorescence spectrum and laser action of PLD Nd:GGG thin films [8].

In this instance, no significant changes in the spectra were observed after annealing (and very similar laser performance was obtained with the post-annealed sample).

A comparison of fluorescence spectra around 1.060μm is shown in figure 4.4. Curve (a) shows the previous lasing guide after it had been annealed, (b) shows the fluorescence from the second lasing guide after an identical anneal and curve (c) is from a piece of 3.35at.% Nd-doped GGG.

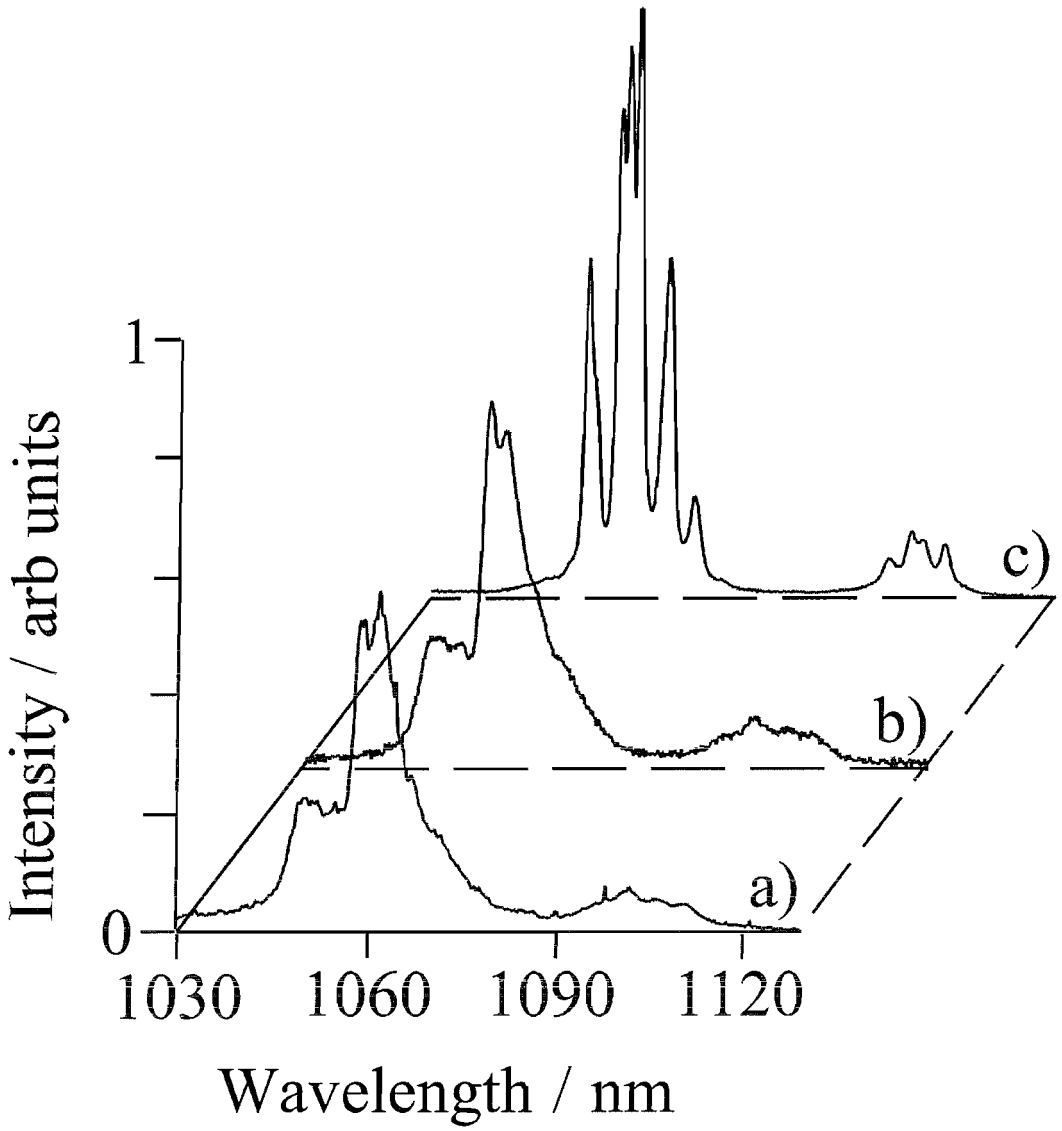

Figure 4.4 Fluorescence spectra for (a) waveguide grown from a ceramic target, (b) waveguide grown from a crystal target, (c) bulk Nd:GGG

To generate any significant improvement in the spectrum may require temperatures closer to the melting point of GGG, (1725°C [24]), instead of temperatures up to 1000°C that were used here.

Figure 4.4 shows clearly that curves (a) and (b) are close to identical and are broadened with respect to the bulk sample. With the curves normalised to the same unit area the peak cross sections of (a) and (b) are lower than (c) by factors of 0.58 and 0.62 respectively. The same broadening occurs around the other laser wavelength

and the peak cross section at 937nm for the lasing guide (b) is reduced by a factor of 0.53 compared to the bulk peak (938nm).

The broadening present in the emission spectra is also a characteristic of the absorption spectrum, shown in figure 4.5. The broadening decreases the peak absorption cross section, but it also means the absorption has a better match to the linewidths of typical diode pump lasers.

The broadening of the emission and absorption spectra is an indication of reduced crystalline quality in the Nd:GGG layer compared to the bulk crystal. This was confirmed by X-ray diffraction spectra of the films [19], which showed variations in peak heights and positions shifted by a few percent relative to bulk Nd:GGG. The reduced crystalline quality is due in part to stress induced defects caused by the 2.9% lattice mis-match between Nd:GGG and YAG. As the film attempts to grow epitaxially on the YAG substrate the difference in lattice constant between GGG and YAG produces strain which modifies the material. Modification of the laser host material can result in spectra of the rare-earth ions significantly changed from that of the bulk crystal.

Another explanation for the broadening is the fact that the films grown were not stoichiometric Nd:GGG (Nd:$Gd_3Ga_5O_{12}$) as they were found to be up to 33% gallium deficient [16]. The extent of the gallium deficiency was found to depend on whether the Nd:GGG target material was a crystal or a ceramic, and the growth temperature (provided by the CO_2 laser).

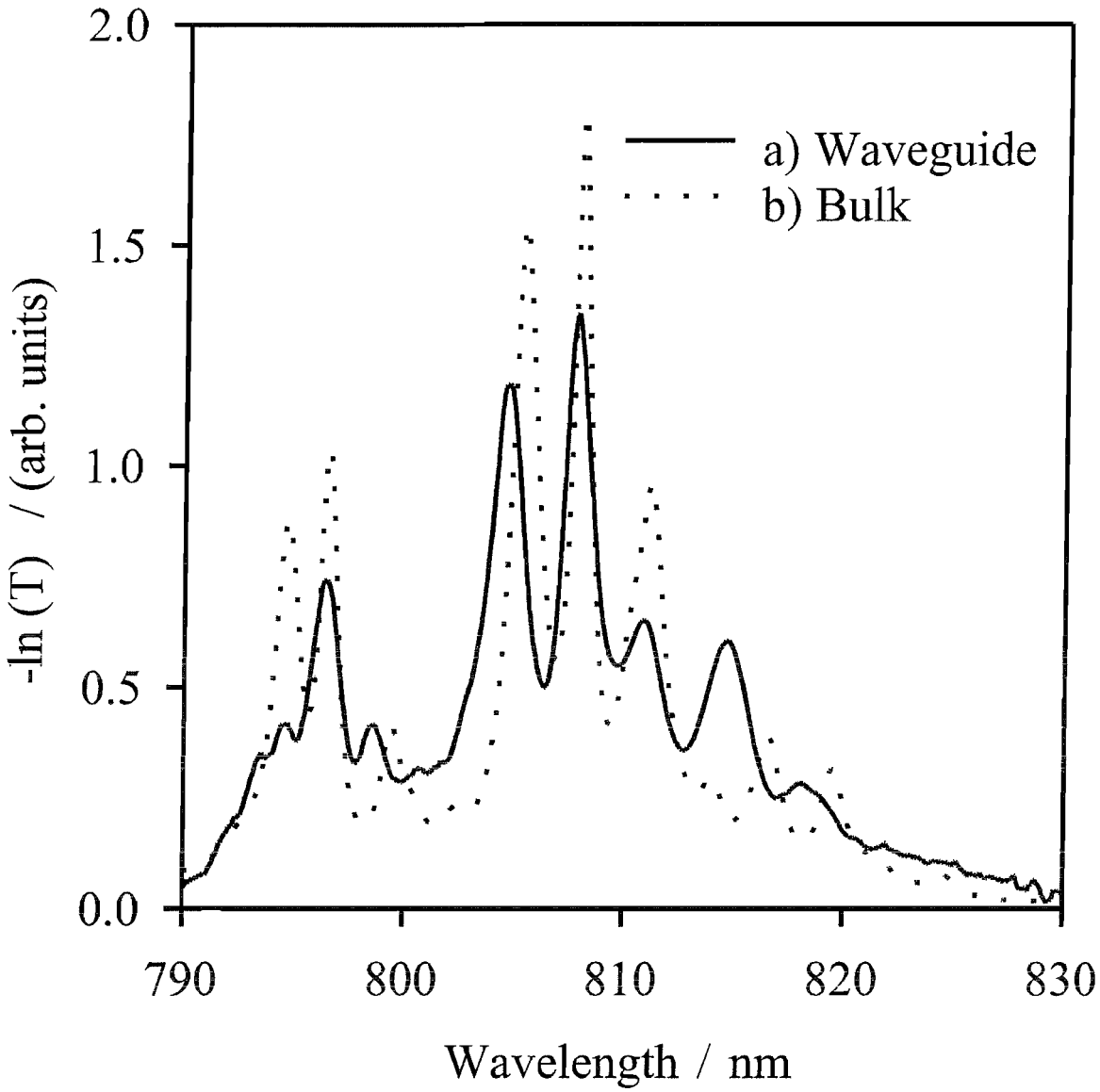

Figure 4.5 Absorption spectra comparing (a) waveguide grown from a crystal target and (b) a sample of bulk GGG

As an additional spectroscopic analysis, low temperature fluorescence spectroscopy was carried out to compare the spectra of a number of films, all grown from crystal targets but which showed varying visible surface quality. The samples were sealed in a cryostat with a wide transmission glass window, under vacuum conditions, and cooled to liquid helium temperatures. Fluorescence spectra were then obtained with a Ti:sapphire pump laser at 808nm as described in chapter 3, section 3.7. These investigations would help to establish the optimum growth conditions for Nd:GGG on YAG. Figure 4.6 shows recorded spectra for a bad quality film (a), good quality films (all similar to (b)), and a sample of bulk Nd:GGG (c).

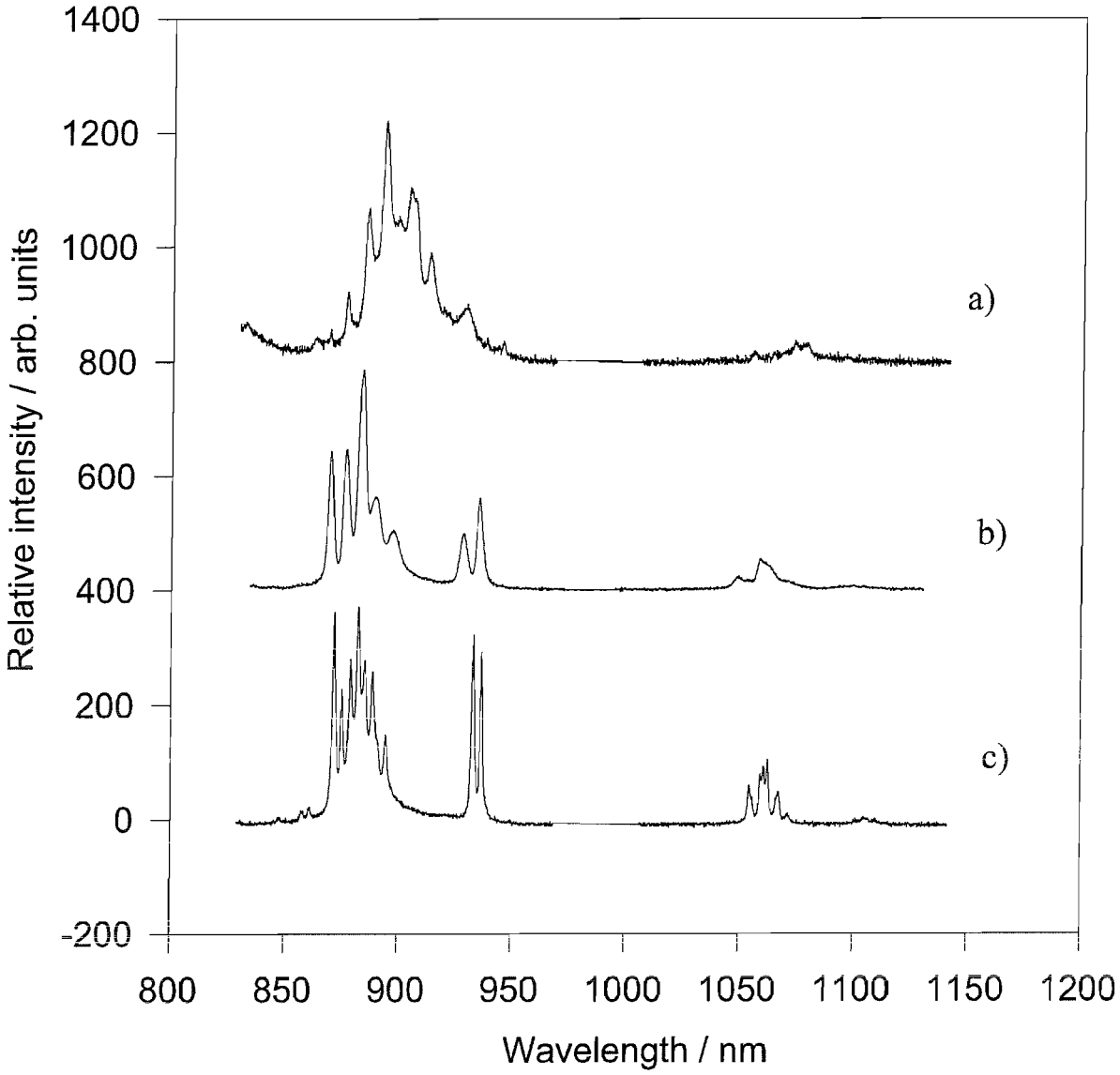

Figure 4.6 Low temperature fluorescence from a bad quality Nd:GGG film (a), a good quality Nd:GGG film (b) both grown from crystal targets, and a bulk sample (c)

The film with the fluorescence spectrum shown in figure 4.6(a) was grown at a significantly lower temperature than the other films, resulting in a greatly reduced gallium content. Further work is required to prevent this gallium loss, as even the best quality films grown from a single crystal target were gallium deficient. The growth temperature is obviously crucial, but other areas to investigate include the target to substrate distance and altering the conditions for growth depending on the type of target used. Adverse spectral changes, such as the broadened spectra described here, can partially offset the benefits offered from a waveguide geometry, so optimisation of the growth parameters is important.

The main goal in growing these films was to produce films with a reduced number of surface particulates as these accounted for the majority of the scattering loss in the previous guides [8]. The single crystal target used here has a uniform density which was not guaranteed from the ceramic composite target used before. The films produced appeared transparent and flaw free to the eye, and under a microscope the particulate count was reduced by a factor of ~20 compared to the previous films [19]. The films grown with this target modification were therefore expected to produce a significant improvement in previously reported laser performance [8].

4.3.4 Waveguide transmission measurements

In order to test the laser performance of these films a neodymium doped guide was cut to a length of 1.2mm and end-polished to an optically smooth finish. The film appeared to be clear, clean, of good quality, and visually homogeneous with very few large surface particulates.

Transmission measurements (described in chapter 3, section 3.8.1), were taken to gauge the waveguide loss before laser experiments were attempted. The total transmission was 90%, pointing to a good launch efficiency into the high numerical aperture waveguide, and a low loss. This transmission figure suggested a significant improvement in the 6dB/cm scattering loss reported for the first Nd:GGG waveguide laser fabricated by PLD [8]. Based on this result waveguide laser experiments were carried out. The waveguide loss was investigated further in section 4.3.8.

4.3.5 Waveguide laser results around 1.060μm

The 1.2mm length of crystal was chosen to be similar to that used in the previous work [8], enabling direct performance comparisons. The length was, in fact, shorter than required for optimum laser performance.

A laser cavity was formed using plane dielectric mirrors with a high reflectivity at 1.060μm. The mirrors were attached to the end-faces of the waveguide, as described

in chapter 3 (section 3.9). The waveguide was longitudinally pumped using a Ti:sapphire laser tuned to the strong neodymium absorption around 740nm. Very similar results were later obtained using the more commonly used and stronger absorption at 808nm. Optimum launch efficiencies were achieved using a x16 microscope objective. A laser threshold of 2.2mW (5.6mW) of absorbed (incident) power was obtained. This is a factor of ten higher than the predicted incident threshold of 0.6mW (from equation 2.53). This prediction was made assuming a loss of 0.5dB/cm and using spectroscopic parameters obtained from modifying the values for the bulk crystal based on the spectroscopy of the as grow film [4,8]. The calculation used pump and signal spot sizes measured with a CCD camera.

As yet there is no clear explanation for the higher than predicted threshold, although some other unaccounted for loss in the cavity or errors in the assumptions made could be responsible.

Lasing initially occurred at 1.060μm, corresponding to the most intense peak of the waveguide fluorescence spectrum (figure 4.3(a)), and at higher pump powers simultaneous lasing at 1.060μm and 1.062μm was observed on a number of longitudinal modes. At a pump level approximately ten times higher than threshold, lasing modes occurred across a broad band from 1.059μm to 1.063μm.

Using an output coupler with a 2.2% transmission at 1.060μm, the threshold increased to 3.7mW of absorbed power. Figure 4.7 gives the output versus input power characteristics of this laser, showing a slope efficiency of 20% with respect to absorbed power.

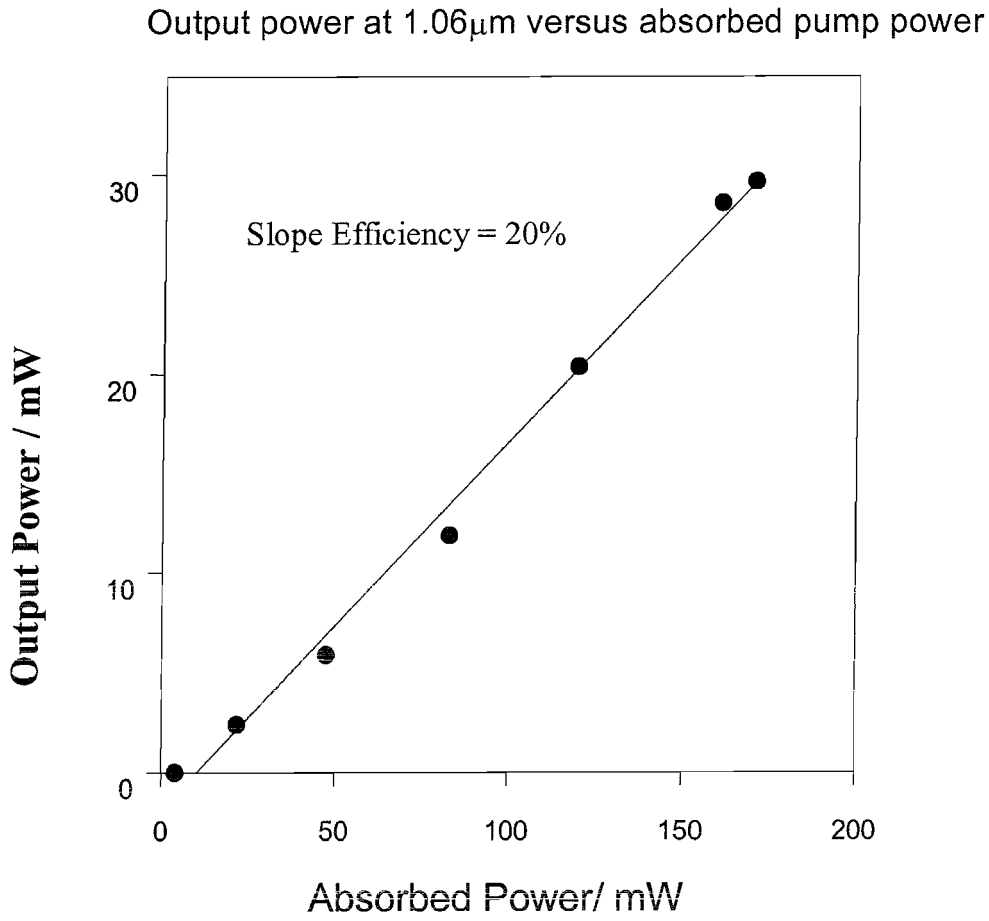

Figure 4.7 Output power versus absorbed pump power for the 1.060μm Nd:GGG waveguide laser, using a 2.2% output coupler

Despite the fact that this is a highly multi-mode waveguide (many guided modes were observed from the prism coupling experiment described earlier), observation of the output using a CCD camera showed a single spatial mode for both the laser and for the transmitted pump light. The spatial profiles were close to Gaussian in both planes of the guide. From the size of the imaged output on the camera, the spot sizes ($1/e^2$ half-widths) in the guided and non-guided planes were calculated as 3.0μm and 48μm at 1.060μm, and 2.4μm and 44μm at 808nm. These results suggest the mode is well confined, with the beam waist about one third the width of the waveguiding layer. This is as expected for the fundamental mode of a highly multi-mode waveguide.

4.3.6 Waveguide laser results around 940nm

After annealing the sample the laser performance of the quasi-three-level $^4F_{3/2} \rightarrow {}^4I_{9/2}$ transition, corresponding to the fluorescence spectrum in figure 4.3(b), was tested. To the author's knowledge this was the first report of Nd:GGG lasers operating at this wavelength. The laser cavity was formed with mirrors of high reflectivity at 940nm. The same laser pump wavelength of 808nm was used and a x10 microscope objective gave the optimum launch efficiency. A laser threshold of 9mW (25mW) of absorbed (incident) power was obtained. As observed for the 1.060μm transition, the actual threshold was a factor of ten higher than the 2mW incident power threshold predicted from laser theory (equation 2.51). A propagation loss term of 0.5dB/cm was used in this calculation and a reabsorption loss of ~0.1dB/cm was taken into consideration. The spectroscopic parameters such as τ and σ_e were estimated, as before, from values for the bulk crystal, and the pump and signal spot sizes used in the calculation had been measured with a CCD camera. At pump powers three times above threshold, five or six lasing modes were observed at wavelengths between 936nm and 937nm. This wavelength region corresponds to the most intense waveguide fluorescence peak of figure 4.3(b).

Output couplers with 2% and 13% transmission at 937nm gave corresponding increases in the threshold absorbed power to 16mW and then 60mW. Figure 4.8 gives the output versus input power characteristic of the 937nm laser transition using the 2% output coupler, which yields a slope efficiency of 20% with respect to absorbed power.

Unfortunately the pump source available was not sufficiently powerful to make a slope efficiency measurement with the 13% output coupler. The output from the waveguide was observed to have a single spatial mode with spot sizes of 2.9μm in the guided plane and 48μm in the non-guided plane.

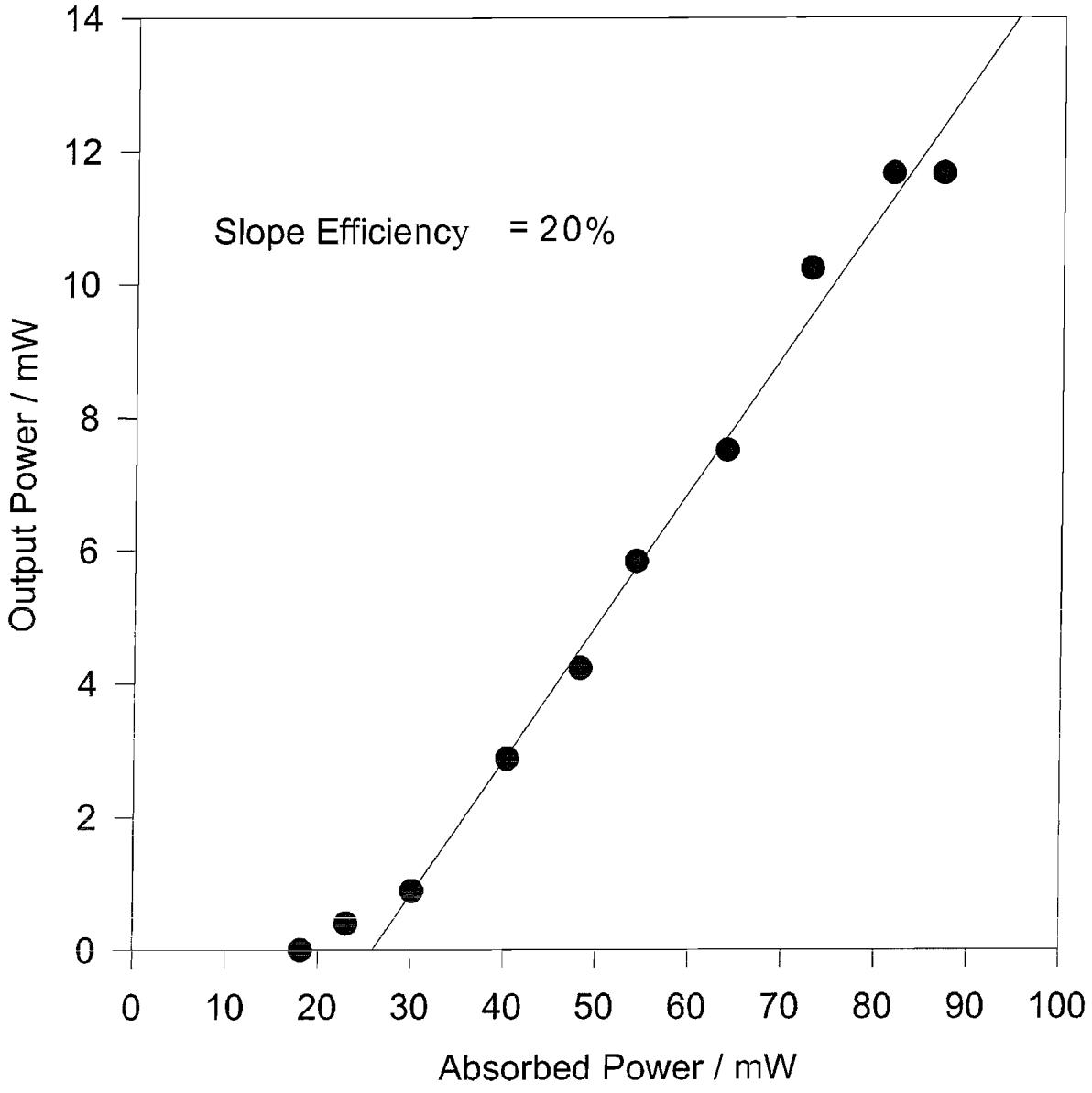

Figure 4.8 Output power versus absorbed pump power for the 937nm Nd:GGG waveguide laser, using a 2% output coupler

4.3.7 Waveguide laser polarisation

The waveguide laser output was investigated using a polarising beam splitter and found to be unpolarised at both 1.060μm and 937nm. This is due to the isotropic nature of the GGG crystal, and in the case of a waveguide it also shows that there is no significant difference in loss between the transverse electric and transverse magnetic fundamental modes.

4.3.8 Waveguide loss

The efficient lasing suggests low waveguide loss and this was quantified using the method of Findlay and Clay [25], as described in chapter 3 section 3.8.2. The results of this analysis are shown in figure 4.9. The labels on the graph data points show the transmission of the various mirrors used.

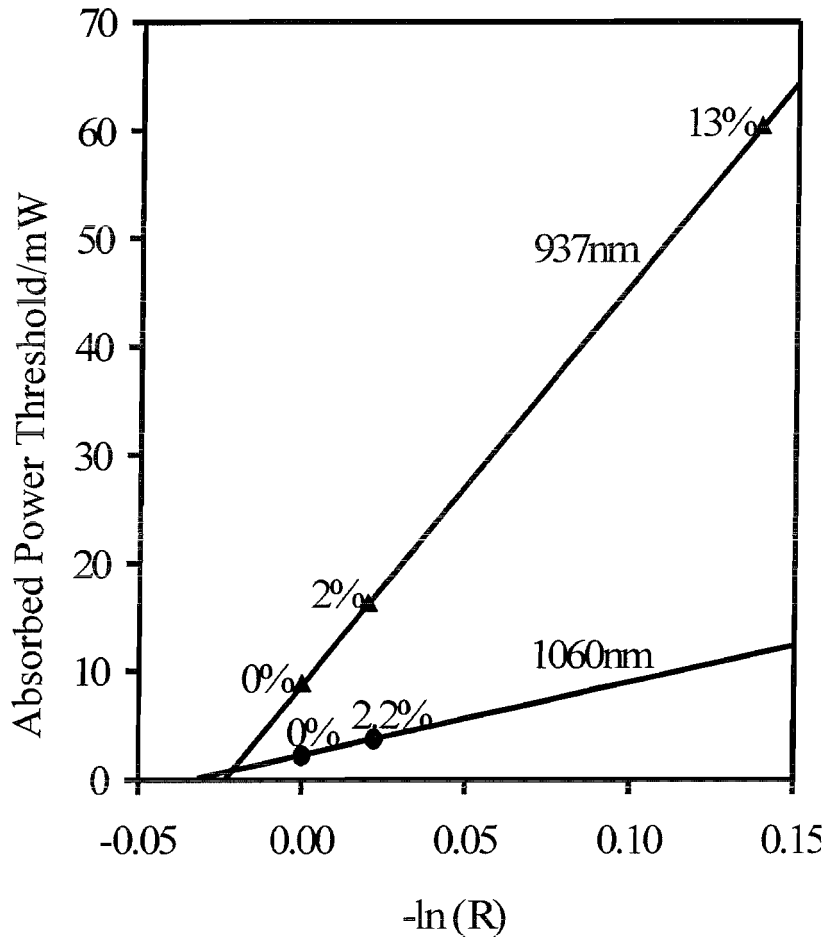

Figure 4.9 Absorbed pump power threshold for lasing versus logarithm of output coupler reflectivity for 1.060μm and 937nm laser operation

The figure shows the threshold at 1.060μm found with a high reflector mirror and a 2.2% output coupler. The thresholds found at 937nm with a high reflector mirror, a 2% and 13% output coupler were also plotted on figure 4.9. The x-intercept values for these plots correspond to loss figures of (0.58±0.13) dB/cm and (0.42±0.11) dB/cm for the 1μm and 937nm transitions respectivly, the major source of error is taken to be

the uncertainty in the coupling efficiency into the waveguide. However the 937nm transition is quasi-three-level, and so suffers from an additional ground state re-absorption loss, calculated to be ~0.1dB/cm for bulk Nd:GGG from the thermal population at room temperature and the relevant absorption cross section. The 937nm transition then has a true value of waveguide scattering loss of ~0.3dB/cm, which is believed to be the lowest loss reported so far for any waveguide grown by PLD.

The 20% slope efficiency ($s\varepsilon$) obtained from the 1.060μm laser in section 4.3.5 is consistent with a passive internal loss of <1dB/cm. Assuming all of the launched pump power is absorbed, the loss was estimated from equation 2.60 (expression 4.4):

$$s\varepsilon = \left(\frac{T}{T + L_{guide}}\right)\frac{\upsilon_L}{\upsilon_p}(1 - e^{-\alpha_p l})\frac{dS}{dF} \qquad 4.4$$

The terms in the equation are as defined previously in chapter 2. L_{guide} is the round trip waveguide propagation loss exponent, $-2\alpha_g l$. dS/dF is a quantity that contains the overlap and geometrical factors associated with the conversion of pump photons into laser emission. Assuming the pump and laser spot sizes do not vary significantly through the laser medium, dS/dF is given by equation 4.5 (from reference 26):

$$\frac{dF}{dS} = \frac{w_{Lx} w_{Ly}\left(2w_{px}^2 + w_{Lx}^2\right)^{1/2}\left(2w_{py}^2 + w_{Ly}^2\right)^{1/2}}{\left(w_{px}^2 + w_{Lx}^2\right)\left(w_{py}^2 + w_{Ly}^2\right)} \qquad 4.5$$

Rearranging the equation yields a value of $19m^{-1}$ for α_g, the single pass loss in the cavity. This is equivalent to 0.8dB/cm , in rough agreement with the results from the Findlay Clay method. A similar estimate from the slope efficiency at 937nm (obtained from data in figure 4.8) is also consistent with a passive internal loss of <1dB/cm.

These loss results are an order of magnitude improvement over that previously reported [8] and are related to the observed reduction in areal density of surface particulates.

4.3.9 Pulsed laser deposited Nd:GGG waveguides - Summary

In summary, this section has shown improved laser action of a thin film waveguide grown by PLD. A laser threshold as low as 2.2mW of absorbed power has been achieved. The crystalline Nd:GGG planar waveguide lased at wavelengths centred around 1.060μm and, it is believed for the first time, on the quasi-three-level transition at 937nm. Slope efficiencies of 20% were obtained for both transitions. The waveguides had the lowest loss reported so far (~0.5dB/cm) for films grown by PLD.

An eventual aim is to make active waveguide devices with high power diode-bar pumping, this section has shown PLD to be an attractive method for fabricating waveguide films with a high numerical aperture which could allow proximity coupling to diode-bars.

4.4 High numerical aperture waveguides fabricated by direct bonding

This section details waveguides fabricated by direct bonding, the second method of fabricating high numerical aperture waveguides investigated in this thesis. Direct bonding has proved an ideal fabrication method for high NA waveguides as it allows very dissimilar materials to be bonded together with ease, without the constraints of epitaxial growth.

4.4.1 Fabrication

The fabrication technique is not precisely documented partly because it forms commercially sensitive information and partly because there are a number of subtleties suggested for preparing different types of material for bonding. The optimum process parameters for bonding have not been clearly defined although a good review of the subject is given in reference 27. The process relies on bonding high quality bulk material together via Van der Waals forces, it does not place any restriction on the materials to be bonded apart from that they should have similar thermal-expansion coefficients. An examination of the literature gives the following basic method for direct bonding.

Precision finished crystal or glass components, polished smooth and flat to <~1nm roughness are assembled and optically contacted. When the flat and clean surfaces are at distances of less than a few hundred nanometres, attractive Van der Waals forces pull the two together. The two polished surfaces snap together and become bonded in atomic contact. The structure is heated (annealed) to increase the bonding strength of some materials, but at temperatures below that at which diffusion effects take place between the layers [28]. The bonding of some materials, for example ferroelectrics, benefits from heat treatment up to a few hundred degrees Celsius. This helps bring the surfaces closer together and the bond strength can be increased sufficiently for further processing such as dicing or polishing. An additional aid to the technique can be an hydrophilic treatment [29] of the surfaces before bonding. The surfaces are rinsed with de-ionised water and when they are contacted, hydroxl groups become trapped allowing H bonds to form between the contacted layers. This leads to increased bonding strength. After bonding the structure is mechanically and chemically stable. The structure formed is strong enough to withstand all the usual finishing operations and the deposition of optical coatings, just like a conventional single crystal or glass.

To fabricate a planar waveguide the material forming the core is bonded to the substrate and then polished down to the required thickness. A cladding layer can be attached to the waveguide core in similar manner if required. The composites are described as direct bonded or in some previous work as thermally bonded [5]. There are no bonding agents used so the reflections at the interfaces are mainly due to differences in the refractive indices between the materials. Waveguides produced this way are usually of high quality as scattering loss is restricted to that from imperfections in the optical surfaces of the components and, possibly, to subsurface damage from polishing.

4.4.2 Details of samples investigated

The three different samples used to investigate the performance of waveguides fabricated by direct bonding, are detailed in table 4.1. The NA of the structures was found from equation 4.2 using values of refractive index quoted at 633nm. The

thickness of the samples was measured by examination of the end faces under an optical microscope.

Sample	Guide material	Guide thickness (μm)	Guide length (cm)	Substrate material	Cladding material	NA
1	1at.% Nd:YAG n=1.81633 [30]	8	0.4	YAG n=1.81523 [30]	YAG n=1.81523	0.06
2	1at.% Nd:GGG n=1.965 [18]	17	1.9	YAG n=1.81523	-	0.75
3	1at.% Nd:YAG n=1.81633	22	1.4	Glass n=1.62	-	0.82

Table 4.1 Details of the contact bonded waveguides used in this study, samples 2 and 3 have no cladding layer

The material combinations in table 4.1 were chosen to be close to those already fabricated by other techniques. This meant direct comparisons between waveguides fabricated with the technique of contact bonding could be made with other fabrication methods.

The Nd:YAG on YAG waveguide (sample 1) was similar to structures previously grown by liquid phase epitaxy. The small index difference between the core and the substrate is provided by the 1 at.% neodymium doping, leading to a low numerical aperture.

Sample 2 was similar to the waveguides fabricated by pulsed laser deposition, described previously in this chapter (section 4.3), and has a high numerical aperture.

Lastly sample 3 is made of a Nd:YAG core on a glass substrate with no cladding layer, giving a very high NA of 0.82. This sample demonstrates the wide range of materials that can be bonded and was designed to have a NA high enough to make the structure suitable for proximity coupling to diode-bars.

The waveguide structures were evaluated to establish their optical properties compared to other fabrication techniques.

Their spectroscopy, lasing characteristics and propagation losses were investigated using a Ti:sapphire pump laser operating around 807nm and the experimental techniques described in chapter 3.

4.4.3 Waveguide spectroscopy

The fluorescence spectra around the four-level transition ($^4F_{3/2} \rightarrow {}^4I_{11/2}$) at 1.06μm were obtained for the three waveguides. The spectra were found to be the same as those obtained from bulk samples of the same material. The bonding process had resulted in no modification of the core material so the spectra of the rare-earth ions remained unchanged compared to the bulk crystal.

In contrast the technique of PLD resulted in fluorescence spectra significantly different to bulk material.

This is illustrated with a comparison of the fluorescence around 1.060μm for sample 2 and a Nd:GGG on YAG waveguide grown by PLD, shown in figure 4.10.

While it is possible to fabricate low NA Nd:YAG on YAG waveguides by LPE with no noticeable change in spectroscopy, high NA waveguides must be Gallium doped and an accompanying spectral broadening is obtained.

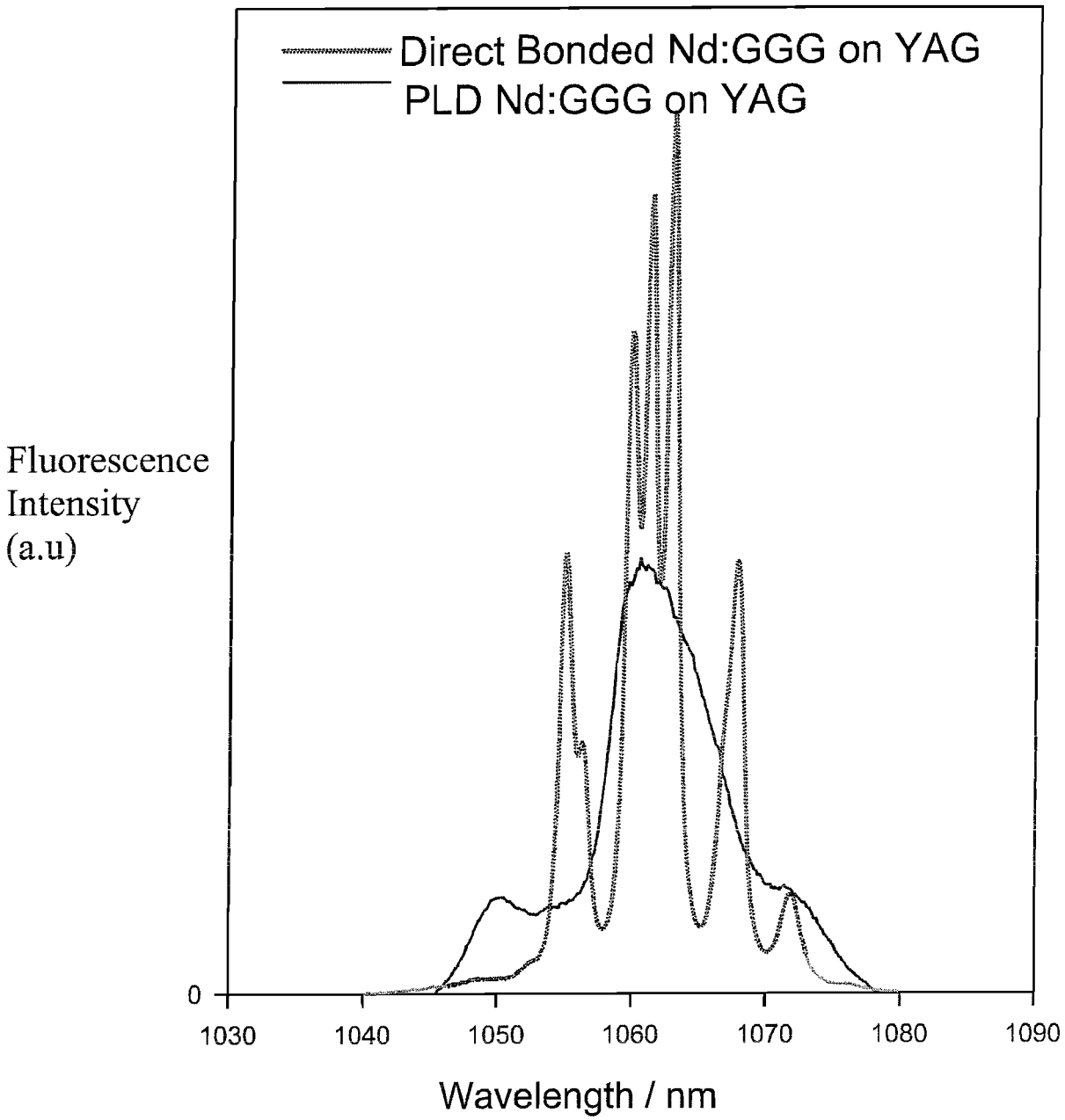

Figure 4.10 Comparison of fluorescence spectra between a PLD and a contact bonded sample

The fluorescence lifetimes of samples 1, 2 and 3, obtained from measurements of the fluorescence decay on an oscilloscope, also agreed closely with those from bulk samples. This was further confirmation of the high crystalline quality and bulk spectroscopic characteristics of the waveguide layer.

4.4.4 Waveguide laser experiments

The waveguide was longitudinally pumped using a Ti:sapphire pump laser tuned to the strong neodymium absorption around 807nm. The pump light was launched through a x5 microscope objective. The laser cavity was formed using plane dielectric mirrors with a high reflectivity at 1.060μm attached to the end faces of the waveguide, as described in chapter 3 (section 3.9), or the Fresnel reflections from the polished end faces. There was no attempt made in these investigations to optimise laser performance by using the best pump spot size, or length of crystal. The primary aim was to assess the waveguide propagation loss using the method of Findlay and Clay [25], which eliminates any dependence on the pump and laser geometry providing they remain the same throughout the experiment.

4.4.5 Waveguide loss

The threshold absorbed power needed to produce lasing at 1.064μm in samples 1 and 3 and at 1.062μm in sample 2 was determined using a variety of different output couplers. This follows the method of Findlay and Clay described in chapter 3 section 3.8.2. The results obtained for the three samples are given in figure 4.11.

The results obtained from figure 4.11 show that samples 1 and 3 have propagation losses of 0.7dB/cm and sample 2 has a propagation loss of 0.4dB/cm. A low propagation loss is crucial to efficient device operation and these values show that direct bonding is capable of producing low loss waveguides. The propagation losses for these guides are comparable to loss figures for a number of other methods of rare-earth doped waveguide fabrication.

While the losses are not as low as YAG guides grown by liquid phase epitaxy (~0.1dB/cm) [17], they are still low enough to suggest that efficient device performance will be possible.

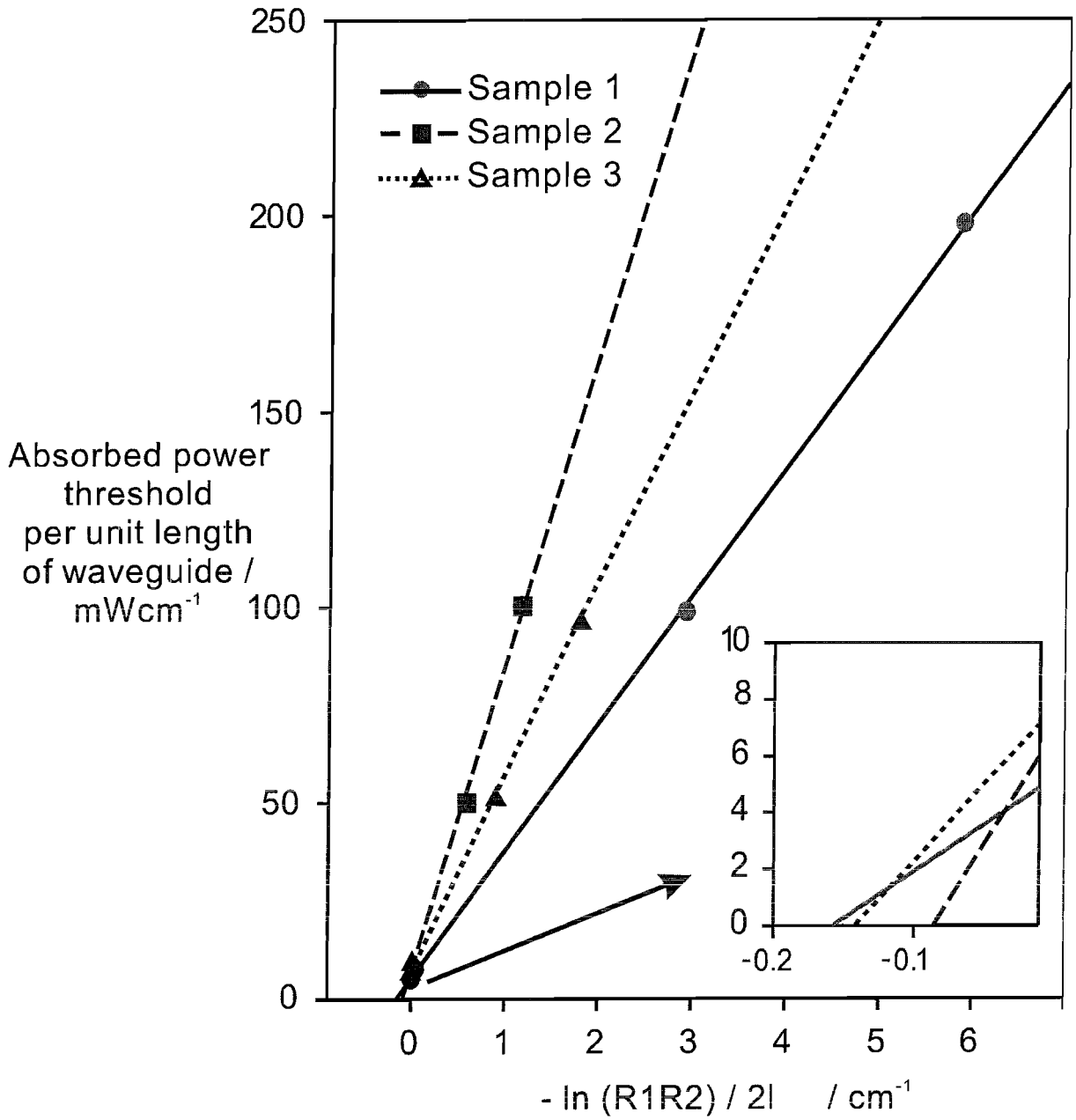

Figure 4.11 Modified Findlay-Clay plot for samples 1, 2 and 3. The position of the intercept on the x axis gives the value of the loss coefficient

4.4.6 Waveguide laser performance

To test the laser behaviour of these low loss waveguides the slope efficiency for each device was measured using an output coupler with a nominal transmission of 3.5%. The results are shown in figure 4.12.

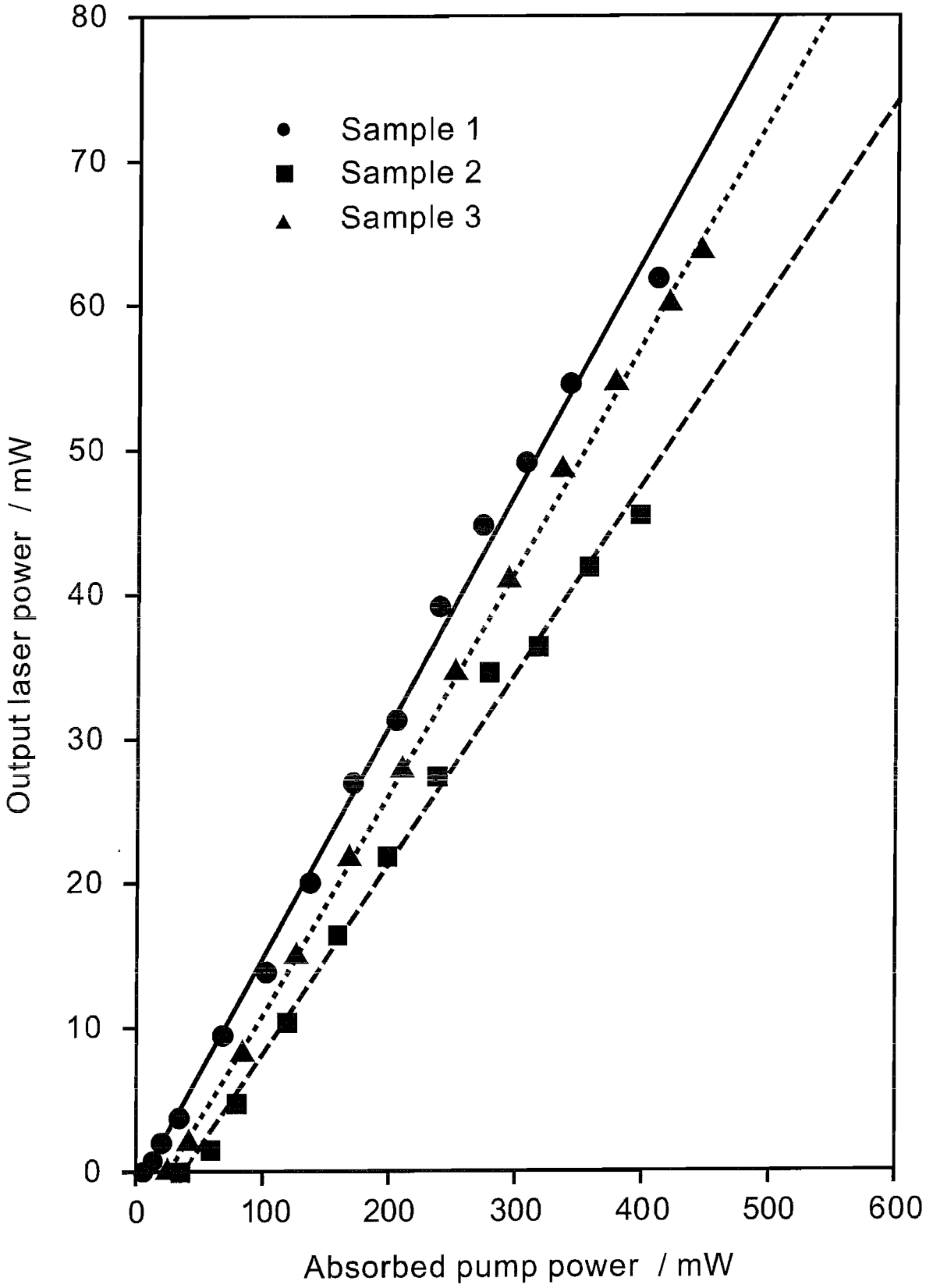

Figure 4.12 Output power at 1.060μm against absorbed pump power for the samples

Figure 4.12 gives slope efficiencies of 16%, 13% and 15% with respect to absorbed power for samples 1, 2 and 3 respectively. However the pumping geometry had not

been fully optimised for laser performance so higher slope efficiencies may be obtainable with improvements in the experimental set-up. The range of laser thresholds shown on figure 4.12 was also due to the non-optimised pump launch conditions for each sample. Table 4.1 shows the variation in waveguide samples and each waveguide would be expected to have different optimum launch conditions for the lowest threshold operation.

Slope efficiency ($s\varepsilon$) results can suggest values of propagation loss when analysed using equation 4.4. Overall the slope efficiencies obtained from these waveguide lasers suggest propagation losses consistently less than 1dB/cm. This is similar to loss figures found from Findlay Clay analysis.

The high NA guides were multi-mode in nature, but by altering the pump launch conditions all the waveguide samples could be made to operate in a single mode in the guided direction. Multi-mode output was observed from all of the waveguide samples in the non-guided direction.

4.4.7 Waveguide transmission with angle

The high NA characteristics of these waveguides was further investigated by measuring the transmission, versus the angle between the guide plane and the propagation axis of the launched pump light. The transmission results are shown in figure 4.13.

The plots show that, as expected, the high NA waveguides, Nd:GGG on YAG and Nd:YAG on glass, are relatively insensitive to the input angle of the pump beam, while the Nd:YAG on YAG waveguide has a far lower angular acceptance.

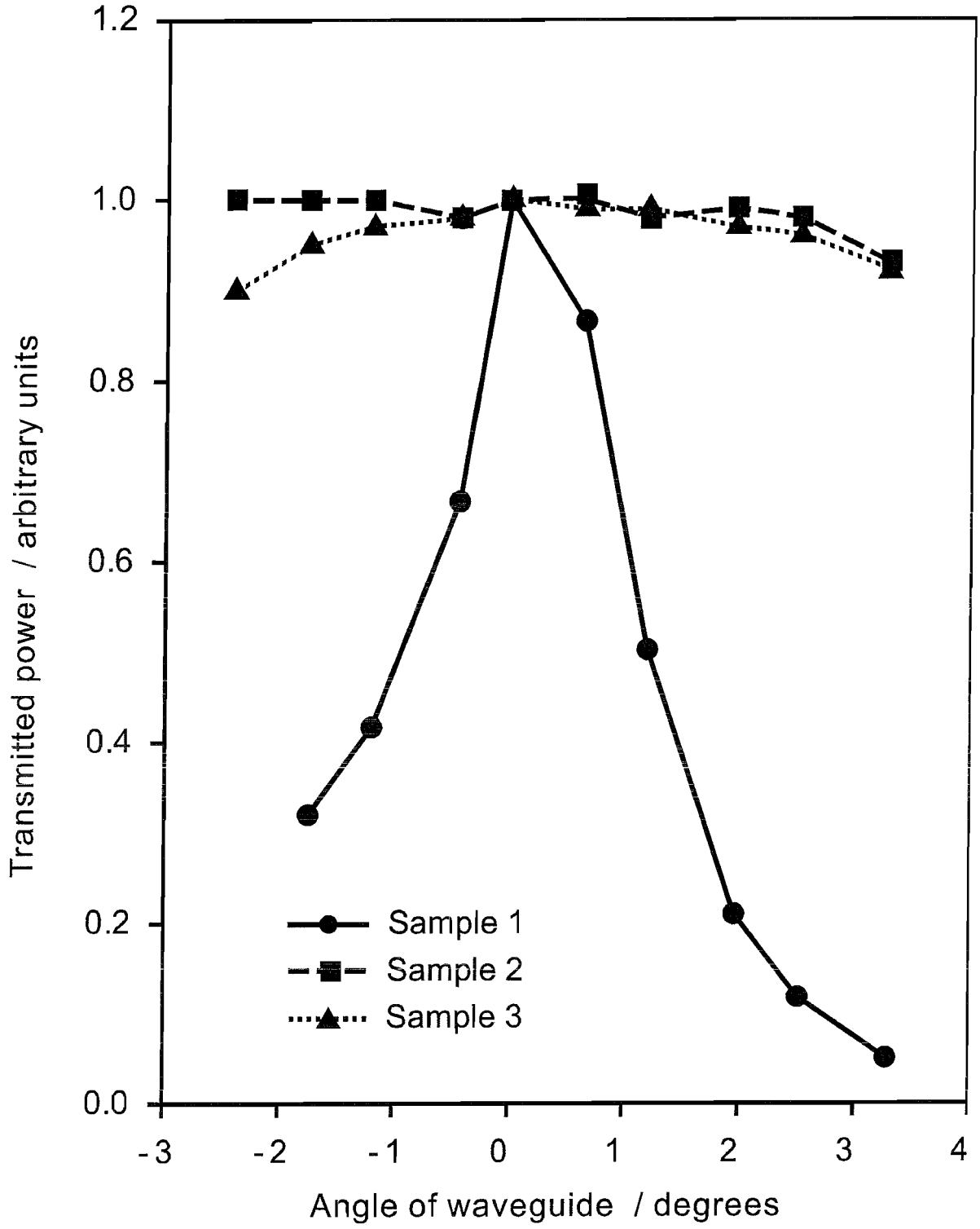

Figure 4.13 Transmitted Ti:sapphire power plotted versus the end face angle of the waveguide relative to the propagation axis of the input light

4.4.8 Direct bonded waveguides for diode-bar pumping

Direct bonding has been shown, in the last section, to be a successful fabrication technique for waveguides composed of dissimilar materials, producing high NA, low loss structures. Waveguides suitable for high-power diode-bar pumping require a NA of greater than ~0.3 for core thicknesses of <5μm, as is illustrated in figure 4.1. A Nd:YAG core with sapphire substrate and cladding layers provides a good practical choice for such a waveguide. The structures investigated here had the sapphire substrate orientated with the (001) direction parallel to the plane of the waveguide core, and in the direction of propagation of the waveguide laser output. The high NA (0.46) of this combination allows core dimensions as small as 4μm to be used. Both materials have high physical strength, good bonding behaviour and high thermal conductivities. They also have similar thermal expansion coefficients which is important as a thermal annealing step is applied in the bonding process, and thermal gradients will arise in the materials as a result of high-power diode-bar pumping. Initial investigations with this material combination were with asymmetric slab waveguides 2cm in length. Loss results and sample details are tabulated in table 4.2.

Guide material	Guide thickness (μm)	Guide length (cm)	Substrate material	NA	α_g, loss (dB/cm)
1at% Nd:YAG n=1.81633[30] at 633nm	8	2	Sapphire n=1.76[31] at 800nm	0.46	0.2
1at% Nd:YAG n=1.81633[30] at 633nm	4	2	Sapphire n=1.76[31] at 800nm	0.46	0.5

Table 4.2 Details of the Nd:YAG on sapphire contact bonded waveguides

Two samples were fabricated by direct bonding and had Nd:YAG core sizes of 4μm and 8μm. The high optical quality of these guides was confirmed by Ti:sapphire end pumping and measuring the threshold versus the output coupling to determine the propagation losses at 1.064μm [25].

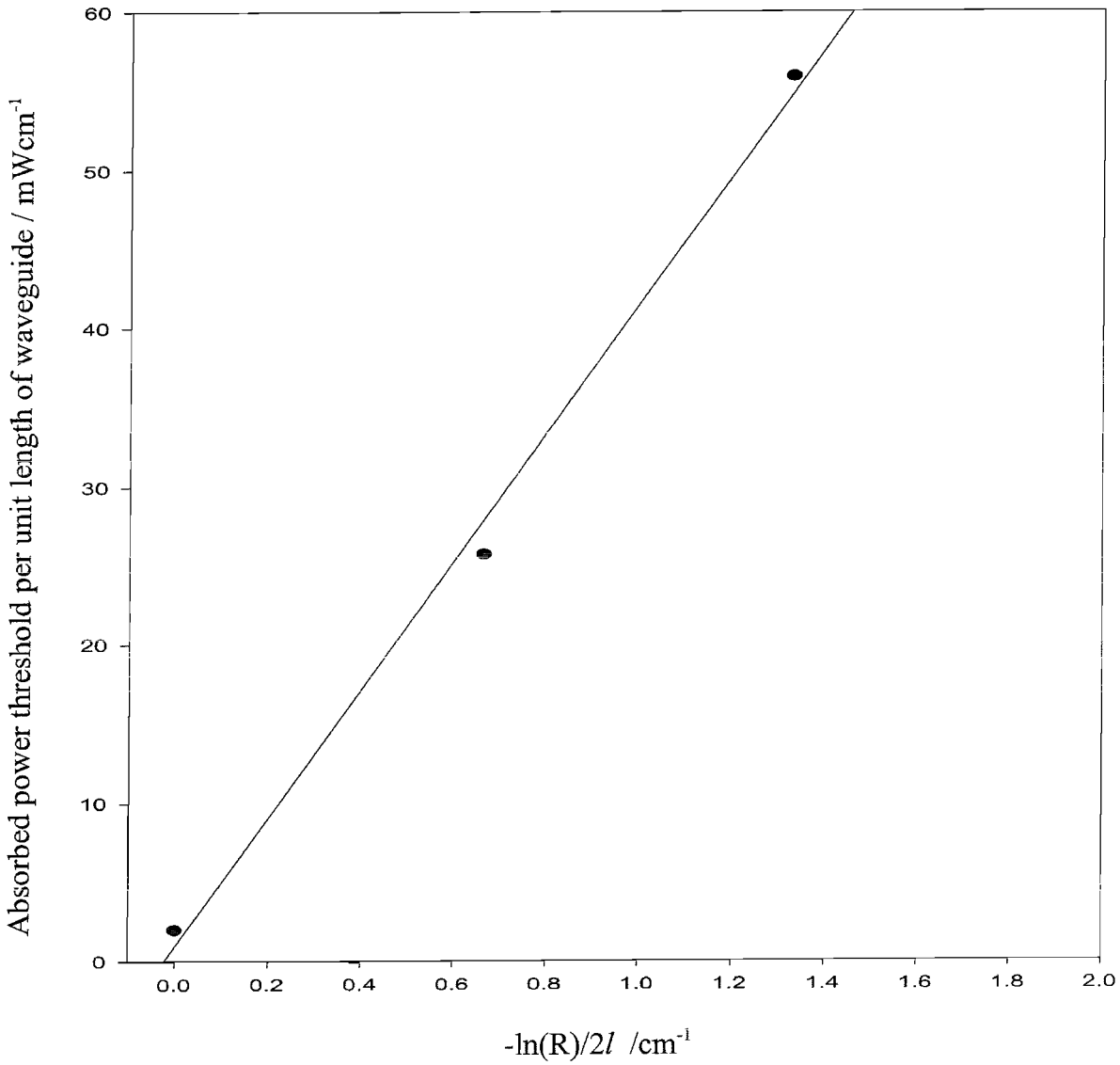

Figure 4.14 Modified Findlay-Clay plot for the 8μm Nd:YAG/sapphire waveguide.

The modified Findlay-Clay plots are shown in figures 4.14 and 4.15 for the 8μm and 4μm guides respectively. The position of the intercept on the x-axis gives the value of the loss coefficient. The losses were measured to be ~0.2dB/cm for the 8μm guide and ~0.5dB/cm for the 4μm guide.

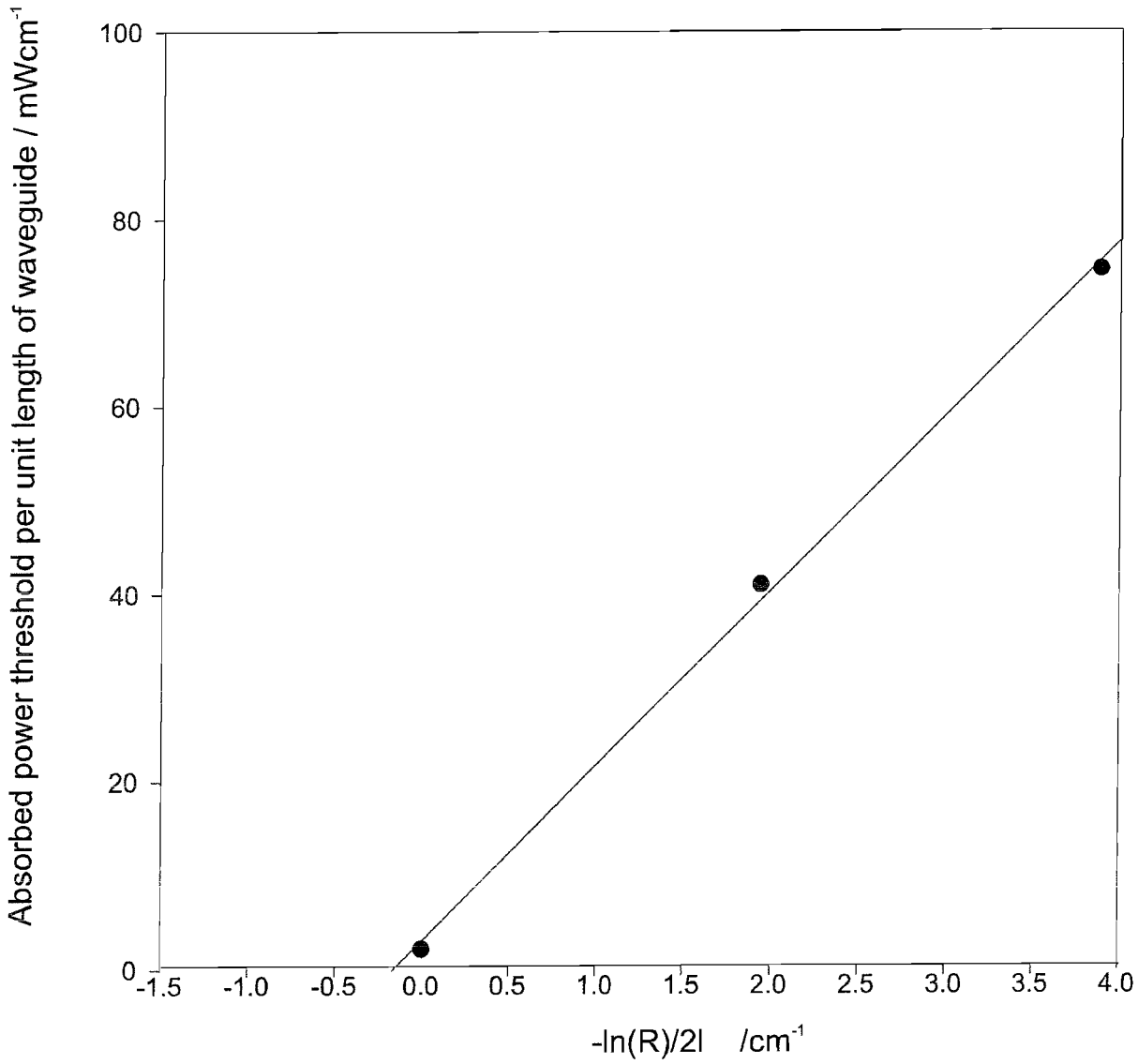

Figure 4.15 Modified Findlay-Clay plot for the 4μm Nd:YAG/sapphire waveguide.

These waveguides were used in high-power experiments, with diode-bar pumping, details of which will be given in chapter 6. Other waveguide structures fabricated by direct bonding and using the same material combination of YAG and sapphire will be discussed in chapter 7.

4.4.9 Direct bonded waveguides – Summary

This section has described the fabrication and lasing characteristics of waveguides produced by direct bonding. In summary, it has shown direct bonding to be a very

attractive method for fabricating low loss waveguides, with spectral characteristics identical to bulk material. Efficient laser action has been observed from the waveguides, which typically have propagation losses of <1dB/cm. The technique has the ability to produce waveguides with high numerical apertures, and also to successfully bond very dissimilar materials, the most extreme example here being a YAG crystalline laser host bonded to a glassy substrate.

Planar thin films appear to be particularly attractive for high power devices due to the good thermal properties of the planar slab geometry and power scalability. Relevant thermal issues will be discussed in the next chapter. The aim now is to use the planar waveguides that have been described here with high power diode-bar pumping, to realise highly compact lasers and amplifiers capable of multi-Watt output powers. Work towards this goal is discussed in chapter 6.

4.5 References

[1] A.Faulstich, H.J.Baker, D.R.Hall, Opt. Lett., **21**, pp.594-596 (1996)

[2] D.P.Shepherd, C.L.Bonner, C.T.A.Brown, W.A.Clarkson, A.C.Tropper, D.C.Hanna, H.E.Meissner, Opt. Commun., **160**, pp.47-50 (1999)

[3] C.L.Bonner, T.Bhutta, D.P.Shepherd, A.C.Tropper, D.C.Hanna, H.E.Meissner, in *'Technical Digest of Conference on Lasers and Electro-Optics'*, 1999, paper CThD6

[4] C.L.Bonner, A.A.Anderson, R.W.Eason, D.P.Shepherd, D.S.Gill, C.Grivas, N.Vainos, Opt. Lett., **22**, pp.988-990 (1997)

[5] C.T.A.Brown, C.L.Bonner, T.J.Warburton, D.P.Shepherd, A.C.Tropper, D.C.Hanna, H.E.Meissner, Appl. Phys. Lett., **71**, pp.1139-1141 (1997)

[6] C.L.Bonner, C.T.A.Brown D.P.Shepherd, W.A.Clarkson, A.C.Tropper, D.C.Hanna, B.Ferrand, Opt. Lett., **23**, pp.942-944 (1998)

[7] G.K.Hubler, Mater. Res. Bull., **17**, pp.26-27 (1992)

[8] D.S.Gill, A.A.Anderson, R.W.Eason, T.J.Warburton, D.P.Shepherd, Appl. Phys. Lett., **69**, pp.10-12 (1996)

[9] A.A.Anderson, R.W.Eason, M.Jelinek, L.M.B.Hickey, C.Grivas, C.Fotakis, K.Rogers, D.Lane, in *'Technical Digest of Conference on Lasers and Electro-Optics – Europe,'* 1996, paper CTuG8

[10] M.Ezaki, M.Obara, H.Kumagai, K.Toyoda, Appl. Phys. Lett., **69**, pp.2977-2279 (1996)

[11] S.J.Field, D.C.Hanna, A.C.Large, D.P.Shepherd, A.C.Tropper, P.J.Chandler, P.D.Townsend, L.Zhang, Opt. Comm., **86**, pp.161-166 (1991)

[12] S.J.Field, D.C.Hanna, D.P.Shepherd, A.C.Tropper, P.J.Chandler, P.D.Townsend, L.Zhang, Opt. Lett., **17**, pp.52-54 (1992)

[13] M.Shimokozono, N.Sugimoto, A.Tate, Y.Katoh, M.Tanno, S.Fukuda, T.Ryuoh, Appl. Phys. Lett., **68**, pp.2177-2179 (1996)

[14] J.T.Cheung, J.Horwitz, Mater. Res. Bull., **27**, pp.30-36 (1992)

[15] J.T.Cheung in *'Pulsed Laser Deposition of Thin Films,'* D.B.Chrisey and G.K.Hubler eds., pp.1-22, John Wiley and Sons Publishers (1994)

[16] A.A.Anderson, *'Crystalline Planar Waveguide Lasers Fabricated by Pulsed Laser Deposition'*, PhD Thesis, University of Southampton, pp. 13-22 and pp.63-81 (1998)

[17] I.Chartier, B.Ferrand, D.Pelenc, S.J.Field, D.C.Hanna, A.C.Large, D.P.Shepherd, A.C.Tropper, Opt. Lett., **17**, pp.810-812 (1992)

[18] D.L.Wood, K.Nassau, Appl. Opt., **29**, pp.3704-3707 (1990)

[19] A.A.Anderson, C.L.Bonner, D.P.Shepherd, R.W.Eason, C.Grivas, D.S.Gill, N.Vainos, Opt. Comm., **144,** pp.183-186 (1997)

[20] R.Ulrich and R.Torge, Appl. Opt., **12**, pp.2901-2908 (1973)

[21] J.Geusic, H.M.Marcos, L.G.Van Uitert, Appl. Phys. Lett., **4**, pp.182-184 (1964)

[22] Kh.Bagdasarov, G.A.Bogomolova, M.M.Gritsenko, A.A.Kaminskii, A.M.Kevorkov, A.M.Prokhorov, S.E.Sarkisov, Sov. Phys. Dokl., **19**, pp.353 (1974)

[23] B.Comaskey, B.D.Moran, G.F.Albrecht, R.J.Beach, IEEE J. Quantum Electron., **QE-31**, pp.1261 (1995)

[24] M.Allibert, C.Chatillon, J.Mareschal, F.Lissalde, J. Crystal Growth, **23**, 289 (1974)

[25] D.Findlay, R.A.Clay, Phys. Lett., **20**, pp.277-278 (1966)

[26] W.A.Clarkson, D.C.Hanna, J. Modern Optics, **36**, pp.483-498 (1989)

[27] J.Haisma, B.A.C.M.Spierings, U.K.P.Biermann, A.A. van Gorkum, Appl. Opt., **33**, (1994)

[28] O.M.Akselsen, J. Mat. Sci., **27**, pp.569-579 (1992)

[29] K.Eda, M.Sugimoto, Y.Tomita, Appl. Phys. Lett., **66**, pp.827-829 (1995)

[30] D.Pelenc, *'Guide d'onde laser en Nd:YAG et Yb:YAG per E.P.L.'*, PhD Dissertation, Département Optronique du LETI, C.E.N.G. 85X 38041 Grenoble, France (1992)

[31] A.C.DeFranzo, B.G.Pazol, Appl. Opt., **32**, p.2224 (1993)

Chapter 5 High intensity, high-power pumping of Nd:YAG

5.1 Introduction

This chapter describes some of the problems that can be encountered when pumping the very confined volume of a planar waveguide with the high average power of a diode-bar. Section 5.2 gives details of a model and experimental investigations into the effects of upconversion and bleaching of the absorption. It is shown that high pump intensities, such as those found in diode-bar pumped waveguides, can make these effects significant, leading to reduced gain and increased thermal input. This effect adds to the normal thermal-loading due to the difference in energy between the pump and the signal photons being taken up by non-radiative decay, as illustrated in chapter 2, figures 2.4 and 2.5. The thermal load can have detrimental effects on the laser material and its output such as increased thermal population of the lower laser levels, lensing, aberrations, birefringence and even stress induced fracture. These effects illustrate the importance of thermal load considerations and in section 5.3 the thermal management capabilities of a planar waveguide are assessed and compared with those of bulk rod and slab-shaped gain media.

5.2 Upconversion and bleaching in a Nd:YAG amplifier

5.2.1 Introduction and theoretical background

In laser devices operating on the four-level 1.064μm transition in Nd:YAG, the population density of the upper laser level ($^4F_{3/2}$) is usually clamped at a relatively low value. The spectroscopic parameters for the transition, such as lifetime and cross sections are well known under these conditions and the behaviour of the device can be well predicted. However, the advent of high-power diode-bars combined with beam-shaping techniques, and developments in rare-earth-doped planar waveguides, increasingly leads to gain materials being pumped at excitation intensities in the region of, or greater than, the saturation intensity. Under these conditions device performance is less predictable.

Recent reports of intensely-pumped devices include; a Nd:YAG bulk laser pumped by a beam-shaped 20W diode-bar with a beam area of 170 x 155 μm^2 [1], and a planar waveguide Nd:YAG amplifier pumped by a 1.2W diode array with spot sizes of 2 x 148 μm^2 [2]. This was a high small-signal gain amplifier where there was no clamping of the upper laser level population. In both of these examples the intensity greatly exceeds the pump saturation intensity of $2x10^8 W/m^2$. This demonstrates that it is now possible to achieve a very high inverted population. Other devices with intense pumping regimes include, quasi-three-level lasers where the upper laser level population must at least match that of the thermally-populated lower laser level, and also Q-switched lasers where a high inversion density may occur.

An intense pumping regime brings about new effects which may change the system parameters required for optimum performance. For instance, it would seem that intense pumping allows the use of more heavily doped samples because the self-quenching of Nd^{3+} is eliminated as the ground state is emptied. Face-pumped slab devices could then take advantage of this property. However, at high inversion densities laser performance can in fact decrease because of upconversion mechanisms such as energy-transfer.

These mechanisms have already been studied in Nd-doped glasses [3], Nd:YLF [4] and the relevant upconversion mechanisms in various other Nd-doped crystals, including YAG, have been identified by Guyot et al [5]. These investigations show that Auger energy-transfer upconversion from the $^4F_{3/2}$ upper laser level is the main loss mechanism.

The Auger process is illustrated in figure 5.1. It was investigated with increasing dopant concentration in Nd- doped YAG using spectroscopic techniques by Dr. Stephan Guy at University of Lyon.

Experiments on the impact of the loss mechanism on an actual device, namely a Nd:YAG amplifier, were carried out at the ORC, University of Southampton.

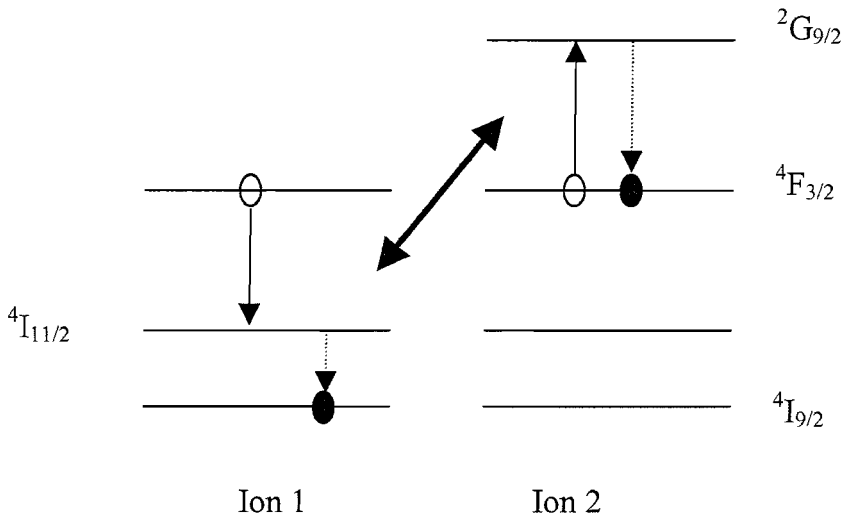

Figure 5.1 Schematic diagram showing Auger upconversion

Auger upconversion starts with two neighbouring ions in the metastable upper laser level $^4F_{3/2}$. One ion drops down to the ground state, via the $^4I_{11/2}$ level, and transfers its energy to its neighbour which is then promoted to a higher excited state. In turn this excited ion relaxes down to the $^4F_{3/2}$ level mostly via multi-phonon emission. In this way the Auger process leads both to a reduction in the available gain and to heating of the host lattice via non-radiative decay. Therefore, accurate knowledge of the Auger rate is desirable in order to appropriately design intensely-pumped systems. Without an appropriate design device performance will be degraded by the upconversion process reducing optical efficiency and increasing the thermal load.

5.2.2 Rate equation model

The rate equations used to model the Auger process in the Nd^{3+} ion are developed here. The derived upper laser level population, N_2, is then used in section 5.2.3 to analyse the performance of the Nd:YAG amplifier.

The Auger process described in figure 5.1 can be summarised as,

$$^4F_{3/2} + {}^4F_{3/2} \rightarrow {}^4I_{11/2} + {}^4G_{9/2} \rightarrow {}^4I_{9/2} + {}^4F_{3/2}$$

The other energy-transfer process that is known to occur in Nd^{3+} is cross-relaxation [6]. This process is shown in figure 5.2.

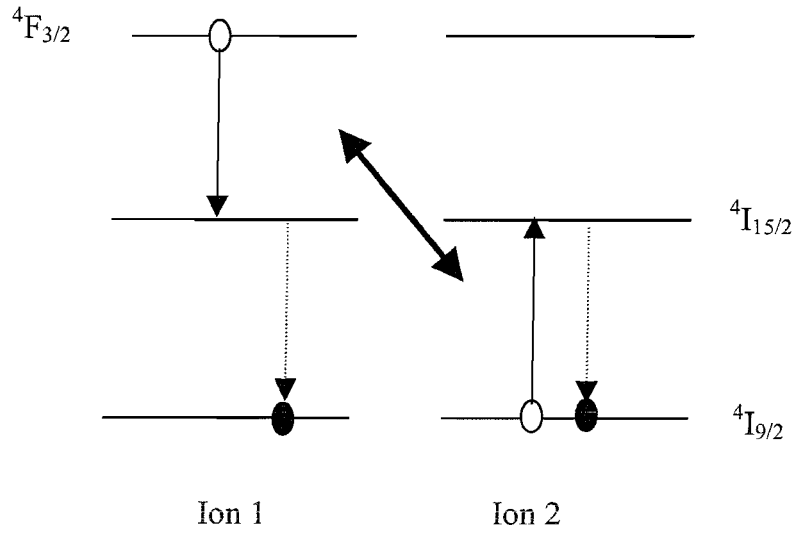

Figure 5.2 Schematic diagram of the cross relaxation process in Nd^{3+}

Cross relaxation involves part of the excitation energy of one ion being transferred to an unexcited ion, so that they both find themselves in the $^4I_{15/2}$ level. The ions then dissipate the shared energy via fast multi-phonon relaxation to the ground-state level:

$$^4F_{3/2} + {}^4I_{9/2} \rightarrow 2\ {}^4I_{15/2} \rightarrow {}^4I_{9/2} + {}^4I_{9/2}$$

As the multi-phonon decay rates are much faster than the other mechanisms, it is possible to model the system using only the upper laser level $^4F_{3/2}$, and the ground state level $^4I_{9/2}$, as the other levels are not occupied for a significant time. The rate equation for the system can be written as:

$$dN_2 / dt = W_p N_1 - N_2 W_{rad} - W_{cr} N_2 N_1 - W_{up} N_2 N_2 \qquad 5.1$$

$$N_1 + N_2 = 1 \qquad 5.2$$

where N_1 and N_2 are the $^4I_{9/2}$ and $^4F_{3/2}$ population density fractions, W_{upc}, W_{cr} and W_{rad} are respectively, the Auger upconversion, cross-relaxation and radiative relaxation rates, $W_p = \sigma_a I_p / h\nu_p$ is the pump rate, σ_a is the pump absorption cross-section, I_p is the incident pump intensity, and ν_p is the pump frequency. Combining 5.1 and 5.2 leads to:

$$dN_2 / dt = \tau^{-1} I_p / I_{p,sat} - \tau^{-1}(1 + I_p / I_{p,sat})N_2 - W_{upc} N_2 N_2 \qquad 5.3$$

where $\tau = (W_{rad}+W_{cr})^{-1}$ is the lifetime at low excitation levels, $W_{upc} = W_{up}-W_{cr}$ is the net upconversion rate, and $I_{p,sat} = h\nu_p/\sigma_a\tau$ is the pump saturation intensity (for which a factor of two reduction in the absorption occurs). This equation is the basis for the modelling of Nd^{3+} devices here. The population density of the laser level under CW excitation is obtained by setting d/dt=0.

Stimulated emission has not been taken into account (although it could be added into the equation), because the main investigation here is of small-signal gain. In a steady state regime, the upper laser level population versus the pump power is given by setting the right hand side of equation 5.3 equal to zero. This gives,

$$N_2 = \frac{-(1+p) + \sqrt{(1+p)^2 + 4p\tau W_{upc}}}{2\tau W_{upc}} \qquad 5.4$$

where $p = I_p/I_{p,sat}$. This expression will be used to analyse results from the Nd:YAG amplifier in section 5.2.3 but two important points can be made here. Firstly, the relevant intensity parameter is its ratio to the saturation intensity; secondly the key parameter required in the study of upconversion effects is the τW_{upc} product. This represents the ratio between the net upconversion rate and the downconversion rate. When τW_{upc} tends to zero the upper level laser population, N_2, is given by the expected expression [7]:

$$N_2 = \frac{I}{I_{p,sat} + I} \qquad 5.5$$

5.2.3 Amplifier experiment

This section describes an experimental illustration of the effect of upconversion on small-signal gain in a Nd:YAG amplifier.

The ideal small-signal gain of a four-level amplifier can be found using a rate equation method similar to that used in chapter 2 [7]. Where, for a laser at threshold, the gain in the cavity (the small-signal gain) is equal to the losses. In this ideal, weak power excitation case the small-signal gain is proportional to the absorbed power and neither upconversion nor saturation effects occur.

The aim of the amplifier experiment here is not to maximise the amplifier performance, but instead to observe the effect of upconversion on small-signal gain under intensely-pumped conditions. With this goal in mind, steps were taken to ensure that the signal remained small, gain saturation did not occur, and the only loss in the sample was due to the energy-transfer upconversion (Auger) mechanism. The experimental set up used is shown in figure 5.3.

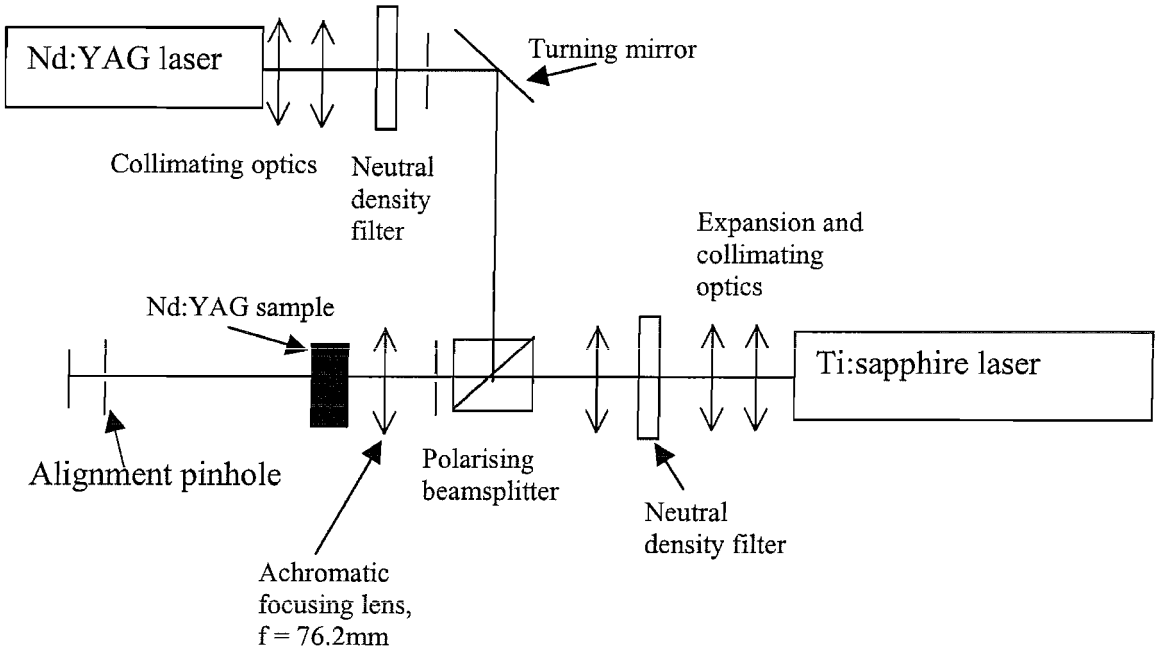

Figure 5.3 Experimental set-up for the Nd:YAG amplifier experiment

The 1 at.% Nd:YAG bulk crystal used as the gain medium was 1mm long, 4mm in diameter, uncoated and end-polished. It was end-pumped by a Ti:sapphire laser operating at 807nm and the signal was provided by a diode-pumped Nd:YAG laser at 1.064μm.

Amplification requires that the signal and pump beams travel with good spatial overlap through the sample. This was achieved by designing the experiment such that the beams were well collimated within the sample. The focusing optics used to achieve collimated beams of the required widths are shown in figure 5.3. The pump and signal beams were focused at the same point in the sample by an achromatic lens. Spot sizes were measured using a Merchantek Beamscope placed directly in the path of the beam and at various points along it. The variation of spot size with position revealed that both beams had confocal parameters approaching 1cm. The beams were therefore well collimated over the 1mm sample length and waist sizes of 40μm and 28μm were measured for the Nd:YAG and Ti:sapphire beams respectively. The final adjustment of the beam overlap was achieved by optimising the gain observed in the amplifier. However after this optimisation the angle between the beams was observed to be 2.3°. This illustrated how difficult it was to achieve a good overlap in this experiment.

The intensity at which signal saturation occurs is given by $I_{s,sat}=h\nu_s/\sigma_e\tau$ [7]. Taking the widely used value of τ(230μsecs) and cross-section, σ_e ($3.5\times10^{-23}m^2$) for the 1at.% Nd-doped YAG sample gives $I_{s,sat}$ =2.3kW/cm^2. The spot sizes achieved here result in a saturation power of 58mW. Neutral density filters were placed in front of the signal beam to give <2mW input at the sample, thus maintaining an unsaturated signal. Thermal effects were minimised by mounting the sample on a well conducting aluminium mount. For the pump absorption, saturation is calculated to occur at 17kW/cm^2 (with $\sigma_a = 6.2\times10^{-24}m^2$), corresponding to a power of 210mW with the spot sizes chosen here. Under intense pumping, up to twice the pump saturation power, there was no evidence of any thermally-induced line shift in the Nd:YAG fluorescence spectrum previously reported by Kushida [8], and others. This was investigated by collecting and examining the Nd:YAG fluorescence at 90° to the pump beam. The fluorescence was imaged into an OMA 2000 triple grating

spectrograph, with a resolution of 0.3nm, and the spectra at low and high pump powers were found to be identical. This verifies good thermal management of the sample within the set up.

Under the conditions described above yellow upconverted light was clearly visible in the sample. Fluorescence at wavelengths longer than 0.9μm was observed using a large area silicon detector linked to an oscilloscope with colour filters used to block the residual pump light and any shorter wavelength fluorescence. The position of the sample relative to the achromatic lens was optimised for minimum pump absorption (i.e. the position of highest saturation of the absorption and hence the most intense-pumping). The small-signal amplification was then measured by comparing the transmitted signal level with and without the pump beam and taking care to account for any residual pump light and spontaneous emission. This was measured using a Newport power meter placed after the sample, and the signal and pump beams were blocked as necessary.

The rate equation model outlined in section 5.2.2 was used here in a numerical analysis of this particular amplifier set up. The gain exponent, g_0, achieved in the sample can be obtained from the waveguide laser theory in chapter 2.

$$g_0 = \int \sigma_e n_2 \phi dV \qquad 5.6$$

Here ϕ represents the signal distribution (normalised with respect to cross-sectional area). The parameter n_2 refers to the actual population density as opposed to the fractional densities discussed earlier (section 5.2.2) when developing rate equations for the upconversion process, ($n_2=N_2 n_{tot}$, where n_{tot} is the total population density and $\Delta n= (n_2-n_1) = (N_2-N_1)n_{tot}$). The signal and pump beams are assumed not to diverge as the beams in the experiment were designed to be collimated in the sample. The value of the inverted population $n_2(x,y,z)$ was determined from the pump intensity $I_p(x,y,z)$. The relationship between n_2 and I_p is given by equation 5.4, which takes the Auger effect into account.

The pump intensity distribution at the input face of the crystal is Gaussian and, assuming no divergence, $I_p(x,y,z)$ can be written as:

$$dI_p(z)/dz = -(n_{tot} - n_2)\sigma_a I_p(z) \qquad 5.7$$

To calculate the gain exponent g_0, the cross-sectional area was sub divided into 100x100 cells from $-3w_p$ to $3w_p$, where w_p was the pump beam waist. The result of the calculation was not significantly changed by increasing the number of cells suggesting that this is an accurate analysis. For each cell, the actual intensity over the sample length was computed using 5.7 where $n_2(I_p)$ was given by equation 5.4.

Thus with a knowledge of the intensity distribution over the sample, the integration 5.6 was carried out.

The plotted experimental data points were a close fit to the gain curve generated by this model based on upconversion losses in the sample (equation 5.6), and also accounting for bleaching of the absorption (see details in the next section). Figure 5.4 shows the data points and some predicted curves for various different Auger upconversion rates.

A factor of 1.4 was required to fit the experimental data to the initial linear part of the theoretically calculated plot in figure 5.4. This may perhaps, in part, correspond to the 10% of pump photons reported to be absorbed by dead sites [9] in Nd:YAG. The scaling factor also accounted for a decrease in beam overlap which can be attributed to the difficulty in achieving perfect beam alignment. The value of the upconversion product, τW_{upc}, deduced from this amplifier experiment is $\tau W_{upc}=2\pm1$.

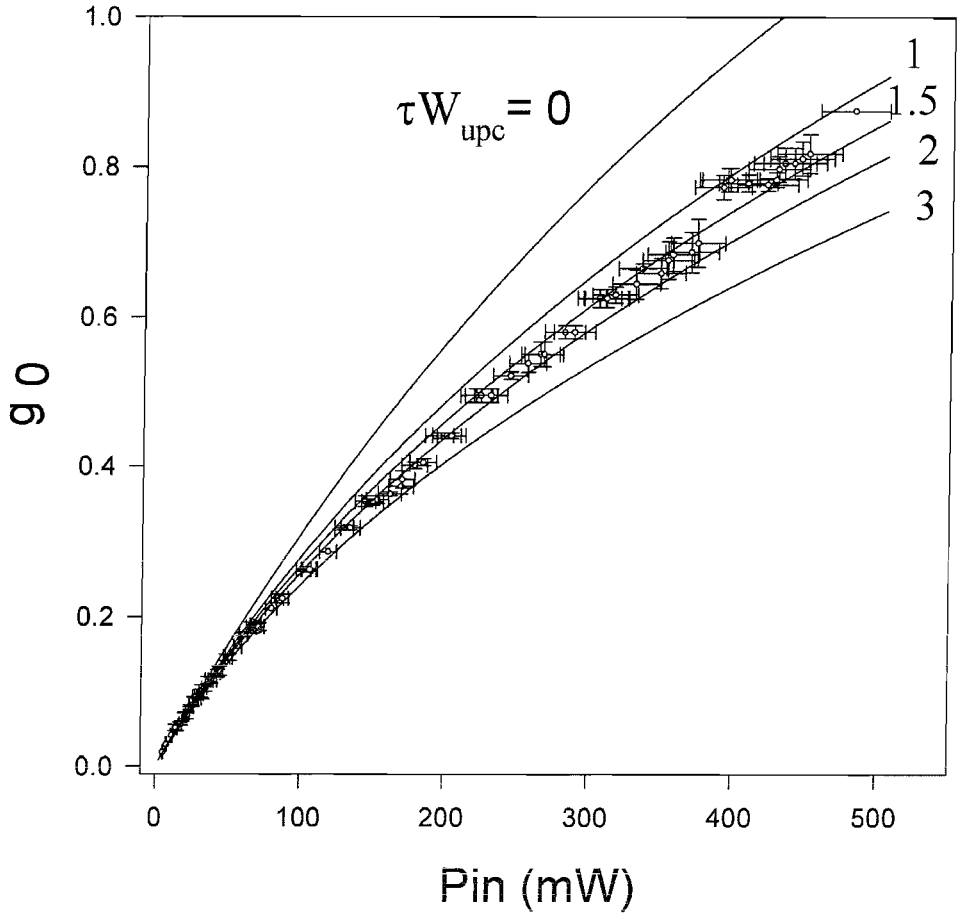

Figure 5.4 A graph of non-normalised gain exponent versus incident pump power forthe Nd:YAG amplifier. Symbols are experimental points. Solid lines are theoretical calculations with different rates of upconversion

Auger upconversion was separately investigated using spectroscopic techniques with thin films of Nd-doped material by Dr. Stephan Guy at the University of Lyon. A reduction in fluorescence lifetime was observable at high pumping intensities due to upconversion. These decay characteristics were used to determine the τW_{upc} product for different neodymium doping concentrations [10], giving a value of, $\tau W_{upc}=1.5\pm0.3$ for 1 at.% Nd:YAG (corresponding to an Auger upconversion rate of $\sim 7\times10^{-3}s^{-1}$ $(6.5\times10^{-3}\pm1.3\times10)s^{-1}$), in very good agreement with the value of τW_{upc} found from the amplifier experiment. These results allow the following study of the effect of upconversion on an end-pumped Nd:YAG amplifier to be carried out with some degree of confidence.

5.2.4 Modelling study

This section presents a modelling study of a typical end-pumped Nd:YAG small-signal amplifier. The effect of upconversion processes that reduce the small-signal gain and add to the heating within the crystal are taken into consideration. The computer modelling shows a deviation from the ideal case which comes both from upconversion, and from a change in the spatial distribution of the inversion due to the saturation of the absorption.

The upconversion rate measured from the amplifier experiment (section 5.2.3) and the spectroscopic study of fluorescence decay [10] is used here to quantify the impact of the Auger process on the Nd:YAG system. The rate equation model described in section 5.2.2 has given an expression for the inverted population versus the excitation intensity (equation 5.4). The use of the experimentally determined τW_{upc} parameter substituted in equation 5.4 leads to the actual inverted population for a given intensity.

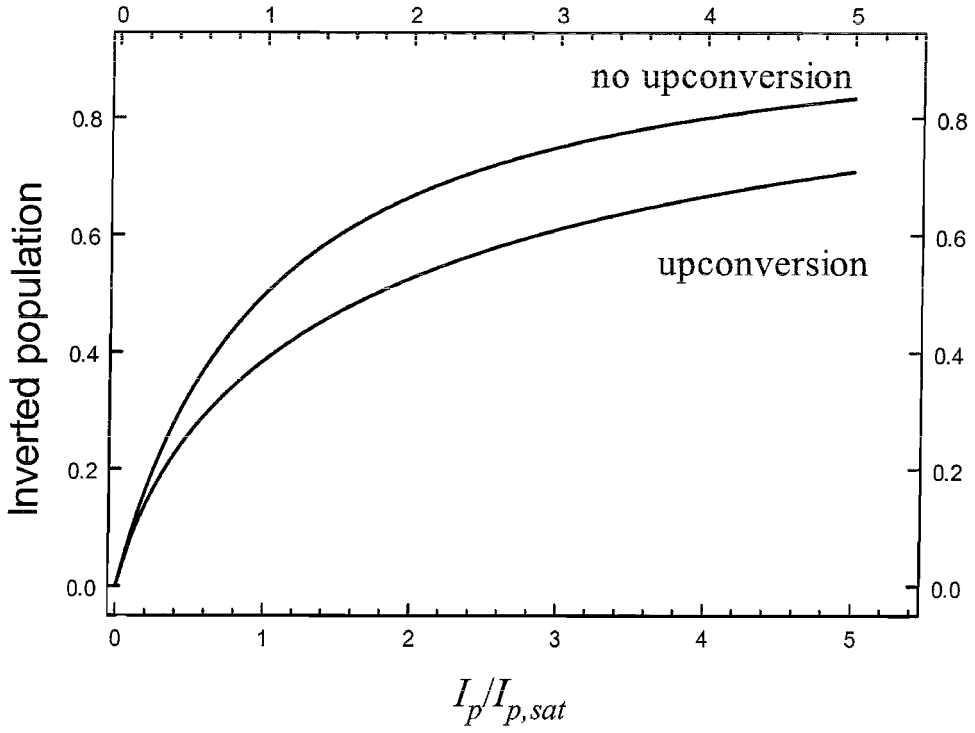

Figure 5.5 Computed plot of the variation of inverted population fraction versus normalised incident intensity

A plot of the inverted population fraction versus intensity is shown in figure 5.5 for a 1at.% Nd- doped sample, i.e. using τ=230μs and τW_{upc}=1.5. Also shown for comparison is a simulated curve (upper curve) with the upconversion rate set to zero. The figure shows that Auger upconversion reduces the inverted population, and should be taken into consideration at incident intensities greater than ~$0.2I_{p,sat}$. $I_{p,sat}$ is a spectroscopic constant dependent upon the pumping scheme used; its value is 17 and 43 kW/cm^2, for Ti:sapphire and diode-pumping respectively. The different values of $I_{p,sat}$ are due to the different pump absorption efficiencies. The absorption length of the Nd:YAG material with Ti:sapphire pumping and with diode-bar pumping was measured to be ~1mm and ~3mm respectively.

A change in the spatial distribution of the inversion, and hence the gain, as a function of pump intensity is important in understanding the behaviour of end-pumped devices. Some numerical examples will be described later in this section to illustrate this point. However, an example can be given now of the way that the spatial distribution of the inversion can change under pumping saturation.

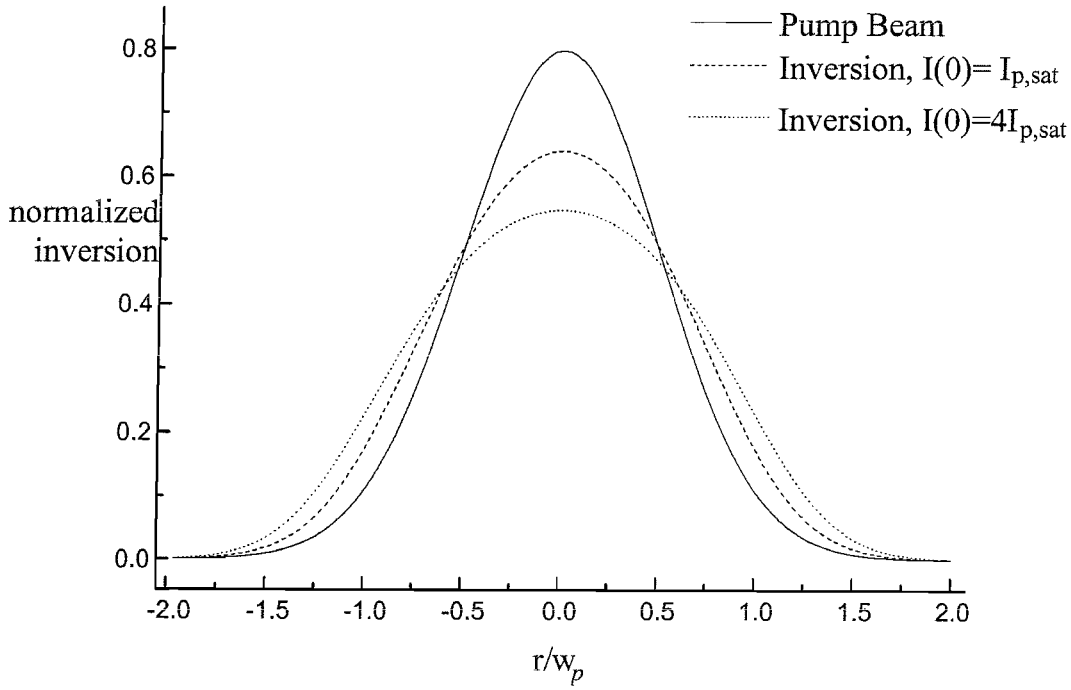

Figure 5.6 Plots of the population-inversion density, (normalised to the same unit area), as a function of the radial co-ordinate for different pumping intensities

Figure 5.6 shows the spatial distribution of inversion at the input face, for different values of the intensity at the centre of a circular Gaussian pump beam. It shows that the saturation of the pump leads to a broadening of the inverted distribution. The broadening becomes more pronounced as the pump intensity increases, and due to this behaviour the pumped area is effectively larger. This results in a reduction in the small-signal gain.

In order to calculate the gain for typical end-pumped devices, the points illustrated in figures 5.5 and 5.6 have to be considered. Equation 5.4 is used which takes into account the upconversion, and then the actual propagation of the beam through the sample is calculated. The model presented here is based on the procedure and results taken from the amplifier experiment (section 5.2.3).

Gaussian collimated beams are assumed to propagate through the sample described by equation 5.7, and the inverted population versus the intensity is obtained from the rate equation solution 5.4. The spectroscopic characteristics of 1at.% Nd:YAG are used for a sample length equal to two absorption lengths, giving an 85% unsaturated absorption, typical of many actual devices.

The figures and modelling are kept quite general with P_{abs}/P_{sat} used as a pumping parameter. P_{sat} is the incident power at which the saturation intensity is achieved in the centre of the pump beam, so it contains information about the pumping source and spot sizes. The absorbed power is normalised, rather than the incident power, as in the ideal case the gain exponent is linear with respect to P_{abs}. This choice of pump power normalisation makes the reduction in gain, due to upconversion and a changing inversion profile, clearer.

The variation of the calculated gain versus the absorbed power is plotted in figure 5.7, with the pump and signal beam set to have the same size.

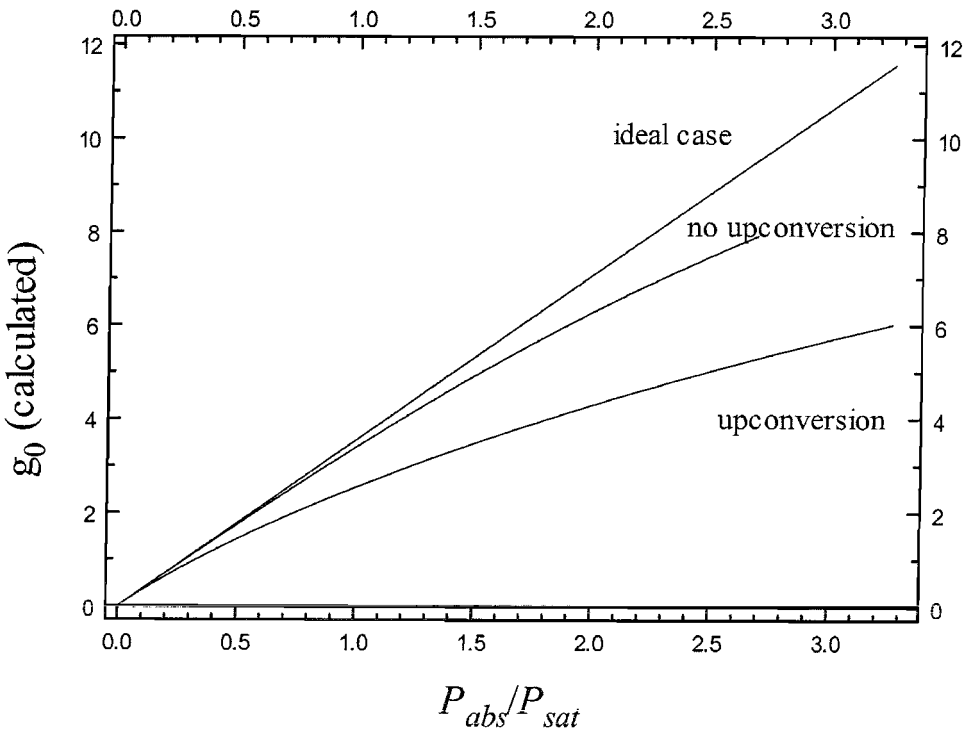

Figure 5.7 Computed gain exponent versus normalised absorbed pump power for three different scenarios

To further understand the gain behaviour, three gain curves were calculated and plotted in figure 5.7 for the following three scenarios. The lowest curve in figure 5.7 shows the effect of both upconversion and the bleaching of the pump absorption, the middle curve shows no upconversion effects but still shows the effects of bleaching, and lastly the highest curve (an ideal case) with no upconversion and no bleaching of the beam is shown. In a situation where no upconversion or bleaching occurs the population, and thus the small-signal gain exponent, will be linear with respect to absorbed pump power (as seen in equation 5.3). From equation 5.6 and also from the waveguide laser threshold equation in chapter 2 (equation 2.53), the small-signal gain exponent can be written as:

$$g_0 = \frac{2\sigma_e \tau P_{abs}}{\pi h \upsilon_p (w_p^2 + w_L^2)} \qquad 5.8$$

Here $P_{abs} = P_{in}(1-e^{-\alpha l})$, where P_{in} is the launched power.

The threshold equation (2.53) is rearranged and the losses (including the waveguide propagation loss exponent L_{guide}) replaced with g_0, (gain exponent) leading to equation 5.8. The expression gives the gain achieved from weak power excitation when neither upconversion nor saturation phenomenon occur, and is what we call the 'ideal' case. This equation has been widely used in many papers [2], and its useful limit is now discussed.

Figure 5.7 shows that the actual gain deviates significantly from the ideal curve as soon as absorbed powers exceed ~$0.5P_{sat}$. When there is no upconversion present, the gain is reduced by more than 10% as soon as the absorbed power exceeds $1.8P_{sat}$. In this case the reduction occurs due to the change in the distribution of the inversion. In terms of equation 5.8, the change means the pump beam seems bigger (as shown by the broadening in figure 5.6). When this broadening is included in equation 5.8 it results in a decrease in the overlap integral and so a decrease in the gain.

The overlap behaviour can be investigated to show the deviation between the actual gain and the ideal case for different ratios of w_p/w_L. The results are shown in figure 5.7, and the graphs show the bigger the pump beam size, the bigger the deviation.

As w_p/w_L approaches zero (delta-function pumping), the overlap integral is not significantly affected by a change in the inversion distribution which remains like a delta function compared to the signal. In this case the reduction is only due to upconversion and for $P=P_{sat}$ a reduction in the gain exponent of about 20% is obtained compared to the ideal case.

However in the other extreme situation, when the pump distribution is much wider than the signal distribution, the reduction in gain is strong because all the gain occurs in the centre of the beam. Now for $P=P_{sat}$ the reduction in gain is about 40%, i.e half the gain reduction arises from upconversion and half from changing the inversion distribution.

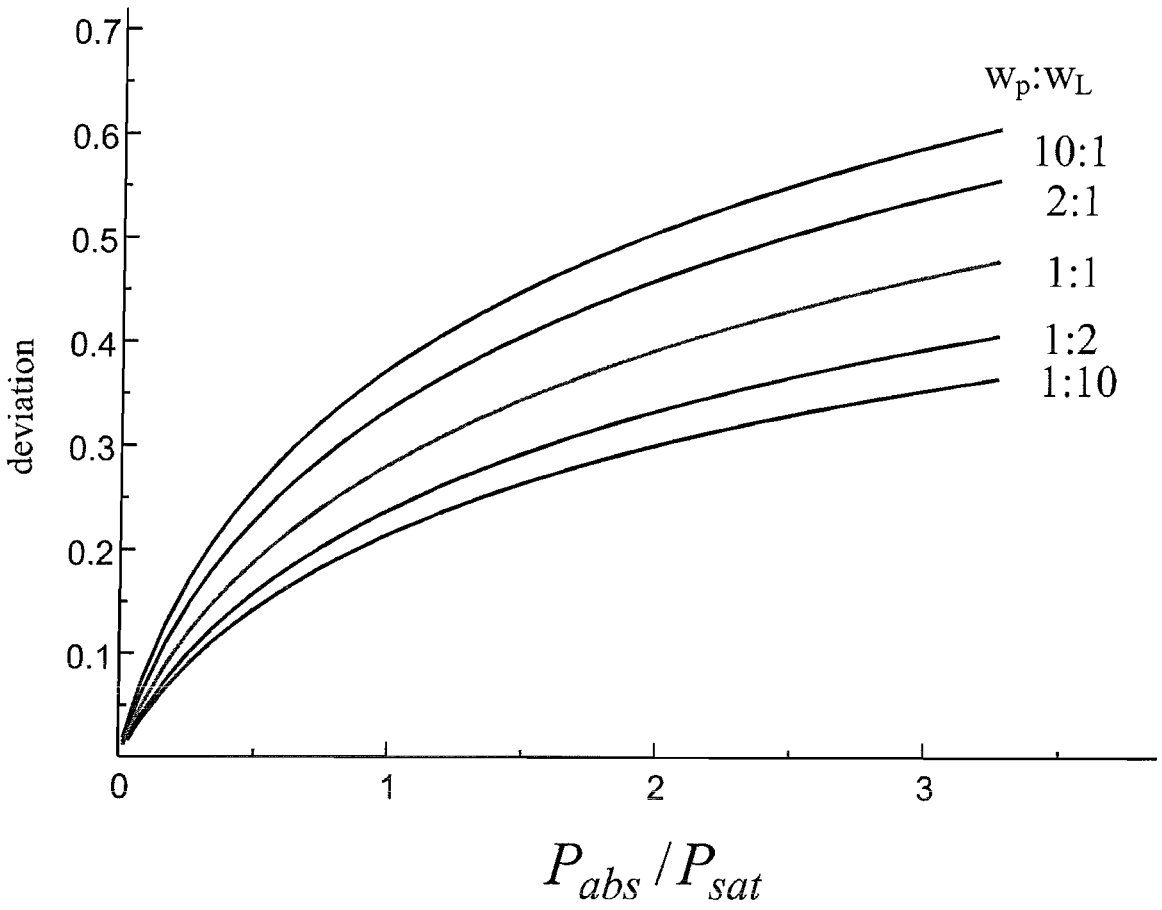

Figure 5.8 The deviation of the gain from the ideal case versus normalised absorbed power, for different ratios of w_p/w_L

It should be noted that this has implications for the thermal loading within the YAG host crystal. The main processes leading to heat loading in Nd:YAG materials are: (1) the quantum defect between the pump photons and the emitted photons (either emitted spontaneously or via stimulated emission), (2) the multi-phonon decays involved in the upconversion process, (3) the multi-phonon decays that follow from the cross-relaxation process, and (4) it has also been suggested that there is some nonradiative decay from the $^4F_{3/2}$ level, corresponding to typically about 10% of the total spontaneous decay [9]. This last process has not been included in the estimates that follow. The transition rates and the amount of heat produced per event decide which process has the dominant heating effect. As already described, the rates will depend on the size of the inversion density and this is largely dependent on the type of device. For instance, very different inversion densities would be expected in a low-loss CW laser compared to a Q-switched laser, or a high small-signal gain amplifier compared to an amplifier operating in the saturated regime.

For the comparison here, the heating effect due to the quantum defect in a diode-pumped Nd:YAG laser (about 25% of the incident pump power) is plotted and compared to the heating effect expected from the upconversion process assuming no clamping of the population. The upconversion heating depends on the upconversion rate over the whole sample. In the Auger process each upconversion event (equation 5.4) results in a quantum of heat equal to the energy of the laser level, ΔE. Therefore the heating resulting from upconversion is:

$$H_{upc} = W_{upc} \int n_2^2 dV \Delta E \qquad 5.9$$

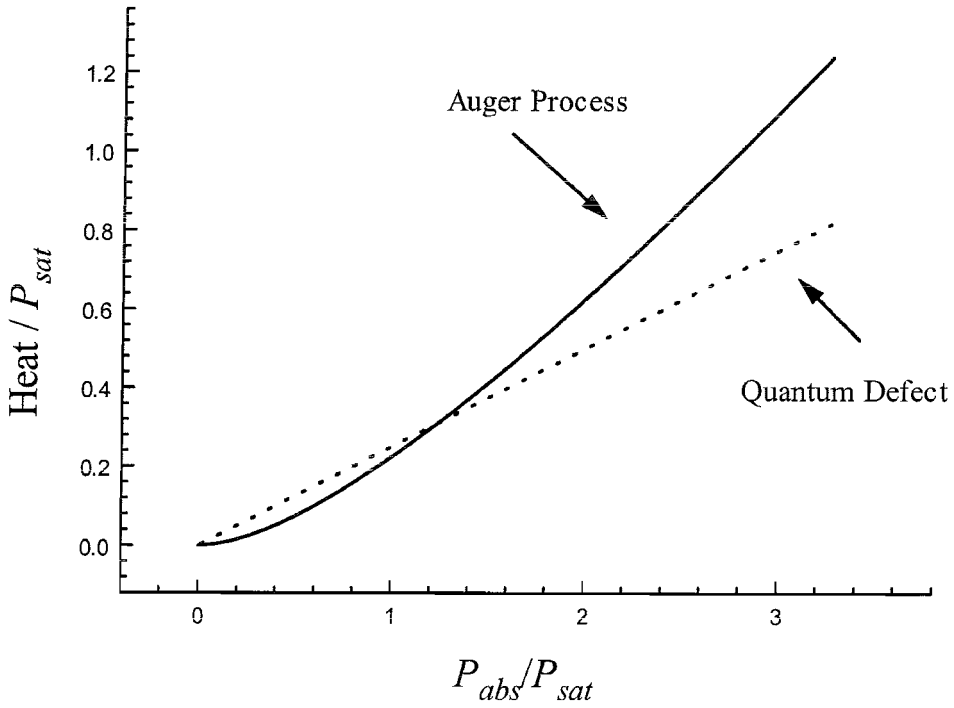

Figure 5.9 Thermal loading due to the quantum defect and the Auger process

Figure 5.9 shows the computed heating processes (1) and (2) in the sample (which is taken to be two absorption lengths long), for different absorbed powers, and with equal pump and signal spot sizes (w_p=w_L). This shows that the thermal loading due to the upconversion effect can be considered negligible for powers lower than ~0.3 P_{sat}.

However, at higher pump powers it becomes more significant, and will eventually balance the quantum defect heating at around $P=P_{sat}$. Above this point thermal loading due to upconversion is the dominant heating process. As the upconversion rate will be much higher in the centre of the pump beam than in the wings, the induced thermal gradient will be steeper in this case than that obtained from the quantum defect for the same overall heat input. This implies that for high-inversion Nd:YAG devices upconversion effects will contribute to and, in some cases will even dominate, the thermal loading of the gain medium.

5.2.5 Upconversion and bleaching in a Nd:YAG amplifier - Summary

Upconversion effects (Auger energy-transfer) in Nd:YAG have been investigated in this section by building an amplifier operating at pump powers up to twice the saturation power. The rate-equation analysis outlined in section 5.2.2 was successfully used to model the effect of upconversion on small-signal gain in the Nd:YAG amplifier. The upconversion parameter calculated from the amplifier experiment was in very good agreement with that obtained in separate spectroscopic studies of the fluorescence lifetime shortening [10]. In the case of 1at.% Nd:YAG the τW_{upc} product, representing the ratio between the net upconversion rate and the down-conversion rate, is equal to 1.5, however it rises sharply with doping level [10]. This corresponds to an Auger upconversion rate of $\sim 7 \times 10^{-3} s^{-1}$. This is significantly smaller than that previously reported [5] and is in fact very similar to the value found for neodymium-doped glasses [3].

Modelling end-pumped amplifiers, has shown that the Auger upconversion becomes significant in reducing the gain as soon as the absorbed power exceeds $\sim 0.5P_{sat}$, where P_{sat} is the power for which saturation intensity is achieved in the centre of the beam. The change in the distribution of the inversion due to the saturation of the pump absorption was found to significantly degrade the small-signal gain. The larger the spot size ratio w_p/w_L, the larger the degradation. The deviation of the actual gain exponent from that assuming no upconversion or saturation of the inversion absorption is very significant. It can be up to 25% depending on the ratio w_p/w_L, with absorbed powers of just $0.5P_{sat}$. It has also been shown that if pumping intensities near

the saturation intensity are used, then the thermal loading due to upconversion can become as important as that from the quantum defect.

Developments such as higher power and higher brightness diode-bars, improved beam-shaping, and the use of waveguide geometries continue to advance the area of diode-pumped Nd:YAG lasers. Thus it is expected, and indeed it has already been found, that pumping intensities near the saturation level will be reached [11]. Except in the case of a low-loss CW laser cavity where the inversion is clamped to a low level, this will inevitably lead to high inversion densities. It has been shown that in this case the Auger upconversion process will result in significant reduction of the small-signal gain (in combination with bleaching effects) and will also significantly increase the thermal loading.

5.3 Thermal effects in a waveguide

5.3.1 Introduction

Design considerations for high average power bulk lasers are now dominated by the need to remove heat efficiently and to reduce the thermal effects caused by temperature gradients across the gain medium. A slab shape has been recognised to offer improved thermal behaviour over a rod, and there are many reports of high power diode-pumped lasers and amplifiers utilising a slab geometry with a variety of different pumping schemes [12-15]. A planar waveguide is an extreme case of such a geometry and the implications this has for the thermal properties of the material will be discussed in this section. Comparisons with bulk rod and slab laser geometries will be made. The first comparison concerns temperature distribution in the material, the second thermal stress. Then a preliminary investigation into thermal lensing will be described.

5.3.2 Temperature distribution

The thermal distribution within slab (ΔT_s) and rod (ΔT_r) shaped laser media has been reported in work by Eggleston and Byer [16] among others. The equations are

presented here for completeness and are developed (appendix A) for use later in this section to describe a planar waveguide. The following analysis is carried out with reference to figure 5.10, showing a slab and rod of isotropic material.

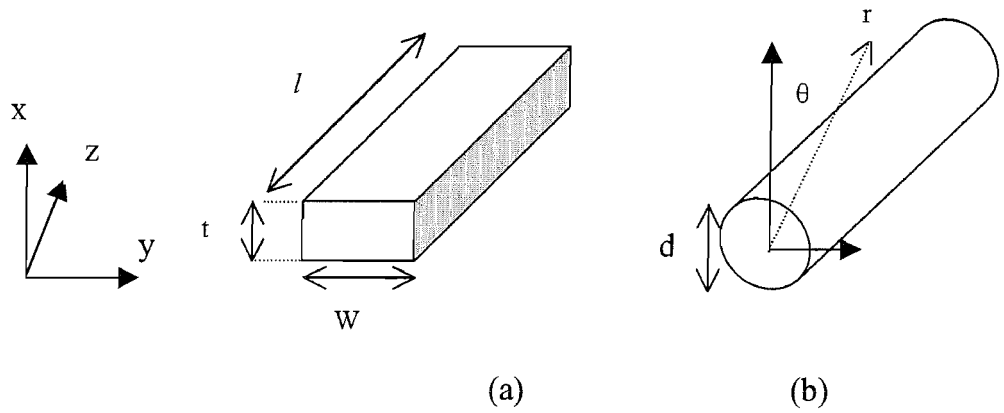

Figure 5.10 The slab (a) and rod (b) shaped systems

The heat input per unit volume is Q (x,y,t) or Q (r,θ,t) Wcm^{-3}, and it is assumed to be independent of z. The assumption is also made that the crystal faces normal to the z-direction are not cooled, and that at the other faces the thermal boundary conditions are independent of z. The temperature distribution in the medium is then described by the time dependent equation:

$$\frac{C\rho}{k}\dot{T} = \nabla^2 T + \frac{Q}{k} \qquad 5.10$$

where k is the thermal conductivity ($Wcm^{-1}K^{-1}$), C is the specific heat ($Jg^{-1}K^{-1}$), ρ is the density (gcm^{-3}) and T is the temperature (K) of the material. The slab (figure 5.10 (a)) is cooled and pumped through the faces normal to the x direction. Under CW pumping equation 5.10 reduces, for the slab, to:

$$\nabla^2 T = \frac{\partial^2 T(x)}{\partial x^2} = -\frac{Q}{k} \qquad 5.11$$

This equation describes a slab of infinite extent, in the y- direction, and assumes a homogeneous thermal loading, resulting in heat flow in the x- direction only. The thermal boundary conditions at the surface, x= ±t/2 are given by 5.12 and 5.13:

$$T\Big|_{x=\pm t/2} = T_C \qquad 5.12$$

$$\frac{\partial T}{\partial x}\Big|_{x=\pm t/2} = \pm\frac{\lambda}{k}\left[T_C - T\Big|_{x=\pm t/2}\right] \qquad 5.13$$

where T_C is the surrounding coolant temperature, t is the slab thickness and λ is the surface heat transfer coefficient ($Wcm^{-2}K^{-1}$). Expressions 5.11-5.13 have the solution:

$$\Delta T_s = \frac{Qt}{2\lambda} + \frac{Qt^2}{8k} - \frac{Qx^2}{2k} \qquad 5.14$$

Within the rod shape (figure 5.10(b)) it is convenient to calculate the temperature distribution under uniform (i.e. constant Q) CW pumping, with a cylindrical co-ordinate system. This leads to the heat flow equation (5.12) having the solution:

$$\Delta T_r = \frac{Qd}{4\lambda} + \frac{Qd^2}{16k} - \frac{Qr^2}{4k} \qquad 5.15$$

Equations 5.14 and 5.15 can now be used to compare the temperature rise in a slab to that in a rod. They are set to have the same value of Q, i.e. the same pump power is assumed to be distributed in the same overall volume of material. The ratio of the maximum temperature rises is then:

$$\frac{\Delta T_r^{max}}{\Delta T_s^{max}} = \frac{d}{2t}\left(\frac{4k + d\lambda}{4k + t\lambda}\right) \qquad 5.16$$

For YAG, sapphire and most other laser materials used in this thesis: $4k > d\lambda, t\lambda$. For example YAG has $k \sim 11 Wm^{-1}K^{-1}$ and sapphire has $k \sim 25 Wm^{-1}K^{-1}$ [17].

Equation 5.16 is then approximated to:

$$\frac{\Delta T_r^{max}}{\Delta T_s^{max}} \cong \frac{d}{2t} \qquad 5.17$$

This ratio is inversely proportional to the slab thickness clearly showing that there is a lower temperature rise in a thin slab than in a rod under similar pump conditions. This advantage is illustrated for YAG in figure 5.11. This shows the temperature rise in a 5mm diameter rod and a 1mm thick slab, with the same amount of heat deposited (5W) over the same pumped volume of laser material.

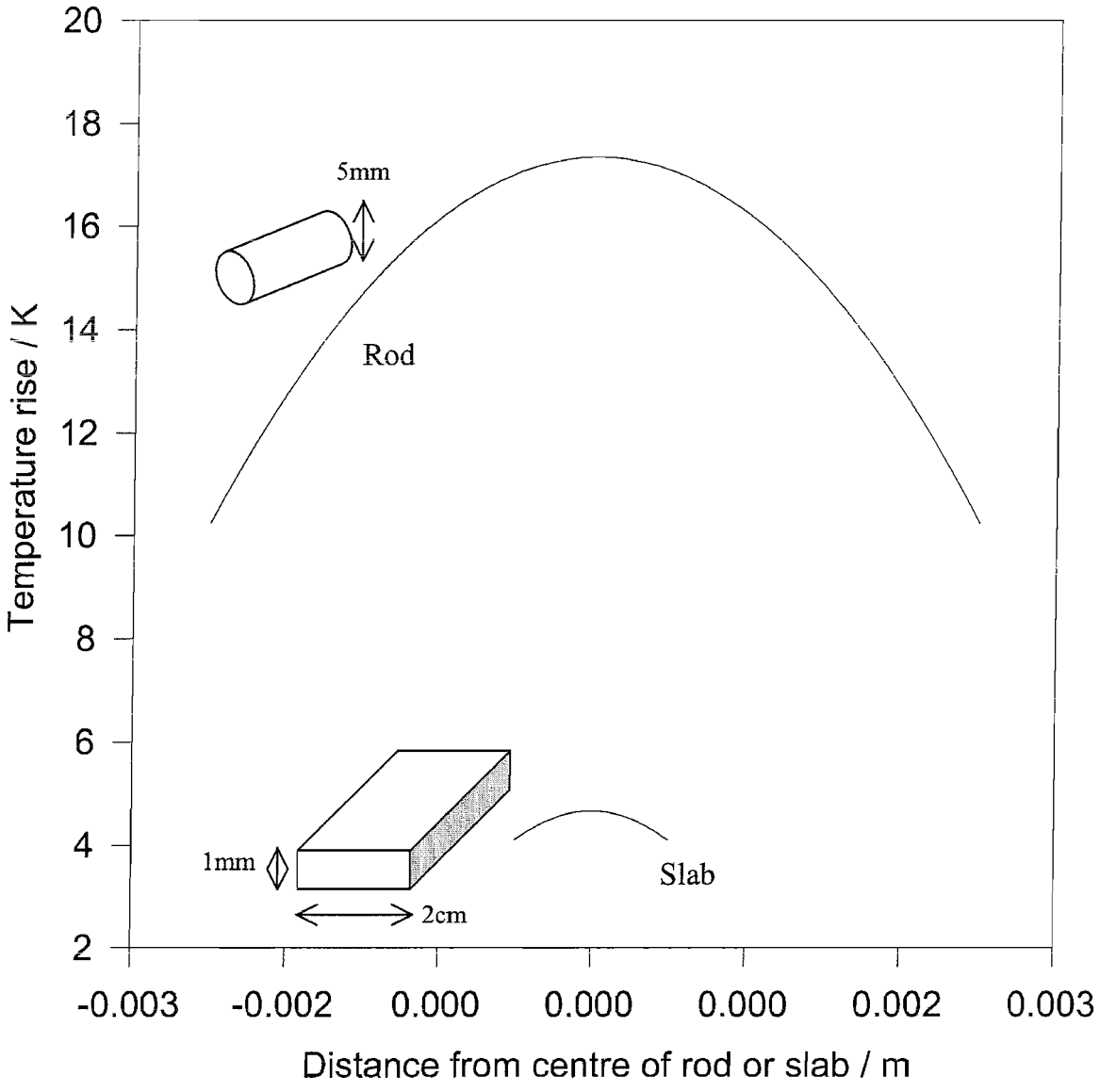

Figure 5.11 Comparison of the temperature distribution in a rod and a slab

A planar waveguide, such as is described throughout this thesis is approaching the limits of a slab geometry in one extreme, and a comparison between a slab and a waveguide will now be made. The expected temperature distribution in a waveguide is derived in appendix A from solution of the one dimensional heat flow equation 5.11. The results are used in the following analysis.

Figure 5.12 illustrates the thin slab and planar waveguide structures that are compared in the following discussion.

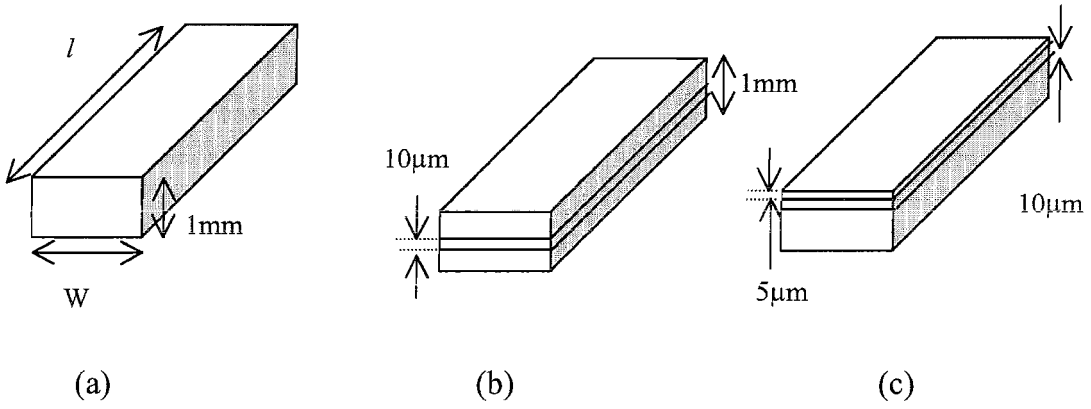

Figure 5.12 Thin slab and planar waveguide structures

Typical examples of these structures are high quality, low loss waveguides that have been fabricated by LPE with cores from 3- ~100μm thick on substrates around 0.5mm thick [18], or direct bonded waveguides (for example those described in chapter 4), that can have sub-10μm cores on substrates of 1-2mm thickness.

In the comparison made here the overall volume of the material is the same for both the slab and the waveguide. All the samples are 1mm thick and the same input pump power converted to heat is used. However, a different value of Q (heat input per unit volume) is used in each case. The model is adjusted to make it more relevant to a planar waveguide shape by assuming all of the heat is deposited only in the core. The 5W of heat power is therefore assumed to be deposited into just the 10μm thick core of the waveguides shown in figure 5.12 (b) and (c), but into the entire 1mm slab thickness of figure 5.12 (a). This obviously results in a greater thermal load in the waveguide than in the slab. The graphs in figure 5.13 were produced for YAG material using k = $11 Wm^{-1}K^{-1}$ and $\lambda = 6100 Wm^{-2}K^{-1}$. This value of λ, surface heat

transfer co-efficient, is representative of the co-efficient for water-cooled heatsinks that were used in this thesis [19]. The zero position on the x-axis corresponds to the centre of the heat deposition (the slab centre or the centre of the waveguide core), and cooling is from both faces.

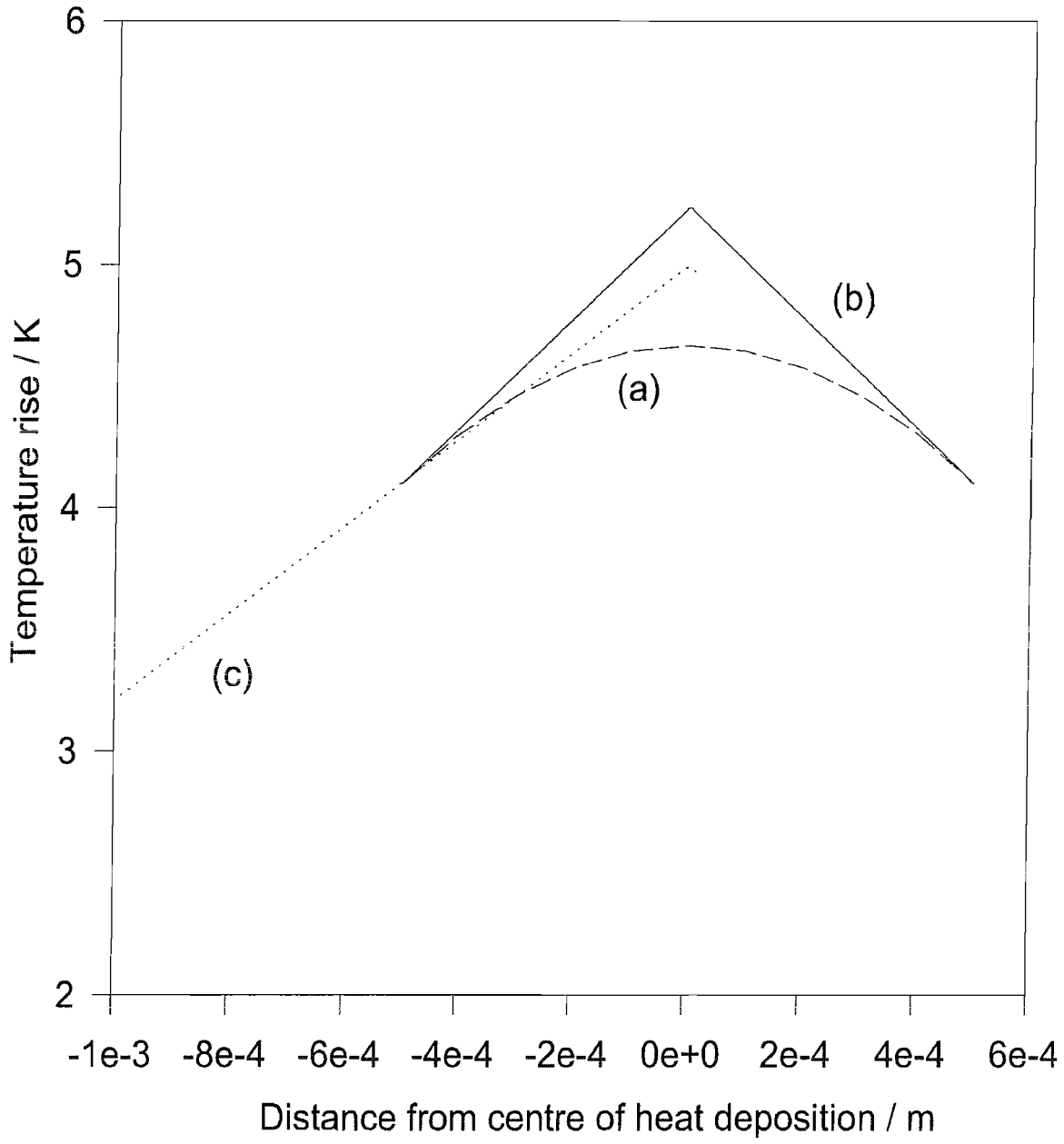

Figure 5.13 Comparison of the temperature distribution in a thin slab and a waveguide. Curves (a), (b) and (c) correspond to the structures illustrated in figure 5.12

The plot illustrates that the maximum temperature rise in a planar waveguide (modelled as a non-uniformly pumped slab) is higher than in a uniformly pumped slab

of the same overall thickness, but that the difference is not large. This implies that the thermal management capabilities of the waveguide are slightly worse than that of the slab. However, other benefits brought about by the waveguide geometry, such as optical confinement, can overcome the slight thermal disadvantage.

This analysis shows that it is the overall thickness of the slab that is the dominant geometrical factor in the temperature rise produced in the material. Therefore waveguides with thinner substrates should perform better than those with thicker substrates, where the temperature rise in the material will be higher. Figure 5.13 also shows that off-setting the waveguide core from the centre of the slab (so that it is nearer to the coolant) can help to reduce the temperature rise.

Extending this analysis can include different heat transfer coefficients (λ), for example air-cooling and water-cooling, either side of the slab (see Appendix A). This has been used in experiments described in chapters 6 and 7, and shows that cooling one side of the slab only leads to a doubling of the temperature rise shown in figure 5.13, from around 5K to around 10K. Additionally, in a planar waveguide with one-sided cooling the closer the waveguide layer to the cooled face, the less the temperature difference is across the whole waveguide structure. These analyses will be used in the next chapter to interpret some of the laser results from high-power diode-bar pumped planar waveguides.

5.3.3 Thermal stresses

Temperature gradients in a material result in mechanical stresses. The stress fracture limit occurs when the stress at the rod's surface ($\sigma_{surface}$) exceeds the maximum surface stress that the material can withstand. The maximum surface stress at which fracture occurs, (σ_{max}), depends on the mechanical properties of the particular material. It can be described by [16]:

$$\sigma_{max} = \frac{R_s \alpha E}{(1-\upsilon)k} \qquad 5.18$$

where E is the Young's modulus, υ is the Poisson's ratio, α is the thermal expansion coefficient of the material and $R_s=(\sigma_{max})M_s$, where M_s is a material figure of merit.

The thermal stress fracture limit for a rod and a slab has been examined by Eggelston and Byer [16], and here just the results of the analysis are used. The equations [16] are given in terms of the thermal loading per unit length P_{rod}/l and P_{slab}/l and here refer to the thermal power loading in the material at the stress fracture limit. In equations 5.19 and 5.20 $P_{rod(slab)}$ is the total thermal power absorbed by the rod (or slab).

The maximum deposited heat power per unit length before stress fracture occurs in a rod is:

$$\frac{P_{rod}^{max}}{l} = 8\pi R_s \qquad 5.19$$

and in a slab is:

$$\frac{P_{slab}^{max}}{l} = 12R_s\frac{W}{t} \qquad 5.20$$

The ratio of equations 5.19 and 5.20 is:

$$\frac{P_{slab}^{max}}{P_{rod}^{max}} = \frac{3}{2\pi}\left(\frac{W}{t}\right) \qquad 5.21$$

This shows that a slab shape is able to absorb greater thermal power per unit length than a rod, providing the aspect ratio of the slab is greater than ~2. Clearly high aspect ratio slabs will have higher thermal stress fracture limits than rods, and this advantage scales inversely with t, the slab thickness. These advantages of slab shape laser media have been exploited by groups working in the field of high-power laser devices [e.g.20, 21].

The thermal stress fracture limit of a waveguide (a non-uniformly pumped slab) is related to the thermal loading and temperature distribution within the waveguide, as described in section 5.3.2. As the temperature rise in a waveguide was found to be slightly higher than in a slab (figure 5.13), the thermal stress fracture limit for a waveguide will therefore be slightly lower than for a uniformly pumped slab shape. However, the waveguide still maintains a stress fracture advantage over a rod and the fracture limit still scales with the aspect ratio of the whole structure.

5.3.4 Thermal lensing and birefringence

The thermal gradients and stresses discussed in the previous section produce variations in the refractive index (Δn) of the gain medium. This can lead to a rod geometry, with a radial and tangential temperature distribution, having a different refractive index change in both the radial and tangential directions depending on the elastooptical coefficients (C) of the material. For instance C_{radial} = 0.017 and $C_{tangential}$=0.0025 in Nd:YAG. The principle axes of the birefringence are radially and tangentially directed at each point in the rod cross section and incoming linearly polarised light experiences depolarisation. If a polariser is placed in the laser cavity to ensure a linearly polarised output, there will be a significant 'birefringence loss', increasing the overall cavity loss. Some techniques have been developed to counteract this [22], but these use extra components, adding to the complexity of the cavity.

However, in a slab geometry, the one dimensional heat flow results in a benign birefringence behaviour with well defined axes [14], leading to zero stress induced 'birefringence loss' for light polarised along the x or y axes.

In addition to birefringence, thermal focussing can occur due to the change of refractive index with temperature and stress, and also due to end-face curvature from thermal expansion effects. In a rod geometry this leads to an approximately spherical lens [16]. For instance, for an end-pumped Nd:YAG laser rod with 5W of absorbed power in a spot size with radius ~290μm, (around half the radius of the rod) and other material parameters as in the Nd:YAG sample described in section 5.2, the thermal lens has been found to be ~40cm [23]. At higher pump powers the thermal lens

becomes more extreme and can be as short as 5-10cm. Compensation techniques commonly used include grinding concave end faces onto the rod and using a compensating lens and curved mirror in the cavity. However the thermal lens is actually biaxial, having different focal lengths for radially and azimuthally polarized light, and cannot be fully compensated for [16].

Some of these problems can be avoided by pumping a slab shaped gain medium where the one dimensional heat flow results in a correctable cylindrical thermal lens. A zig-zag optical path scheme within a slab (or coplanar-pumped folded-slab) [15], can also be used to reduce the focussing effects and to design resonators capable of good single-mode TEM_{00} performance. This type of geometry can combine good pump mode matching with the scalability and simplicity of side-pumping.

In work related to this, other groups have shown that using a line-focus to produce a planar pumped region beam can have some interesting advantages [23]. These include the simpler coupling optics, the near-planar heat flow and the increased surface-to-volume ratio in slab-shaped gain media which can reduce the temperature rise at the centre of the pumped crystal. This is important for temperature sensitive laser materials. In addition, power scaling a device with planar geometry can be achieved by simply lengthening the pump beam cross-section, for example by adding in more diode-bars, and avoiding crystal damage. This technique of using a line-focus and scaling the pump beam tangentially is considered to be a promising method for power scaling diode-pumped Cr:LiSAF lasers [24].

A planar waveguide can be considered as a slab with its thin active gain region and large surface area extending over a large width. However, a further advantage of a waveguide geometry is that the thermal focussing in the cooling direction is overcome by optical guidance in the core. The possibility of a thermal lens in the non-guided direction is experimentally investigated in the next section.

5.3.5 Thermal lens experiment

In order to investigate any thermally induced effects in the non-guided plane of a Nd:YAG waveguide, an experiment was devised to monitor any noticeable focusing

of a helium-neon probe beam travelling through the gain medium under intense, (non-lasing) pumping conditions.

Under non-lasing conditions the population of the upper laser level is not clamped as it is under laser conditions, so a large population inversion can build up. As shown in section 5.2, a large population density in the upper laser level leads to upconversion and additional heating effects (see equation 5.9) in the medium. This experiment therefore attempts to illustrate a worse-case scenario for a pumped laser material.

The experimental apparatus was carefully set up and aligned as shown in figure 5.14

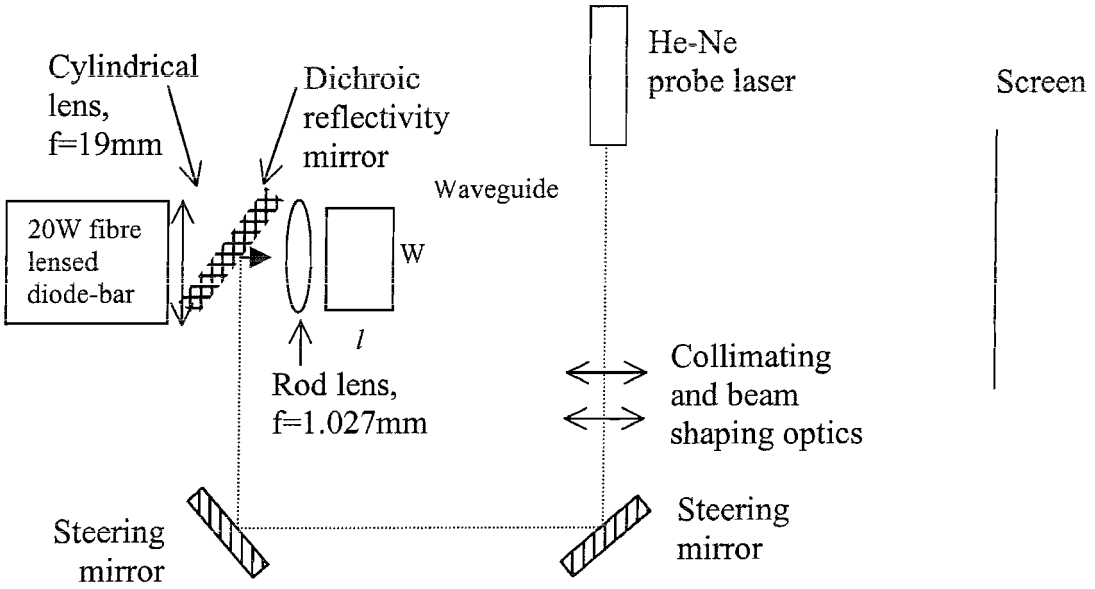

Figure 5.14 Experimental set-up for thermal lens investigation

The waveguide was diode-bar end-pumped with a fibre-lensed 20W diode bar, following the technique described in chapter 6. This experiment was designed to mirror the pumping scheme and cylindrical lens focusing used in the majority of diode-bar pumped waveguide laser experiments in this thesis. The aim of this was to provide an accurate representation of any thermal effects present in these waveguide experiments. The waveguide was an 8μm thick Nd:YAG layer direct bonded to a 2mm thick sapphire substrate. The waveguide sample was 6mm long (*l*), sufficient to absorb the pump beam, and 1cm wide (W). It was mounted on a water cooled

heatsink. The pump beam was focused with a cylindrical lens in the non-guided direction and a spherical-aberration-free rod lens in the guided direction. The pump spot size waist radius at the input face of the waveguide was measured to be 2μm x 1mm in the guided and non-guided directions respectively. An efficient launch of pump light into the waveguide was important, and the launch x absorption (ηA) parameter was measured to be 50%. Overall the pump scheme resulted in 6W of absorbed pump power in the waveguide.

A helium-neon laser, collimated to a measured spot size radius of approximately 700μm was aligned parallel to the pump beam and directed along the same path by the use of a mirror as shown in figure 5.14. The mirror angled at 45^0, was highly transmitting (T=94%) for the pump wavelength of 808nm, and highly reflecting (R=94%) at the probe wavelength. The helium-neon probe beam was launched into the waveguide and the output was viewed on a screen.

The divergence of the probe beam was examined qualitatively on the screen, both with and without diode-bar pumping. No discernible difference in divergence was seen between either case. A typical end-pumped rod laser with similar absorbed pump power would produce a thermal lens of focal length, typically 10-40cm, (section 5.3.4). To gauge the divergence of the probe beam from such a lens, spherical lenses of varying focal lengths from 160mm – 900mm were positioned in place of the waveguide. All of these lenses produced a noticeable focusing of the helium-neon beam. It can therefore be inferred that any thermal lens present in the waveguide under intense pumping must be weak, with a focal length greater than 900mm. This preliminary experiment so far confirms the excellent thermal management capabilities of a slab shape that are inherent in a planar waveguide. Further work in this area could involve interferrometric techniques to provide a quantitative analysis [25].

5.3.6 Thermal effects in a waveguide - Conclusions

This section has analysed and compared the thermal management of a rod, a slab and a waveguide laser. The clear conclusions are that a slab shape offers significant advantages over a rod due to one dimensional heat flow, instead of radial heat flow

characteristic of a cylindrical gain medium. Similar, but slightly higher, temperature rises and thermally induced stress values were predicted in a planar waveguide compared to a bulk slab-shaped laser media. However, the other advantages characteristic of a waveguide such as its compact nature and optical confinement properties should also be taken into consideration. In a planar waveguide the guidance overcomes thermally induced focussing in one plane and the temperature variation in the other plane can be small. An initial investigation into thermal lensing in the waveguide under diode-bar pumping revealed no significant thermal lens in this plane. However further work needs to be done in this area to quantify the preliminary results. Planar waveguides offer a clear route to scaling devices to higher powers and a number of groups are working in this area.

The techniques that were used to make multi-Watt waveguide devices in the course of this thesis are detailed in chapters 6 and 7.

5.4 References

[1] W.A.Clarkson, R.Koch, D.C.Hanna, Opt. Lett., **21**, pp.737-739 (1996)

[2] D.P.Shepherd, C.T.A.Brown, T.J.Warburton, D.C.Hanna, A.C.Tropper, B.Ferrand, Appl. Phys. Lett., **71**, pp.876-878 (1997)

[3] S.A.Payne, G.D.Wilke, L.K.Smith, W.F.Krupke, Opt. Comm., **111**, pp.263-268 (1994)

[4] P.J.Hardman, W.A.Clarkson, G.J.Friel, M.Pollnau, D.C.Hanna, Opt. Comm., **35**, pp.647-655 (1999)

[5] Y.Guyot, H.Manaa, J.Y.Rivoire, R.Moncorgé, N.Garnier, E.Descroix, M.Bon, P.Laporte, Phys. Rev. B, **51**, pp.784-799 (1995)

[6] V.Lupei, A.Lupei, S.Georgescu, C.Ionescu, Opt. Comm., **60**, pp.59-63 (1986)

[7] A.E.Siegman, *'Lasers'*, University Science Books, pp.292-294 (1986)

[8] T.Kushida, Phys. Rev., **185**, pp.500-508 (1969)

[9] T.Y.Fan, IEEE J. Quantum Electron., **QE-29**, pp.1457-1459 (1993)

[10] S.Guy, C.L.Bonner, D.P.Shepherd, D.C.Hanna, A.C.Tropper, B.Ferrand, IEEE J. Quantum Electron. **QE-34**, pp.900-909 (1998)

[11] C.T.A.Brown, *'Nd – doped Crystal Waveguide Lasers and Amplifiers'*, PhD Thesis, University of Southampton, pp.75-93 (1997)

[12] U.Brauch, A.Giesen, M.Karszewski, C.Stewen, A.Voss, Opt. Lett., **20**, pp.713-715 (1997)

[13] A.Giesen, H.Hugel, A,Voss, K.Wittig, U.Brauch, H.Opower, Appl. Phys. B, **58**, pp.365-372 (1994)

[14] W.Koechner, *'Solid State Laser Engineering'*, Springer - Verlag, Berlin, Chaps 6.3 and 7.3 (1996)

[15] T.M.Baer, D.F.Head, P.Gooding, G.J.Kintz, S.Hutchinson, IEEE J. Quantum Electron. **QE-28**, pp.1131-1138 (1992)

[16] J.M.Eggleston, T.J.Kane, K.Kuhn, J.Unternahrer, R.L.Byer, IEEE J. Quantum Electron. **QE-20**, pp.289-301 (1984)

[17] D.N.Nikogosyan, *'Optical and Laser related Materials'*, John Wiley and Sons, Chichester, UK, (1997)

[18] B.Ferrand, D.Pelenc, I.Chartier, Ch.Wyon, J. Crys. Growth. **128**, pp.966-969 (1993)

[19] C.T.A.Brown, *'Nd – doped Crystal Waveguide Lasers and Amplifiers'*, PhD Thesis, University of Southampton, pp.140-144 (1997)

[20] S.Basu, R.L.Byer, Appl. Opt., **29**, pp.1765-1771 (1990)

[21] A.Faultich, H.J.Baker, D.R.Hall, Opt. Lett., **21**, pp.594-596 (1996)

[22] W.A.Clarkson, N.S.Felgate, D.C.Hanna, Opt. Lett., **24**, pp.820-822 (1999)

[23] J.Blows, J.M.Dawes, T.Omatsu, J. Appl. Phys., **83**, pp.2901-2906 (1998)

[24] D.Kopf, J.Aus der Au, U.Keller, G.L.Bona, P.Roentgen, Opt. Lett., **20**, pp.1782-1784 (1995)

[25] W.A.Clarkson, D.C.Hanna, in *'Optical Resonators-Science and Engineering'*, R.Kossowsky et al. (eds.), Kluwer Academic Publishers, pp.327-361 (1998)

Chapter 6 Diode-Bar Pumped Waveguide Lasers

6.1 Introduction

The laser diode-bar is growing in importance as a high-power, efficient, compact pump source for solid-state laser applications where CW powers of 10-100W are required. The major drawback of using a diode-bar as a pump source is the poor spatial quality of its output beam (see table 3.1 in chapter 3). Many designs have been developed to efficiently couple the highly asymmetric and non-diffraction limited output into various solid-state laser media. For pumping bulk materials the beam has been circularised using fibre-coupling [1], lens ducts [2] and other beam shaping methods [3,4]. High-power fibre lasers have used beam shaping combined with a double-clad geometry [5] or v groove designs [6]. This need to manipulate the spatial properties of the diode-bar output beam increases the complexity of the device and reduces the overall efficiency of the system.

A planar waveguide has a structure which is inherently compatible with the output from a diode-bar. Its shape offers the possibility of a device with reduced intermediary optics, or even none at all with a proximity coupling technique. In addition, and as discussed in the previous chapter, a slab geometry is well suited to managing the large thermal load deposited in a laser material during high power diode-bar pumping. This realisation, along with the known attraction of high gains due to optical confinement, has been the driving force behind work on high-power planar-waveguide lasers.

Two approaches to coupling the diode-bar output into a waveguide have been reported to date; face-pumping and in-plane pumping. The face-pumping technique, developed by Faulstich et al [7], has used relatively thick waveguides (or thin bulk slabs). The pump light is launched through the surface of the waveguide and the laser signal propagates along the guide. This type of device is attractive as it requires no specific focusing to couple the pump light into the waveguide core. Power scaling, using a number of diode-bars, can easily be envisaged through the large surface area of the slab face. One major disadvantage with this pumping scheme though, is the

poor single pass pump absorption in the core leading to the use of a reflective pumping chamber.

This chapter describes work on an in-plane pumping approach using simple cylindrical [8] or rod lens [9] focusing. The first part of the chapter gives details of the coupling techniques used for end-pumping with the relevant waveguide laser results. These results were obtained with bulk cylindrical lens focusing and more recently, rod lens focusing. The second section discusses two methods of diode-bar side-pumping; cylindrical lens focusing and proximity coupling.

The main aim of the chapter will be to demonstrate efficient coupling of diode-bars to sub-10μm waveguides, and then to investigate the lasing characteristics of simple monolithic plane/plane waveguide laser cavities. In these preliminary studies no other components, such as Q-switches etc, have been integrated into the cavity and as yet, no steps towards active mode control have been taken.

6.2 In-plane diode-bar coupling for end-pumped lasers

Consideration has already been given to the parameters associated with efficient coupling of the highly divergent output beam of the diode-bar into a waveguide, (chapter 4). This will not be discussed further here except to reinforce that the pump beam divergence must be compatible with the numerical aperture (NA) of the waveguide in the x (guided)- direction. In addition the output from the diode-bar must be focused and efficiently captured within the width of the waveguide.

6.3 Diode-bar end-pumped lasers

6.3.1 Bulk cylindrical lens array coupling

The first method used to couple the fibre-lensed diode-bar (OptoPower Corp.) pump beam into a waveguide was an arrangement of four bulk cylindrical lenses shown in figure 6.1. The diode-bar used here operated at around 807nm with a line width (FWHM) of 3nm. The maximum output power from the bar was 20W at an operating

current of 28.5 Amps. The diode-bar output was collimated using an acylindrical fibre lens (as described in chapter 3, section 3.2) to provide a vertical beam waist radius of ~160μm. Measurement of the divergence angle of the beam, (described in chapter 3, section 3.10) gave estimates of M_x^2= 2.3 and M_y^2= 2600 for the packaged device.

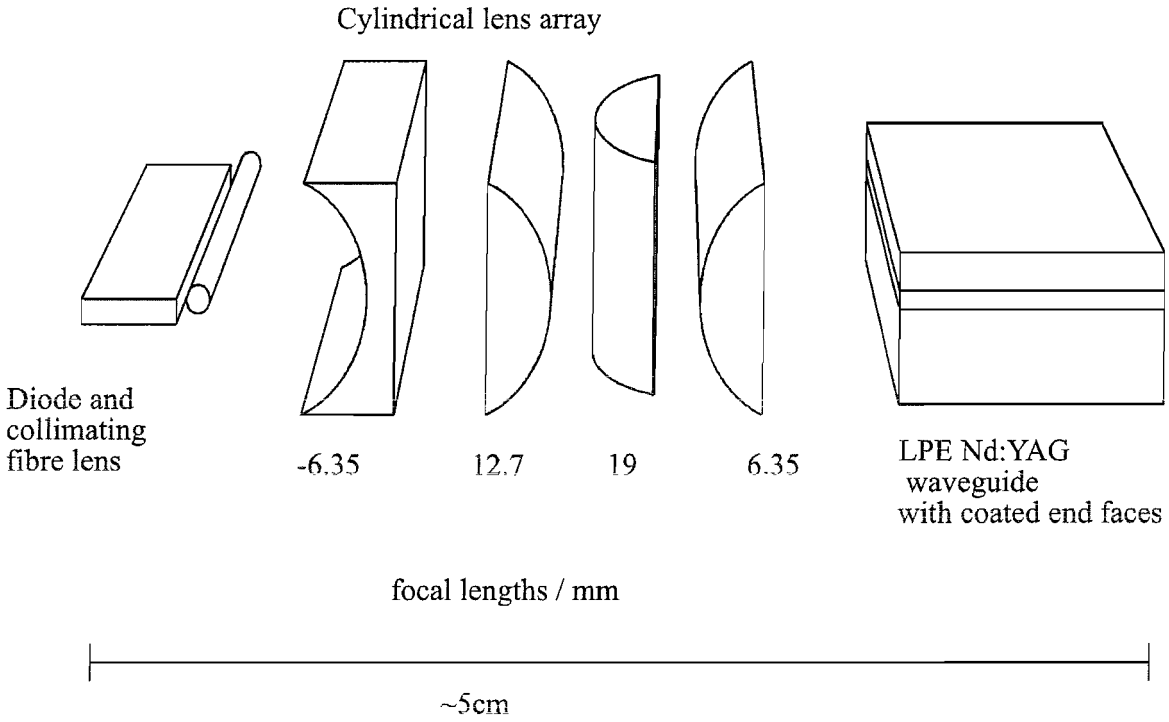

Figure 6.1 Schematic diagram of the end-pumped waveguide laser showing the focusing lens array.

The collimated output from the diode was initially expanded in the fast axis by a cylindrical X2 telescope before being focused with a 6.35-mm focal-length cylindrical lens. A single 19-mm focal-length cylindrical lens was used in the slowly diverging axis. This combination resulted in a line focus at the waveguide face, with measured spot sizes of 15μm and 1.3mm in the guided and non-guided directions respectively. Because of the highly divergent output from the diode-bar all measurements of spot size in this section, unless otherwise stated, have been defined as the aperture radius at which 86.5% of the total power is transmitted. This is a good approximation to the second moment of the intensity distribution for multi-mode beams [10]. The angular divergence of the focused pump beam was calculated to be 0.05 radians in the guided direction, suitable for coupling into a waveguide with a low NA.

These initial experiments used a 5mm long waveguide with an 80μm thick 1.5at.% Nd- doped YAG core on an undoped 500μm thick YAG substrate. The waveguide was grown by liquid-phase-epitaxy (LPE) [11]. A further 90μm layer of undoped YAG was grown on top of the core as a protective cladding. This also helped reduce scattering losses. The LPE technique has been shown to produce good quality waveguides, with typical losses of less than 0.1dB/cm [12]. The neodymium gives an index increase of 4.8×10^{-4} per 1at.% doping [13] to provide guiding behaviour. This corresponds to a NA of 0.051, just large enough to contain the diode-bar pump.

6.3.2 Practical testing of an end-pumped waveguide laser using a lens array

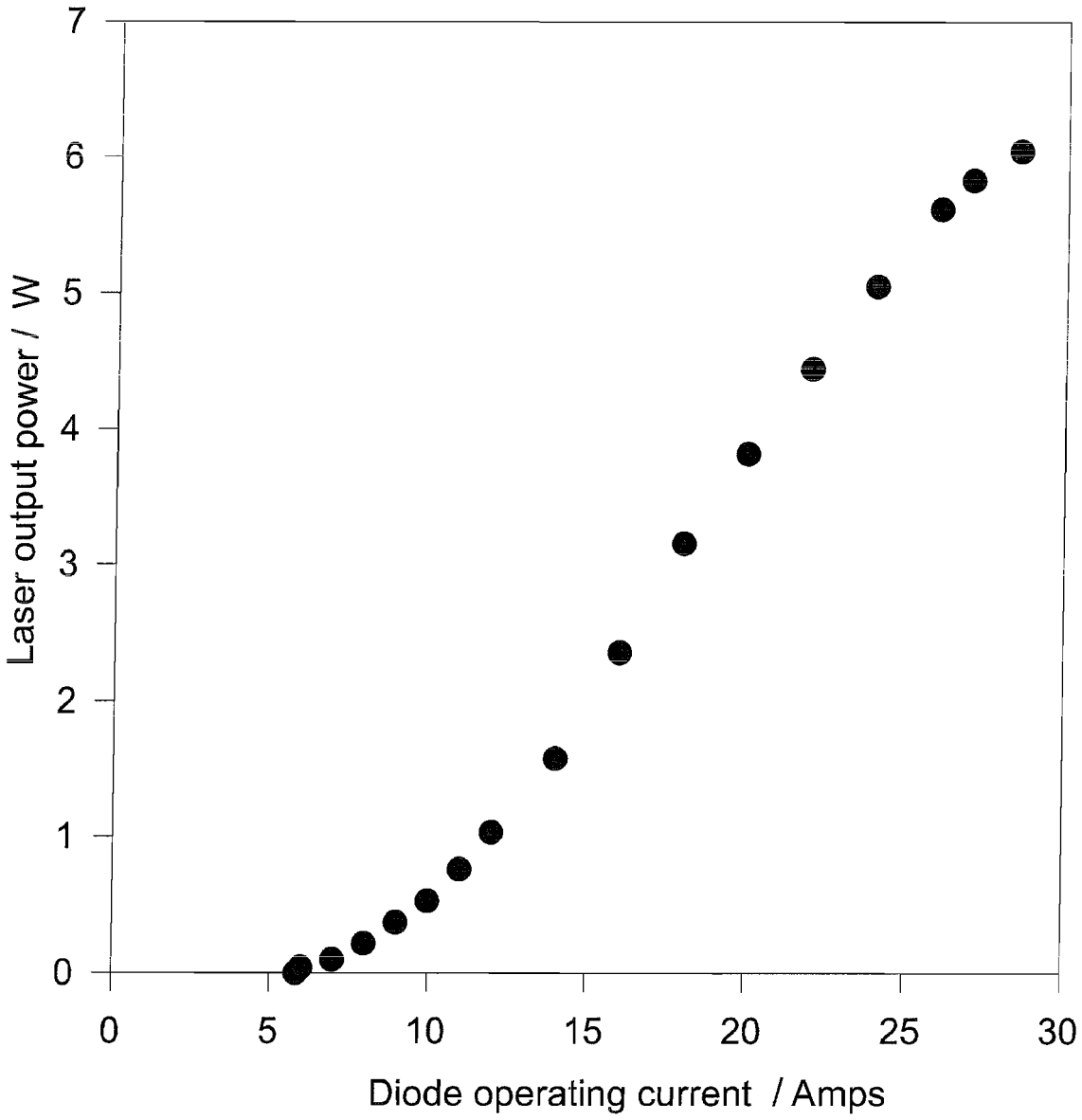

Figure 6.2 Output power of the 80μm waveguide laser versus diode current

The laser cavity (shown in figure 6.1) was formed by directly coating mirrors onto the plane-parallel end-faces of the waveguide, leading to an overall device length, from diode facet to waveguide laser output coupler, of just 5cm. The input face was nominally highly reflecting at the laser wavelength while the output face of the waveguide had a 5% transmission. The waveguide was mounted upon a heatsink cooled by continuously circulating water, which was operated with a coolant temperature of 15°C. A maximum output power of 6.2W at 1.064μm was obtained, for an incident pump power of 16.5W after the cylindrical lens array. This is shown later in this section to be close to theoretical predictions. At these powers no optical damage was seen on the waveguide face with CW pumping from the diode-bar.

The dependence of 1.064μm output power on diode current is shown in figure 6.2.

The 38% conversion efficiency from incident to output power, at maximum operating current (corresponding to 31% overall optical-to-optical conversion efficiency), confirms efficient coupling of the diode-bar output into the waveguide. The maximum laser output was optimised at the maximum diode operating current. Due to space restrictions within the system, the input pump power was then varied by changing the diode operating current. However this method also results in a change in the operating wavelength of the diode from 801nm at threshold, to 807.5nm at the peak pump power. Thus output power versus incident pump power was not plotted, as this would give an artificially high slope efficiency.

Output beam M^2 values, measured using a Coherent Modemaster, were found to be as low as 3 and 140, in the guided and non-guided directions respectively. These values were seen to deteriorate to ~ 5 and 160 if the waveguide was mounted upon an uncooled heatsink, or if poor thermal contact was made between the waveguide and the heatsink. The waveguide heatsink coolant temperature was then decreased further, to 2 °C, at which point condensation began to form on the waveguide despite a constant flow of dry N_2 over the device. This cooling produced a slight improvement in beam quality in the guided direction, but no significant change in the values in the non-guided direction. The laser mode profiles at a power of 6W and with M^2 values of 4 and 160 are shown in figure 6.3.

a)

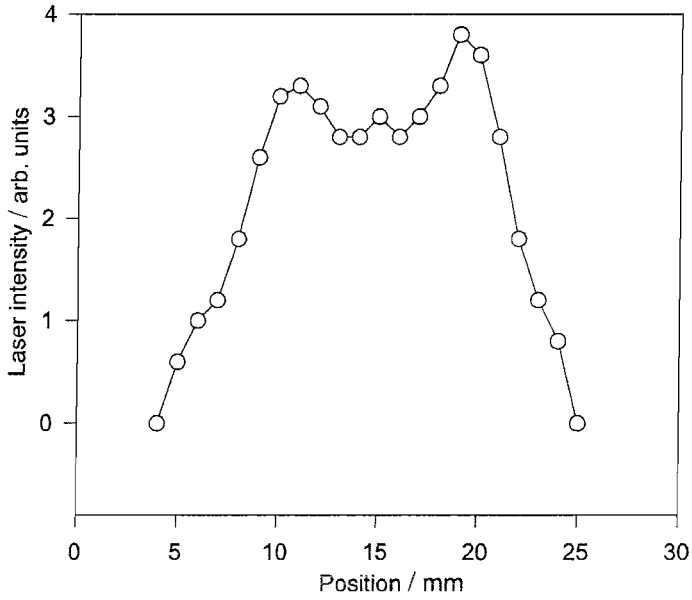

b)

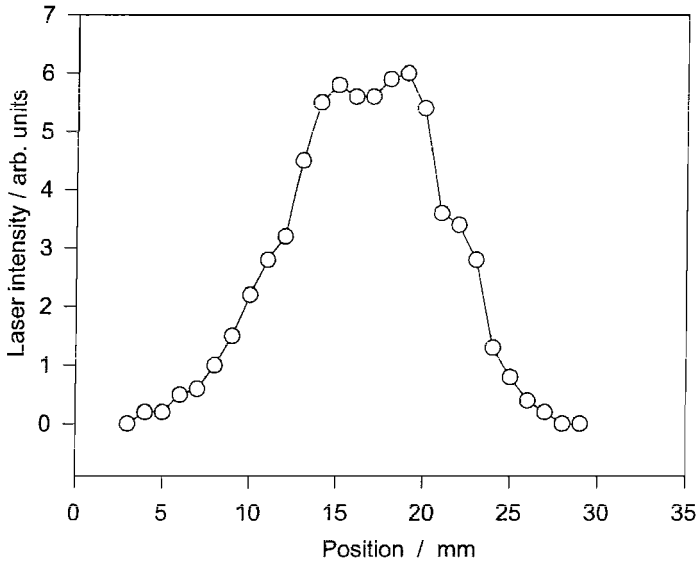

Figure 6.3 Laser mode intensity profiles in the (a) guided and (b) non-guided directions, measured 27.5cm from the waveguide end-face. The curves are a guide for the eye.

The profiles, which were measured using the thin slit technique described in chapter 3, section 3.10 show multi-mode lasing, giving a rectangular output beam shape. The radius, W, of the laser spot in the far field was measured using the variance method

[10]. The laser waist spot radii, W_o, were then calculated, accounting for the measured M^2 values, to be 48μm and 2.3mm in the guided and non-guided directions respectively, indicating that the laser mode essentially fills the 80μm by 6mm guide cross section region. A calculation of the propagation of the W_o=2.3mm, M^2=160, laser beam in the non-guided direction shows that this beam is well collimated over the 5mm length of guide. The W_o=1.3mm, M^2 =2600 pump beam expands to W=1.9mm by the end of the waveguide. Thus the pump beam remains smaller than the laser mode, allowing good energy extraction.

In these experiments the choice of core thickness was limited to this highly multi-mode guide by the availability of suitable coated waveguides. For the three-layer symmetric planar waveguide used here calculations show the waveguide supports eleven TE and eleven TM modes at 807nm, and eight of each polarisation at 1.064μm. The fundamental mode beam radii ($1/e^2$ of intensity) are calculated to be 32μm at both the pump and laser wavelengths.

The extent to which the guidance is playing a role in this experiment can be assessed by comparing the figure for the beam radii with the minimum average spot sizes for the same length of bulk material [14]. Taking into account the M^2 values of the pump (2.3) and laser (~3) beams, the minimum average spot sizes are 41μm and 54μm, respectively. It is clear that this size of waveguide core is close to the boundary between bulk and guided behaviour.

The waveguide laser theory developed in chapter 2 (equation 2.53), predicts a laser threshold of ~330mW for this waveguide laser. The analysis used here takes the average spot sizes for the pump and laser beam and assumes that the beams do not diverge significantly over the length of the waveguide. The slope efficiency ($s\varepsilon$) is then estimated from equations 4.4 and 4.5 [15] to be ~45%. It is reasonable to assume that all of the diode power incident on the waveguide end-face is both launched and absorbed, as the waveguide is 5mm long (greater than an absorption length) and has a core 80μm thick. This method predicts a waveguide laser output of 7.4W, quite close to the 6.2W observed.

The difference in these figures could be due to some pump power being reflected from, and not transmitted through, the input mirror. As already stated, the theoretical calculation has also assumed a launch and absorption efficiency of 100% which might not be achieved in practice.

Overall this is an efficient waveguide laser which performed close to the theoretical limit. However, the main drawback with the lens array focusing scheme described here is that the smallest obtainable pump spot sizes are ~10μm. This is due to the physical size of the lenses and to aberrations in the system as a whole. Waveguide core sizes must therefore be at least ~30μm making it difficult to use single mode waveguides and thus obtain single mode output. However the lens array technique does not require high numerical aperture (NA) waveguides.

The design and testing of coupling optics suitable for pumping much smaller core sizes (<10μm) will be discussed in the next section. This technique focuses to smaller spot sizes using rod lenses but requires higher NA waveguides. Details of the numerical aperture requirements and methods of fabricating such waveguides were discussed in chapter 4.

6.3.3 Rod lens coupling of diode-bars to waveguides

The overall aim in this section is to obtain the full advantage from the guided geometry by coupling diode-bars to much smaller core size waveguides. Pump focusing is provided by a single, high numerical aperture, graded-index rod lens instead of the cylindrical lenses shown in figure 6.1. Such rod lenses are able to provide tighter focusing than bulk cylindrical lenses, allowing the use of thinner waveguides which support fewer modes. Rod lenses are also compact and could lead to a simpler experimental arrangement with fewer components. Figure 6.4 shows a schematic diagram of the optical system used. The diode-waveguide distance is <3cm.

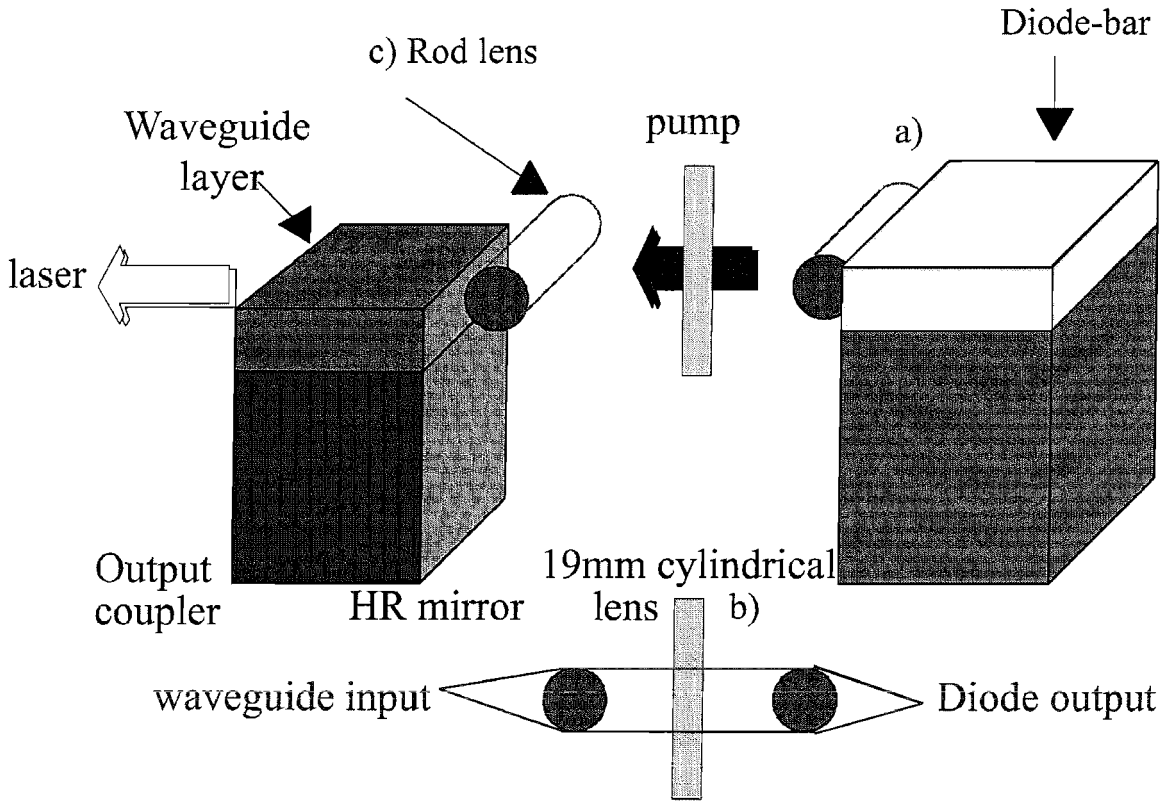

Figure 6.4 Schematic diagram of the diode-bar to waveguide coupling optics. The lenses are: a collimating fibre lens (a), a bulk cylindrical lens (b), a re-focusing rod lens (c)

The output from the diode-bar is collimated with a fibre lens as described previously in this work. A graded-refractive-index rod lens, designed to be corrected for spherical aberration up to an NA of 0.5, is placed in front of the waveguide as the re-focusing element in the guided plane. A single 19-mm focal-length cylindrical lens was used in the non-guided plane. Lenses b and c are mounted such that they can be rotated relative to each other and are on three-axis positioners, allowing movement and adjustment for optimum coupling. The facet of the diode-bar is thus imaged onto the core end-face of the waveguide.

For a cylindrical fibre or rod lens the spot size at the focal point, w_{focus}, with a collimated beam of spot size $w_{incident}$ incident on the lens, is given by [16]:

$$w_{focus} \approx \frac{FM^2\lambda}{\pi w_{incident}} \qquad 6.1$$

where F is the focal length of the rod lens. The use of simple cylindrical rods would lead to significant spherical aberration when trying to make spot sizes of <6-8μm [17]. It was therefore very important that lenses corrected for this form of aberration were used. All of the rod lenses used in the work described in this thesis were obtained from Doric Inc., Canada and were spherical-aberration-free up to a NA of 0.5. For a typical fibre lensed diode-bar with M^2=2, λ = 807nm, and a beam spot size radius $w_{incident}$ =160μm, incident on a spherical-aberration-free rod lens of focal length F=1.027mm, the diffraction-limited focused spot size predicted from equation 6.1 is 3.25μm. The focused spot sizes produced by a Ti:sapphire laser focused through a range of such lenses were measured using a Merchantek Beamscope, placed directly in the path of the beam, and at various points along it. These results were in good agreement with equation 6.1 and confirmed the spherical-aberration-free nature of the lenses.

The focused spot size produced depends heavily on the M^2 of the pump source. For diode-bar pumping, rod lenses of various different focal lengths were tested with different waveguides in order to optimise the launch efficiency in each case.

6.3.4 Diode-bar end-pumped waveguide lasers using rod lens coupling

The 807nm, 20W fibre-lensed, OptoPower diode-bar used in these experiments had a measured power of 17W and a M^2 of 1.5 after the collimating fibre lens. This M^2 combined with the cylindrical and rod lens coupling optics produced a final measured line focus radii of approximately 2mm by 1-4μm, depending on the final rod lens used.

For diode-bar pumping the experimental arrangement was as shown in figure 6.4. The waveguide was mounted on a water-cooled heatsink and a lower limit to the launch efficiency of the diode-bar and rod lens into the guide was found, assuming 100% of the launched light was absorbed. This assumption is a good approximation as the absorption length for the diode pump light was measured to be 3.4mm. A measurement of all of the power before and after the waveguide when the diode beam

is optimally coupled was taken. The launch efficiency for each guide was found using these measurements and taking account of the Fresnel reflections, as described in chapter 3, section 3.6. The results are included in the following section.

6.3.4.1 An 8μm Nd:YAG on sapphire waveguide laser

The initial investigations of coupling efficiency used direct bonded Nd:YAG on sapphire, asymmetric slab waveguides, with core sizes of 4μm and 8μm. Both waveguides were ~2cm in length. The waveguide samples were evaluated under Ti:sapphire end-pumping as described in chapter 4, section 4.4.8 [18, 19], and found to have losses <0.5dB/cm.

Using the rod lenses available a 1.5mm diameter, 1.027-mm focal-length lens gave the best coupling efficiency into the 8μm guide. A lower limit to the optimum launch efficiency was measured to be 73%.

A waveguide laser was constructed around this waveguide to verify the high diode-bar coupling efficiency. A laser resonator was constructed as described in chapter 3, section 3.9. The input mirror was highly-reflecting at 1.064μm and had 92% transmission at the pump wavelength. The output mirror was nominally 50% reflective at 1.064μm. The output laser signal was passed through a colour (bandpass) filter to remove any unabsorbed pump light and then detected with a large area silicon detector. Power measurements were made with a Coherent 810 optical power meter and the beam quality of the laser was characterised by measuring M^2 with a Coherent Modemaster. The maximum laser output power was 3.7W with measured M^2 values of 10 X 85, in the guided and non-guided directions respectively. The output power was less than obtained from the diode-bar pumped LPE Nd:YAG guide in section 6.3.2, even though care had been taken to use the correct pump spot size.

Factors that resulted in extra waveguide loss could account for this difference in output power. The direct bonded waveguide used in this experiment had a higher propagation loss (0.2dB/cm, chapter 4 table 4.2) than the LPE guide, however a greater output coupling was used to compensate for this. The use of thin dielectric

mirrors butted to the waveguide end-faces to form the laser cavity, instead of directly coating the end-faces could lead to non-uniform reflectivity across the end-faces, extra loss and uncertainty in the value of the output coupling.

Thermal issues should also be considered when comparing the two waveguide laser results. As shown in chapter 5, the thickness of the waveguide core influences the temperature rise in the waveguide under diode-bar pumping. This heat deposited in the gain medium could reduce the laser performance. More careful thermal management of these waveguide lasers may be required, for instance by reducing the overall thickness of the slab and including a thin waveguide cladding layer. Positioning the waveguide core close to a cooled surface (a heatsink) may also help.

The output power of this 8μm Nd:YAG/sapphire waveguide was expected to increase with a shorter length of waveguide sample. At 19mm the waveguide is several absorption-lengths long, which contributes excess loss to the cavity. In order to investigate this the waveguide was cut back to 7mm and the end-face re-polished to an optically smooth finish.

A launch efficiency of 73% was again obtained using the same coupling optics. The laser resonator was constructed using the same thin dielectric input mirror as before. The optimum output coupling was found experimentally using the mirrors available. A mirror that had 77% reflectivity at 1.064μm and was also highly-reflecting at the pump wavelength, 807nm, gave a maximum output power of 3.4W. However, this was lower than the output from the longer waveguide.

The reduction in output power could have happened for a number of reasons including an increased loss perhaps due to scratches or greater non-parallelism of the waveguide end-faces, that may have been introduced into the cavity when the sample was cut and re-polished. The dependence of 1.064μm laser output power on diode current is shown in figure 6.5.

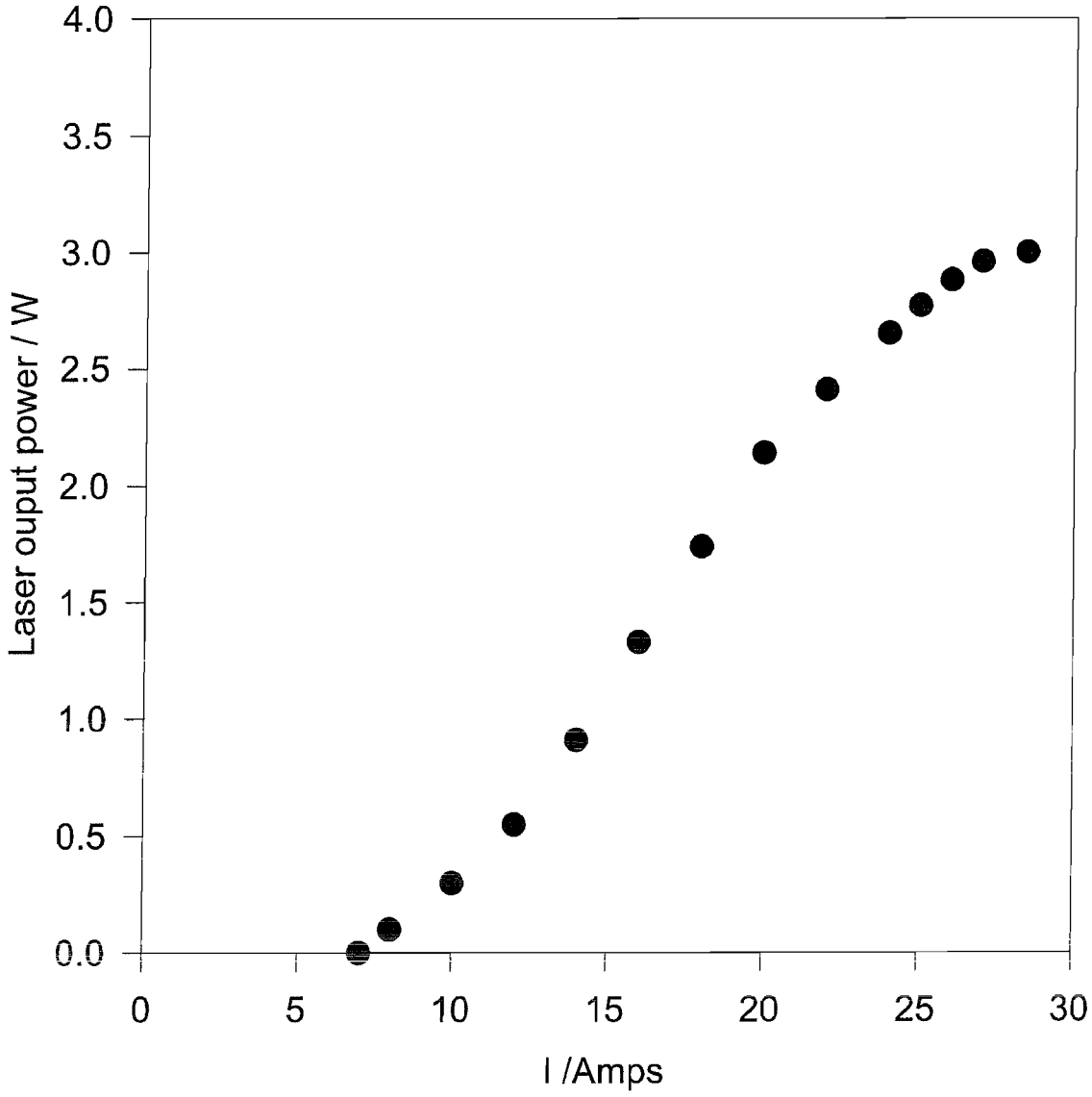

Figure 6.5 Output power of the 8μm waveguide laser versus diode current

The overall 20% optical-to-optical conversion efficiency from 17W of incident pump to 3.4W of output power confirms efficient coupling of the diode-bar output into the waveguide. The waveguide laser output was investigated using a polarising beam splitter and found to be unpolarised. This shows that there was no significant difference in loss between the transverse electric and transverse magnetic modes in the waveguide. A method of increasing the loss in one transverse mode relative to the other, in order to obtain a linearly polarised output, will be investigated in the next chapter.

A natural extension of this work was an investigation of lasing on the quasi-three-level neodymium $^4F_{3/2} \rightarrow {}^4I_{9/2}$ 946nm transition. The more favourable 1.064μm

transition was suppressed with a suitable choice of mirrors. The thin dielectric input mirror chosen was highly-reflecting (98%) at 946nm and only 5% reflecting at 1.064μm. The output mirror provided 20% output coupling at 946nm with only 10% reflectivity at 1.064μm. Both mirrors were highly transmitting for the pump wavelength.

From the quasi-three-level laser theory developed in chapter 2, this 7mm long waveguide with a pump spot of 2μm x 4mm and this particular resonator design should have a 946nm laser threshold of 1.08W. The same theory predicts a higher 1.064μm laser threshold of 1.79W.

A laser resonator was constructed with the thin mirrors and the waveguide output was observed with a triple grating spectrograph. Suitable pump filters were used to remove any residual, unabsorbed diode-bar pump light, however no laser action at 946nm was observed. The use of two high reflectivity mirrors at 946nm and cooling the waveguide by cooling the circulating liquid coolant in the waveguide heat sink, (but without causing condensation to form), also failed to achieve laser action at 946nm.

In order to investigate what might be preventing the onset of lasing the 946nm and 1.064μm fluorescence from the waveguide was monitored as the input current to the diode-bar, and thus the pump power into the waveguide, was increased. The 946nm fluorescence increased to a maximum value and was then clamped. The 1.064μm transition then took all the gain and increased steadily with diode power.

These results are shown in figure 6.6. Amplified spontaneous emission (ASE) at 1064nm is believed to be inhibiting 946nm laser action in this waveguide. Such behaviour has also been observed to occur in fibre lasers [20]. The ASE extracts the large gain available at 1.064μm, thus preventing lasing at the lower gain 946nm wavelength.

This could be reduced by increasing the loss at the longer (four-level) wavelength, for example by using filters or the cut-off properties of a waveguide [21].

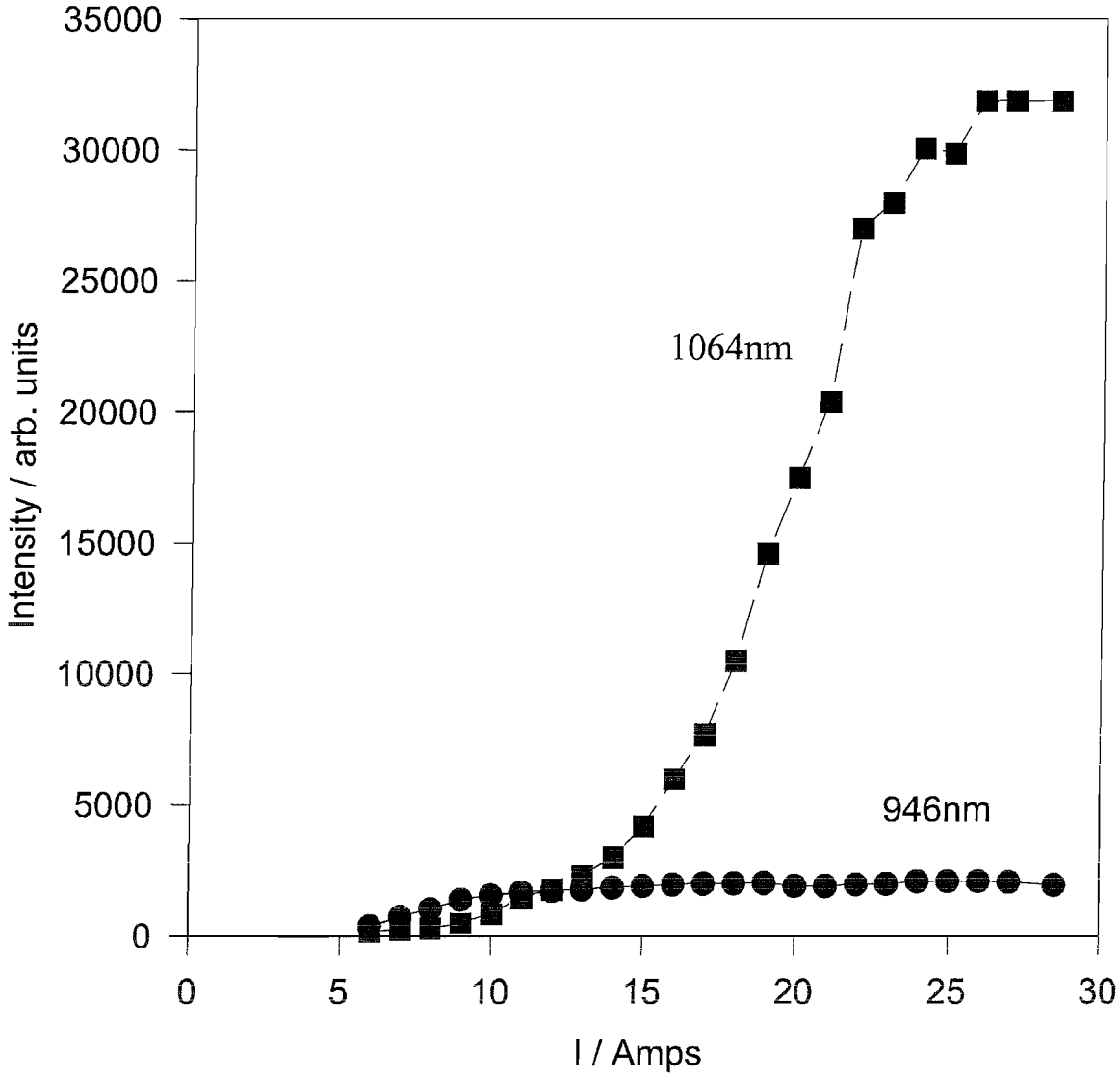

Figure 6.6 Fluorescence intensity at different Nd:YAG wavelengths with increasing diode current

For this planar waveguide further optimisation of the cavity length and mirror transmissions could decrease the threshold at 946nm to the point where lasing could occur before ASE took all the gain.

6.3.4.2 A 4μm Nd:YAG on sapphire waveguide laser

A different rod lens was required to give the best coupling efficiency into the 4μm guide. Experimentally a 1mm diameter, 0.685-mm focal-length lens was the most suitable. It gave a lower limit to the optimum launch efficiency of 60%. It is therefore

clear that a diode-bar can be efficiently coupled to both the 8μm and the 4μm direct bonded waveguides.

A waveguide laser was constructed around the 4μm waveguide to verify the high diode-bar coupling efficiency. Thin dielectric mirrors were butted to the end-faces of the waveguide, the input mirror was highly-reflecting at 1.064μm and had 92% transmission at the pump wavelength, 807nm. The output mirror was 20% reflective at 1.064μm and highly-reflecting at 807nm. This lead to a maximum laser output power of 2.5W, lower than for the 8μm waveguide. The significant difference in the output power from these two Nd:YAG lasers could be due to extra cavity losses produced by poor mirror adhesion and non-parallel waveguide end-faces, as well as the lower coupling efficiency.

The thickness of this waveguide requires tight focusing optics. The 0.685mm focal length lens used here has a working distance of just 0.185mm and the thin dielectric mirrors forming the laser resonator are ~170μm thick. Therefore it would be better to use mirrors directly coated to the end-faces of the waveguide. The lens must also be accurately positioned very close to the end-face of the waveguide. Manual adjustments at the micron level are possible with the three- and six- axis positioners used in the experimental set-up. However these resonator alignment factors were also thought to be responsible for the lower-than-expected performance of the waveguide laser.

6.4 Diode-bar coupling for side-pumped lasers

The coupling of diode-bars to waveguides using a side-pumping geometry has also been investigated. The main advantages with this technique are that the pump distribution is insensitive to the horizontal pump beam quality, making it very compatible with the output from a diode-bar and it can be easily scaled in power. The disadvantage is that the pump and laser signal beams propagate at 90^0 to one another, so the overlap between the two beams may be worse than for an end-pumped laser, resulting in a higher threshold and a lower slope efficiency. Initially the side-pumped geometry was investigated with a diode-bar focused into a waveguide using lenses.

However the eventual aim was towards a simpler, proximity coupled set-up with no intervening optics at all.

6.4.1 Lens array coupling

The first method used to side-couple the fibre-lensed diode-bar pump beam into a waveguide was four bulk cylindrical lenses, shown schematically in figure 6.1. This side-pumping technique was used to investigate the effect on laser performance of varying the pumping length of the waveguide, while keeping a constant pumping width. The waveguide chosen was the 80μm Nd:YAG waveguide fabricated by LPE and used in the laser described in section 6.3.2. The pumping geometry is illustrated schematically in figure 6.7.

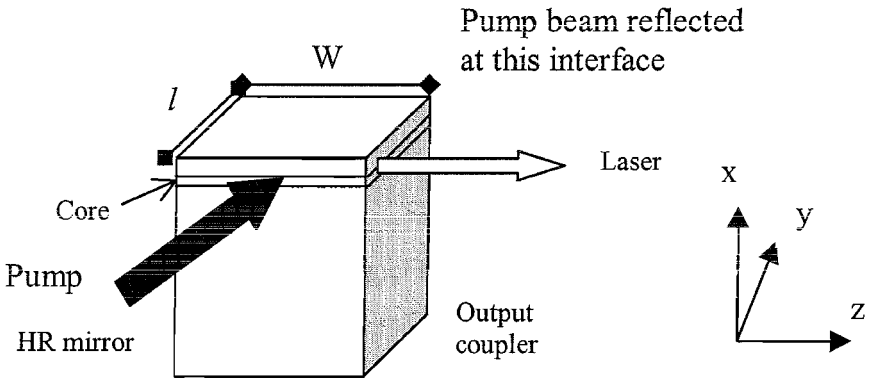

Figure 6.7 Schematic illustration of the geometry of side-pumping

The alignment and mounting procedure for the guide and diode-bar was as described earlier in this chapter for end-pumping, (section 6.3.2).

The first sample was 3mm in length (*l*) and pumped at its 5mm wide input face (W). The second waveguide was just 1.5mm in length (*l*), but the same width.

The laser cavities were formed by directly coated mirrors on the plane-parallel side-faces of the waveguide. This made a monolithic, very compact device. One side-face was nominally highly reflecting at the laser wavelength of 1.064μm, while the output face of the waveguide had a 5% transmission

A high reflectivity mirror at the pump wavelength (808nm) was attached to the back-face of the waveguide when required, to double pass the pump beam and maintain an efficient pump absorption. The results of the investigation are summarised in table 6.1.

Sample	W (mm)	*l* (mm)	Maximum output power (W)	M_x^2 x M_y^2
1	5	3	3.0	-
2	5	1.5	1.7	4x30

Table 6.1 Summary of side-pumped laser results

The smaller waveguide (sample 2) had a maximum output power and slope efficiency less than the larger dimension waveguide (sample 1). However the output was less divergent and had a lower M^2 in the non guided direction than the longitudinally pumped waveguide laser in section 6.3.2. This advantage, due to the smaller emission area of the gain, will be discussed further in chapter 7.

Overall these side pumped waveguide lasers did not perform as well as the end-pumped waveguide. The output powers obtained were considerably less, due mainly to the worse overlap between the pump and signal beams. However this side-pumping experiment provided a step towards the ultimate aim of side-pumping via proximity coupling.

6.4.2 Proximity coupling

Coupling a diode-bar pump beam into a waveguide with no intervening optics, leads to a simple and highly-compact arrangement, suitable for side-pumped lasers based on high NA waveguides. The initial demonstration [22] of the technique, described in this section, used an 808nm, 10W diode-bar from JenOptik and a waveguide with an 8μm thick core. However the technique will be of more practical use with a thicker, five-layer structure, investigated in chapter 7. The diode's fast-axis divergence was calculated by determining the spot size from the second moment of the beam intensity

profile (as described in chapter 3). The divergence, θ_{div}, was found to be 0.47 radians, corresponding to an NA of 0.45. The waveguide was an 8μm-thick, Nd:YAG core contact-bonded to a sapphire substrate, giving a NA approximately equal to that required to confine the pump beam. The scheme is shown schematically in figure 6.8:

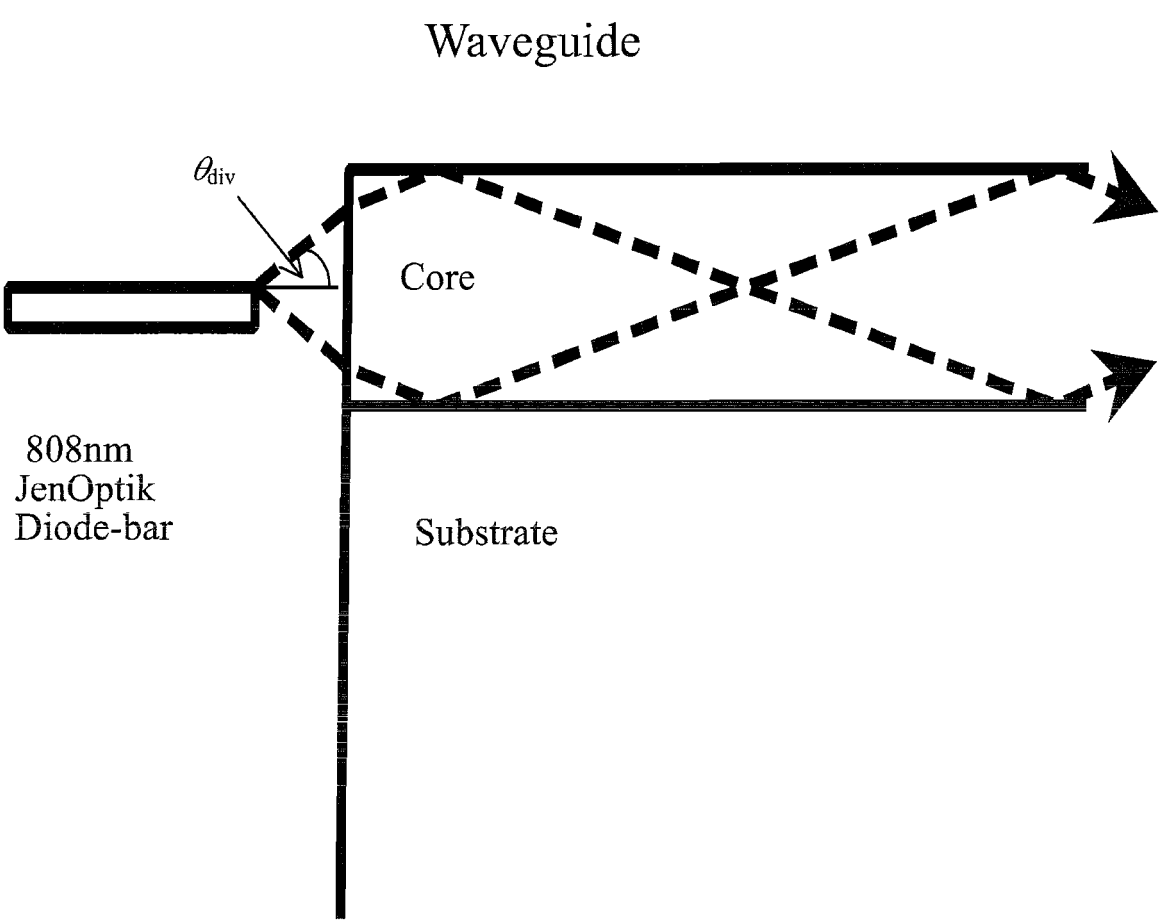

Figure 6.8 Schematic diagram of proximity coupling

The waveguide was cut and end-polished to dimensions of 18mm (W) and ~2mm (*l*), with reference to figure 6.7. This meant the waveguide was considerably wider than the 10mm emitting dimension of the diode-bar.

As the guide and diode-bar were gradually brought together measurement of their separation, optimisation of the fluorescence signal, and observation of the diffraction pattern of unabsorbed pump after the waveguide, were all used to achieve optimum orientation and positioning. The experimental technique and set-up are described more fully in chapter 3, section 3.11. Although physical contact was made between the diode-bar and waveguide, observing the diode-bar under a microscope suggested

that its actual emitters were slightly recessed from the plane of contact by a distance of ~9μm. The fluorescence was observed to increase with decreasing separation and figure 6.9 shows a picture of one end of the diode and waveguide observed through the microscope.

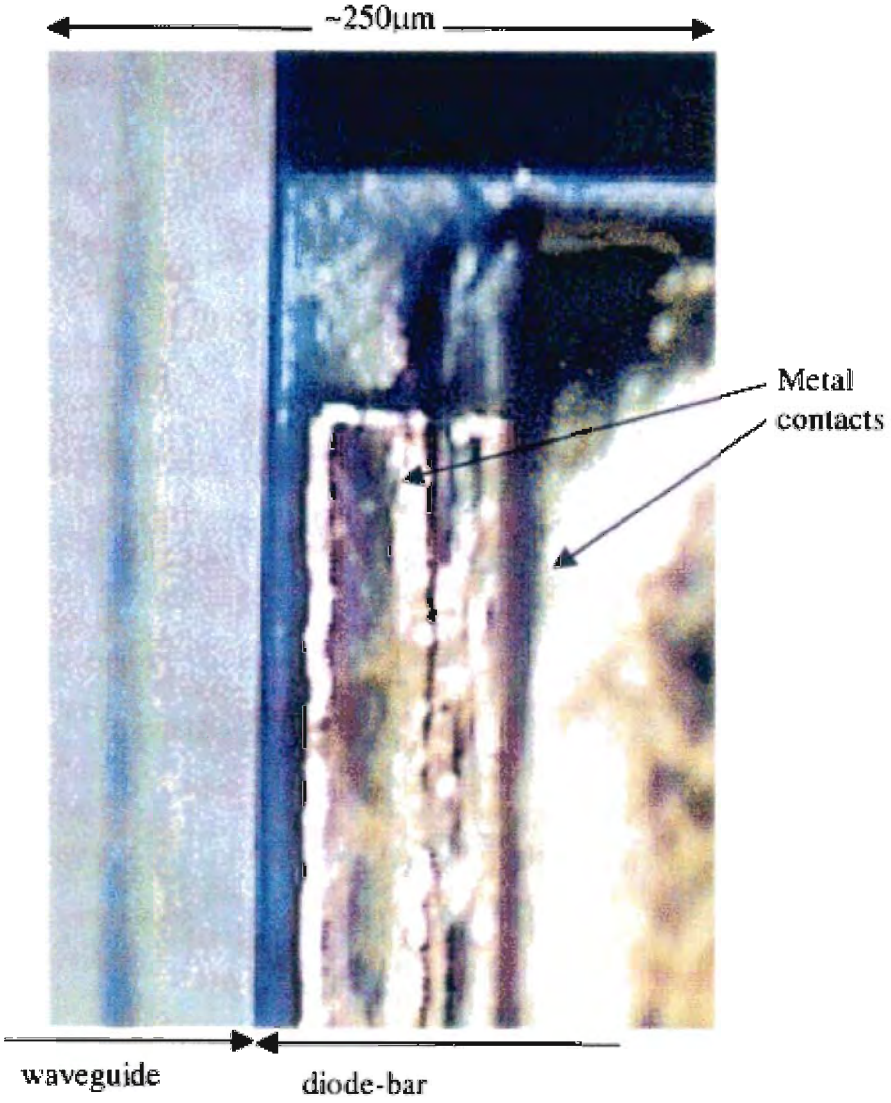

Figure 6.9 Microscope picture showing the plan view of the proximity coupled diode and waveguide

The product of single-pass absorption efficiency (over 2mm) and launch efficiency was measured to be 45%. The absorption length for the optimally-tuned diode-bar is around 3mm. This implies a very high launch efficiency of ~90%, a value consistent with an 8μm guide at a minimum separation from the emitters of 9μm. A side-pumped laser was constructed around this efficient and compact coupling system by

placing a high-reflectivity mirror at 1.064μm on one end-face and a 23% output coupler at 1.064μm on the other. A pump mirror was also used to double-pass the pump light through the waveguide. For 6W of incident power, the initial results produced over 0.5W of waveguide-laser output. However some of this output was in directions implying that internal reflections off the four polished side-faces was allowing different lasing paths within the waveguide. At this preliminary stage of investigating the technique no attempt has been made to suppress these reflections, although the presence of multiple lasing paths is an indication of the high gain available in the cavity.

The exceptionally close nature of this coupling scheme had some noticeable effects on the diode emission wavelength, particularly when the pump beam was reflected back and double passed through the laser cavity. The diode emission wavelength was observed to fluctuate between two wavelengths, one at 807nm and one at 809nm. These are either side of the neodymium absorption peak, and so affect the performance of the laser. Without the pump mirror in place the fluctuations were considerably less and the diode wavelength was more stable at 808nm. In the future this fluctuation could be reduced with an anti-reflection coating on the front face of the waveguide and selection of a longer waveguide pumping length. The initial demonstration of proximity coupling will be extended to a more practical, five-layer structure in the next chapter.

6.5 Diode-bar pumped waveguides – Summary

This chapter has discussed a number of techniques for diode-bar pumping waveguides. Bulk cylindrical optics were used with a relatively thick (80μm) waveguide core. Rod lens focusing was used to couple diode-bars into thinner waveguide cores, and an initial demonstration of the proximity coupling technique has been described.

The results outlined in this chapter show that high-power diode-bar pumped waveguide lasers, with multi-Watt output powers, are achievable with current technology. The challenge now is to improve the output beam quality and to scale the

devices to even higher powers and consistently high slope efficiencies. Steps towards realising this will include optimising waveguide cavity lengths, and using dielectric mirror coatings on the waveguide end-faces instead of butting thin mirrors to form laser cavities. In addition employing efficient methods of heat removal will be important.

6.6 References

[1] for example Th.Graf, J.E.Balmer, Opt. Lett., **18**, pp.1317-1319 (1993)

[2] R.J.Beach Appl. Opt., **35**, pp.2005-2015 (1996)

[3] W.A.Clarkson, D.C.Hanna, Opt. Lett., **21**, pp.375-377 (1996)

[4] S.Yamaguchi, T.Kobayashi, Y.Saito, K.Chiba, Opt. Lett., **20**, pp.898-900 (1995)

[5] H.Po, J.Cao, B.Laliberte, R.Minns, R.Robinson, B.Rockney, R.Tricca, Y.Zhang, Electron. Lett., **29**, p.1500 (1993)

[6] D.J.Ripin, L.Goldberg, Elec. Lett., **31**, pp.2204-2205 (1995)

[7] A.Faulstich, H.J.Baker, D.R.Hall, Opt. Lett., **21**, pp.594-596 (1996)

[8] C.L.Bonner, C.T.A.Brown D.P.Shepherd, W.A.Clarkson, A.C.Tropper, D.C.Hanna, B.Ferrand, Opt. Lett., **23**, pp.942-944 (1998)

[9] D.P.Shepherd, C.L.Bonner, C.T.A.Brown, W.A.Clarkson, A.C.Tropper, D.C.Hanna, H.E.Meissner, Opt. Commun., **160**, pp.47-50 (1999)

[10] M.W.Sasnett, in '*The Physics and Technology of Laser Resonators,*' D.R.Hall and P.E.Jackson eds. Chap 9, IOP Publishing (1989)

[11] B.Ferrand, D.Pelenc, I.Chartier, Ch.Wyon, J. Crys. Growth. **128**, pp.966-969 (1993)

[12] I.Chartier, B.Ferrand, D.Pelenc, S.J.Field, D.C.Hanna, A.C.Large, D.P.Shepherd, A.C.Tropper, Opt. Lett., **17**, pp.810-812 (1992)

[13] D.Pelenc, *'Guide d'onde laser en Nd:YAG et Yb:YAG per E.P.L.'*, PhD Dissertation, Département Optronique du LETI, C.E.N.G. 85X 38041 Grenoble, France (1992)

[14] Chapter 2, section 2.3.5

[15] W.A.Clarkson, D.C.Hanna, J. Modern Optics, **36**, pp.483-498 (1989)

[16] A.Nicia, Appl. Opt., **20**, pp.3136-3145 (1981)

[17] C.T.A.Brown, *'Nd –doped Crystal Waveguide Lasers and Amplifiers'*, PhD Thesis, University of Southampton, p.106 (1997)

[18] D.Findlay, R.A.Clay, Phys. Lett., **20**, pp.277-278 (1966)

[19] C.T.A.Brown, C.L.Bonner, T.J.Warburton, D.P.Shepherd, A.C.Tropper, D.C.Hanna, H.E.Meissner, Appl. Phys. Lett., **71**, 1997, pp.1139-1141 (1997)

[20] J.Nilsson, J.D.Minelly, R.Paschotta, A.C.Tropper, D.C.Hanna, Opt. Lett., **23**, pp.355-357 (1998)

[21] C.T.A.Brown, J.Amin, D.P.Shepherd, A.C.Tropper, M.Hempstead, J.M.Almeida, Opt. Lett., **22**, pp.1778-1780 (1997)

[22] C.L.Bonner, T.Bhutta, D.P.Shepherd, A.C.Tropper, D.C.Hanna, H.E.Meissner, in '*Technical Digest of Conference on Lasers and Electro-Optics*', 1999, paper CThD6

Chapter 7 Spatial mode control

7.1 Introduction

In order for high-power planar waveguide devices, such as those described in the last chapter, to have a successful future and find a niche in the laser applications marketplace, serious efforts must be made to improve the quality of the output beam. This chapter will describe the spatial mode control techniques used during the course of this thesis and discuss a few other methods that could be useful in improving beam quality in the future.

The first part of the chapter presents a study into improving guided direction mode quality. Two methods were used; coating an unclad waveguide with a thin metal layer, reducing the M^2 values in the guided direction and in addition, producing a TE polarised laser output [1], and using a waveguide with a double-clad structure to improve the beam in the guided direction [2]. The second part of the chapter examines how large M^2 values observed in the non-guided direction of a waveguide laser beam can be reduced. Techniques for achieving this could involve tighter pump focusing, for instance with a microlens array. Alternatively the high gain of the waveguide device could be used in combination with an unstable resonator design [3]. An initial study in this area is described, involving an unusual plane/plane unstable resonator cavity with a reduced geometrical output coupling area. Other areas such as diffractive optics, that have not yet been applied to a crystal waveguide laser, will also be considered as a means to overcome the inherent lack of lateral confinement in a planar geometry.

7.2 Spatial mode control in the guided direction

7.2.1 Thin metal overlayer - Introduction

A straightforward, and therefore attractive, mechanism for controlling the modal losses in a waveguide results from coating the waveguide with a thin metal film [4]. This technique has previously been shown to produce a linearly-polarised, transverse-

electric field (TE) output from a Nd:YAG on YAG planar waveguide pumped by a Ti:sapphire laser. A polarised output may be useful for frequency conversion applications, but the significant additional benefit of the technique was that some improvement in guided direction M^2 values was obtained [1]. Here, the metal overlayer approach was applied to a more extreme case; that of a diode-bar pumped Nd:YAG on sapphire waveguide.

7.2.1.1 Metal overlayer - Theory

A metal overlayer can lead to a polarised output because the transverse magnetic (TM) modes of the waveguide penetrate it more deeply and so have higher losses compared to the TE modes [1]. A thin metal layer can also have the effect of exciting a surface plasmon resonance (SPR) for the TM modes, which further enhances the TM mode coupling into the lossy metal. A surface plasmon is a TM mode guided by the interface between two media whose dielectric constants have real parts of the opposite sign. A dielectric and a metal have dielectric constants that fulfil this requirement in the visible and infra-red part of the spectrum. So with these materials TE polarised light will not excite a SPR and instead the TM modes of the waveguide will see the greatest propagation loss.

The operation of an unpolarised multimode slab waveguide device coated with a thin metal film and guiding both TE and TM modes, can be described in terms of coupled modes [5]. The surface plasmon mode (SPM) is guided by the interface between the dielectric core (in this case YAG) and the metal layer. The TM modes couple to this SPM in varying degrees, as the strength of the coupling depends on how closely phase matched a particular TM mode is to the surface plasmon mode. The coupling of some of the TM polarised light out of the waveguide core into the metal overlayer results in higher TM losses and thus preferential TE laser operation.

For a multimode waveguide device the evanescent part of any higher-order laser mode extends further into a surface layer than the evanescent part of the fundamental mode. So the metal overlayer also causes increased loss for higher order TE modes. The result is that the device has the lowest propagation losses for the TE polarised fundamental mode.

7.2.1.2 Metal overlayer - Experimental technique

Previous workers in an initial attempt to approach single mode output in the guided direction using a thin metal overlayer, deposited an approximately 50nm thick Au film on the surface of an 8.3μm core size Nd:Ga:Lu:YAG on YAG planar LPE waveguide [1]. A laser resonator was constructed and, when pumped with a Ti:sapphire laser, a linearly polarised TE output was obtained from the device. In addition a >2 times decrease in guided direction M^2 was observed. The near diffraction-limited output (M^2=1.2) from the waveguide was obtained without any noticeable degradation in laser performance.

Here, a waveguide with a larger numerical aperture, suitable for diode-bar pumping, was investigated. The 19mm long waveguide sample consisted of an 8μm 1at. % neodymium doped YAG core direct bonded [6] to a sapphire substrate, with no cladding layer. Results presented in chapter 6 have already shown that this waveguide has low propagation loss and is suitable for diode-bar pumping. The waveguide was first cleaned and then coated with a layer of gold using an Edwards Thermal Evaporator. The thickness of the gold film was measured to be 60nm with a Tencor Alphastep 2000 surface profiler. The gold was etched from the end-faces of the waveguide to remove any excess which had coated these areas during the deposition. In order to test the lasing behaviour of the sample it was pumped with a 20W fibre lensed diode-bar (OptoPower Corp.), operating at 808nm in the TE polarisation. Focusing the diode-bar pump light into the waveguide was achieved with a rod lens of focal length of 1.027mm and a 19-mm focal-length cylindrical lens, (as described in chapter 6 section 6.3.4).

The experimental set-up is shown in figure 7.1. The laser resonator was formed in the usual way with thin dielectric mirrors held on the waveguide end-faces with fluorinated liquid and glue. The waveguide laser operated on the four-level transition around 1.06μm and the input mirror was highly reflecting at this wavelength. Two different output couplers were used; one with a nominal 50% transmission at 1.064μm and the other with 3.5% transmission.

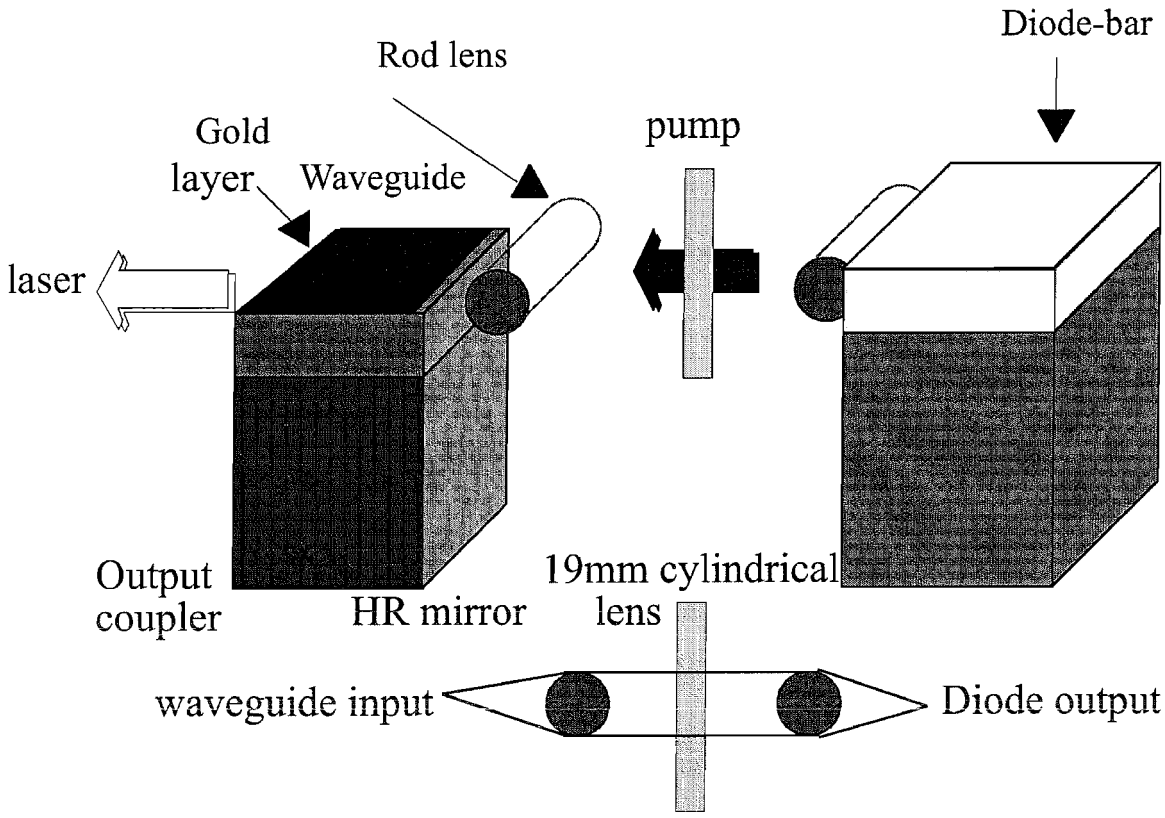

Figure 7.1 Schematic diagram of the experimental set-up for diode-bar pumping a gold coated waveguide

Previous results from the same waveguide laser set-up, but without a metal overlayer gave a maximum output power of 3.7W with 50% output coupling at the laser wavelength. M^2 values of 10 X 85 were measured in the guided and non-guided directions respectively. Now with gold completely covering the top surface of the waveguide the M^2 values improved to 3 X 45 in the guided and non-guided directions respectively. However, this improvement was also accompanied by a 40% drop in output power, due to the overall increase in propagation loss.

In an effort to avoid pump power loss some of the gold (nearest the diode) was etched away leaving the device with one pump absorption length uncoated. Just a 5mm section of gold coating at the end of the device still gave an improvement in the laser beam quality, with M^2 values of 6 X 40 measured in the guided and non-guided directions respectively. The output power was now measured to be 2.5W, 30% less than the original value.

The metal overlayer technique clearly needs further investigation but has been shown to give some degree of mode control in the guided direction. The same investigation could also be carried out on a thinner waveguide, initially supporting fewer modes in the guided direction. However a thinner waveguide requires tighter focusing optics and mirrors coated onto the end-faces, making the scheme more complex.

Instead, another method of obtaining a diffraction-limited output from the waveguide was devised, utilising a double-clad waveguide design.

7.2.2 Double-clad waveguides - Introduction

Double-clad structures were first employed in high-power fibre lasers [7] to effectively capture a diode-bar pump beam. Such a fibre has a single-mode, rare-earth-doped lasing core surrounded by a much larger, higher NA, inner-cladding used to confine the pump beam. The diode light is gradually absorbed on each pass through the doped region, and a single-spatial-mode laser is produced.

A planar guide, however, needs a larger size of core relative to its inner-cladding. This is necessary to avoid increasing the absorption length for the pump light beyond the waveguide fabrication lengths currently possible. This means the device operates differently to a double-clad fibre laser. The planar waveguide laser has its output spatial mode controlled by the dopant confinement and not the optical confinement provided by the core. So instead of cladding pumping a single-mode core the planar device works by gain mode selection in a multimode guiding structure.

The theory behind the double-clad waveguide design will now be discussed in greater depth, followed by some fabrication details. Results for proximity-coupled, diode-bar, side-pumped Nd^{3+}- and Yb^{3+}- doped YAG double-clad waveguide lasers will then be given. These structures both gave multi-Watt, single-guided mode laser outputs.

7.2.2.1 Double-clad waveguides - Design

A typical guiding structure for a high-power double-clad fibre device is shown in figure 7.2 (a).

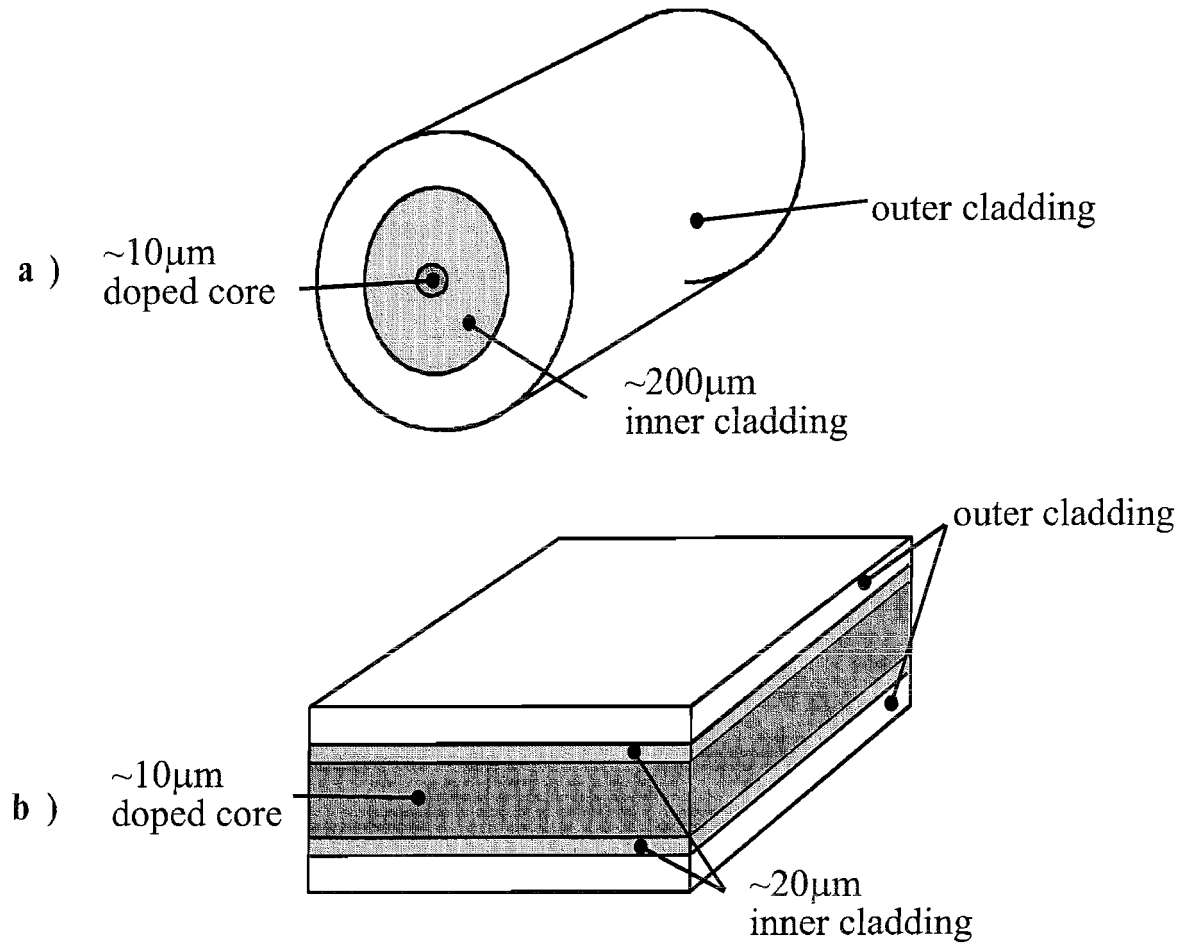

Figure 7.2 Typical double-clad waveguide designs for high-power diode-pumped lasers and amplifiers in (a) fibre and (b) planar geometries.

The single-mode core is surrounded by a larger, multi-mode, inner cladding. An outer cladding, of a much lower refractive index surrounds this. The non-diffraction-limited diode pump beam, after circularisation, is contained within the high numerical aperture (NA) waveguide formed by the two claddings. The pump radiation is gradually absorbed by the core with each pass, increasing the effective pump absorption length compared to bulk material. Other design modifications can be made,

such as an off-centre core [8] to absorb any pump propagating in helical modes that would have otherwise missed interacting with the doped core.

The design for a planar double-clad structure (figure 7.2 (b)) is limited by the length of device that can be fabricated with low propagation losses. Unlike a fibre geometry the planar waveguide cannot tolerate the increased length necessary for pump absorption, therefore the typical design has the doped core occupying a significant amount of the overall pumped region. This results in increased absorption efficiency for a bouncing ray model and an increase in the overlap of the doped region with the guided pump modes. However the greater overlap that the higher order modes of the waveguide, formed by the inner-cladding, have with the doped gain region may increase the possibility of a non-diffraction-limited output.

The two double-clad planar waveguide structures described in this thesis have an outer cladding of sapphire, an inner cladding of undoped YAG and an inner core of rare-earth-doped YAG. The outer guiding structure has an NA of 0.46, which has been shown in chapter 4 to provide sufficient confinement for the output of a diode-bar. Guidance in the central core is provided by the increase in refractive index associated with rare-earth doping. The refractive index values in this waveguide design are shown in table 7.1 [2] and the refractive index profiles of the waveguide structures are shown in figure 7.3 (a).

	808nm	941nm	1029nm	1064nm
Sapphire (n_0)	1.760	1.757	1.755	1.755
YAG	1.8212	1.8175	1.8154	1.8147
10at. % Yb:YAG	-	1.8187	1.8166	-
1at. % Nd:YAG	1.8216	-	-	1.8151

Table 7.1 Relevant refractive indices for the double-clad planar waveguides at pumping and lasing wavelengths

The tabulated values for the increase in refractive index due to doping are quoted at 633nm. Observations show that the index difference does not change dramatically with wavelength [9], so these values should also be valid at the lasing wavelengths around 1.1μm.

a)

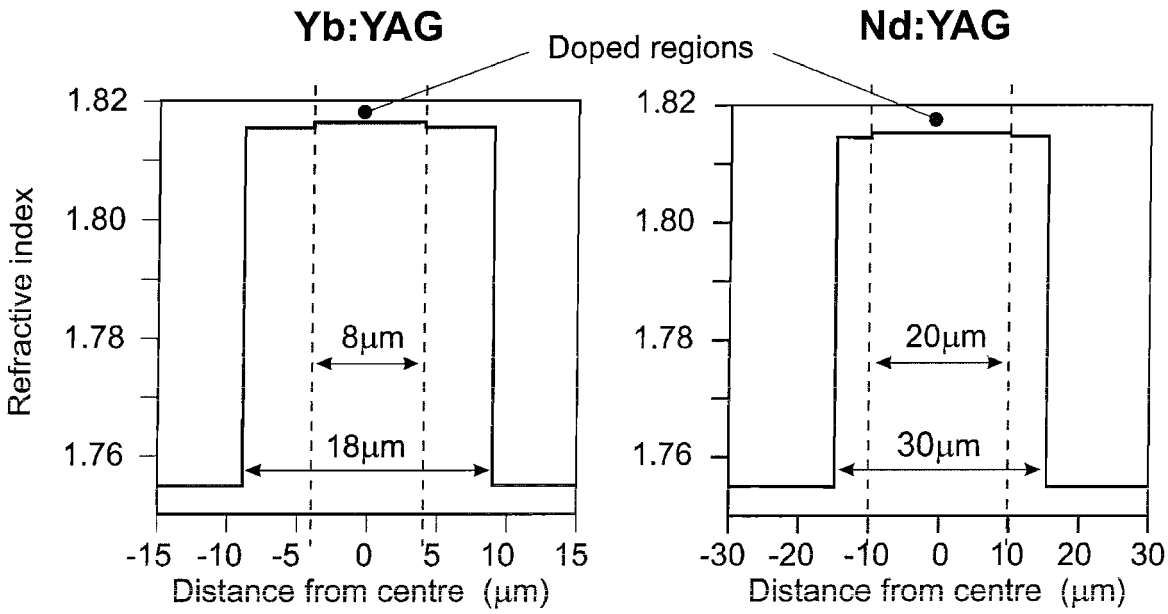

Figure 7.3(a) Five-layer refractive index profiles for the double-clad Yb^{3+}- and Nd^{3+}-doped waveguides

In order to calculate the predicted propagation modes in the core waveguide (i.e assuming an infinite inner cladding) at the laser wavelength the three-layer symmetric slab waveguide model (section 2.2.3) was used.

Figure 7.3 (b) shows the predicted propagation modes (TE are shown here). Both waveguides can be seen to allow two propagation modes, both of which still have a significant intensity at the point where they would reach the outer cladding layer.

Figure 7.3 (c) takes another scenario and shows the predicted TE modes for the laser in the inner cladding guide, (i.e assuming no core and an infinite outer cladding layer). In these figures the fundamental mode and the highest order mode only are shown.

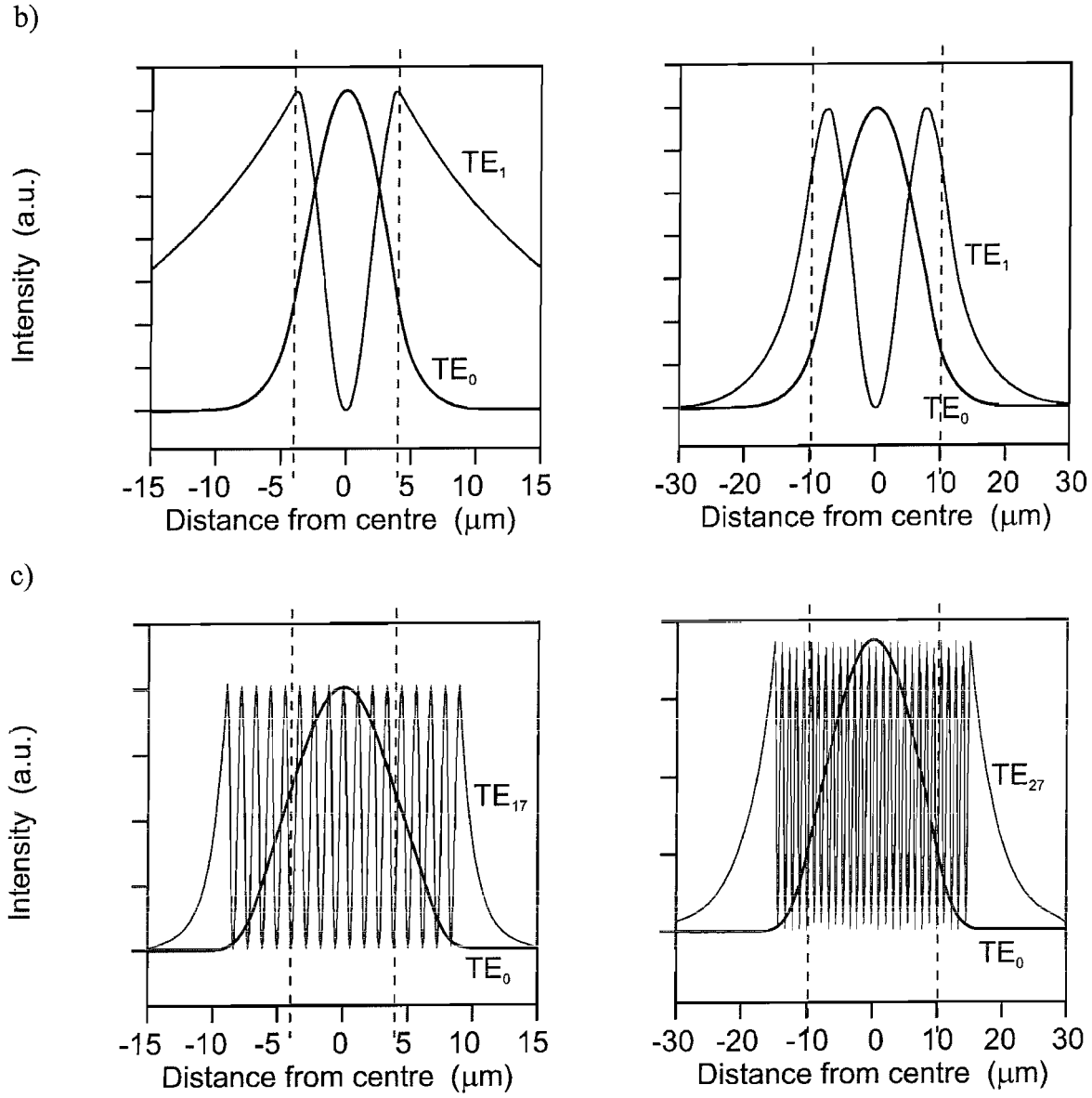

Figure 7.3 Theoretical mode profiles for the three-layer core (b) and cladding (c) waveguides.

The three-layer theory shows that the Nd^{3+} structure supports 28 modes and the Yb^{3+} supports 18. Figure 7.3 (c) shows that the higher order modes of the cladding guide have a significant overlap with the gain region. Thus a multi-mode laser output would be expected from a structure with dopant throughout the cladding waveguide. However the fundamental laser mode has the best overlap with the actual doped region, and the smallest mode size, so should reach laser threshold first. Once this fundamental mode is above threshold it is able to saturate the available gain in the confined, doped region. This stops the higher order modes from reaching threshold and a single-mode output is obtained. The fundamental mode that operates under

these conditions is in fact a mode of the overall multi-mode five-layer structure, and not one of the modes shown in figure 7.3.

It is now necessary to consider if the index change arising from rare-earth doping the core has any effect at all on the mode. Figure 7.4 shows the effect the doping has on the fundamental mode of both waveguide structures.

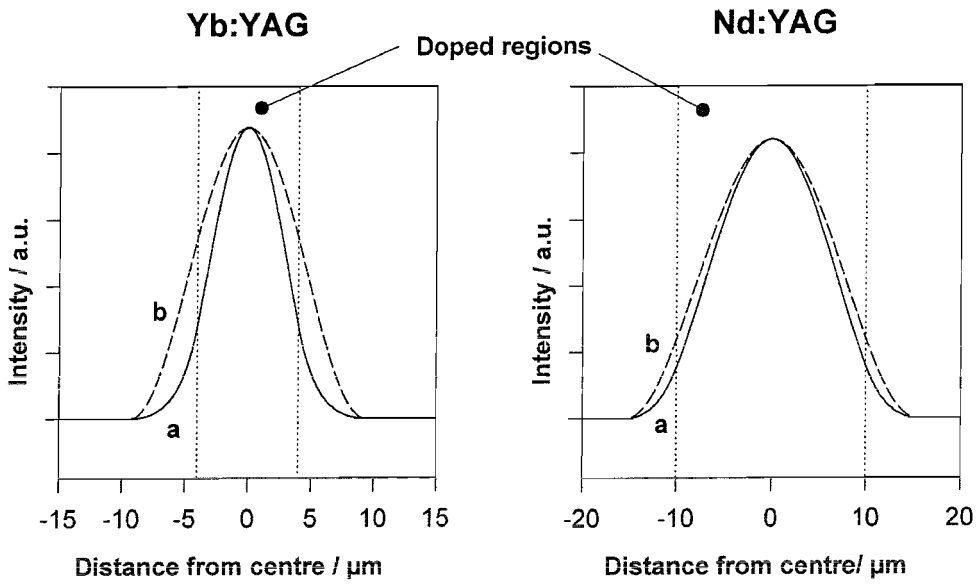

Figure 7.4 Comparison of the theoretical fundamental mode profiles of the five-layer structures (a) with and (b) without a refractive index change due to rare-earth doping

Figure 7.4 clearly illustrates that the increase in refractive index leads to a tighter confinement of the mode to the doped region. This confinement will lower the threshold for the fundamental mode, but may in turn make it more difficult to saturate the gain fully.

From this discussion and figures 7.3 and 7.4 it can be seen that mode of operation of these double-clad waveguide lasers differs from the regime of cladding-pumping. In a truly cladding-pumped device the doped core size is much smaller than the inner cladding, and the lasing mode is associated with the core guiding structure only. The single-mode waveguide effectively has an infinite cladding layer. A more accurate

description of the new regime would be gain-mode selection. It applies in a situation where the mode of the core has an appreciable intensity at the boundary with the outer cladding region. A problem with this design may arise as the core to cladding size ratio approaches 1. The higher order modes may then overlap with regions of unsaturated gain and start to lase. Experiments so far have shown that ratios of 0.67 for Nd:YAG and 0.44 for Yb:YAG give single-mode outputs.

The advantage of such high ratios is the increased absorption efficiency. This is of particular relevance to planar devices, but large mode areas can also be of interest in high-power pulsed fibre lasers in order to increase energy storage capabilities. This has already inspired work on large mode area fibres [10] where the fundamental mode of a multi-mode core is selected by only doping the central region. A cladding-pumped version of this fibre design has also recently been reported [11], but in this case the mode selection is still strictly from amongst those associated with the core rather than the overall structure. However, it is possible that the desire for further increases in power could push double-clad fibre lasers into the high core to cladding ratio regime. It is also interesting to note that a core-doped bulk laser, also made by direct bonding, has recently been demonstrated which shows enhanced beam quality over a uniformly-doped rod [12]. In this case mode selection occurs between those modes allowed by the optical resonator rather than those allowed by a multi-mode waveguide.

7.2.2.2 Double-clad waveguides – Fabrication and characterisation

The five-layer planar double-clad structures were fabricated by the direct bonding technique [6]. Details of each layer thickness in both structures are given in figure 7.3 (a). The 10at.% Yb^{3+}- doped YAG core was 8μm thick and sandwiched between two 5μm layers of undoped YAG forming the inner cladding. YAG has good thermal and mechanical properties and bonds well to the ~1mm thick sapphire forming the outer cladding material. The Nd- doped five-layer structure has a slightly thicker inner core. It had a 20μm 1at.% Nd^{3+}- doped YAG core surrounded on both sides by 4μm of undoped YAG and then ~1mm of sapphire as the outer cladding.

The double-clad structures were characterised using the Yb^{3+}- doped guide pumped by a Ti:sapphire laser [2]. The size of the waveguide was 10mm x 5mm in the non-guided plane. The absorption length was estimated from reference 13 to be ~1.1mm at 941nm and 968nm, and ~1.9mm at 915nm. This length is expected to increase for the double-clad guide by, approximately, the ratio of the undoped to doped areas of the pump region. Ti:sapphire pumping was at 915nm as the pump laser had greatest output power here, resulting in an absorption length of 4.3mm. The waveguide was end-pumped in the 5mm direction and the resonator was formed with thin dielectric mirrors butted to the end-faces. For the initial waveguide characterisation care was taken to couple the pump light into the waveguide so that a fundamental pump mode was propagating. This was observed by imaging the output onto a CCD camera. The 1.029μm lasing threshold was monitored with different output mirror reflectivity, (after the method of Findlay and Clay, see chapter 3 section 3.8.2) and the waveguide was found to have a propagation loss of 0.2dB/cm [2]. This is similar to loss values measured for two-layer direct bonded waveguides [6, 14].

Close to 100% launch efficiency into the waveguide was obtained and a highly efficient waveguide laser was formed by one HR mirror and one bare end-face of the waveguide. The slope efficiency (76%) was close to the quantum limit for 915nm pumping (89%) and further illustrates the high quality of the waveguide structure.

The mode profile of the lasing output was investigated using a CCD camera and a Coherent Modemaster M^2 meter. The pump focusing optics were altered to couple into the higher order modes of the five-layer structure and the modes were viewed on a CCD camera, despite this only a single mode waveguide laser output was observed. A clean, single-lobed output is not however sufficient proof of single-mode diffraction-limited behaviour, (as discussed in the section on M^2 in chapter 2), however when M^2 measurements were taken with a Coherent Modemaster, a value of $M^2 = 1.2$ was found in the guided direction. This confirmed the single-mode, guided direction output from the five-layer structure.

7.2.2.3 Double-clad waveguides – Proximity coupling

The excellent quality, five-layer structures were combined with the technique of proximity coupling in a step towards a compact high-power, diffraction-limited device.

The initial demonstration of a proximity coupled waveguide laser had been with a two-layer structure, with an 8μm thick core. The waveguide was side-pumped by a 7W diode-bar and further details can be found in chapter 6 (section 6.4.2.). As a first experiment this demonstrated the overall feasibility of the pumping technique. Now the 1cm long x 5mm wide, double-clad, Nd^{3+}- and Yb^{3+}- doped waveguides described theoretically in section 7.2.5 were proximity-side-pumped with 20W diode-bars, at 807nm and 941nm respectively. The proximity coupling technique has been described in section 3.11. Work on the Yb^{3+}- doped YAG waveguide was carried out by the author at the Optoelectronics Research Centre, University of Southampton. The laser results from the Nd^{3+}- doped YAG waveguide were obtained by Ray Beach, Maxios Laser Corporation, California, USA. The neodymium doped waveguide results have been included for completeness and are reproduced in figure 7.7 with the kind permission of Ray Beach.

The larger overall pumping area of the five-layer structures meant that aligning the waveguide and diode-bar was easier than for the 8μm core waveguide previously attempted. An upper limit to the combined launch and absorption efficiency was measured to be 63% for the Yb^{3+}- doped sample. This measurement was taken by comparing the pump power before and after the waveguide. However it was not possible to catch all the pump light after the waveguide, so the measurement must be taken as an upper limit only. The 5mm dimension (l) of the double-clad waveguide is approximately one absorption length for the diode pump, so the launch efficiency is expected to be close to 100%. Figure 7.5 shows laser output power verses incident pump power for the Yb:YAG laser.

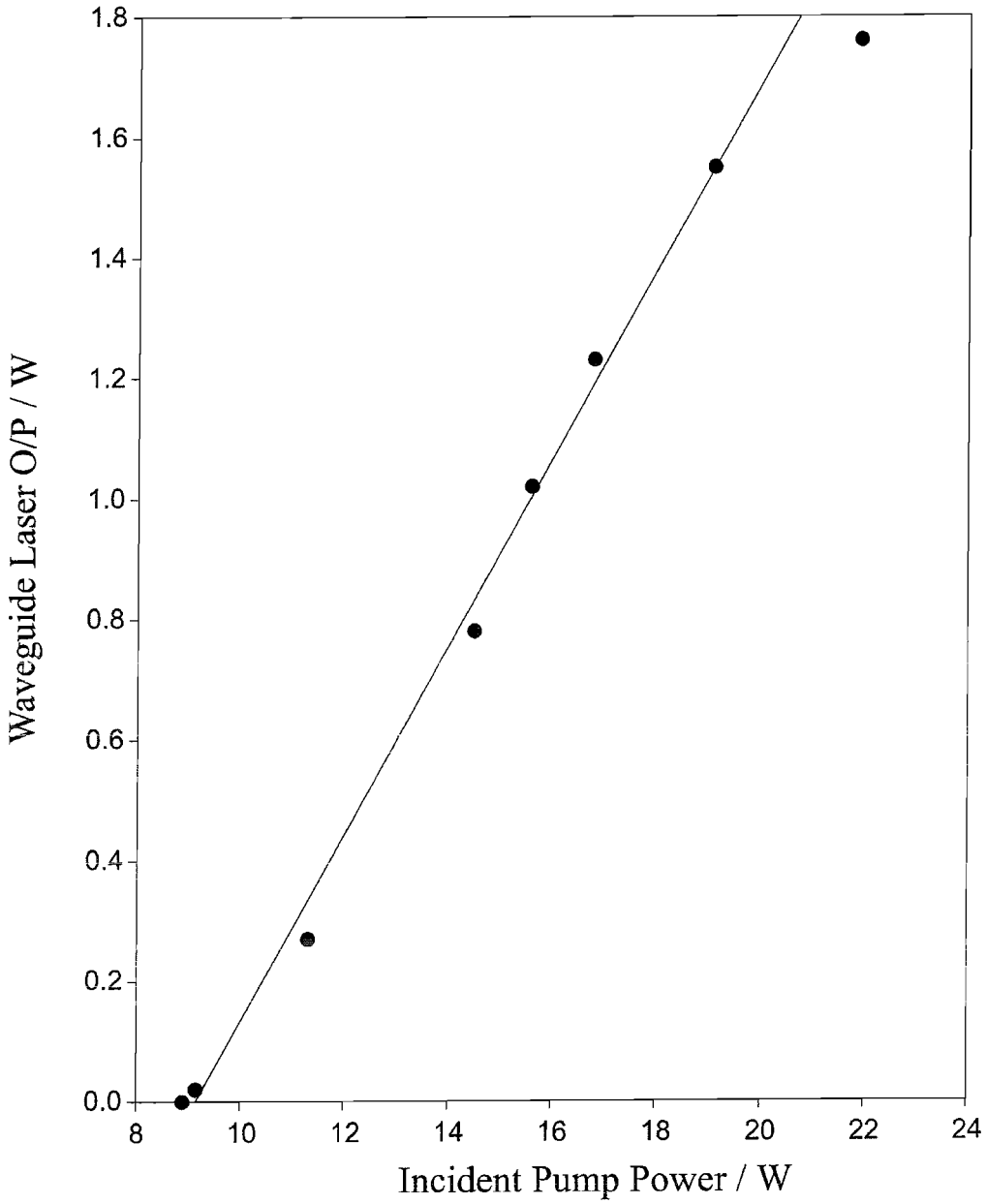

Figure 7.5 Output power versus incident pump power for the double-clad, proximity-coupled Yb:YAG laser

Figure 7.5 shows results taken using a 7.5% output coupler, resulting in a slope efficiency of 14.5% with respect to incident power. This gives a slope efficiency of at least 23% with respect to absorbed power, with a Fresnel reflection taken into account. Optimising laser output at the highest pump level gave a maximum output power of 2.2W. A mirror was used to reflect any unabsorbed pump light back into the waveguide, but no further increase in output power was obtained. The lasing wavelength was found to be 1048nm, this is the transition to the highest Stark level of the $^4F_{7/2}$ ground level. The 1048nm transition has a lower emission cross-section than

the more common 1029nm lasing line, but it suffers from less reabsorption loss and so preferentially lases in some cases [15].

The mode quality of the output beam was analysed by measuring the far-field output profile of the beam in the guided direction. A scan was made of the vertical intensity profile of one section of the output, this scan is shown in figure 7.6.

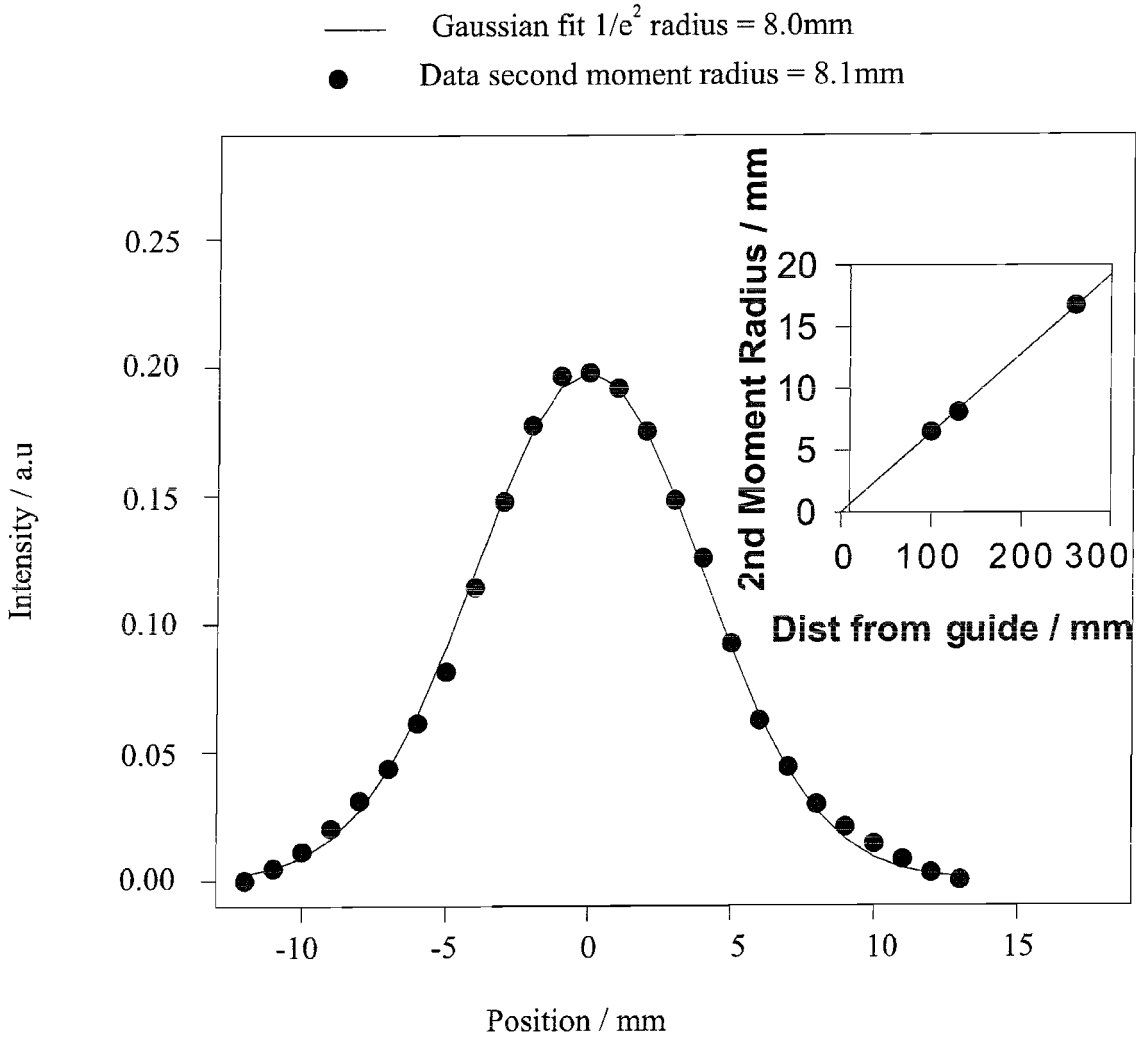

Figure 7.6 Measured far-field intensity profile in the guided direction with a Gaussian fit. Inset shows the measured second moment radius at various distances from the waveguide output.

The plot in figure 7.6 shows that the results fit well to a Gaussian. Measurement of the second moment radius at various distances from the waveguide output gives a divergence of 64.1 mrad. The calculated radius of the fundamental mode of the

Yb:YAG five-layer guide is 5.26μm, leading to an output divergence of 63.4 mrad. The divergence observed is therefore consistent with the laser operating on the fundamental mode with an M^2 very close to 1. In contrast the output in the non-guided plane, although in a single lobe, is highly multi-mode with a divergence suggesting an $M^2 \sim 300$. This is as expected for such a large area of gain with, as yet, no attempt to control the mode in this direction.

The laser output was TE polarised, as observed with Ti:sapphire pumping [2]. This linearly polarised output is in contrast to the randomly polarised output previously observed with two-layer YAG on sapphire waveguides, and is perhaps an indication of the increased stress in the five-layer structures, leading to a difference in TE and TM propagation losses and/or mode sizes that is sufficient to give a polarised laser emission. At present it is not known if such effects are responsible for this behaviour, but in practice this is a very convenient way of obtaining a polarised output which may be useful for future application to non-linear frequency conversion.

Figure 7.7 shows the results obtained by Ray Beach from the Nd:YAG five-layer structure using a 60% reflectivity output coupler.

This laser can be seen to operate at a lower threshold (~5W) and with higher efficiency than the double-clad Yb:YAG laser. A slope efficiency of ~20% with respect to incident power was obtained, and with maximum pump power a laser output of 4W was measured. The output divergence from this laser was again observed to be consistent with a fundamental guided mode output. The laser output was at 1.064μm and was TE polarised.

Both the techniques outlined so far show that a significant degree of mode control is possible in the guided direction while still retaining the simple monolithic, planar waveguide structure. Now methods of spatial mode control in the non-guided direction will be examined with the aim of producing a diode-bar pumped, high-power, fully diffraction-limited device.

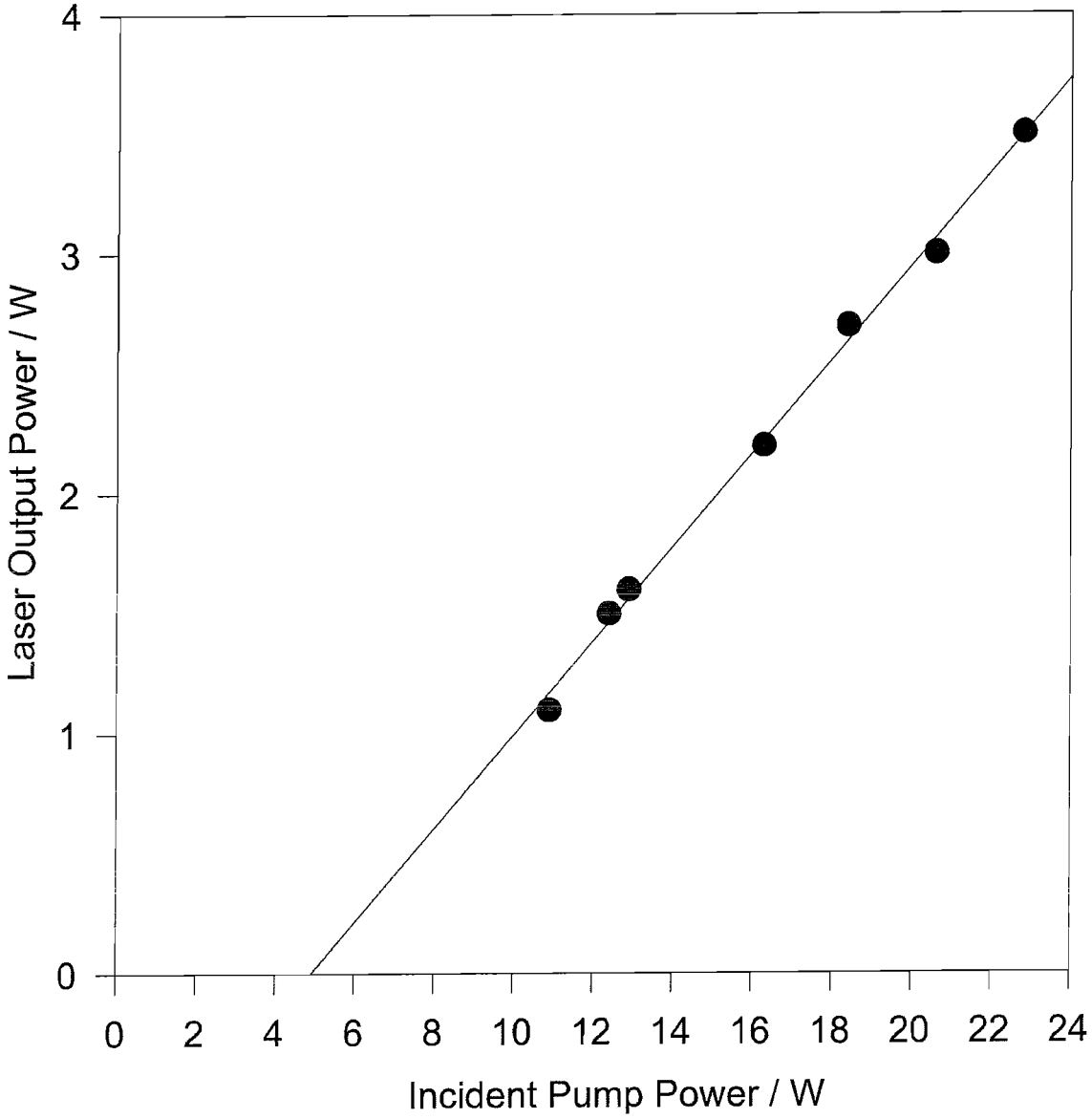

Figure 7.7 Output power verses incident pump power for the double-clad, proximity-coupled Nd:YAG laser

7.3 Spatial mode control in the non-guided direction

The lack of lateral confinement in a planar waveguide results in a large M^2 value for the laser beam in the non-guided direction. Many applications require a laser output with close-to-diffraction-limited (low M^2) performance in both the guided and non-guided directions. Methods of improving the beam quality in the non-guided direction will now be considered.

7.3.1 Tighter pump confinement

A simple idea for increasing the laser beam brightness in the non-guided direction is to focus and confine the pump beam more tightly. This could be achieved with a device such as a microlens array or a similar beam concentrator [16], perhaps combined with side wall guidance. The input width of the planar waveguide itself can then be reduced. A reduction in the diameter of a laser medium (the slab width in this case) increases the fraction of laser power in the lowest order modes. Thus the beam quality of the output is improved. This can be seen by characterising the gain medium in terms of its Fresnel number [17]. A rod-shape laser medium of length l, width (or diameter) 2a and operating at laser wavelength λ, has a Fresnel number, N_F written as:

$$N_F = \frac{a^2}{l\lambda} \qquad 7.1$$

Extending this to a planar waveguide layer of thickness (depth) d suggests:

$$N_F = \frac{ad}{l\lambda} \qquad 7.2$$

From the assumption that the diameter of the lowest order mode of a laser rod is of the order of $(l\lambda)^{1/2}$ [17], it is suggested that the diameter of the lowest order mode of a planar waveguide slab would be $(l\lambda)^{1/2}$ in the guided direction, but extend to approximately fill the waveguide in the non-guided direction. It follows that the cross-sectional area of the lowest order mode of the waveguide is of the order of $a(l\lambda)^{1/2}$. This leads to the ratio of the laser medium cross sectional area to the lowest order mode cross sectional area being significantly less than the Fresnel number. The Fresnel number can be much larger than unity. This means that the lowest order mode will extract less than the fraction $\sim 1/N_F$ of the energy available. This can be improved by reducing the diameter of the gain medium (the slab width, 2a). Then the fraction of power in the lowest order modes will be increased, resulting in a reduction in the M^2 of the output. However, it is important to remember that the diameter of the gain

should also be maintained to be greater than the pump beam width to ensure a high coupling efficiency into the waveguide.

This technique of reducing the gain diameter was used with the 80μm thick LPE Nd:YAG on YAG waveguide sample and an experimental set-up described in chapter 6. The original 6mm wide waveguide sample was cut and re-polished to form two samples; one 3mm wide, the other 1.5mm wide. The experimental set-up is shown in figure 7.8. The pump source was a 20W diode-bar and the waveguides were end-pumped with cylindrical lens array focusing, as shown first in figure 6.1.

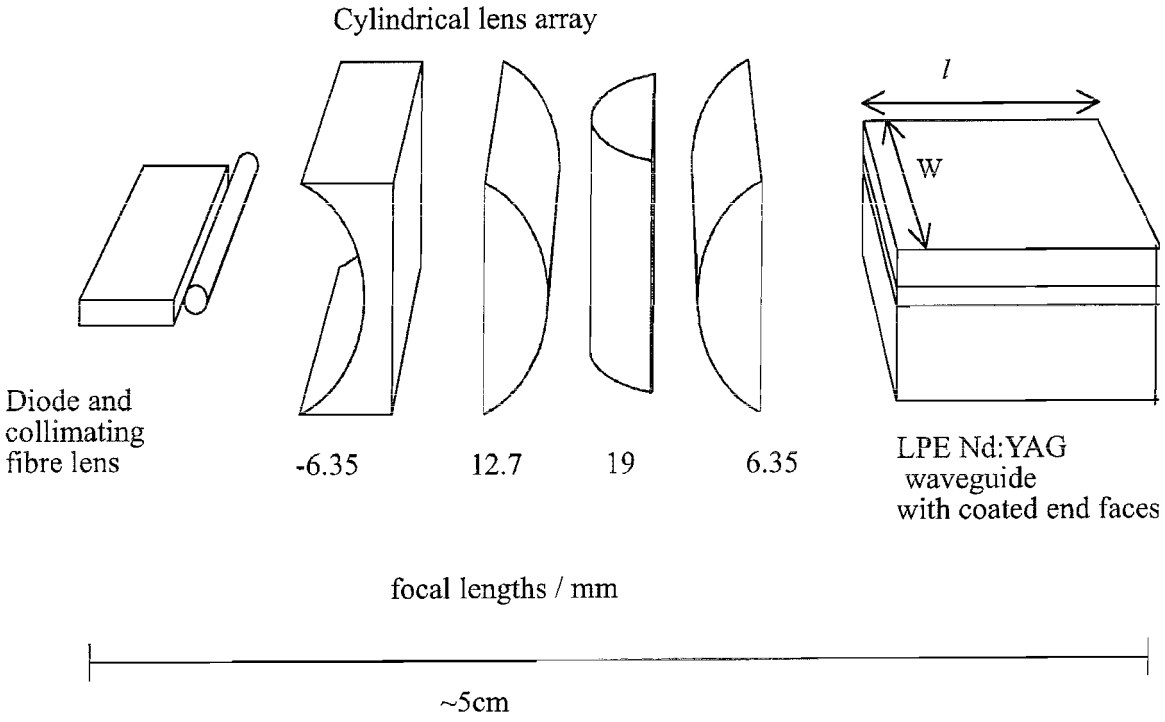

Figure 7.8 Reducing gain diameter: experimental set-up

Waveguide dimensions		Waveguide laser performance		
W (mm)	*l* (mm)	Output power (W)	M_x^2, M_y^2	Optical-to-optical conversion efficiency (%)
6	5	6	3 x 140	39
3	5	3	4 x 85	18
1.5	5	2.2	5 x 30	16

Table 7.2 Summary of waveguide laser results

The lasers all operated at 1.064μm and the results are shown in summary form in table 7.2. The performance of the original sample reported in chapter 6 is also given in the table for comparison purposes. There was a decrease in laser output power in these waveguides compared to the 5mm wide LPE waveguide sample. This was thought to be due to a reduced coupling efficiency of the focused diode-bar pump spot into the narrow end-face of the crystal. Despite this, the experiments did show that reducing the width of the laser medium had a beneficial effect on the beam quality in the non-guided direction. The overall improvement was not that dramatic though which suggests that other laser designs may prove to be more suitable. Rib or broad-stripe structures fabricated by ion-beam etching or milling techniques [18], may be a future way to access the benefit from a reduction in waveguide lateral dimension.

7.3.2 Unstable resonators

A more promising method for reducing the M^2 parameter in the non-guided direction is the unstable resonator [19, 20]. An unstable resonator is particularly suitable for high gain, large mode volume, high-power lasers. The technique involves using mirrors which diffract some of the beam out of the resonator, giving a geometric output coupling. With an unstable resonator the lowest order transverse mode can have a large mode volume as well as the lowest loss, leading to a high power output with good spatial coherence. An unstable resonator design has been used successfully in devices with high-gain, slab-shaped gain media such as CO [21] and CO_2 lasers [22], and also in a high-power monolithic Nd:YAG laser [23]. It has also been shown to work well with a relatively thick waveguide laser [3]. This particular waveguide design used a 200μm thick, 10mm wide Nd:YAG core contact bonded to a YAG substrate and an unstable resonator in the non-guided direction. The device gave M^2 values of 4.3 and 1.5 in the guided and non-guided directions respectively with an overall output power of 5W.

This last result prompted an initial investigation into making some form of unstable resonator. The preliminary experiments were carried out with a 19mm long, 5mm wide, 8μm thick Nd:YAG on sapphire waveguide. An unusual resonator based on a plane/plane cavity was explored. The pump source was a 20W fibre lensed diode-bar

(OptoPower Corp.) operating at 808nm. A 1.027-mm focal-length rod lens focused the diode-bar into the waveguide in the guided direction and focusing in the non-guided direction was provided by a 19-mm cylindrical lens, (see section 6.3.4). The laser resonator was formed in the usual way with thin dielectric mirrors. The laser operated on the four-level transition around 1.06μm and both input and output mirrors were highly reflecting at this wavelength. The input mirror was glued in place, and the mirror at the output face was held with a drop of fluorinated liquid. Output coupling through the exposed bare end-face was achieved by moving the output mirror across the back face of the waveguide. This method of varying the output coupling geometrically was tested to see if it resulted in any improvement in the beam quality.

Results from this cavity were compared to previous results (chapter 6) from the same waveguide laser with an output coupler, of nominally 50% transmission at 1.064μm, fully across the back face of the sample. With no spatial mode control the laser (reported in chapter 6, section 6.3.4.1) gave an output power of 3.7W and had an M^2 value of 85 in the non-guided direction. The optimum results from the new cavity design showed M^2 reduced from 85 to ~22 with half the output face covered with the mirror and a corresponding output power of 2.5W. This initial unstable/stable resonator technique has made some improvement in non-guided direction M^2, although as this was also accompanied by a reduction in output power the technique clearly needs to be optimised further.

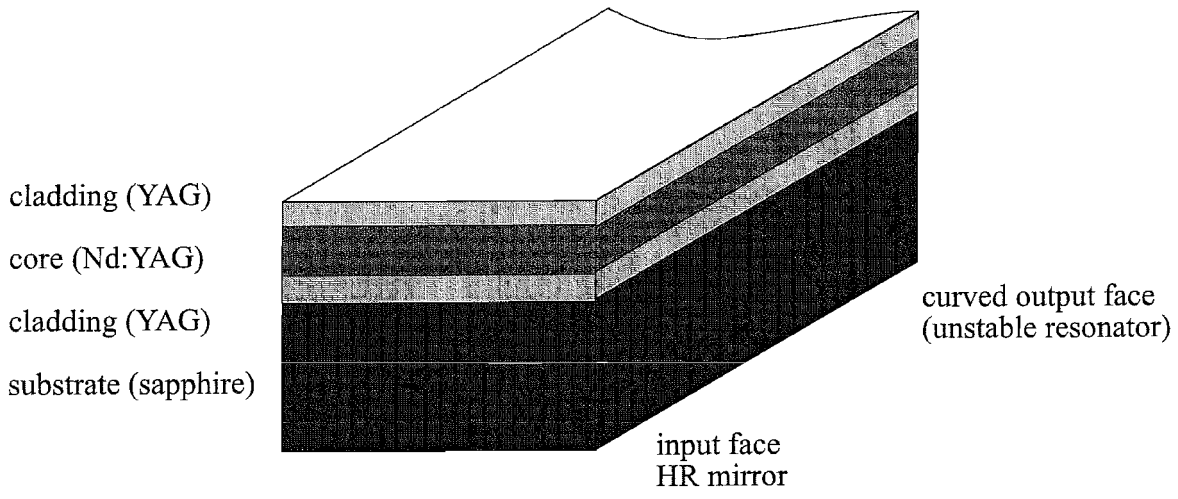

Figure 7.9 Possible design for an unstable resonator cavity in a planar waveguide

An unstable resonator made by curving one end-face of the waveguide may be a future possibility. This type of waveguide design is illustrated in figure 7.9. However, the fabrication issues associated with this device structure would need to be considered carefully.

7.3.3 Other methods to improve modal properties of a laser

Various other techniques providing modal discrimination in a laser cavity have been developed. Some of these will be briefly outlined here with a view to perhaps incorporating them into a future waveguide laser.

Resonators with unconventional mirrors have been successfully used to improve the modal properties of lasers . Examples include; variable reflectivity mirrors used in conjunction with unstable resonators [24, 25], and variable phase mirrors giving a flat near-field pattern in CO_2 lasers [26]. Intracavity mode selection elements have also been used to modify a laser beam profile and select a single higher order output mode. Elements fabricated from thin wire grids gave good power conversion efficiencies (~80% of multi-mode performance) for a CO_2 laser [27], and a spatial filter in the form of a grid of opaque strips flattened the beam profile of a Nd:YAG laser [28]. Arrays of semiconductor lasers have also benefited from some of these external resonator designs. Methods have included Fourier spatial filtering [29] and Talbot cavities and filters [30].

In addition to the techniques described so far diffractive optics can enhance laser cavity performance. Conventional mirrors can be replaced with diffractive optical elements in the cavity. A single diffractive element has already been demonstrated to discriminate against high order modes and produce a flattop laser beam from a bulk Nd:YAG laser [31]. A second diffractive element placed in the cavity, or an intracavity phase plate can provide further mode selection.

A further technique for improving the output mode quality of a waveguide laser is using a taper design. The wide end of the taper supports a large number of spatial modes and the narrow end of the taper can be designed to support fewer modes, or just a single one. The technique of adiabatic expansion has been demonstrated in

passive planar glass devices [32] and flared waveguide sections have been used to maintain fundamental mode operation in diode lasers [33].

Another approach to obtaining a high quality laser output is with a master oscillator/power amplifier (MOPA) [34] system. This involves using a well behaved, low power laser as the master oscillator and the output from this laser is then fed into a power amplifier stage, which could be a waveguide amplifier [35], to achieve high power operation. High output powers and improvements in spatial mode quality have also been achieved using a side-pumped multiple pass zig-zag laser design. The planar geometry of a waveguide lends itself to such a system where a relatively narrow signal beam could sweep out a broad gain region [36]. These designs and pumping schemes could perhaps in future be used in a waveguide device.

It may be possible to fabricate an unconventional mirror coating onto a planar waveguide end-face, or include a diffractive optical element in the cavity to aid mode selection or use the shape of the waveguide to improve the output quality of the laser. However it is important to try to maintain the attractive features of the planar waveguide; that is its simplicity and its monolithic nature, and avoid too complex a waveguide structure. Some of the ideas mentioned above offer ways of obtaining excellent spatial mode quality, but care must be taken to ensure that the performance of the overall waveguide laser continues to offer advantages over a bulk system.

7.4 Spatial mode control - Summary

This chapter has outlined a number of techniques for improving the beam quality of a waveguide laser both in the guided direction (with a metal overlayer or a double-clad design) and the non-guided direction (with reduced lateral dimensions, an unstable resonator etc). The aim is to produce high-power, close-to-diffraction-limited laser output from a waveguide. As this goal is approached the planar waveguide laser will become more attractive as a high-power, solid-state laser source with applications spanning the research, industrial and medical fields.

7.5 References

[1] C.T.A.Brown, R.D.Harris, D.P.Shepherd, A.C.Tropper, J.S.Wilkinson, B.Ferrand, IEEE Photon. Technol. Lett., **10**, pp.1392-1394 (1998)

[2] C.L.Bonner, T.Bhutta, D.P.Shepherd, A.C.Tropper, IEEE J. Quantum Electron., **36**, pp.236-242 (2000)

[3] A.A.Chesworth, D.Pelaez-Millas, H.J.Baker, D.R.Hall, Lasers 97, Munich, (1997)

[4] H.Nishihara, M.Haruna, T.Suhara, *'Optical Integrated Circuits'*, McGraw-Hill, New York, pp.18-21 (1989)

[5] C.R.Lavers, R.D.Harris, S.Hao, J.S.Wilkinson, K.O'Dwyer, M.Brust, D.J.Schriffin, J. Electroanal. Chem., **387**, pp.11-22 (1997)

[6] C.T.A.Brown, C.L.Bonner, T.J.Warburton, D.P.Shepherd, A.C.Tropper, D.C.Hanna, H.E.Meissner, Appl. Phys. Lett., **71**, 1997, pp.1139-41 (1997)

[7] for example V.Dominic, S.MacCormack, R.Waarts, S.Sandres, S.Bicknese, R.Dohle, E.Wolak, P.S.Yeh, E.Zucker, in *'Technical Digest of Conference on Lasers and Electro-Optics / Europe'*, 1998, post-deadline paper CPD11

[8] J.A.Alvarez-Chavez, J.Nilsson, P.W.Turner, W.A.Clarkson, C.C.Renaud, R.Sevas-Aguilar, D.C.Hanna, A.B.Grudinin, in *'Technical Digest of OSA Topical Meeting on Novel Lasers and Devices-Basic Aspects'*, Munich, 14-16 June 1999, paper LWA5

[9] D.Pelenc, *'Guide d'onde laser en Nd:YAG et Yb:YAG per E.P.L.'*, PhD Dissertation, Département Optronique du LETI, C.E.N.G. 85X 38041 Grenoble, France (1992)

[10] H.L.Offerhaus, N.G.Broderick, D.J.Richardson, R.Sammut, J.Caplen, L.Dong, Opt. Lett., **23**, pp.1683-1685 (1998)

[11] H.L.Offerhaus, J.A.Alvarez-Chavez, J.Nilsson, P.W.Turner, W.A.Clarkson, D.J.Richardson, in *'Technical Digest of Conference on Lasers and Electro-Optics'*, 1999, post-deadline paper CPD10

[12] A.Lucianetti, R.Weber, W.Hodel, H.P.Weber, A.Papashvili, V.A.Konyushkin, T.T.Basiev, Appl. Opt., **38**, pp.1777-1783 (1999)

[13] P.Lacovara, H.K.Choi, C.A.Wang, R.L.Aggarwal, T.Y.Fan, Opt. Lett., **16**, pp.1089-1091 (1991)

[14] D.P.Shepherd, C.L.Bonner, C.T.A.Brown, W.A.Clarkson, A.C.Tropper, D.C.Hanna, H.E.Meissner, Opt. Commun., **160**, pp.47-50 (1999)

[15] D.Pelenc, B.Chambrez, I.Chartier, B.Ferrand, C.Wyon, D.P.Shepherd, D.C.Hanna, A.C.Large, A.C.Tropper, Opt. Commum., **115**, pp.491-497 (1995)

[16] R.J.Beach, Appl. Opt., **35**, pp.2005-2015 (1996)

[17] A.E.Siegman, Appl. Opt., **13**, pp.353-367 (1974)

[18] N.Sugimoto, Y.Ohishi, Y.Katoh, A.Tate, M. Shimokozono, S.Sudo, Appl. Phys. Lett., **67**, pp.582-584 (1995)

[19] A.E.Siegman, '*Lasers*' University Science Books, pp.891-922 (1986)

[20] K.Kuba, T.Yamamoto, S.Yagi, Opt. Lett., **15**, pp.121-123 (1990)

[21] A.D.Colley, F.Villarreal, H.J.Baker, D.R.Hall, Appl. Phys. Lett., **54**, pp.1950-1952 (1994)

[22] P.E.Jackson, H.J.Baker, D.R.Hall, Appl. Phys. Lett., **54**, pp.1950-1952 (1989)

[23] H.Liu, S-H.Zhou, Y.C.Chen, Opt. Lett., **23**, pp.451-453 (1998)

[24] G.Giuliani, Y.K.Park, R.L.Byer, Opt. Lett., **5**, pp.491-493 (1980)

[25] S.De Silvestri, P.Laporta, V.Magni, G.Valentini, G.Cerullo, Opt. Commun., **77**, pp.179-184 (1990)

[26] P.-A.Bélanger, R.L.Lechance, C.Paré, Opt. Lett., **17**, pp.739-741 (1992)

[27] K.M.Abramski, H.J.Baker, A.D.Colley, D.R.Hall, Appl. Phys. Lett., **60**, pp.2469-2471 (1992)

[28] V.Kermene, A.Saviot, M.Vampouille, B.Colombeau, C.Froehly, Opt. Lett., **17**, pp.859-861 (1992)

[29] E.M.Philipp-Rutz, Appl. Phys. Lett., **26**, pp.475-477 (1975)

[30] J.R.Leger, M.L.Scott, W.B.Weldkamp, Appl. Phys. Lett., **52**, pp.1771-1773 (1988)

[31] J.R.Leger, D.Chen, Z.Wang, Opt. Lett., **19**, pp.108-110 (1994)

[32] A.F.Milton, W.K.Burns, IEEE J. Quantum Electron., **13**, pp.828-835 (1977)

[33] T.Tamanuki, T.Sasaki, M.Kitamura, Opt. and Quantum Electron., **28**, pp.513-517 (1996)

[34] M.A.Krainak, A.W.Yu, IEEE J. Quantum Electron., **32**, pp.112-117 (1996)

[35] D.P.Shepherd, C.T.A.Brown, T.J.Warburton, D.C.Hanna, A.C.Tropper, B.Ferrand, Appl. Phys. Lett., **71**, pp.876-878 (1997)

[36] T.M.Baer, D.F.Head, P.Gooding, G.J.Kintz, S.Hutchinson, IEEE J. Quantum Electron. **QE-28**, pp.1131-1138 (1992)

Chapter 8 Conclusion

8.1 Summary of results

This thesis has reported on progress towards diode-bar pumped crystal waveguide lasers with a high-power, high-quality output.

Much of the work reported in this thesis represents the first attempts to construct diode-bar pumped waveguide structures. This meant new techniques of waveguide fabrication capable of producing high NA waveguides had to be found and tested. Novel coupling schemes for coupling the divergent output from high-power diode-bars into the waveguide were devised. Work into the effect that such high intensity pumping might have on the waveguide laser material was also required. Then, once the device was seen to be capable of high-power operation, methods of controlling and improving the output were investigated.

A high numerical aperture (NA) waveguide is required to accommodate the highly divergent output from a diode-bar pump source. Three types of waveguide fabrication technique have been looked at in this thesis; liquid phase epitaxy (LPE), pulsed laser deposition (PLD) and direct bonding. The method of direct bonding was found to be particularly well suited to fabricating high NA waveguides for diode-bar pumped devices. The technique of LPE had already been shown to produce good quality, low loss waveguides, with spectroscopy similar to the bulk material [1]. However, there are limits to the material combinations that can be used and any lattice mismatch between the substrate and the core layer to be grown must be small. This means that waveguide lasers fabricated by LPE have been limited to the materials YAG, GGG and YLF. In general, the technique does not appear to be well suited to growing high NA waveguides.

This thesis has described the successful fabrication of high NA waveguides by PLD and direct bonding. A Nd:GGG on YAG waveguide fabricated by PLD was investigated and found to have the lowest loss (<0.5dB/cm) so far reported for a PLD layer (waveguide or otherwise) [2]. The waveguide lased both on the four-level laser

transition at around 1μm and, it is believed for the first time, on the quasi-three-level transition at a wavelengths around 940nm [3]. Although the material combination of GGG/YAG grown here gave a suitably high NA (0.75) for diode-bar pumping, good PLD film growth requires materials with similar lattice structure and similarly sized lattice constants. This requirement, similarly to LPE, limits the choice of material combinations and thus the waveguide NA that can be produced. In addition, the PLD process often results in high optical scattering losses in the waveguide and spectroscopy dissimilar to the bulk material. For these reasons PLD is not yet a reliable method of reproducibly fabricating high NA waveguides suitable for diode-bar pumping.

Direct bonding was found to be an excellent waveguide fabrication technique, reliably producing good quality waveguides with losses <0.5dB/cm and in some cases as low as 0.2dB/cm. There are few limits to the material combinations available for bonding so both low and high NA waveguides can be fabricated. Nd:GGG on YAG (NA=0.75), Nd:YAG on YAG (NA=0.06), Nd:YAG/sapphire (NA=0.46) and even Nd:YAG on glass (NA=0.82), waveguide lasers were demonstrated and these laser materials had the same spectroscopic characteristics as the bulk material [4]. Both YAG and sapphire have good thermal properties, similar thermal expansion co-efficients, they bond well together and provide a sufficiently high NA to contain the divergent diode-bar output. As a consequence, the YAG/sapphire waveguide combination fabricated by direct bonding is now the high NA waveguide of choice for diode-bar pumping [5].

Pumping the very confined volume of a planar waveguide with the high average power of a diode-bar leads to a high pump intensity and the effects that this might have on the waveguide were investigated. Auger energy-transfer upconversion had previously been identified as the main upconversion loss mechanism in Nd-doped crystals. The Auger upconversion parameter, carefully measured spectroscopically, was found here to be consistent with a bulk amplifier experiment [6]. The upconversion rate was measured to be $7x10^3s^{-1}$ and was around five times smaller than that found previously [7]. Modelling studies have then shown the effect that this

upconversion has on the gain, and also how the saturation of the absorption affects the gain available in an intensely pumped system.

Modelling end-pumped amplifiers, has shown that the Auger upconversion becomes significant in reducing the gain as soon as the absorbed power exceeds ~$0.5P_{sat}$, where P_{sat} is the power for which saturation intensity is achieved in the centre of the beam. The change in the distribution of the inversion due to the saturation of the pump absorption was also found to significantly degrade the small-signal gain. The larger the spot size ratio w_p/w_L, the larger the degradation. The reduction in gain can be up to 25% depending on the ratio w_p/w_L, with absorbed powers of just $0.5P_{sat}$, and in addition the upconversion leads to a significant additional heat load in the gain material.

The associated heat load for an intensely pumped system was also modelled to compare the performance of a waveguide with bulk slab and rod shaped gain media. The conclusions drawn from this are that a slab shape offers significant advantages over a rod due to the one dimensional heat flow, instead of the radial heat flow that is characteristic of a cylindrical gain medium. Similar, but slightly higher, temperature rises and thermally induced stress values were predicted in a planar waveguide compared to a bulk slab-shaped laser medium. This modelling suggests that the waveguide design with the best thermal management capabilities would be one fabricated in a thin slab, with a thin waveguide cladding layer and with the waveguide core positioned close to a cooled surface (a heatsink). Even though a slightly higher thermal load is predicted in a planar waveguide compared to a bulk slab-shaped laser media it is important to consider that the waveguide has other advantages such as its compact nature and optical confinement that should be taken into consideration.

Significant advances in coupling diode-bar pump lasers to planar waveguides have been made. High-power (20W) fibre-lensed diode-bars were coupled into the waveguides using a number of different methods. The first of these methods was bulk cylindrical lens coupling and led to an end-pumped planar waveguide with a maximum output power of 6.2W [8]. This device had an optical-to-optical conversion efficiency of 31% and an output beam quality (M^2) of 3 x 140 in the guided and non-guided directions respectively. End-pumping using high NA, graded refractive index

rod lens focussing provided a more compact pumping arrangement, and allowed the production of much smaller focussed spot sizes. This scheme required the use of high NA waveguides and output powers in excess of 3W were achieved with an overall optical-to-optical conversion efficiency of 20%.

Bulk cylindrical lens coupling and rod lens coupling were also both successful in demonstrating diode-bar side-pumped planar waveguide lasers. However, the most novel side-pumping technique was that of proximity coupling the diode-bar to the waveguide with no intervening optics. A first demonstration of this compact pumping scheme produced over 0.5W of output power from a simple Nd:YAG planar waveguide laser, with 6W of incident pump power provided by the diode-bar. The coupling efficiency into the 8μm-thick waveguide was found to be ~90% [9].

In the final experimental chapter of the thesis some techniques for improving the quality of the spatial mode output from the waveguide laser were demonstrated. In the guided direction an overlaid metal coating was used to increase the loss of the higher order TE modes in the cavity. This resulted in a slight improvement in the spatial mode quality of the laser and also leads to a polarised output as the loss of all the TM modes is increased [10]. A more successful technique was the use of a double-clad planar waveguide structure. A five-layer Yb:YAG structure was proximity coupled to a diode-bar pump laser and 2.2W of output power was obtained at a maximum pump power of 22W [11]. In the guided direction the divergence of the output was consistent with the laser operating in the fundamental mode with an M^2 very close to 1. Similar experiments with a five-layer Nd:YAG structure gave a laser output of 4W. Unlike a fibre where pump absorption can take place over a long length of gain medium, the design of double-clad, planar structures is limited by the length of device that can be fabricated with a low propagation loss. This results in the planar waveguides having a high core-to-cladding size ratio to achieve sufficient pump absorption over their short length. Thus mode selection occurs in the device due to the confinement of the gain, rather than the cladding pumping of a single-mode core as is normally the case in fibre lasers.

In the non-guided direction the technique of reducing the width of the gain region, and thus increasing the fraction of laser power in the lower order modes was the simplest

tested. However, this produced an improvement in M^2 values accompanied by a reduction in output laser power. An initial investigation into an unstable resonator cavity design as a means to improving M^2 in the non-guided direction was promising. The lasing output from a diode-bar pumped waveguide laser with rod-lens coupling showed an improvement in M^2 from 85 to ~22, while the output power was observed to decrease from 3.7W to 2.5W. From these preliminary results it seems as though a double-clad structure combined with an unstable resonator design may be the best technique for improving waveguide laser beam quality.

The results summarised here show how research has progressed in stages towards the goal of a compact high-power laser exploiting the benefits of a planar waveguide geometry to create a simple, efficient device with as few components as possible. A number of the results have been the first of their kind reported and future work in the field will be needed to improve many aspects of the device design.

8.2 Future Work

The future of diode-bar pumped waveguide devices will probably be dependent both on the ever increasing availability and reliability of higher power diode-bar pump lasers, and also on the improvements that can be made in the output spatial mode quality of diode-bar pumped waveguide lasers.

Future work leads on from the topics discussed in this thesis in a number of directions. A high priority must be given to methods of improving the output beam quality. A planar waveguide comprises a slab-shaped high-gain core region, similar to that available in CO_2 lasers. Unstable resonator techniques have been successfully used to improve the spatial mode of CO_2 lasers, and initial investigations seem to point to methods based on unstable resonator techniques also being of use with planar waveguides. It may be possible, with the direct bonding technique, to construct a curved waveguide end-face to form part of a monolithic unstable resonator cavity, but an extended cavity design could also be employed.

Another technique for improving the output mode quality of a waveguide laser is using a taper design. The wide end of the taper supports a large number of spatial

modes and the narrow end of the taper can be designed to support fewer modes, or just a single one. The wide, multi-mode taper end would allow diode-bar pumping, but the laser would be forced into single-mode operation by the narrow taper end. If an adiabatic expansion occurs the laser would maintain single-mode operation, even in the multi-mode section. The technique of adiabatic expansion has been demonstrated in passive planar glass devices [12]. More recently flared waveguide sections have been used to maintain fundamental mode operation in diode lasers [13], producing high-power, low divergence diffraction-limited output at 1.5μm. Direct bonding may be a suitably versatile fabrication technique for the construction of such waveguide tapers or instead, a basic planar structures produced by direct bonding could be patterned by another process such as indiffusion.

In the future a waveguide amplifier, a device that has not been studied in the course of this work, could be investigated. A waveguide structure is an attractive option for an optical amplifier as the confinement of the pump and signal radiation to the waveguide core can lead to higher gains for lower pump powers than in bulk amplifiers. In addition it may be possible to maintain the spatial quality of the signal laser in the non-guided direction of the waveguide. An applications area for such an amplifier might be in a master oscillator/power amplifier (MOPA) [14] system. In this arrangement the master oscillator is provided by a well behaved, low power laser source, which can be modulated to provide a pulsed output if desired. The output from this laser is then fed into a power amplifier stage, which could be a waveguide amplifier, to achieve high power operation. The MOPA approach has been demonstrated in semiconductors and bulk lasers and the area of waveguide amplifiers looks promising.

The excellent thermal management capabilities of a slab shape are well recognised. The side-pumped planar geometry also lends itself to multiple pass zig-zag laser designs where a relatively narrow signal beam could sweep out a broad gain region [15]. These designs and pumping schemes could perhaps in future be used in a waveguide device.

There is great potential for providing integrated functions within waveguide devices but additional work is needed to fully realise and exploit it. In principle, elements such as switches, filters and reflectors could be incorporated into the waveguide to create a versatile device, and this could perhaps be integrated with a butted semiconductor pump source. While YAG offers few of the attractive properties of a material like $LiNbO_3$, the direct bonding technique could allow components such as a saturable absorber Q-switch (Cr:YAG) to be attached to a section of gain material. Polarisation control would also be possible and TE polarised output has already been demonstrated both with a metal coating on an unclad waveguide, and in a five-layer direct bonded structure. In addition a non-linear section of the waveguide device, for example periodically poled $LiNbO_3$ could frequency-double the output from a Nd:YAG waveguide laser source.

Waveguide lasers and amplifiers are therefore well placed to provide compact solutions in applications areas requiring multi-Watt output powers with a small device footprint. However, further work seems to be needed to improve the spatial mode quality of these planar waveguide devices, without adding significant complexity to the waveguide cavity. It will then be possible to fully exploit the inherent compact nature, functionality and good thermal characteristics of a planar crystal waveguide, in an active high-power device.

8.3 References

[1] B.Ferrand, D.Pelenc, I.Chartier, Ch.Wyon, J. Crys. Growth. **128**, pp.966-969 (1993)

[2] A.Anderson, R.W.Eason, L.M.B.Hickey, M.Jelinek, C.Grivas D.S.Gill, N.Vainos, Opt. Lett., **22**, pp.1556-1558 (1997)

[3] C.L.Bonner, A.A.Anderson, R.W.Eason, D.P.Shepherd, D.S.Gill, C.Grivas, N.Vainos, Opt. Lett., **22**, pp.988-990 (1997)

[4] C.T.A.Brown, C.L.Bonner, T.J.Warburton, D.P.Shepherd, A.C.Tropper, D.C.Hanna, H.E.Meissner, Appl. Phys. Lett., **71**, pp.1139-41 (1997)

[5] D.P.Shepherd, C.L.Bonner, C.T.A.Brown, W.A.Clarkson, A.C.Tropper, D.C.Hanna, H.E.Meissner, Opt. Commun., **160**, pp.47-50 (1999)

[6] S.Guy, C.L.Bonner, D.P.Shepherd, D.C.Hanna, A.C.Tropper, B.Ferrand, IEEE J. Quantum Electron. **QE-34**, pp.900-909 (1998)

[7] Y.Guyot, H.Manaa, J.Y.Rivoire, R.Moncorgé, N.Garnier, E.Descroix, M.Bon, P.Laporte, Phys. Rev. B, **51**, pp.784-799 (1995)

[8] C.L.Bonner, C.T.A.Brown D.P.Shepherd, W.A.Clarkson, A.C.Tropper, D.C.Hanna, B.Ferrand, Opt. Lett., **23**, pp.942-944 (1998)

[9] C.L.Bonner, T.Bhutta, D.P.Shepherd, A.C.Tropper, D.C.Hanna, H.E.Meissner, in '*Technical Digest of Conference on Lasers and Electro-Optics*', 1999, paper CThD6

[10] C.T.A.Brown, R.D.Harris, D.P.Shepherd, A.C.Tropper, J.S.Wilkinson, B.Ferrand, IEEE Photon. Technol. Lett., **10**, pp.1392-1394 (1998)

[11] C.L.Bonner, T.Bhutta, D.P.Shepherd, A.C.Tropper, IEEE J. Quantum Electron., **36**, pp.236-242 (2000)

[12] A.F.Milton, W.K.Burns, IEEE J. Quantum Electron., **13**, pp.828-835 (1977)

[13] T.Tamanuki, T.Sasaki, M.Kitamura, Opt. and Quantum Electron., **28**, pp.513-517 (1996)

[14] M.A.Krainak, A.W.Yu, IEEE J. Quantum Electron., **32**, pp.112-117 (1996)

[15] T.M.Baer, D.F.Head, P.Gooding, G.J.Kintz, S.Hutchinson, IEEE J. Quantum Electron. **QE-28**, pp.1131-1138 (1992)

Appendix A: Temperature distribution in a waveguide – a non-uniformly pumped slab

The approach taken in this analysis is to use a one dimensional heat flow equation to model the temperature distribution in a planar waveguide. This technique models the waveguide as a non-uniformly pumped slab, following the method used in reference 1 and described in chapter 5 for a slab shaped material.

(i) Double-sided cooling

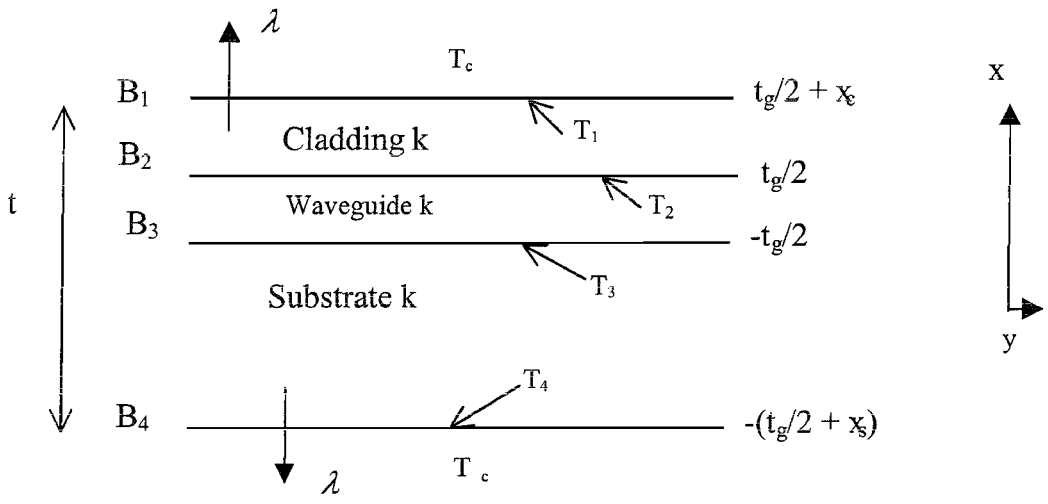

Figure 1 Illustration of the waveguide geometry used in temperature distribution modelling

The waveguide geometry shown in figure 1 was used.

The steady-state heat input per unit volume is Q (x,y) Wcm^{-3}, and is assumed to be independent of z. The waveguide is assumed to be cooled through the faces normal to the x direction. The heat transfer coefficient is λ at each surface.

The analysis is based on a slab of infinite extent in the y-direction so that heat flow is in the x-direction only.

The temperature distribution in the medium must then obey the equation:

$$\nabla^2 T = \frac{\delta^2 T(x)}{\delta x^2} = \begin{Bmatrix} 0 \\ -\frac{Q}{k} \\ 0 \end{Bmatrix} \quad \text{for} \quad \begin{matrix} x > \frac{t_g}{2} \\ -\frac{t_g}{2} \le x \le \frac{t_g}{2} \\ x < -\frac{t_g}{2} \end{matrix} \qquad \text{A1}$$

Where T_c is the temperature of the cladding and substrate heat sinks, $T_1 - T_4$ are the temperatures of the boundaries B_1-B_4, k is the thermal conductivity ($Wcm^{-1}K^{-1}$). t is the slab thickness, and t_g, t_s and t_c are the waveguide, substrate and cladding thicknesses respectively.

Equation A1 has T varying quadratically in the core of the waveguide and linearly in the cladding and substrate and has solutions of the form:

$$T(x) = \begin{Bmatrix} ax + b \\ cx^2 + dx + e \\ fx + g \end{Bmatrix} \quad \text{for} \quad \begin{matrix} x > \frac{t_g}{2} \\ -\frac{t_g}{2} \le x \le \frac{t_g}{2} \\ x < -\frac{t_g}{2} \end{matrix} \qquad \text{A2}$$

and has boundary conditions:

B1 $\quad -k\frac{\delta T}{\delta x} = \lambda(T_1 - T_c) \quad ax+b=T_1 \quad$ where: $x=x_c+t_{g/2}$

B2, B3 $\quad \frac{\delta T}{\delta x}$ continuous $\quad$ T continuous

B4 $\quad k\frac{\delta T}{\delta x} = \lambda(T_4 - T_c) \quad fx+g=T_4 \quad$ where: $x=-x_s-t_{g/2}$

Solving the heat flow equation in the guided region and applying the boundary condition produces the following coefficients:

$$a = -Qt_g\left(\frac{\frac{1}{\lambda}+\frac{x_s}{k}+\frac{t_g}{2k}}{\frac{2k}{\lambda}+x_c+x_s+t_g}\right) \qquad b = g = -\frac{ak}{\lambda}\left(1+\frac{\lambda x_c}{k}+\frac{\lambda t_g}{2k}\right)+T_c$$

$$c = -\frac{Q}{2k} \qquad d = a+\left(\frac{Qt_g}{2k}\right)$$

$$e = b-\frac{Qt^2{}_g}{8k} \qquad f = a+\frac{Qt_g}{k}$$

A3

Substitution of the coefficients a-g (A3) into equation A2 leads to a description of the temperature distribution within the planar waveguide. The model has been used in chapter 5 to calculate the temperature rise expected in an 10μm Nd:YAG waveguide mounted on a water cooled heatsink.

(ii) One-sided cooling

The analysis of cooling the slab from one side only, i.e with different heat transfer coefficients (λ) at each surface, is carried out using the 1 D heat flow equation as described in part (i) of this appendix.

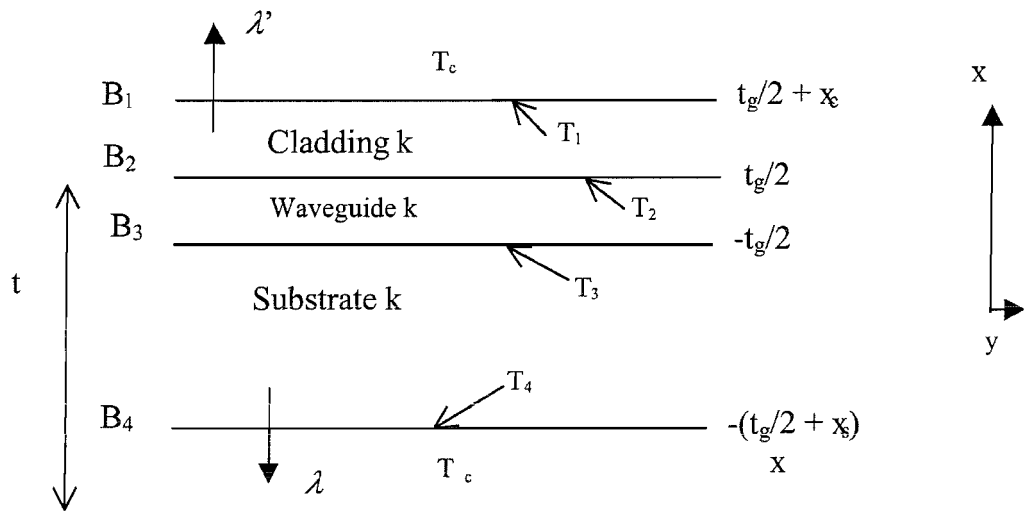

Figure 2 Illustration of the waveguide geometry used in temperature distribution modelling, with one-sided cooling

The temperature distribution in the slab medium shown in figure 2 is described by equation A1. In A1 T varies quadratically in the core of the waveguide and linearly in the cladding and substrate, it has solutions of the form A2, shown below:

$$T(x) = \begin{Bmatrix} ax + b \\ cx^2 + dx + e \\ fx + g \end{Bmatrix} \quad \text{for} \quad \begin{matrix} x > \frac{t_g}{2} \\ -\frac{t_g}{2} \le x \le \frac{t_g}{2} \\ x < -\frac{t_g}{2} \end{matrix} \qquad \text{A2}$$

and boundary conditions:

$$\text{B1} \qquad -k\frac{\delta T}{\delta x} = \lambda'\left(T_1 - T_c\right) \qquad ax+b=T_1 \qquad \text{where: } x=x_c+t_{g/2}$$

B2, B3	$\frac{\delta T}{\delta x}$ continuous	T continuous	
B4	$k\frac{\delta T}{\delta x} = \lambda\left(T_4 - T_c\right)$	$fx+g=T_4$	where: $x=-x_s-t_{g/2}$

Solving the heat flow equation in the guided region and applying the boundary condition produces the following coefficients:

$$a = -Qt_g\left(\frac{\frac{1}{\lambda}+\frac{x_s}{k}+\frac{t_g}{2k}}{\frac{k}{\lambda'}+\frac{k}{\lambda}+x_c+x_s+t_g}\right) \qquad b = g = -a\left(\frac{k}{\lambda'}+x_c+\frac{t_g}{2}\right)+T_c$$

$$c = -\frac{Q}{2k} \qquad d = a+\left(\frac{Qt_g}{2k}\right)$$

$$e = b-\frac{Qt^2{}_g}{8k} \qquad f = a+\frac{Qt_g}{k}$$

A3

Substitution of the coefficients a-g (A3) into equation A2 leads to a description of the temperature distribution within a planar waveguide with different heat transfer coefficients (e.g two different methods of cooling) at its faces.

References

[1] J.M.Eggleston, T.J.Kane, K.Kuhn, J.Unternahrer, R.L.Byer, IEEE J. Quantum Electron. **QE-20**, pp.289-301 (1984)

Appendix B: Publications arising from work reported in this thesis

B1 Refereed Journal Papers:

Bonner, C.L., Anderson, A.A., Eason, R.W. and Shepherd, D.P., Gill, D.S., Grivas, C. and Vainos, N, 'Performance of a low loss pulsed laser deposited Nd:$Gd_3Ga_5O_{12}$ waveguide laser at 1.06 μm and 0.94 μm', Optics Letters, **22** pp. 988-990, (1997)

Brown, C.T.A., **Bonner, C.L.,** Warburton, T.J., Shepherd, D.P., Tropper, A.C. and Hanna, D.C, 'Thermally bonded planar waveguide lasers', Applied Physics Letters, **71** pp.1139-1141, (1997)

Anderson, A.A., **Bonner, C.L.,** Shepherd, D.P., Eason, R.W., Grivas, C., Gill, D.S. and Vainos, N, 'Low loss (0.5 dB/cm) Nd:$Gd_3Ga_5O_{12}$ waveguide layers grown by pulsed laser deposition', Optics Communications, **144**, pp.183-186, (1997)

Guy, S., **Bonner, C.L.,** Shepherd, D.P., Hanna, D.C., Tropper, A.C and Ferrand, B, 'High-Inversion densities in Nd:YAG: upconversion and bleaching' IEEE Journal of Quantum Electronics, **34**, pp.900-909, (1998)

Bonner, C.L., Brown, C.T.A., Shepherd, D.P., Clarkson W.A., Tropper, A.C, Hanna, D.C. and Ferrand, B. 'Diode-bar end-pumped high-power Nd:$Y_3Al_5O_{12}$. planar waveguide laser', Optics Letters, **23** pp.942-944, (1998)

Shepherd, D.P., **Bonner, C.L.,** Brown, C.T.A., Shepherd, D.P., Clarkson, W.A., Tropper, A.C, Hanna, D.C. and Meissner, H, 'High-numerical-aperture, contact-bonded, planar waveguides for diode-bar-pumped lasers', Optics Communications, **160**, pp.47-50, (1999)

Bonner, C.L., Bhutta, T., Shepherd, D.P. and Tropper, A.C., 'Double-clad structures and proximity coupling for diode-bar-pumped planar waveguide lasers', IEEE J. Quantum Electron., **36**, pp.236-242, (2000)

B2 Conference Publications:

Anderson, A.A., **Bonner, C.L.,** Eason, R.W., Shepherd, D.P., Gill, D.S., Grivas, C. and Vainos, N. 'A low-loss waveguide laser grown by pulsed laser deposition', Proc 11, Paper CWQ1, Conference on Lasers and Electro-Optics, Baltimore, USA, 1997

Bonner, C.L., Anderson, A.A., Eason, R.W., Shepherd, D.P., Gill, D.S., Grivas, C., and Vainos, N. 'Nd:GGG PLD waveguide lasers', Miniature Coherent Light Sources in Dielectric Media, Les Houches Summer School, 1997

Shepherd, D.P., Brown, C.T.A., **Bonner, C.L.,** Guy, S., Clarkson W.A., Hanna, D.C., Tropper, A.C and Ferrand, B. '1.5W diode-pumped monolithic planar waveguide laser', Post deadline paper. PD1.1, Conference on Lasers and Electro-Optics-Pacific Rim, Chiba, Japan, 1997

Bonner, C.L., Shepherd, D.P., Brown, C.T.A., Anderson, A. A., Warburton, T.J., Tropper, A.C., Eason, R.W. and Hanna, D.C. 'High numerical aperture planar waveguides', Technical Digest Page 112, National Quantum Electronics Conference 13, Cardiff, U.K, 1997

Brown, C.T.A., Shepherd, D.P., Harris, R.D., **Bonner, C.L.,** Tropper, A.C., Clarkson, W.A., Hanna, D.C. and Ferrand, B. 'Towards a high-power, brightness-enhanced, polarised, diode-bar pumped planar waveguide laser', Post deadline paper PD1, OSA Annual Meeting, Long Beach, USA, 1997

Bonner, C.L., Brown, C.T.A., Shepherd, D.P., Clarkson W.A., Tropper, A.C, Hanna, D.C. and Ferrand, B. 'A diode-bar pumped, high-power, planar Nd:$Y_3Al_5O_{12}$ waveguide laser', Paper CThT5, Conference on Lasers and Electro-Optics San Francisco, USA, 1998

Bonner, C.L., Brown, C.T.A., Shepherd, D.P., Clarkson W.A., Harris, R.D., Tropper, A.C, Hanna, D.C. and Ferrand, B. 'In-plane diode-bar pumped, multiwatt,

Nd:$Y_3Al_5O_{12}$ planar waveguide lasers', Paper CTuB1 (Invited), Conference on Lasers and Electro-Optics-Europe, Glasgow, UK, 1998

Tropper, A.C., **Bonner, C.L.,** Brown, C.T.A., Shepherd, D.P., Clarkson W.A., Hanna. D.C. 'Diode-bar pumped, planar waveguide lasers', Paper TuN1 (Invited), LEOS, Orlando, USA, 1998

Bonner, C.L., Bhutta, T., Shepherd, D.P., Tropper, A.C, Hanna, D.C. and Meissner, H, 'Proximity-coupled, diode-bar-pumped, waveguide laser', Paper CThD6, Conference on Lasers and Electro-Optics, Baltimore, USA, 1999

Bhutta, T., **Bonner, C.L.,** Shepherd, D.P., Tropper. A.C. 'Diode-bar-pumped planar waveguide lasers: double - clad structures and proximity coupling', Paper 8-1, Technical Digest pp.69, National Quantum Electronics Conference 14, Manchester, UK, 1999